NNT/NL : 2020AIXM0001/001ED000

THÈSE DE DOCTORAT

Soutenue à Aix-Marseille Université
le 11 octobre 2023 par

Vlad DEDU

Search for CP violation in semileptonic B meson decays at the LHCb experiment

Discipline
Physique et Sciences de la Matière

Spécialité
Physique des Particules et Astroparticules

École doctorale
Physique et Sciences de la Matière (ED 352)

Laboratoire/Partenaires de recherche
Centre de Physique des Particules de Marseille (CPPM)
Large Hadron Collider beauty (LHCb)

Composition du jury

Cristinel DIACONU CPPM (CNRS/IN2P3)	Président du jury
Emi KOU IJCLab (CNRS/IN2P3)	Rapporteuse
Matthew CHARLES LPNHE (CNRS/IN2P3)	Rapporteur
Lucia GRILLO University of Glasgow	Examinatrice
Marcello ROTONDO INFN-LNF	Examinateur
Olivier LEROY CPPM (CNRS/IN2P3)	Directeur de thèse
Anton POLUEKTOV CPPM (CNRS/IN2P3)	Co-directeur de thèse

Affidavit

I, undersigned Vlad Dedu, hereby declare that the work presented in this manuscript is my own work, carried out under the scientific direction of Anton Poluektov and Olivier Leroy, in accordance with the principles of honesty, integrity and responsibility inherent to the research mission. The research work and the writing of this manuscript have been carried out in compliance with both the french national charter for Research Integrity and the Aix-Marseille University charter on the fight against plagiarism.

This work has not been submitted previously either in this country or in another country in the same or in a similar version to any other examination body.

Marseille
July 03, 2023

Acknowledgements

First of all, I want to express my gratitude to my supervisor, Anton Poluektov, for always being there and helping with any possible issue I had, either scientific or personal. Your presence and guidance have been invaluable to my work which ultimately resulted in this thesis. You were always available to discuss and answer my questions (even during the Covid-19 pandemic). I am very grateful for your patience and pedagogical abilities to discuss and explain the same topic several times if needed in order to make sure I understand it. In general, I consider myself very lucky to have had you as supervisor and to have worked with you for these three years. I have learned a lot from you during this time, and it is close to impossible to compare myself at the start of the PhD and now, at the end of it, in terms of the knowledge and experience I acquired under your guidance. Finally, I want to thank you for reading this thesis and providing many useful comments and suggestions.

I want to thank Olivier Leroy for his general guidance and advice and for his help with various specific aspects of the analysis. I also thank Olivier for reading this thesis several times and providing very useful comments. Furthermore, I want to express my appreciation for the support from both the previous and actual members of the LHCb group in Marseille. I thank Dorothea and Julien for many friendly discussions and scientific advice. Special thanks goes to Raul and Resmi for their help with some parts of the analysis. Finally, I want to thank the rest of my PhD and postdoc friends from Marseille: Bianca, Lauri, Nemer, Jacopo, Gaya, Bogdan, Andy and Chen for their support, help and many friendly interactions.

Many thanks go to Matthew Charles and Emi Kou for agreeing to be part of my defense jury as rapporteurs. Thank you for reading this thesis and for the numerous comments and suggestions you provided. Your feedback was extremely helpful and it helped me to better understand some parts of the thesis, see the bigger picture, and express those ideas more carefully and more clearly. In addition, I wish to thank the LHCb semileptonic working group, in particular Biljana, Lucia, Greg and Marcello, for providing many valuable comments and suggestions on the analysis as it progressed. I also want to thank Adam, Yipeng and Manuel for their help with some technical issues. Special thanks go to Lucia and Marcello for agreeing to be part of my defense jury as examinateurs and for their useful comments and discussions that followed.

Last but not least, I want to thank my family and friends for supporting me during the three years of the PhD journey. Special thanks go to Irina for her support during the last months and the writing of this thesis.

Liste de publications et participation aux conférences

Liste des publications réalisées dans le cadre du projet de thèse:

1. V. Dedu, Measurement of *CP*-violating observables in $\overline{B}^0 \to D^{*+}\mu^-\overline{\nu}_\mu$ decays at the LHCb experiment, JRJC 2021- Journées de Rencontres Jeunes Chercheurs. Book of Proceedings. 2022.

2. V. Dedu and A. Poluektov, Towards the precision measurement of *CP* violation in $B \to D^*\mu\nu$ decays at LHCb, [arXiv:2304.00966], JHEP 07 (2023) 063

Participation aux conférences et écoles d'été au cours de la période de thèse:

1. GDR-InF annual workshop, Nov 2021, Paris, France

2. IN2P3 School Of Statistics, May 16-20 2022, Carry-le-Rouet, France

3. 2022 European School of High-Energy Physics, Nov 31-Dec 13 2022, Israel

Contents

Résumé

La mesure d'effets violant *CP* dans les désintégrations semileptoniques, telles que $B^0 \to D^{*-}\mu^+\nu_\mu$, permet de tester le Modèle Standard (MS) sans ambivalence: toute violation de *CP* impliquerait sans ambiguïté la présence de Nouvelle Physique (NP) dans ces désintégrations. Selon certains scénarios de NP, la distribution angulaire de $B^0 \to D^{*-}\mu^+\nu_\mu$ donne lieu à certains termes antisymétriques par les transformations discrètes P (parité) et CP (conjugaison de charge et parité) qui sont rigoureusement absents dans le MS. L'analyse présentée dans cette thèse propose une nouvelle méthode ne dépendant d'aucun modèle spécifique pour mesurer ces termes, tout en annulant les termes présents dans le MS et donc les incertitudes théoriques ou expérimentales qui leur sont associées.

L'analyse est réalisée en utilisant 5,4 fb^{-1} de données de collisions proton-proton (pp) collectées au cours des années 2016-2018 du Run 2 par le détecteur LHCb du CERN. Grâce à des techniques d'approximation spécifiques permettant d'évaluer les paramètres cinématiques du neutrino échappant à la détection, on peut de mesurer, d'une part, des asymétries par la transformation CP qui démontreraient la présence de NP et, d'autre part, les asymétries par la transformation P qui devraient être nulles par principe quelque soit le modèle (MS ou NP) et qui permettent ainsi de contrôler la méthode. L'ajustement aux données d'un modèle discrétisé est effectué pour extraire les couplages NP des asymétries *CP*.

Les incertitudes systématiques les plus importantes sont prises en compte et estimées. Des bruits de fond qui polluent l'échantillon de données sélectionnées peuvent donner naissance à des asymétries par P ou CP non nulles et peuvent produire des biais dans la mesure des couplages de NP. Un ajustement par maximum de vraisemblance est effectué pour estimer les différentes fractions de bruit de fond dans les données. L'ampleur des biais est estimée à l'aide d'une simulation MC des bruits de fond produisant des asymétries. En outre, la mesure des couplages de NP peut également être biaisée par des effets instrumentaux, tels qu'un mauvais alignement du détecteur ou une non-uniformité des efficacités de reconstruction. Les biais lié à l'alignement des éléments du détecteur est estimé à l'aide d'une simulation MC artificiellement désalignée. Une approche basée sur les données utilisant un échantillon de contrôle complètement symétrique quelque soient les scénarios NP est proposée pour contrôler tous les biais liés aux efficacités de reconstruction.

L'ajustement aux asymétries P insensibles à la NP donne des résultats cohérents avec les attentes, validant ainsi la méthode utilisée. Quant aux asymétries *CP* sensibles à la NP, les valeurs des résultats de l'ajustement sont masquées jusqu'à la finalisation de l'analyse et seules les valeurs des incertitudes statistiques et systématiques sont donnés.

Abstract

The measurement of *CP*-violating effects in B meson semileptonic decays serves as a null test of the Standard Model (SM): any *CP* violation would unambiguously imply the presence of New Physics (NP) in these decays. Certain NP scenarios give rise to observable parity- and *CP*-odd terms in the otherwise parity-even $B^0 \to D^{*-}\mu^+\nu_\mu$ angular distribution. The analysis presented in this thesis proposes a novel model-independent method to measure the parity- and *CP*-odd terms while effectively cancelling out the parity-even terms and their associated theory uncertainty.

The analysis is performed using 5.4 fb^{-1} of proton-proton (pp) collision data collected during the 2016-2018 years of Run 2 by the LHCb detector at CERN. Using approximation techniques to reconstruct the neutrino and consequently, the kinematic parameters that describe the angular distribution, parity and *CP* asymmetries can be constructed. The *CP* asymmetries are sensitive to the various NP couplings while the parity asymmetries are expected to be zero whether in SM or NP due to theoretical considerations and can serve as a useful control channel. A binned template fit is performed to extract the NP couplings from the *CP* asymmetries in data using NP templates derived from Monte-Carlo (MC) simulation.

The most significant systematic uncertainties are considered and estimated. Parity- and *CP*-odd effects which may arise in backgrounds that pollute the signal data sample can produce biases in the NP couplings measurement. A binned maximum likelihood fit is performed to estimate the various background fractions in data. The magnitudes of the biases are estimated using MC simulation of the specific background processes where parity-odd effects are possible. Furthermore, the NP couplings measurement may also be biased by parity- and *CP*-odd instrumentation effects such as detector misalignment and non-uniform reconstruction efficiencies. The bias due to the misalignment of detector elements is estimated using artificially misaligned MC simulation. A data-driven approach using the control sample that is completely parity-even even in NP scenarios is proposed to control any parity-odd effects which may appear in the reconstruction efficiency.

The results of the fit to the *CP* asymmetries are still blinded and only the statistical and estimated systematic uncertainties are reported for this channel. However, the fit to the parity asymmetries as a control channel is unblinded and the results are consistent with the expectations considering the uncertainties.

Synthèse en Français

Cadre théorique

Le Modèle Standard (MS) est la théorie la plus aboutie de la physique des particules depuis sa formulation dans les années 1970. Il décrit les particules élémentaires et leurs interactions en termes de trois des quatre forces connues dans la nature : la force électromagnétique, la force forte et la force faible (le modèle standard ne tient pas compte de la gravitation). Le modèle standard a passé de nombreux tests et la grande majorité des observations expérimentales sont conformes à ses prédictions. Une propriété importante prédite par le modèle standard est l'universalité de la saveur leptonique (LFU en anglais pour *Lepton Flavor Universality*). Elle stipule que l'interaction des leptons avec les bosons de jauge électrofaibles est indépendante de la saveur des leptons. Plusieurs expériences, dont LHCb, Belle, Belle2 et BaBar, ont testé cette propriété dans diverses désintégrations des hadrons b avec des leptons dans l'état final. De nombreux résultats provenant de toutes ces expériences montrent des tensions de 2-3σ par rapport aux prédictions MS du LFU. Collectivement, tous les écarts par rapport au MS récemment mesurés dans les désintégrations des beaux hadrons sont connus sous le nom d'*anomalies de saveur*.

Généralement, les tests LFU sont effectués en mesurant les rapports des fractions d'embranchement des désintégrations de hadrons beaux où seuls les leptons de l'état final sont différents. Le principal avantage de ces mesures de rapport est que la plupart des incertitudes théoriques et expérimentales sont annulées. Les deux principales classes de désintégrations pour lesquelles des tests LFU sont effectués sont les transitions $b \to s\ell^+\ell^-$ et $b \to c\ell\nu_\ell$. En ce qui concerne le canal $b \to c\ell\nu_\ell$, les deux principales observables qui ont suscité un grand intérêt ces dernières années sont les rapports $\mathscr{R}(D)$ et $\mathscr{R}(D^*)$ pour lesquelles le résultat expérimental moyen combinée est à plus de 3σ de la prédiction MS [1]. Ces rapports sont donnés par

$$\begin{aligned}
\mathscr{R}(D) &= \frac{\mathscr{B}(B \to D\tau\nu_\tau)}{\mathscr{B}(B \to D\ell\nu_\ell)},\ \ell = \mu, e,\\
\mathscr{R}(D^*) &= \frac{\mathscr{B}(B \to D^*\tau\nu_\tau)}{\mathscr{B}(B \to D^*\ell\nu_\ell)},\ \ell = \mu, e.
\end{aligned} \tag{0.1}$$

Pour compléter la recherche directe de la non-universalité de la saveur leptonique, d'autres observables sensibles aux effets NP dans $b \to c\ell\nu_\ell$ ont été proposées. Cette thèse suit l'approche donnée dans [2] et se concentre sur la mesure d'observables violant *CP* comme moyen de contraindre et de distinguer les différents scénarios de

NP. Les effets violant CP dans $b \to c\ell\nu_\ell$ ne peuvent apparaître que comme des effets cinématiques dans les distributions angulaires. Par conséquent, pour accéder aux observables violant CP, les distributions angulaires doit être reconstruites. Comme dans ces désintégrations les tensions entre les résultats expérimentaux et les prédictions du MS sont observées jusqu'à présent dans les rapports impliquant des leptons τ, cela suggère la présence de NP dans les désintégrations $b \to c\tau\nu_\tau$. Cependant, comme les τ se désintègrent dans des états finaux qui incluent un ou deux neutrinos qui ne peuvent pas être reconstruits dans l'expérience, ces désintégrations sont très difficiles à traiter et la quantité de mouvement des τ, $\vec{p}_\tau$, ne peut pas être reconstruite avec une bonne précision. Il est donc logique de commencer par mesurer les effets de violation de CP dans $B^0 \to D^{*-}\mu^+\nu_\mu$ puisque sa distribution angulaire est entièrement reconstruite. Même si les anomalies de saveur sont de préférence expliquées par la NP dans $b \to c\tau\nu_\tau$, la même NP peut affecter $b \to c\mu\nu_\mu$ et peut conduire à des écarts mesurables par rapport au SM dans la distribution angulaire de $B^0 \to D^{*-}\mu^+\nu_\mu$.

La distribution angulaire de $B^0 \to D^{*-}\mu^+\nu_\mu$ est entièrement décrite par quatre paramètres cinématiques: la masse invariante au carré du système leptonique q^2 et les trois angles d'hélicité indiqués sur la figure 1. Les angles sont définis dans les cadres référentiels au repos de leur particule mère intermédiaire respective. L'axe z est choisi de telle sorte qu'il est aligné avec la direction du D^{*-} dans le référentiel au repos du B^0. Les angles ont les définitions suivantes

- $\boldsymbol{\theta_D}$ est l'angle polaire entre la direction du méson $\overline{D}^0$ et la direction opposée du méson B^0 dans le référentiel au repos du méson D^{*-} ($\theta_D \in [0,\pi]$)
- $\boldsymbol{\theta_\ell}$ est l'angle polaire entre la direction du μ^+ et la direction opposée du méson B^0 dans le référentiel au repos W^{*+} ($\theta_\ell \in [0,\pi]$)
- $\boldsymbol{\chi}$ est l'angle azimutal entre le plan contenant les μ^+ et ν_μ provenant du W^{*+} et le plan contenant les $\overline{D}^0$ et π^- provenant du D^{*-} ($\chi \in [0,2\pi]$)

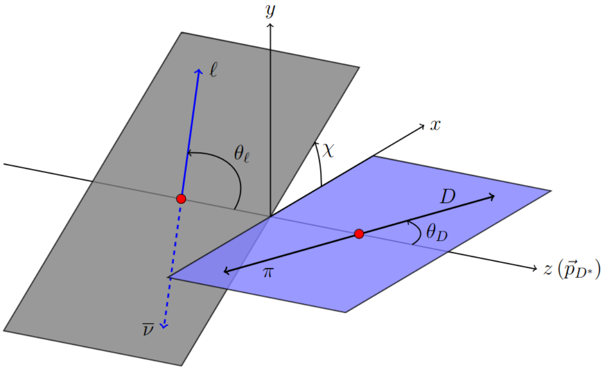

FIGURE 1: Angles d'hélicité de la désintégration $\overline{B} \to D^*(\to D\pi)\ell\overline{\nu}_\ell$. Figure extraite de [3].

Généralement, les désintégrations semileptoniques de mésons B sont traitées théoriquement par la *théorie effective des champs.* Cette approche traite le MS comme une approximation à basse énergie (effective) d'une théorie NP plus complète, où la NP est plus lourde que le MS. Les effets des nouveaux degrés de liberté introduits par la NP peuvent être paramétrés en ajoutant de nouveaux termes au lagrangien du MS, ou alternativement, à l'hamiltonien, appelés *opérateurs de Wilson* et leurs coefficients associés. Dans le cas de la désintégration $B^0 \to D^{*-}\mu^+\nu_\mu$, l'hamiltonien effectif qui inclut toutes les contributions NP possibles est donné par

$$\begin{aligned}\mathcal{H}_{eff} = \frac{4G_F}{\sqrt{2}} V_{cb}\{&[(1+g_L)\bar{c}\gamma^\mu P_L b + g_R \bar{c}\gamma^\mu P_R b]\,\bar{\ell}\gamma_\mu P_L \nu_\ell \\ &+ [g_S \bar{c} b + g_P \bar{c}\gamma^5 b]\,\bar{\ell} P_L \nu_\ell + g_T \bar{c}\sigma^{\mu\nu} P_L b \bar{\ell}\sigma_{\mu\nu} P_L \nu_\ell + h.c.\},\end{aligned} \tag{3}$$

où $G_F = 1.662787 \times 10^{-5}\,\mathrm{GeV}^{-2}$ est la constante de Fermi, V_{cb} est l'élément de la matrice CKM, P_L est l'opérateur de projection de chiralité gauche et les opérateurs de Wilson contribuant et leurs coefficients sont le vecteur gauche (g_L), le vecteur droit (g_R), le scalaire (g_S), le pseudoscalaire (g_P) et le tenseur (g_T). Le MS correspond au cas où $g_L = g_R = g_S = g_P = g_T = 0$.

La distribution angulaire complète de $B^0 \to D^{*-}\mu^+\nu_\mu$ est dérivée dans [2] en termes d'hamiltonien effectif NP le plus général présenté dans l'équation 3 et elle comprend à la fois des termes conservant CP et des termes violant CP avec différents facteurs de suppression. Les termes non supprimés violant CP sont donnés dans le Tab. 1 et sont tous proportionnels à $\sin\chi$ ou $\sin 2\chi$. On peut voir qu'en mesurant ces termes, on accède à deux couplages NP différents : la partie imaginaire du couplage vectoriel droit $\mathrm{Im}(g_R)$ et la partie imaginaire de l'interférence entre les couplages pseudoscalaire et tensoriel $\mathrm{Im}(g_P g_T^*)$. Une discussion sur les modèles NP qui sont exclus et ceux qui sont favorisés si l'on mesure que g_R ou $g_P g_T^*$ est non nul est donnée dans [2].

Coefficient	Couplage	Fonction angulaire
$\mathrm{Im}(\mathcal{A}_\perp \mathcal{A}_0^*)$	$\mathrm{Im}[(1+g_L+g_R)(1+g_L-g_R)^*]$	$-\sqrt{2}\sin 2\theta_\ell \sin 2\theta_D \sin\chi$
$\mathrm{Im}(\mathcal{A}_\parallel \mathcal{A}_\perp^*)$	$\mathrm{Im}[(1+g_L-g_R)(1+g_L+g_R)^*]$	$2\sin^2\theta_\ell \sin^2\theta_D \sin 2\chi$
$\mathrm{Im}(\mathcal{A}_{SP} \mathcal{A}_{\perp,T}^*)$	$\mathrm{Im}(g_P g_T^*)$	$-8\sqrt{2}\sin\theta_\ell \sin 2\theta_D \sin\chi$
$\mathrm{Im}(\mathcal{A}_0 \mathcal{A}_\parallel^*)$	$\mathrm{Im}[(1+g_L-g_R)(1+g_L+g_R)^*]$	$-2\sqrt{2}\sin\theta_\ell \sin 2\theta_D \sin\chi$

TABLEAU 1: Termes violant CP non supprimés dans la distribution angulaire, leurs couplages et les fonctions angulaires auxquelles ils contribuent [2]

Le détecteur LHCb au LHC

Le Grand Collisionneur de Hadrons (LHC en anglais pour *Large Hadron Collider*) est le plus grand accélérateur et collisionneur de particules jamais construit, installé dans un tunnel d'une circonférence de 27 km. Il est situé à 100 m sous terre près de Genève, en Suisse, et est exploité par le Conseil Européen pour la Recherche Nucléaire (CERN). Le LHC est un accélérateur de hadrons à deux anneaux où les faisceaux de protons (ou d'ions lourds) sont accélérés dans des directions opposées dans les deux anneaux. Les faisceaux entrent en collision en quatre points différents le long de l'anneau du LHC, où quatre expériences (ATLAS, CMS, ALICE et LHCb) sont installées pour étudier les résultats des collisions.

Le LHC a fonctionné pendant plusieurs périodes avec de longs arrêts entre les périodes de prise de données. La première période de prise de données est appelée *Run 1*, qui s'est déroulée entre 2010 et 2012. L'énergie du centre de masse ($\sqrt{s}$) pendant le Run 1 était de 7 TeV pour 2010 et 2011, et de 8 TeV pour 2012. Après le Run 1, un arrêt appelé *Long Shutdown 1* (LS1) entre 2013-2015 a eu lieu afin de mettre à niveau les détecteurs et l'accélérateur. La deuxième période de prise de données est appelée *Run 2* et a duré de 2015 à 2018 avec l'énergie du centre de masse augmentée à 13 TeV. Après 2018, un autre arrêt appelé *Long Shutdown 2* (LS2) a eu lieu jusqu'en 2022 afin de poursuivre la mise à niveau des expériences LHC et d'augmenter l'énergie du centre de masse à 14 TeV.

L'objectif principal du détecteur LHCb est d'étudier les désintégrations des hadrons b et c (beauté et charme) et d'étudier les processus de violation de CP dans ces désintégrations. Au cours des collisions pp, des paires de quarks $b\overline{b}$ et $c\overline{c}$ sont produites et elles s'hadronisent immédiatement, formant des états liés tels que les mésons ou baryons b et c. Le point de l'espace où les faisceaux de protons ont interagi et produit le hadron b est appelé vertex primaire (PV). Les hadrons b ont généralement une durée de vie de l'ordre de ~ 1 ps et voyagent donc sur quelques mm avant de se désintégrer en d'autres particules. Le point où le hadron b se désintègre est appelé vertex secondaire (SV). Le hadron b est ensuite reconstruit par ses produits de désintégration.

Afin de relever les défis posés par les désintégrations des hadrons b, le détecteur LHCb doit répondre à certaines exigences :

- Comme les hadrons b ont des vertex de désintégration déplacés de quelques mm par rapport au PV, LHCb doit être capable de détecter ces vertex et de faire la distinction entre les PV et les SV.

- La quantité de mouvement des particules chargées doit être mesurée très précisément afin d'obtenir une masse invariante exacte du b-hadron. Cela permet de distinguer les désintégrations du b-hadron des autres désintégrations et de réduire ainsi le bruit de fond combinatoire.

- Afin de distinguer les différentes désintégrations ayant la même topologie, LHCb doit être capable d'identifier très bien les différentes particules (μ, K, π)

- Un bon système de déclenchement (*trigger system* en anglais) est nécessaire pour faire face à la grande luminosité instantanée afin de sélectionner les événements de signal de manière efficace tout en limitant à une taille raisonnable de stockage

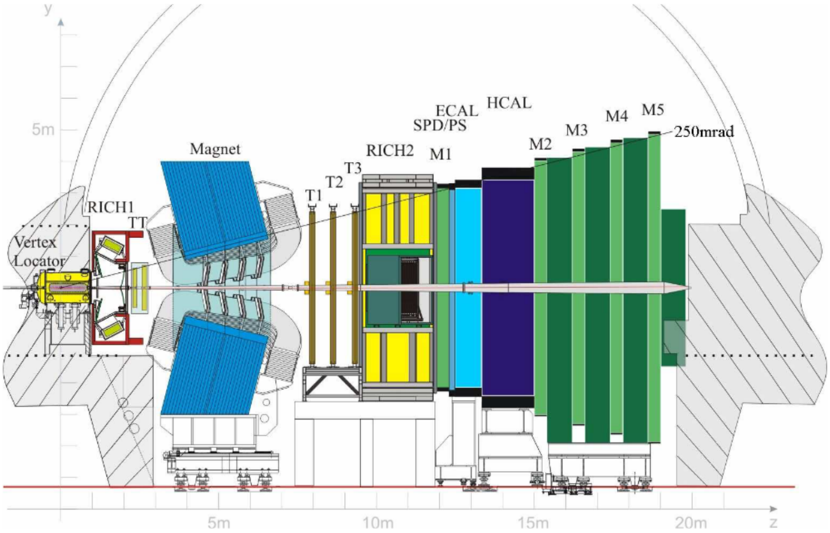

FIGURE 2: Disposition du détecteur LHCb dans le plan $y-z$ [4]

Le détecteur LHCb est composé de nombreux sous-détecteurs et composants individuels, comme le montre la figure 2. Voici un bref résumé des sous-détecteurs qui suivent approximativement l'axe z. À l'origine ($z = 0$), le VErtex LOcator (VELO) est installé autour du point d'interaction. Son rôle est de mesurer très précisément et de distinguer les positions 3D des vertex primaires et des vertex déplacés (secondaires). Un aimant est utilisé pour courber les trajectoires des particules chargées afin de déterminer leur quantité de mouvement. Les autres stations de poursuite sont le Tracker Turicensis (TT) et les trackers T1-T3, placés respectivement avant et après l'aimant. Deux détecteurs sont utilisés pour l'identification des hadrons chargés, les détecteurs RICH1 et RICH2, placés avant et après l'aimant. Ensuite, le calorimètre électromagnétique (ECAL) et le calorimètre hadronique (HCAL) permettent d'identifier et de mesurer l'énergie des particules chargées et neutres. Enfin, cinq stations muoniques (M1-M5) sont utilisées pour mesurer les muons, la station M1 étant placée avant les calorimètres.

Analyse expérimentale

La première recherche d'observables violant CP dans la désintégration semileptonique $B^0 \to D^{*-}\mu^+\nu_\mu$ est effectuée dans cette thése. L'échantillon de données utilisé pour la mesure est constitué des données prises par LHCb au cours des années 2016, 2017 et 2018 de la période du Run 2 du LHC à une énergie de centre de masse $\sqrt{s} = 13\,\text{TeV}$. L'ensemble des données correspond à une luminosité intégrée de $5{,}4\,\text{fb}^{-1}$. La désintégration $B^0 \to D^{*-}\mu^+\nu_\mu$ est reconstruite comme une combinaison $\overline{D}^0\mu^\pm$ où un $\pi^\pm$ supplémentaire est ajouté au D^0 pour former le candidat D^*. Ensuite, le méson $\overline{D}^0$ est reconstruit avec le mode $D^0 \to K^+\pi^-$.

Afin de reconstruire les quantités cinématiques qui sont essentielles pour cette analyse, c'est-à-dire les trois angles définis dans la Fig. 1 et q^2, une approximation sur l'impulsion du neutrino doit être faite. Il y a deux approches pour approximer la quantité de mouvement du neutrino non détecté, la première est basée sur une approximation du référentiel au repos du méson B, tandis que la seconde utilise l'information topologique pour résoudre une équation quadratique et obtenir le moment du neutrino jusqu'à une ambiguïté double.

Une fois l'approximation du neutrino obtenue, afin d'améliorer la résolution des paramètres cinématiques, un re-ajustement complet de l'arbre de désintégration qui inclut toutes les informations cinématiques possibles (y compris l'approximation du neutrino manquant) et toutes les corrélations possibles est mise en œuvre.

Un ajustement par maximum de vraisemblance est mis en œuvre dans l'echantillon des données afin d'estimer la fraction des désintégrations du signal et les contributions des divers bruits de fond avec la même signature d'état final que le signal $B^0 \to D^{*-}\mu^+\nu_\mu$. Les bruits de fond peuvent être divisés en deux catégories : les bruits de fond semileptoniques et les bruis de fond de double charme. Les bruits de fond semileptoniques sont constitués de désintégrations d'autres mésons B qui produisent un D^{*-} et un μ^+ primaire ou un muon secondaire provenant d'une désintégration $\tau^+ \to \mu^+\nu_\mu\overline{\nu}_\tau$. Les bruits de fond de double charme sont des désintégrations de mésons B en un D^{*-} et un autre hadron charmé qui se désintègre de manière semileptonique. Les modèles de signal et de tous les bruits de fond physiques sont construits à partir de simulations Monte-Carlo (MC) de chaque processus. Les modèles sont des histogrammes tridimensionnels dans les variables q^2, m^2_{miss} et E^*_μ. Ces variables cinématiques ont été choisies parce qu'elles ont un grand pouvoir de discrimination entre le signal et les divers processus de bruit de fond. Certains des processus de fond qui polluent l'échantillon de données peuvent donner naissance à des asymétries par P ou CP non nulles et produire des biais dans la mesure des couplages de NP. Par conséquent, une estimation de leurs fractions dans l'échantillon de données est nécessaire pour attribuer des incertitudes systématiques.

L'analyse présentée dans cette thèse étudie la distribution angulaire dans les désintégrations de $B^0 \to D^{*-}\mu^+\nu_\mu$ et plus particulièrement les termes asymétriques par P de la distribution angulaire. La fonction densité de probabilité totale de la désintégration peut être écrite comme une somme des composantes symétriques et asymétriques par P, c'est-à-dire

$$P(q^2,\theta_\ell,\theta_D,\chi) = P_{\text{even}}(q^2,\theta_\ell,\theta_D,\chi) + P_{\text{odd}}(q^2,\theta_\ell,\theta_D,\chi), \tag{4}$$

où P_{odd} est la somme des termes proportionnels à $\sin\chi$ et $\sin 2\chi$ indiqués dans le Tab. 1 et peut s'écrire explicitement comme suit

$$P_{\text{odd}}(q^2,\theta_\ell,\theta_D,\chi) = P^{(1)}_{\text{odd}}(q^2,\theta_\ell,\theta_D)\sin\chi + P^{(2)}_{\text{odd}}(q^2,\theta_\ell,\theta_D)\sin 2\chi, \tag{5}$$

où $P^{(1)}_{\text{odd}}$ et $P^{(2)}_{\text{odd}}$ sont les fonctions angulaires qui sont maintenant indépendantes de χ. Les propriétés de symétrie de la distribution angulaire totale peuvent être exploitées afin d'annuler la partie symétrique par P et d'extraire uniquement la composante asymétrique par P d'une manière indépendante du modèle. Les termes $P^{(1)}_{\text{odd}}$ et $P^{(2)}_{\text{odd}}$ peuvent être obtenus en intégrant la densité de désintégration totale avec les poids $\sin\chi$ et $\sin 2\chi$ de la manière suivante :

$$\begin{aligned} P^{(1)}_{\text{odd}}(q^2,\theta_\ell,\theta_D) &= \frac{1}{\pi}\int_{-\pi}^{\pi} P(q^2,\theta_\ell,\theta_D,\chi)\sin\chi d\chi, \\ P^{(2)}_{\text{odd}}(q^2,\theta_\ell,\theta_D) &= \frac{1}{\pi}\int_{-\pi}^{\pi} P(q^2,\theta_\ell,\theta_D,\chi)\sin 2\chi d\chi. \end{aligned} \tag{6}$$

De cette manière, les quantités $P^{(1)}_{\text{odd}}$ et $P^{(2)}_{\text{odd}}$ qui représentent les composantes asymétrique par P (en $\sin\chi$ et $\sin 2\chi$) de la densité de désintégration totale sont obtenues séparément et le reste de la distribution angulaire (symétrique par P) avec ses incertitudes est annulé.

Selon le Tab. 1, le terme $\sin\chi$ a des contributions provenant à la fois du couplage vectoriel de droite g_R et de l'interférence entre les courants pseudoscalaires et tensoriels $g_P g_T^*$ tandis que le terme $\sin 2\chi$ a des contributions provenant uniquement de g_R. Dans l'approximation où les couplages NP sont petits par rapport au couplage SM, c'est-à-dire $g_R \ll 1$ et $g_P g_T^* \ll 1$, les relations suivantes peuvent être écrites

$$\begin{aligned} P^{(1)}_{\text{odd}}(q^2,\theta_D,\theta_\ell) &= \text{Im}(g_R)F^{(1)}_{RH}(q^2,\theta_D,\theta_\ell) + \text{Im}(g_P g_T^*)F^{(1)}_{PT}(q^2,\theta_D,\theta_\ell), \\ P^{(2)}_{\text{odd}}(q^2,\theta_D,\theta_\ell) &= \text{Im}(g_R)F^{(2)}_{RH}(q^2,\theta_D,\theta_\ell). \end{aligned} \tag{7}$$

Les fonctions $F^{(1)}_{RH}$ et $F^{(2)}_{PT}$ sont obtenues par simulation et sont appelées modèles NP, tandis que $P^{(1)}_{\text{odd}}$ et $P^{(1)}_{\text{odd}}$ sont extraites des données. Les modèles NP sont générés à l'aide de poids fournis par la bibliothèque logicielle `Hammer` (Helicity Amplitude Model for Matrix Element Reweighting) [5]. Ces poids sont appliquées à l'échantillon de simulation du signal SM pour modifier la forme des distributions observables dans les deux scénarios NP qui nous intéressent. La procédure de pondération repose sur des calculs tensoriels efficaces au niveau de l'amplitude et les seules données d'entrée requises sont les vraies quadri-impulsions (disponibles en simulation) de toutes les particules de l'état final dans la désintégration.

Dans la pratique, où les données expérimentales sont discrètes plutôt que continues, il est commode de construire des asymétries binées. L'asymétrie dans le i-ième bin A_i est donnée par

$$\begin{aligned} A^{(1)}_i &= \frac{N_{\text{bins}}}{N_{\text{signal}}}\sum_{n=1}^{N_i}\sin\chi_n, \\ A^{(2)}_i &= \frac{N_{\text{bins}}}{N_{\text{signal}}}\sum_{n=1}^{N_i}\sin 2\chi_n. \end{aligned} \tag{8}$$

où $N_{\text{signal}} = \sum_i N_i$ est le nombre d'événements de signal dans l'échantillon et N_{bins}

est le nombre de bins avec $1 < i < N_{\text{bins}}$. La sommation est effectuée sur tous les événements dans le i-ième bin. Le terme de normalisation $N_{\text{bins}}/N_{\text{signal}}$ garantit que les asymétries sont indépendantes du nombre d'événements signal dans l'échantillon et de la composante symétriques par P de la densité totale (comme ce serait le cas si la normalisation $1/N_i$ était utilisée).

Le schéma des bins est effectué en deux dimensions dans $\cos\theta_D\, vs.\, \cos\theta_\ell$ afin de capturer l'ensemble de l'espace de phases. Le schéma n'inclut pas des bins dans q^2 telle que cette variable est intégrée. Par conséquent, les asymétries sont obtenues sur l'ensemble de la plage q^2. On a choisi un schéma 2D avec 8 fois 8 bins dans $\cos\theta_{D,\ell}$, ce qui donne un total de 64 bins. Les asymétries de l'équation 8 sont les versions binées des composantes asymétriques par P de la densité de désintégration de l'équation 7 et sont linéairement proportionnelles. La fonction χ^2_{corr} suivante peut donc être utilisée pour ajuster simultanément les asymétries $\sin\chi$ et $\sin 2\chi$ tout en tenant compte de leurs corrélations

$$\chi^2_{\text{corr}} = \sum_i \sum_{a,b=1,2} \Delta A_i^{(a)} \left(\Sigma_i^{-1}\right)^{(ab)} \Delta A_i^{(b)}, \tag{9}$$

où les indices (a,b) représentent les termes $\sin\chi$ et $\sin 2\chi$ et $\Delta A_i^{(a,b)}$ est la différence entre l'asymétrie attendue déterminée à partir des modèles NP et l'asymétrie observée dans les données, i.e.

$$\Delta A_i^{(a,b)} = \frac{\text{Im}(g_R)_{\text{fit}}}{\text{Im}(g_R)_0} A_{RH,i}^{(a,b)} + \frac{\text{Im}(g_P g_T^*)_{\text{fit}}}{\text{Im}(g_P g_T^*)_0} A_{PT,i}^{(a,b)} - A_i^{(a,b)}. \tag{10}$$

Dans Eq. 10, les quantités $A_{RH,i}^{(1,2)}$ et $A_{PT,i}^{(1,2)}$ sont les modèles d'asymétries binées $\sin\chi$ (1) et $\sin 2\chi$ (2) obtenus à partir de la pondération NP de la simulation avec $\text{Im}(g_R)_0$ et $\text{Im}(g_P g_T^*)_0$. Les quantités $A_i^{(1,2)}$ sont les asymétries binées observées dans les données. Enfin, les valeurs des couplages NP déterminées en minimisant la fonction χ^2_{corr} dans l'ajustement sont désignées par $\text{Im}(g_R)_{\text{fit}}$ et $\text{Im}(g_P g_T^*)_{\text{fit}}$. La matrice Σ contient les corrélations entre les asymétries binées $\sin\chi$ et $\sin 2\chi$.

À titre d'exemple, Fig. 3 montre le modèle d'asymétrie *CP* binnée dans le cas de la contribution du couplage vectoriel droit $\text{Im}(g_R) = 0,1i$. Le graphique du haut montre la densité de désintégration totale dans les bins 2D de $\cos\theta_\ell\, vs.\, \cos\theta_D$ où la couleur indique le nombre d'événements qui tombent dans chaque bin. Les premier et deuxième graphiques de la deuxième ligne montrent la densité pondérée de $\sin\chi$ et de $\sin 2\chi$, respectivement. Dans chaque case, la couleur indique maintenant l'ampleur de l'asymétrie (la composante asymétrique par P de la densité). Afin de pouvoir visualiser les incertitudes sur l'asymétrie, les graphiques 2D sont transformé en graphiques 1D présentés dans la troisième ligne. La projection des bins 2D se fait de gauche à droite, rangée par rangée, de bas en haut, i.e. des valeurs négatives aux valeurs positives de $\cos\theta_\ell$ et $\cos\theta_D$. La figure montre que l'asymétrie *CP* pour la contribution NP de $\text{Im}(g_R)$ est non nulle et a des formes spécifiques dans les deux termes $\sin\chi$ et $\sin 2\chi$.

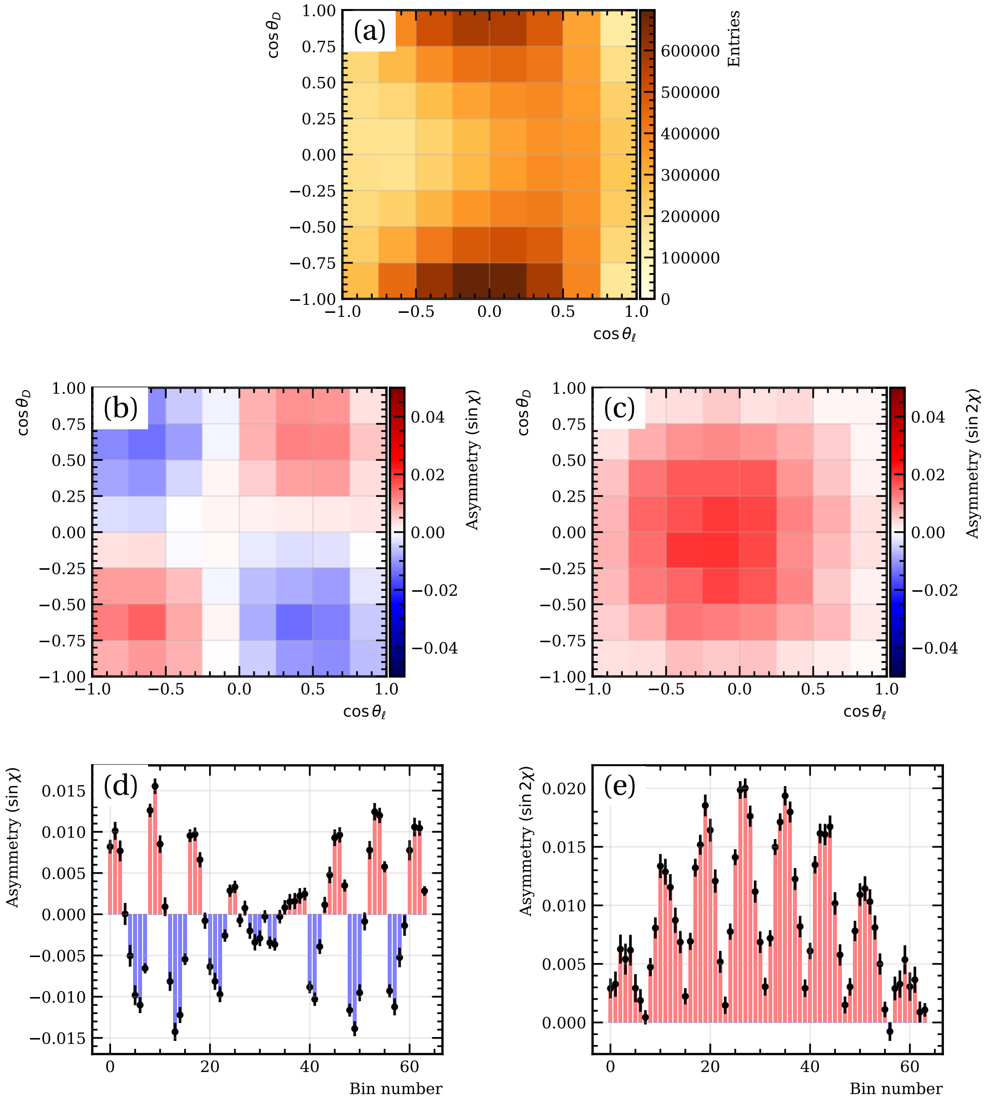

FIGURE 3: Densité des événements (a), asymétries *CP* 2D (b,c) et asymétries *CP* 1D (d,e) des termes $\sin\chi$ et $\sin 2\chi$ dans les variables $(\cos\theta_D, \cos\theta_\ell)$ intégrés sur q^2 dans le cas NP de $\mathrm{Im}(g_R) = 0,1i$.

Avec l'ensemble des données disponibles, cette méthode permet d'obtenir une précision statistique inférieure à 1% pour $\mathrm{Im}(g_R)$ et inférieure à 0,1% pour $\mathrm{Im}(g_P g_T^*)$.

Les effets systématiques qui peuvent produire de faux termes asymétrique par P même dans la distribution angulaire de type MS (symétrique par P) sont ceux qui doivent être soigneusement pris en compte et constituent la principale motivation pour une analyse spécifique visant à mesurer les termes asymétriques par P plutôt que la distribution angulaire complète. Les effets asymétrique par P peuvent être divisés en deux catégories : les effets dans les bruits de fond et les effets d'instrumentation.

Les effets de violation de *CP* ne peuvent apparaître dans les désintégrations semileptoniques que dans les scénarios NP et sont nuls dans le MS. Par conséquent, les effets systématiques asymétrique par *CP* dans les bruits de fond semileptoniques ne sont pas pris en compte. D'autre part, des effets asymétrique par P (mais pas asymétrique par CP) peuvent apparaître dans la désintégration $B \to D^{**}\mu\nu$ (états D^{**} chargés et neutres) qui est le bruit de fond semileptonique partiellement reconstruit dominant dans l'échantillon de données du $B^0 \to D^{*-}\mu^+\nu_\mu$ signal. Dans ces désintégrations, des phases fortes peuvent apparaître en raison de l'interférence de différentes résonances de charme excitées [6]. Ce mécanisme générerait alors une violation de CP dans les désintégrations $B \to D^{**}\mu\nu$ à condition qu'une phase faible soit également présente dans ces désintégrations (ce qui ne peut se produire qu'avec NP). Cependant, en l'absence de phase faible, la phase forte non nulle ne produit qu'une violation de la parité.

Afin d'estimer l'ampleur de l'effet asymétrique par P de phases fortes générées de cette manière, un échantillon de simulation de $B^+ \to D^{**0}\mu^+\nu_\mu$ désintégrations a été utilisé et une différence de phase forte δ_D a été injectée dans l'interférence entre les états $D_1(2420)$ et $D_2^*(2460)$. Cette procédure permet d'obtenir un ensemble de poids qui peuvent ensuite être appliqués aux modèles d'asymétrie. La valeur de la phase forte n'étant pas connue, différentes valeurs de δ_D ont été injectées dans l'échantillon de simulation dans l'intervalle 0°-360° par pas de 45°. Les angles d'hélicité et q^2 sont ensuite calculés à partir des paramètres de désintégration partiellement reconstruits comme pour le signal et les deux modèles d'asymétrie en $\sin\chi$ et $\sin 2\chi$ sont obtenus pour chaque échantillon. Les deux asymétries sont ensuite ajustées à l'aide de la fonction donnée dans Eq. 9 pour obtenir le biais sur la partie imaginaire des deux couplages NP.

La contribution la plus importante au bruit de fond du double charme est donnée par la désintégration ayant la plus grande fraction d'embranchement $B^0 \to D^{*-}D_s^{*+}$ où $D^{*-} \to \overline{D}^0\pi^-$, $D_s^{*+} \to D_s^+\gamma/\pi^0$ et $D_s^+ \to X^0\mu^+\nu_\mu$. Il s'agit d'une désintégration en deux mésons charmés vectoriels avec quatre particules dans l'état final et elle peut donc produire une violation de la parité. Bien que la violation de CP dans ces désintégrations soit possible dans le SM, l'amplitude dominante est donnée par la transition $b \to c$ et, par conséquent, tout effet de violation de CP est supprimé par $|V_{ub}|/|V_{cb}|$ et est donc négligeable. Par conséquent, seuls les effets de violation de la parité dans ces désintégrations sont pris en compte ici. La structure d'amplitude du $B^0 \to D^{*-}[\to \overline{D}^0\pi^-]D_s^{*+}[\to D_s^+\gamma]$ a été mesurée par l'expérience LHCb [7] et les phases fortes mesurées qui régissent le degré de violation de la parité se sont avérées compatibles avec zéro. Une étude des effets de violation de la parité dans ces désintégrations a été menée en utilisant des désintégrations simulées $B^0 \to D^{*-}[\overline{D}^0\pi^-]D_s^{*+}[\to D_s^+\gamma]$ où une violation maximale de la parité a été injectée dans l'échantillon. Le bruit de fond est alors partiellement reconstruit en tant que signal $B^0 \to D^{*-}\mu^+\nu_\mu$ et les modèles d'asymétrie sont obtenus et ajustés avec le modèle NP. Aucun biais significatif dans les couplages NP n'est trouvé, même dans le cas d'une violation de parité maximale. Ce résultat pourrait s'expliquer par le fait que, puisque le photon n'est pas reconstruit et que ses degrés de liberté sont intégrés, l'effet de violation de parité provenant des désintégrations à deux particules des deux mésons vecteurs est annulé.

Les termes angulaires étudiés dans cette analyse sont de nature asymétrique par P puisqu'ils sont proportionnels à $\sin\chi$ et $\sin 2\chi$ où l'angle χ est intrinsèquement une quantité asymétrique par P (chirale). Par conséquent, tout effet chiral dans la procédure de reconstruction, tel que le désalignement de détecteur ou des efficacités de reconstruction qui ne sont pas symétriques par P, peut introduire de fausses contributions asymétriques par P dans la distribution angulaire reconstruite. En particulier, ces effets peuvent entraîner un biais dans l'angle χ et donc peuvent introduire un biais dans la mesure des couplages NP.

Le désalignement des deux moitiés du VELO l'une par rapport à l'autre peut introduire une incertitude significative dans les positions relatives entre le vertex secondaire et le vertex primaire et, par conséquent, dans la reconstruction de la quantité χ, asymétrique par P. La procédure d'alignement de VELO calibre les positions des deux moitiés de VELO en fonction de six degrés de liberté : trois translations (T_x, T_y, T_z) et trois rotations (R_x, R_y, R_z) autour des axes x, y, z. Le biais produit par le désalignement du VELO est estimé à l'aide d'échantillons de simulation de signal artificiellement désaligné. Le biais le plus important provient du désalignement de translation T_y, où un déplacement 2 μm des deux moitiés du VELO l'une par rapport à l'autre a été introduit.

Un autre effet de l'instrumentation qui peut produire des termes asymétriques par P dans la distribution angulaire reconstruite est une efficacité de reconstruction non uniforme. Autrement dit, si l'efficacité contient des termes proportionnels à des quantités asymétriques par P, cela peut biaiser la variable $\sin\chi$ et donc biaiser les couplages NP. Afin de comprendre les effets de ces termes potentiels asymétriques par P dans l'efficacité de la reconstruction des traces des particules, un échantillon de contrôle de données de $B^0 \to D^- \mu^+ \nu_\mu$ est utilisé, où le D^- est reconstruit comme $D^- \to K^+ \pi^- \pi^-$. Cet échantillon de contrôle a été choisi car il ressemble beaucoup à la désintégration du signal $B^0 \to D^{*-} \mu^+ \nu_\mu$, mais comme il consiste en deux désintégrations à trois particules et que le D^- est un méson scalaire, c'est-à-dire qu'il a un spin nul, il ne peut pas produire d'effets de violation de la parité ou du CP.

La désintégration $B^0 \to D^- \mu^+ \nu_\mu$ a les mêmes particules dans l'état final que la désintégration du signal, i.e. $K^+ \pi^- \pi^- \mu^+$. Le pion qui donne la masse invariante $K^+ \pi^-$ la plus petite est utilisé comme un substitut pour le pion lent , i.e. le pion provenant de la désintégration $D^{*-} \to \overline{D}^0 \pi^-$, tandis que l'autre pion est utilisé pour former la combinaison $K^+ \pi^-$ qui sert de substitut à $\overline{D}^0$. Enfin, une fois ces substituts définis, les paramètres cinématiques $q^2, \theta_\ell, \theta_D$ et χ peuvent être calculés et les modèles d'asymétrie $\sin\chi$ et $\sin 2\chi$ peuvent ainsi être obtenus et l'ajustement est effectué pour extraire le biais dans les couplages NP. Une étude démontrant que les échantillons de contrôle et de signal se comportent de manière similaire sous l'action de ces effets symétriques par P est effectué. Comme les distributions cinématiques et topologiques des deux échantillons ne sont pas totalement compatibles, une étude démontrant que le biais ne dépend d'aucune des variables cinématiques et topologiques dans les échantillons de signal et de contrôle est également réalisée. Par conséquent, le biais trouvé par l'ajustement dans les échantillons de contrôle peut être utilisé pour attribuer une incertitude systématique à l'échantillon de signal. En particulier, aucun biais significatif n'a été constaté dans l'échantillon de contrôle.

Une vue d'ensemble des incertitudes systématiques pour les asymétries de parité et du CP est présentée dans les Tab. 2 et 3. L'incertitude systématique dominante dans le cas des asymétries CP est due à désalignement T_y des deux moitiés du VELO l'une par rapport à l'autre. Dans le cas des des asymétries P, le plus dominante incertitude systématique provient de l'effet violant P dans le bruit de fond $B \to D^{**}\mu\nu$.

Systématique attribué	Δ Im$(g_R)^{\text{faux}}$	Δ Im$(g_P g_T^*)^{\text{faux}}$
Misid	1.07×10^{-3}	1.38×10^{-4}
Fake D^* comb	0.23×10^{-3}	0.96×10^{-4}
True D^* comb	1.76×10^{-3}	3.20×10^{-4}
$B^- \to D^{**+}\mu^-\bar{\nu}_\mu$	9.64×10^{-3}	3.67×10^{-4}
$\overline{B}^0 \to D^{*+}D_s^{*-}$	0.41×10^{-3}	1.81×10^{-4}
T_y désalignement	1.44×10^{-3}	3.27×10^{-4}
Échantillon de contrôle	3.27×10^{-3}	7.12×10^{-4}
Total	10.50×10^{-3}	9.55×10^{-4}

TABLEAU 2: Résumé des incertitudes systématiques attribuées dans le cas des asymétries de parité

Systématique attribué	Δ Im(g_R)	Δ Im$(g_P g_T^*)$
Misid	0.85×10^{-3}	2.45×10^{-4}
Fake D^* comb	0.40×10^{-3}	0.70×10^{-4}
True D^* comb	1.45×10^{-3}	1.98×10^{-4}
T_y désalignement	4.81×10^{-3}	6.17×10^{-4}
Échantillon de contrôle	2.78×10^{-3}	6.12×10^{-4}
Total	5.82×10^{-3}	9.27×10^{-4}

TABLEAU 3: Résumé des incertitudes systématiques attribuées dans le cas des asymétries de CP

Les résultats de l'ajustement aux asymétries CP, sensibles aux couplages NP Im(g_R) et Im$(g_P g_T^*)$ sont toujours masqués et seules les incertitudes statistiques et systématiques estimées sont rapportées pour ce canal. Cependant, l'ajustement aux asymétries de parité, insensibles aux couplages NP, en tant que canal de contrôle, n'est pas masqué et les résultats sont cohérents avec les attentes compte tenu des incertitudes pour l'un des couplages NP, tandis que pour l'autre un biais d'environ 2,5 σ est observé. Cela indique un possible effet de violation de la parité non pris en compte dans l'échantillon du signal et fait encore l'objet d'une enquête. Les résultats finaux pour les asymétries de parité et les asymétries CP (masqués) sont présentés dans les Eq. 11 et 12, respectivement.

$$\begin{aligned} \mathrm{Im}(g_R)^{\text{faux}} &= (-0.57 \pm 0.51\ (\text{stat.}) \pm 1.05\ (\text{syst.}))\%, \\ \mathrm{Im}(g_P g_T^*)^{\text{faux}} &= (-0.41 \pm 0.13\ (\text{stat.}) \pm 0.10\ (\text{syst.}))\%. \end{aligned} \tag{11}$$

$$\begin{aligned} \mathrm{Im}(g_R) &= (\mathrm{X.XX} \pm 0.51\ (\mathrm{stat.}) \pm 0.58\ (\mathrm{syst.}))\%, \\ \mathrm{Im}(g_P g_T^*) &= (\mathrm{X.XX} \pm 0.13\ (\mathrm{stat.}) \pm 0.09\ (\mathrm{syst.}))\%. \end{aligned} \tag{12}$$

1 Introduction

The Standard Model (SM) is the theoretical framework which describes all the elementary particles and their interactions. Since its formulation of the SM in the 1960s, its predictions have been tested and validated. An important property predicted by the SM is the so-called Lepton Flavor Universality (LFU), i.e. the interaction of the leptons with the electroweak gauge bosons is independent of the lepton flavor. This property has been tested in the recent years in B meson decays, specifically in $b \to s\ell^+\ell^-$ and $b \to c\ell\nu_\ell$ quark level transitions, and deviations of 2-3σ were observed between theory and experimental results [8]. These tensions, generally referred to as the *b-anomalies*, suggest the presence of New Physics (NP) in these decays. With respect to the semileptonic $b \to c\ell\nu_\ell$ channel, to complement the searches of lepton flavor non-universality, other observables sensitive to NP effects have been proposed. One promising observable that can probe the nature of potential NP in semileptonic decays is CP violation [2, 9]. Any CP-violating effects require the presence of at least two amplitudes with non vanishing weak phase difference. Since in the SM semileptonic decays have a single tree-level amplitude, a measurement of CP-violation in these decays is in effect a *null-test* of the SM.

The CP-violating effects in $b \to c\ell\nu_\ell$ can only appear as kinematical effects in the angular distribution. As a consequence, in order to get access to the CP-violating observables, the angular distribution must be reconstructed. Since the tensions between experimental results and SM predictions are so far observed in the ratios involving τ leptons, this suggests the presence of NP in $b \to c\tau\nu_\tau$ decays. However, since the τ decays into final states that include one or two neutrinos which are not reconstructable in experiment, these decays are very difficult to deal with and the τ momentum, $\vec{p}_\tau$, cannot be reconstructed with good precision. Therefore, it is logical to start by measuring the CP-violating effects in $B^0 \to D^{*-}\mu^+\nu_\mu$ since its angular distribution is fully reconstructable. Even though the b-anomalies are preferably explained by NP in $b \to c\tau\nu_\tau$ the same NP may affect $b \to c\mu\nu_\mu$ and may lead to measurable deviations from the SM in the angular distribution of $B^0 \to D^{*-}\mu^+\nu_\mu$.

Chapter 2 presents the formalism of the SM with a focus on the flavor sector and CP-violation. The effective field theory approach used to describe semileptonic decays is introduced and the NP scenarios which can give rise to CP-violation in the $B^0 \to D^{*-}\mu^+\nu_\mu$ decay are discussed.

The searches of NP effects in B meson decays are pursued at particle colliders such as the Large Hadron Collider (LHC) at CERN. The LHC is a proton-proton (pp) collider where four experiments namely ATLAS, CMS, ALICE and LHCb are installed and collect data. The LHCb detector is designed to exploit the signature features of b-hadron decays and it is thus the optimal place to study the semileptonic B meson decays. The LHC accelerator complex and the LHCb detector are presented in Chapter 3.

The search for *CP*-violation in the semileptonic decay $B^0 \rightarrow D^{*-}\mu^+\nu_\mu$ is described in Chapter 4. The search is performed on 5.4 fb^{-1} of data collected by the LHCb detector at CERN during the years 2016-2018 of Run 2. This analysis makes use of a novel model-independent method to cancel out all the *CP*-even terms (and their uncertainties) in the angular distribution and measure only the NP-sensitive *CP*-odd terms. The undetectable neutrino in the final state is reconstructed using certain approximation techniques and the kinematic parameters which describe the angular distribution of the $B^0 \rightarrow D^{*-}\mu^+\nu_\mu$ decay are obtained. Binned parity and *CP*-asymmetries are then constructed using these kinematic parameters. The *CP* asymmetries channel is sensitive to the NP couplings while the parity asymmetries channel is expected to be zero due to theoretical considerations. A binned asymmetry template fit is implemented and performed on both parity and *CP*-asymmetries in order to extract the values of the NP couplings. The main sources of systematic uncertainties due to parity- and *CP*-odd background and instrumentation effects are considered and estimated. The results of the fit to the NP-sensitive *CP* channel are still blinded, however the fit to the parity channel is unblinded and consistent with the expectations within the estimated uncertainties. The results are summarized in Chapter 5. Finally, conclusions are presented in Chapter 6.

2 Theoretical framework

This chapter offers a description of the Standard Model of particle physics with an emphasis on flavor physics and *CP* violation. The content of the chapter is based on various books and particle physics lecture notes [10–16]. A detailed description of the particles and their interactions in the SM is given in Sec. 2.1. The electroweak interaction and the the flavor physics sector are introduced in Sec. 2.1.5 and the mechanism of *CP* violation in the SM is discussed in Sec. 2.1.6.

An important property predicted by the SM is lepton flavor universality (LFU). This property has been recently tested and deviations with respect to the SM predictions have been observed in decays of mesons containing b quarks such as the $b \to s\ell^+\ell^-$ and $b \to c\ell\nu_\ell$ transitions. The latter are generally known as *semileptonic B* decays. An overview of the direct LFU tests performed in semileptonic decays at several experiments is given in Sec. 2.2.1. To complement the direct LFU searches, *CP*-violating observables in semileptonic decays have been proposed as a null-test of the SM. That is, if *CP* violation is measured it would unambiguously imply the presence of NP in these decays and it would help distinguish and constrain the nature of various NP scenarios. The mechanism that can give rise to *CP* violation in $b \to c\ell\nu_\ell$ decays and the NP implications are discussed in Sec. 2.2.3.

2.1 The Standard Model

The Standard Model (SM) is the most successful theory of particle physics since its formulation in the 1960s. It describes the 12 elementary particles and their interactions in terms of three out of the four forces known in nature: the electromagnetic, the strong and the weak forces (SM does not account for gravity). The Standard Model has passed numerous tests and the vast majority of experimental observations have been in accordance with its predictions. One of the most famous precision tests of the SM is the measurement of the so-called anomalous magnetic moment of the electron which agrees to the SM prediction within 10 parts per billion [17]. This makes quantum electrodynamics (QED), the branch of the SM that incorporates the electromagnetic interaction, the most precisely tested theory in the history of science. Another truly remarkable prediction of the SM was the existence of the Higgs boson, which was discovered by the ATLAS and CMS experiments at the Large Hadron Collider [18, 19]. The Standard Model also offered predictions for the $W^\pm$ and Z bosons, the gluons, the top and charm quark before these particles were actually discovered.

The elementary particles of the SM are shown in Fig. 2.1. A primary classification of the particles is based on their spin, where particles with integer spin are called *bosons*

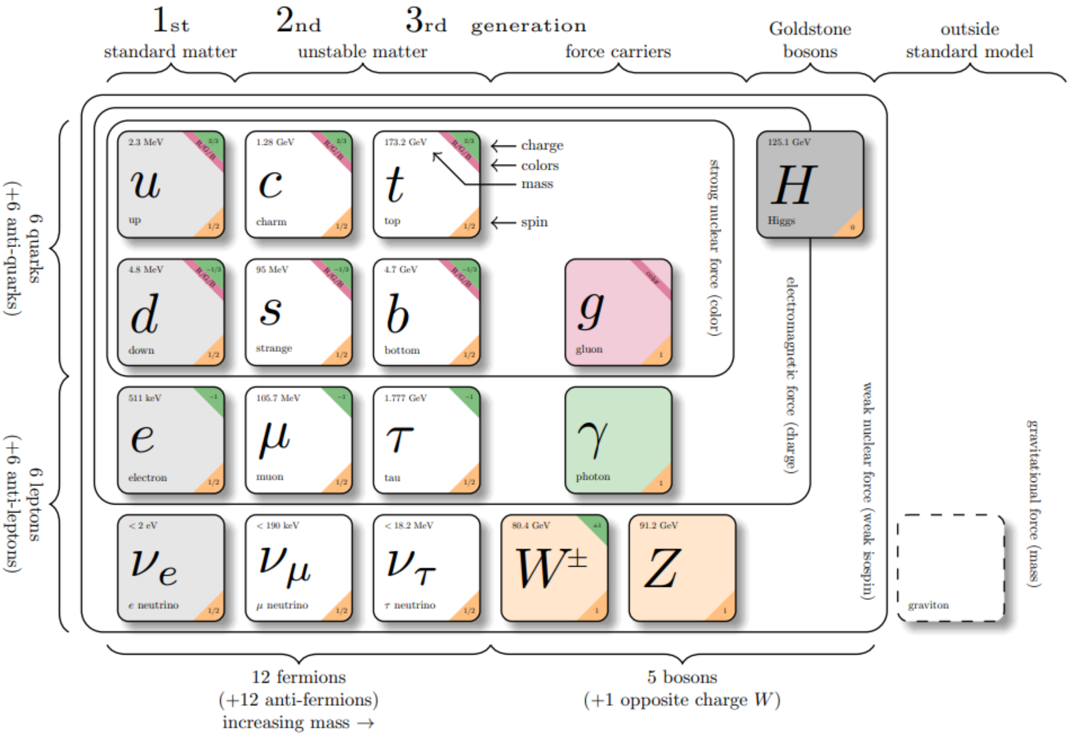

Figure 2.1: Elementary particles of the SM [20]. The properties are taken from [21].

and particles with half-integer spin are called *fermions*. Due to the spin-statistics theorem, which relates the intrinsic spin of the particle with the particle statistics it obeys, fermions obey the Fermi-Dirac statistics. This means that fermions must obey also the Pauli exclusion principle which states that two or more fermions cannot occupy the same quantum state [1].

There are 13 bosons in the SM: 12 vector (i.e. spin-1) and 1 scalar (i.e. spin-0) boson. Each of the three fundamental forces has an associated set of vector bosons, also known as *gauge* bosons, which is exchanged between particles during the interaction and which mediates the momentum transfer. There are eight massless gluons (g) that mediate the strong force, the massive charged $W^{\pm}$ and neutral Z boson that mediate the weak force and the massless photon (γ) which mediates the electromagnetic force. In addition, the scalar Higgs boson is responsible for the mechanism of *spontaneous symmetry breaking* that gives mass to the fermions and the $W^{\pm}$ and Z bosons. The fourth fundamental force, gravity, is assumed in some models to be mediated by a hypothetical boson called *graviton* [22, 23]. However, gravity is not accounted for in the SM.

---

[1] In mathematical terms it is said that the fermions wavefunction is antisymmetric with respect to the swap of two particles while the bosons wavefunction is symmetric.

Force	Strength	Range (m)	Boson
Strong	1	10^{-15}	Gluons (g)
Electromagnetic	10^{-3}	∞	Photon (γ)
Weak	10^{-8}	10^{-18}	$W^{\pm}$, Z
Gravity	10^{-37}	∞	Graviton?

Table 2.1: The four fundamental forces of nature and their relative strengths and ranges [10]

Table 2.1 shows the relative strengths and ranges of the four fundamental forces. As the name suggests, the strong force is the strongest of the four. The strong force only affects particles that possess the charge quantum number known as *color*. Its short range of $\mathcal{O}(10^{-15})$, which is the size of a nucleon, comes from the fact that gluons, even though they are massless, carry color charge and interact between themselves. The electromagnetic force couples to electric charge and is the second strongest force. Since it is mediated by a massless, electrically neutral photon, it has infinite range. The weak force is the weakest of the three forces in the SM and its very limited range of $\mathcal{O}(10^{-18})$ is due to the large mass of the exchanged $W^{\pm}$ and Z bosons. The weak force couples only to so-called *left-handed* particles as it will be discussed in Section 2.1.4. In the SM, the electromagnetic and weak forces are unified via the *electroweak* force and thus they are manifestations of the same underlying interaction, as discussed in section 2.1.5. Finally, gravity is the weakest of the four fundamental forces and as a consequence it is neglected in the context of high-energy physics.

The twelve fundamental fermions are the particles that make up all matter and are divided in two categories: six *quarks* and six *leptons*. The fundamental difference is that quarks possess color charge while leptons do not. Therefore, quarks can interact via strong and electroweak forces while leptons can only feel the electroweak force. The fermions are described by the Dirac equation and as a consequence each particle has a corresponding antiparticle with same mass and opposite charge.

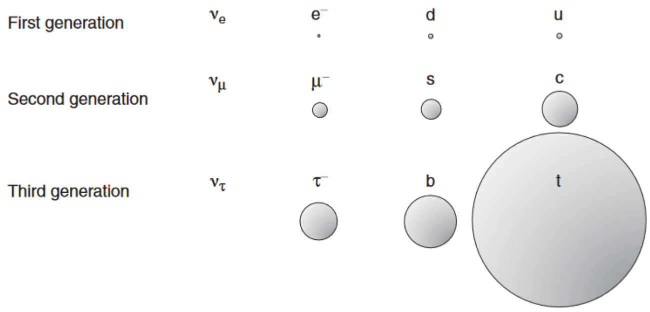

Figure 2.2: Visual representation of the masses of the fundamental fermions [10]

The quarks and leptons can be grouped in three generations of increasing mass, as illustrated in Fig. 2.2. The fact that there are exactly three generations of fermions is not explained in the SM. In the case of leptons, each generation contains one electrically charged lepton, either electron, muon or tau (e^-, μ^-, τ^-) and one associated electrically neutral lepton called neutrino (ν_e, ν_μ, ν_τ). In the SM, the neutrinos have zero mass. The leptons also have a quantum number [2] which reflects the flavor of the lepton for each generation. Lepton flavor is conserved in all interactions. The six leptons have their corresponding antiparticles (e^+, μ^+, τ^+ and $\overline{\nu}_e, \overline{\nu}_\mu, \overline{\nu}_\tau$) which have opposite charge and lepton quantum number.

The six quarks are arranged in a similar way, each of the three generations contains an up-type quark (u, c, t) and a down-type quark (d, s, b). The up-type quarks have electric charge of +2/3 while the down-type quarks have an electric charge of -1/3. Unlike leptons, quarks carry color charge which comes in three values: red, green and blue, in analogy with the primary colors of light. They also possess flavor quantum numbers for each of the three generations [3]. However, unlike lepton flavor, quark flavor conservation is violated in the weak interaction mediated by $W^\pm$ bosons where the so-called flavor changing charged currents (FCCC) exist. Flavor changing neutral currents (FCNC) exist in the SM only at loop level and are highly suppressed. Similar to leptons, each quark has an associated antiquark with opposite quantum numbers.

The quarks can never exist freely and they can only form color neutral objects called *hadrons*. This is also known as color confinement. When quarks are produced, they immediately hadronise, i.e. combine to form colorless hadrons. Hadrons can be either *mesons* which consist of a quark and antiquark pair ($q\overline{q}$) with opposite colors or *baryons* which consist of three quarks (qqq) or antiquarks ($\overline{qqq}$) with the color neutral rgb configuration. More recently, exotic states with four and five quarks known as tetraquarks and pentaquarks were observed [24–26]. One of the first experimental evidence for the existence of the color charge was the discovery of the Ω^- baryon which has the quark content of sss [27]. Since a state with three identical quarks would violate the Pauli exclusion principle, a color property with three distinct values was needed to distinguish between them. The quark model was developed in the early 1960s by Gell-Man and Zweig [28, 29] and it predicted the existence of the Ω^- before it was actually discovered.

2.1.1 Gauge theory

The Standard Model is a quantum field theory (QFT) which is gauge invariant under specific symmetry groups. The groups are particular cases of the special unitary group $SU(n)$ which is the group of $n \times n$ unitary matrices with unit determinant. A complex $n \times n$ matrix is specified by $2n^2$ parameters. The unitarity condition reduces it to n^2 degrees of freedom and the unit determinant constraint finally gives $n^2 - 1$ degrees of freedom. This means that each group has $n^2 - 1$ generators, i.e. traceless, hermitian,

---

[2] These are called electron, muon or tau number. The e^- and ν_e have electron number +1 while their antiparticles e^+ and $\overline{\nu}_e$ have electron number -1. The leptons in one generation have 0 lepton number for the other generations.

[3] For the first generation (u, d) it is isospin while for the other two generations there is charm, strangeness, topness and bottomness (or beauty)

linearly independent $n \times n$ matrices. This in turn means that any special unitary $n \times n$ matrix can be written as a linear combination of the group generators. In the SM, each of three interactions is associated with a symmetry $SU(n)$ group and the number of generators of each group represents the number of vector bosons (also known as gauge bosons) that mediate the interaction. The $SU(n)$ groups relevant to the SM are the cases where $n = 2$ and $n = 3$. The $SU(2)$ group has three generators (2×2 matrices) and it describes the weak interaction and its three vector bosons $W^{\pm}, Z$. The $SU(3)$ group has eight generators (3×3 matrices) and it describes the strong interaction with eight gluons. The electromagnetic interaction is described by the $U(1)$ symmetry group which is the group of unitary matrices of dimension 1, i.e. all complex numbers of absolute value 1. The group has one generator, therefore the electromagnetic force has the photon as its single gauge boson. The electroweak force which is symmetric under $SU(2) \times U(1)$ is a unification of the weak and electromagnetic interactions via the spontaneous symmetry breaking by the Higgs mechanism [30,31]. The Standard Model is therefore a gauge theory with the symmetry group $SU(3) \times SU(2) \times U(1)$.

In the QFT theory of the SM, particles are considered excitations of quantum fields. The fields are mathematical functions that have a value at each point in the space-time four-vector coordinate $x \equiv (x, y, z, t)$. The dynamics of such fields are described via the Lagrangian formalism. In classical theory, the Lagrangian is a function of the generalized coordinates of a system, however in field theory it is replaced by the Lagrangian density which is a function of the fields and their derivatives. The Lagrangian has the property is that it is Lorentz invariant, i.e. it has space-time symmetry. The field equations of motion of a field Φ follow from Hamilton's principle of least action:

$$\partial_\mu \frac{\partial \mathscr{L}}{\partial(\partial_\mu \Phi)} - \frac{\partial \mathscr{L}}{\partial \Phi} = 0, \tag{2.1}$$

where the covariant derivative $\partial_\mu \equiv \frac{\partial}{\partial x^\mu}$ containts the derivatives with respect to each of the four space-time coordinates, $\mu = 1,2,3,4$ and the Einstein summation convention is used on the repeated index μ.

The Lagrangian of a real scalar field ϕ with one degree of freedom which describes a spin-0 particle with mass m is given by

$$\mathscr{L} = \frac{1}{2}(\partial_\mu \phi)^2 - \frac{m}{2}\phi^2. \tag{2.2}$$

Applying Eq. 2.1 to the scalar field Lagrangian gives the equation of motion, known as the Klein-Gordon equation:

$$(\Box + m^2)\phi = 0, \tag{2.3}$$

where $\Box \equiv \partial^\mu \partial_\mu$ is the d'Alembert operator.

A complex scalar field has two degrees of freedom and describes a charged spinless particle with mass m. Its Lagrangian is given by

$$\mathscr{L} = (\partial_\mu \phi)^\dagger (\partial^\mu \phi) - m^2 \phi^\dagger \phi. \tag{2.4}$$

A vector field A_μ has three degrees of freedom and describes particles with spin-1. In case of massless particles such as the photon, there are just two degrees of freedom and the Lagrangian is given by

$$\mathscr{L} = -\frac{1}{4} F^{\mu\nu} F_{\mu\nu} \text{ with } F_{\mu\nu} = \partial_\mu A_\nu - \partial_\nu A_\mu. \tag{2.5}$$

The equations of motion read

$$(\Box g^{\mu\nu} - \partial^\mu \partial^\nu) A_\nu = 0, \tag{2.6}$$

where $g^{\mu\nu}$ is the metric tensor. In the case of the photon as the vector field A_μ, the field equations of Eq.2.6 represent the Maxwell equations of electromagnetism.

The fermions are spin-$\frac{1}{2}$ particles and are described by four-component Dirac fields, also known as Dirac spinors, usually denoted by ψ:

$$\psi(x) = \begin{pmatrix} \psi_1(x) \\ \psi_2(x) \\ \psi_3(x) \\ \psi_4(x) \end{pmatrix}. \tag{2.7}$$

The Lagrangian of fermion fields is given by the Dirac Lagrangian:

$$\mathscr{L}_{Dirac} = \overline{\psi}(i\gamma^\mu \partial_\mu - m)\psi \tag{2.8}$$

where $\overline{\psi} \equiv \psi^\dagger \gamma^0$ and γ^μ with $\mu = 0, 1, 2, 3$ are the 4×4 Dirac matrices. The equation of motion is thus given by the Dirac equation:

$$(i\gamma^\mu \partial_\mu - m)\psi = 0, \tag{2.9}$$

which has two solutions that correspond to particle and antiparticle fields.

The three fundamental interactions can be derived from the condition that their Lagrangian stays invariant under transformations of the symmetry group.

2.1.2 Quantum electrodynamics

The field theory that accommodates the electromagnetic interaction is called quantum electrodynamics (QED). The Lagrangian of charged fermion fields is the Dirac Lagrangian given in Eq. 2.8. This Lagrangian is invariant to $U(1)$ transformations of the form:

$$\psi(x) \rightarrow \psi'(x) = e^{i\alpha} \psi(x), \tag{2.10}$$

where α is an arbitrary phase. This means that the Lagrangian has a *global* $U(1)$ symmetry. The QED interaction can be derived by imposing *local* gauge invariance under $U(1)$ transformations such that the phase α is now a function of the space-time $\alpha \rightarrow \alpha(x)$. The Lagrangian now has to be invariant to transformations of the form:

$$\psi(x) \rightarrow \psi'(x) = e^{i\alpha(x)}\psi(x). \tag{2.11}$$

In order to achieve local gauge invariance, a vector field A_μ must be introduced and the covariant derivative in Eq. 2.8 must be substituted by

$$\partial_\mu \rightarrow D_\mu = \partial_\mu - ieA_\mu. \tag{2.12}$$

This is called the *minimal substitution* rule. The field A_μ transforms as

$$A_\mu(x) \longrightarrow A'_\mu(x) = A_\mu(x) + \frac{1}{e}\partial_\mu \alpha(x), \tag{2.13}$$

where e is the electric charge.

The resulting local gauge invariant Lagrangian contains an additional term that describes the interaction of the vector field A_μ with the charged fermions ψ.

$$\mathscr{L} = \overline{\psi}(i\gamma^\mu \partial_\mu - m)\psi = \mathscr{L}_{Dirac} + e\overline{\psi}\gamma^\mu\psi A_\mu. \tag{2.14}$$

The interaction term $e\overline{\psi}\gamma^\mu\psi A_\mu$ can be written as $j^\mu A_\mu$ where $j^\mu = e\overline{\psi}\gamma^\mu\psi$ is the conserved electromagnetic current with the electric charge e as the associated conserved charge. The full QED Lagrangian is obtained by adding a kinetic term (Eq. 2.5) for the gauge boson A_μ and is invariant to local gauge transformations of Eq. 2.11

$$\mathscr{L}_{QED} = -\frac{1}{4}F^{\mu\nu}F_{\mu\nu} + \overline{\psi}(i\gamma^\mu D_\mu - m)\psi + e\overline{\psi}\gamma^\mu\psi A_\mu. \tag{2.15}$$

Thus, QED completely describes the electromagnetic interaction by having a term that describes the kinematics of the gauge boson identified as the photon, a term that describes the kinematics of the fermions, i.e. the Dirac Lagrangian and the interaction term between the photon and the fermions resulting from imposing local gauge invariance. The coupling strength of QED is defined in terms of the electric charge e as $\alpha = \frac{e^2}{4\pi}$.

The field strength $F_{\mu\nu}$ has the form given in Eq. 2.5 due to the fact that $U(1)$ is an abelian gauge group, i.e. two succesive $U(1)$ transformations commute, since it is just the product of two complex numbers. This is not the case for the other symmetry groups in the SM since $n \times n$ matrices do not commute in general and thus they are referred to as non-abelian gauge groups.

2.1.3 Quantum chromodynamics

The theory that describes the strong interaction is known as quantum chromodynamics (QCD) and it is based on the symmetry group $SU(3)$. The group is specified by eight generators which means that any $SU(3)$ transformation can be written as a linear combination of these eight matrices. The representation of the group is that the quark fields come in color triplets with red, blue and green color states

$$\psi = \begin{pmatrix} \psi_r \\ \psi_g \\ \psi_b \end{pmatrix}. \tag{2.16}$$

The Dirac Lagrangian, where ψ is now a color triplet, has global $SU(3)$ symmetry, i.e. it is invariant under global transformations of the form

$$\psi(x) \to \psi'(x) = e^{i\sum_i \alpha_i T_i}\psi(x), \tag{2.17}$$

where $T_i = \frac{1}{2}\lambda_i$ are the group generators and λ_i are the 3×3 Gell-Mann matrices and $i = 1, \ldots, 8$. The generators do not commute, i.e

$$[T_a, T_b] = i f_{abc} T_c, \tag{2.18}$$

thus $SU(3)$ is a non-abelian gauge group. In order to extend the global gauge invariance to a local gauge invariance, the constants α_i are promoted to functions of space-time $\alpha_i(x)$. Following the same recipe as for QED, to keep the Lagrangian invariant under local $SU(3)$ eight new vector fields G^a_μ are needed and the covariant derivative becomes

$$\partial_\mu \to D_\mu = \partial_\mu - i g_s T^a G^a_\mu, \tag{2.19}$$

where g_s is the strong coupling constant. The field strength in the non-abelian case is given by

$$G^a_{\mu\nu} = \partial_\mu G^a_\nu - \partial_\nu G^a_\mu + g_s f_{abc} G^b_\mu G^c_\nu. \tag{2.20}$$

The final QCD Lagrangian is build in the same way as in the case of QED, with a boson kinetic term, a fermion kinetic term (Dirac Lagrangian) and the resulting interaction term, as follows

$$\mathscr{L}_{QCD} = -\frac{1}{4} G^a_{\mu\nu} G^{a,\mu\nu} + \overline{\psi}(i\gamma^\mu \partial_\mu - m)\psi + g_s \overline{\psi}\gamma^\mu \frac{\lambda^a}{2} \psi G^a_\mu. \tag{2.21}$$

The interaction term $g_s\overline{\psi}\gamma^\mu\frac{\lambda^a}{2}\psi G^a_\mu$ describes the interaction of eight quark currents $j^\mu_a = g_s\overline{\psi}\gamma^\mu\frac{\lambda^a}{2}\psi$ with the gluon gauge fields G^a_μ. Due to the form of the gluon field strength (Eq. 2.20), the kinetic term $-\frac{1}{4}G^a_{\mu\nu}G^{a,\mu\nu}$ contains triple and quartic gluon self-interaction. Since gluons carry color charge, they can interact between themselves, however this is not case for QED as the neutrally charged photon can not interact with itself.

2.1.4 The weak interaction

In the context of the weak interaction it is first useful to define the concepts of *helicity* and *chirality*. Helicity states are defined by the projection of the spin onto the momentum direction. A particle with *right-handed* helicity has the direction of the spin along the direction of the momentum, while a particle with *left-handed* helicity has the direction of the spin opposite to the momentum direction. The concept of chirality is more abstract and has no trivial physical interpretation. For massless particles, the helicity and chirality are equivalent. For fermions, in the Dirac representation, chirality is defined via the matrix $\gamma^5 \equiv i\gamma^0\gamma^1\gamma^2\gamma^3$, thus the chirality states are eigenstates of the γ^5 matrix. A Dirac spinor can be written in terms of its left and right-handed chiral states

$$\psi(x) = \underbrace{\frac{1-\gamma^5}{2}\psi(x)}_{\psi_L} + \underbrace{\frac{1+\gamma^5}{2}\psi(x)}_{\psi_R}, \tag{2.22}$$

using the left-handed and right-handed chiral projector operators

$$P_{L,R} = \frac{1 \pm \gamma^5}{2}. \tag{2.23}$$

Besides the symmetry of the SM with respect to the continuous transformations of the gauge groups and the Lorentz invariance, i.e. symmetry with respect to space-time, there are also *discrete* symmetries under which the SM may or may not be invariant. The fundamental discrete symmetries in the SM are the following

- **Parity (P)**: reverses spatial coordinates $x \to -x$ and thus changes the chirality of the particle. Antiparticles have opposite parity than particles.
- **Charge conjugation (C)**: changes the particle into its antiparticle switching all quantum numbers such as the electric charge or color.
- **Time reversal (T)**: reverses the time coordinate $t \to -t$ and thus changes the sign of the momentum and spin of the particle

Even though each of the individual symmetries could be violated, there is a theorem known as the CPT theorem [32] which establishes that the combined CPT symmetry must be conserved for any Lorentz invariant quantity. The consequence of the CPT symmetry for the fermion fields is that all particles states have an antiparticle with the same mass.

In QED and QCD the quantum numbers of the parity and charge conjugation operations are conserved. This is due to the nature of the QED and QCD interactions and in particular to their interaction term, or equivalently to the current j^μ which is of the form $\overline{\psi}\gamma^\mu\psi$. In the late 1950s the Wu experiment [33] and later the Lederman experiment [34] demonstrated that the weak interaction violates parity. These experiments concluded that the neutrino comes only in one helicity state, namely left-handed, which means that parity is violated maximally in the weak interaction. Since the weak interaction couples only to left-handed fermions, parity violation implies that charge conjugation is also maximally violated in weak processes. In order to accommodate these observations in the theory, the structure of the weak current has to be different than the vector (spin-1) current $\overline{\psi}\gamma^\mu\psi$ structure of QED and QCD. The form of the weak current has to be a bilinear combination of the two spinor fields of the form $\overline{\psi}_1\Gamma\psi_2$ where Γ is a 4×4 matrix based on the Dirac γ^μ matrices. The requirement of Lorentz invariance of the interaction allows only the bilinear forms listed in Table 2.2.

Bilinear	Form	Boson spin
Scalar	$\overline{\psi}_1\psi_2$	0
Pseudoscalar	$\overline{\psi}\gamma^5\psi_2$	0
Vector	$\overline{\psi}_1\gamma^\mu\psi_2$	1
Axial vector	$\overline{\psi}_1\gamma^\mu\gamma^5\psi_2$	1
Tensor	$\overline{\psi}_1(\gamma^\mu\gamma^\nu-\gamma^\nu\gamma^\mu)\psi_2$	2

Table 2.2: Lorentz invariant bilinear covariant currents [10]

The structure of the weak current must therefore be a combination of the scalar (S), pseudoscalar (P), vector (V), axial vector (A) or tensor (T) currents with couplings g_S, g_P, g_V, g_A and g_T, respectively.

The weak current is experimentally established to be a $(V-A)$ current, i.e. vector minus axial vector, and thus the weak current must be of the form

$$j^\mu_{weak}=\frac{g_W}{2\sqrt{2}}\overline{\psi}_1\gamma^\mu(1-\gamma^5)\psi_2=\frac{g_W}{2\sqrt{2}}\overline{\psi}_{1,L}\gamma^\mu\psi_{2,L}, \tag{2.24}$$

where g_W is the weak coupling and $\psi_{L(1,2)}$ are two left-handed spinors [4].

Due to the form of the weak current, and the fact that it includes the left-handed P_L chiral operator given in Eq. 2.22, the weak interaction couples only to left-handed (right-handed) chiral particle (antiparticle) states.

The symmetry group of the weak interaction is $SU(2)$. The three gauge bosons W^a_μ are introduced by the same recipe as $U(1)$ and $SU(3)$ by requiring invariance of the Lagrangian under $SU(2)$ local phase transformations such as

$$\psi(x)'\to e^{i\alpha_i(x)T_i}\psi(x), \tag{2.25}$$

where $i=1,2,3$, $T_i=\frac{1}{2}\sigma_i$ are the three generators and σ_i are the 2×2 Pauli matrices. The generators follow the same commutation rule from Eq. 2.18 as for $SU(3)$. The resulting interaction term in the Lagrangian is

$$\mathscr{L}^{int}_{weak}=g_W\overline{\psi}_L\gamma^\mu\frac{\sigma_a}{2}\psi_L W^a_\mu, \tag{2.26}$$

which describes the interaction of the three W^a_μ bosons with the left handed fermion fields.

Since the generators of $SU(2)$ are 2×2 matrices, the spinors on which they act are defined to be weak isospin *doublets*, in analogy with the color triplets of QCD. The weak isospin can be seen as the charge of the weak interaction and a doublet has a

---

[4] The relation $(1+\gamma^5)\gamma^\mu(1-\gamma^5)=2\gamma^\mu(1-\gamma^5)$ is used to project out the particle and antiparticle fields to their left-handed states

total weak isospin of $I_W = +1/2$ while the z (third) component of I_W distinguishes the two members of the doublet where the upper (lower) member has $I_z = +1/2$ $(-1/2)$. This is in analogy with the intrinsic spin of particles in quantum mechanics which is also described by the Pauli matrices. The weak isospin doublets consist only of left-handed particle (or right-handed antiparticle) chiral states that differ by one unit of electric charge as given below

$$\psi_L = \begin{pmatrix} \nu_e \\ e^- \end{pmatrix}_L, \begin{pmatrix} \nu_\mu \\ \mu^- \end{pmatrix}_L, \begin{pmatrix} \nu_\tau \\ \tau^- \end{pmatrix}_L, \begin{pmatrix} u \\ d \end{pmatrix}_L, \begin{pmatrix} c \\ s \end{pmatrix}_L, \begin{pmatrix} t \\ b \end{pmatrix}_L. \tag{2.27}$$

Since the local invariance to phase transformations of Eq. 2.25 affects only $SU(2)$ left-handed doublets, i.e. the interaction term in the Lagrangian couples the vector fields only to left-handed doublets, the right-handed particles (and left-handed antiparticles) are placed in weak isospin *singlets* with $I_W = 0$:

$$\psi_R = e^-_R, \mu^-_R, \tau^-_R, u_R, d_R, c_R, s_R, t_R, b_R. \tag{2.28}$$

For this reason, the weak interaction symmetry group is also known as $SU(2)_L$. The right-handed neutrinos are chargeless with respect to all three SM interactions, that is they do not carry electric charge, color charge or weak isospin. Therefore, they are not part of the SM.

At this point, the $W_\mu^{(1,2,3)}$ of $SU(2)_L$ are not yet the physical $W^\pm$ and Z bosons of the weak interaction. The massive weak interaction bosons are obtained in the framework of the electroweak theory described in the following section.

2.1.5 Electroweak theory

In the 1960s, Glashow, Weinberg and Salam [35–37] unified the weak and electromagnetic interactions as manifestations of the same underlying electroweak interaction. The electroweak interaction is obtained by requiring local gauge invariance under a new symmetry group $SU(2)_L \times U(1)_Y$, where $U(1)_Y$ replaces the $U(1)$ of electromagnetism and introduces the coupling to a new charge Y called *weak hypercharge*. The quantum number Y is assigned to the left- and right-handed fields such that the following relation is satisfied

$$Q = I_z + \frac{Y}{2}, \tag{2.29}$$

where Q is the electric charge and I_z is the weak isospin. The three quantum numbers of the electroweak interaction for all left-handed and right-handed fermions are given in Tab. 2.3.

	ν_L	ℓ_L	u_L	d_L	ℓ_R	u_R	d_R
I_z	$+\frac{1}{2}$	$-\frac{1}{2}$	$+\frac{1}{2}$	$-\frac{1}{2}$	0	0	0
Y	-1	-1	$+\frac{1}{3}$	$+\frac{1}{3}$	-2	$+\frac{4}{3}$	$-\frac{2}{3}$
Q	0	-1	$+\frac{2}{3}$	$-\frac{1}{3}$	-1	$+\frac{2}{3}$	$-\frac{1}{3}$

Table 2.3: The quantum numbers of weak isospin projection I_z, weak hypercharge Y and electric charge Q for the left-handed and right handed fermions in the SM. Here, ν and ℓ represent the three neutral and charged lepton generations while u and d the three up-type and down-type quark generations

In order to keep the Lagrangian invariant to local $SU(2)_L \times U(1)_Y$ transformations, four vector boson fields must be introduced in the covariant derivative, the three W_μ^a bosons of the weak interaction and a new B_μ boson of $U(1)_Y$. The Lagrangian kinetic term associated to the $SU(2)_L \times U(1)_Y$ bosons of the electroweak interaction is

$$\mathscr{L}_{EW}^{kinetic,bosons} = -\frac{1}{4} W_{\mu\nu}^a W^{\mu\nu,a} - \frac{1}{4} B_{\mu\nu} B^{\mu\nu}, \tag{2.30}$$

where the field strengths are given by

$$\begin{aligned} W_{\mu\nu}^a &= \partial_\mu W_\nu^a - \partial_\nu W_\mu^a + g_W f_{abc} W_\mu^b W_\nu^c, \\ B_{\mu\nu} &= \partial_\mu B_\nu - \partial_\nu B_\mu. \end{aligned} \tag{2.31}$$

At this stage, the gauge fields W_μ^a and B_μ are still massless, as a mass term would violate gauge invariance. The masses of gauge bosons are generated by the mechanism of spontaneous symmetry breaking of the electroweak interaction described later in this section.

Since the right-handed fermion fields are singlets under $SU(2)$, i.e. they have $I_z = 0$, they only couple to the $U(1)_Y$ boson while the left-handed fields couple to the $SU(2)_L \times U(1)_Y$ bosons. Therefore, the covariant derivative which is different for left-handed and right-handed fields reads

$$\partial_\mu \to D_\mu^{L,R} = \partial_\mu - i g_W \frac{\sigma_a^{L,R}}{2} W_\mu^a - i g' \frac{Y}{2} B_\mu, \; a = 1,2,3, \; \sigma_a^R = 0. \tag{2.32}$$

The symmetry of $SU(2)_L \times U(1)_Y$ is spontaneously broken by introducing the Higgs field ϕ as a $SU(2)$ doublet of complex scalar fields with hypercharge $Y = 1$ and weak isospin $I_z = -1/2$

$$\phi(x) = \begin{pmatrix} \phi^+(x) \\ \phi^0(x) \end{pmatrix}. \tag{2.33}$$

The Lagrangian of the Higgs field is the Lagrangian of a complex scalar field introduced in Eq. 2.4, however the field is not free anymore but has a potential $V(\phi)$

$$\mathscr{L}_{Higgs} = (D_\mu \phi)^\dagger (D^\mu \phi) - V(\phi), \tag{2.34}$$

where $D_\mu = D^L_\mu$ as defined in Eq. 2.32. The potential has the form

$$V(\phi) = -\mu^2\phi^\dagger\phi + \lambda(\phi^\dagger\phi)^2, \tag{2.35}$$

with $\mu^2 > 0$ and $\lambda > 0$. A schematic of the Higgs potential is shown in Fig. 2.3. The minimum of this potential does not occur at $\phi = 0$, but instead the minimum is not uniquely determined and occurs at $\phi = e^{i\theta}\sqrt{\frac{\mu^2}{2\lambda}}$. Therefore, the choice of $\theta \in [0, \pi]$ spontaneously breaks the symmetry. In the so-called unitarity gauge, the nonzero *vacuum expectation value* (VEV) of the Higgs potential is given by

$$\langle 0|\phi|0\rangle = \frac{1}{\sqrt{2}}\begin{pmatrix}0\\ v\end{pmatrix}, \tag{2.36}$$

where $v = \frac{2\mu}{\sqrt{\lambda}}$. Expanding the field around the vacuum expectation value and choosing a particular gauge, the Higgs field can be written as

$$\phi(x) = \frac{1}{\sqrt{2}}\begin{pmatrix}0\\ v + H(x)\end{pmatrix}. \tag{2.37}$$

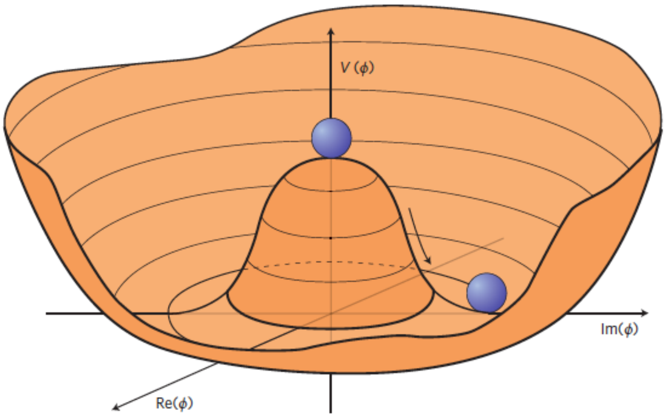

Figure 2.3: Schematic of the Higgs potential. The minimum of the potential is not uniquely determined causing symmetry breaking [38].

The potential in Eq.2.35 can then be written as

$$V = \mu^2 H^2 + \frac{\mu^2}{v}H^3 + \frac{\mu^2}{4v^2}H^4. \tag{2.38}$$

The first term in the potential is of the form $\frac{M_H}{2}H^2$ and it describes a scalar particle with mass $M_H = \mu\sqrt{2}$ which is identified as the Higgs boson. The other terms in Eq.2.38 describe triple and quartic Higgs self-interactions. Introducing Eq. 2.37 in the Higgs Lagrangian of Eq. 2.34 gives mass terms for the gauge bosons and interaction terms between the Higgs field and the gauge bosons. The mass term reads

$$\frac{1}{2}\left(\frac{g_W}{2}v\right)^2(W_1^2+W_2^2)+\frac{1}{2}\left(\frac{v}{2}\right)^2(W^3_\mu,B_\mu)\begin{pmatrix} g_W^2 & g_W g' \\ g_W g' & g'^2 \end{pmatrix}\begin{pmatrix} W^{3,\mu} \\ B^\mu \end{pmatrix}. \tag{2.39}$$

In order to obtain the physical four bosons of the electroweak interaction, i.e. the three massive weak bosons $W^\pm, Z$ and the massless electromagnetic boson A_μ, the following transformations need to be made

$$\begin{aligned} W_\mu^\pm &= \frac{1}{\sqrt{2}}(W_\mu^1 \mp iW_\mu^2), \\ \begin{pmatrix} Z_\mu \\ A_\mu \end{pmatrix} &= \begin{pmatrix} \cos\theta_W & \sin\theta_W \\ -\sin\theta_W & \cos\theta_W \end{pmatrix}\begin{pmatrix} W_\mu^3 \\ B_\mu \end{pmatrix}, \end{aligned} \tag{2.40}$$

where θ_W is the weak mixing angle defined as $\tan\theta_W = \frac{g'}{g_W}$. With this transformation of the fields, the mass term of Eq. 2.39 becomes diagonal and reads

$$M_W^2 W_\mu^+ W^{-\mu} + \frac{1}{2}(A_\mu, Z_\mu)\begin{pmatrix} 0 & 0 \\ 0 & M_Z^2 \end{pmatrix}\begin{pmatrix} A^\mu \\ Z^\mu \end{pmatrix}, \tag{2.41}$$

with the masses of the gauge bosons given by $M_W = \frac{1}{2}g_W v$, $M_Z = \frac{1}{2}\sqrt{g_W^2 + g'^2}\,v$ and $M_A = 0$. In this way, three out of four bosons of $SU(2)_L \times U(1)_Y$ have acquired mass while the photon has remained massless.

The fermion kinetic term is obtained by replacing the covariant derivative of Eq. 2.32 in the Dirac Lagrangian. Writing the Lagrangian explicitly for left-handed doublets and right-handed singlets for quarks and leptons gives

$$\begin{aligned} \mathscr{L}_{EW}^{kinetic,fermions} =& i\overline{\ell}_L\gamma^\mu D_\mu^L \ell_L + i\overline{\ell}_R\gamma^\mu D_\mu^R \ell_R \\ &+ i\overline{q}_L\gamma^\mu D_\mu^L q_L + i\overline{d}_R\gamma^\mu D_\mu^R d_R + i\overline{u}_R\gamma^\mu D_\mu^R u_R. \end{aligned} \tag{2.42}$$

The Dirac mass terms for the fermion fields have the form $m\overline{\psi}\psi = m(\overline{\psi_L}\psi_R + \overline{\psi_R}\psi_L)$ and mix left- and right-handed fields which form different multiplets under $SU(2)$. Therefore, Dirac mass terms are not allowed as they would break gauge invariance of the theory. Masses for the fermions will be added to the Lagrangian in a later step through their interaction with the Higgs in the form of gauge-invariant Yukawa terms. In addition to the kinetic terms that describe the propagation of fermions, i.e. $i\overline{\psi_L}\gamma^\mu\partial_\mu\psi_L$, Eq. 2.42 contains the interactions of the electromagnetic current and the weak charged and neutral currents with the associated $SU(2)_L \times U(1)_Y$ bosons. Using the first lepton generation as an example, the first term of Eq. 2.42 written explicitly using Eqs. 2.32 and 2.40 gives

$$-\frac{g_W}{2}\left(\overline{\nu_L}\;\overline{e_L}\right)\gamma^\mu\begin{pmatrix} \frac{Z_\mu}{\cos\theta_W} & \sqrt{2}W_\mu^- \\ \sqrt{2}W_\mu^+ & \cos\theta_W Z_\mu - 2\sin\theta_W A_\mu \end{pmatrix}\begin{pmatrix} \nu_L \\ e_L \end{pmatrix}. \tag{2.43}$$

The diagonal terms couple leptons of the same flavor to the Z_μ and A_μ bosons, giving the electromagnetic and neutral weak currents. In the case of neutrinos, only the Z boson term survives since they are electrically neutral and can not interact with the photon, while the charged leptons couple to both the Z and the photon. The off-diagonal terms represent the charged current weak interactions and so the $W^\pm$ bosons couple leptons of different flavors. The main difference between quarks and leptons lies in the charged current interactions and it is due to the phenomenon of quark mixing which is a consequence of the mass Yukawa terms as shown later in this section. In general the electromagnetic, neutral and charged weak currents can be written as [5]

$$\begin{aligned} j^\mu_{EM} &= -e \sum_{f=\ell,q} Q_f \overline{\psi_f} \gamma^\mu \psi_f, \\ j^\mu_{NC} &= \frac{g_W}{2\cos\theta_W} \sum_{f=\ell,q} \overline{\psi_f}(C^V_f \gamma^\mu - C^A_f \gamma^\mu \gamma^5)\psi_f, \\ j^{\mu+}_{CC} &= \frac{g_W}{\sqrt{2}} \left(\sum_{i=1,2,3} \overline{\nu_{Li}} \gamma^\mu \ell_{Li} + \sum_{i=1,2,3} \overline{u_{Li}} \gamma^\mu d_{Li} \right), \end{aligned} \tag{2.44}$$

where $e = g_W \sin\theta_W$, $C^V_f = I_{z,f} - 2Q_f \sin^2\theta_W$, $C^A_f = I_{z,f}$ and the quantum numbers I_z and Q for each fermion f are given in Tab. 2.3. The interaction part of the kinetic electroweak Lagrangian can then be written as

$$\mathscr{L}^{int}_{EW} = j^\mu_{EM} A_\mu + j^\mu_{NC} Z_\mu + j^{\mu+}_{CC} W^+_\mu + j^{\mu-}_{CC} W^-_\mu. \tag{2.45}$$

Unlike the masses of the gauge fields which follow from the covariant derivative in the Higgs kinetic term of Eq. 2.34, the fermion masses must be added by hand via the Yukawa Lagrangian of the form

$$\mathscr{L}_{Yukawa} = Y_f \overline{\psi_L} \phi \psi_R + h.c.^{6}, \tag{2.46}$$

where Y_f is the Yukawa coupling for the fermion f. After the spontaneous symmetry breaking, the Higgs field takes the form given in Eq. 2.37 and thus the Yukawa terms become proper gauge-invariant mass terms. Writing explicitly the Yukawa term for the the first lepton generation gives

$$\mathscr{L}^e_{Yukawa} = \frac{Y_e}{\sqrt{2}} \left(\overline{\nu_L}\ \overline{e_L} \right) \begin{pmatrix} 0 \\ v+H \end{pmatrix} e_R + h.c., \tag{2.47}$$

where the term $\frac{Y_e v}{\sqrt{2}}(\overline{e_L} e_R + \overline{e_R} e_L) = \frac{Y_e v}{\sqrt{2}} \overline{e} e$ appears and the mass of the electron is identified as $m_e = \frac{Y_e v}{\sqrt{2}}$. The term proportional to H represents the coupling of the Higgs to electrons. Since the upper component of the Higgs doublet is zero, the neutrino does not acquire a mass term, therefore for the lepton doublets one Yukawa

---

[5] The charged current $j^{\mu-}_{CC}$ associated with the W^-_μ boson has been omitted

[6] h.c. stands for hermitian conjugate

term in the Lagrangian is sufficient. For the quark doublets this is not the case, since both components are massive and writing a single Yukawa term would yield mass only for the down quarks. Consequently, the Yukawa term for up quarks must be written in terms of $\widetilde{\phi} = i\sigma_2\phi^* = \begin{pmatrix} v + H^* \\ 0 \end{pmatrix}$ which has a nonzero upper component.

The most general gauge-invariant Yukawa Lagrangian accounting for all three generations of quarks and leptons can be written as

$$\mathscr{L}_{Yukawa} = Y^d_{ij}\overline{q_{Li}}\phi d_{Rj} + Y^u_{ij}\overline{q_{Li}}\widetilde{\phi} u_{Rj} + Y^\ell_{ij}\overline{\ell_{Li}}\phi \ell_{Rj} + h.c., \tag{2.48}$$

where $Y^d_{ij}, Y^u_{ij}, Y^\ell_{ij}$ are arbitrary non-diagonal complex matrices with $i, j = 1,2,3$. It can be seen that these matrices couple fermions from different generations and thus give rise to the phenomenon of mixing. For the quark sector, after the spontaneous symmetry breaking, the Yukawa Lagrangian becomes

$$\begin{aligned} \mathscr{L}^{quarks}_{Yukawa} &= Y^d_{ij}\frac{v}{\sqrt{2}}\overline{d_{Li}}d_{Rj} + Y^u_{ij}\frac{v}{\sqrt{2}}\overline{u_{Li}}u_{Rj} + h.c., \\ &= M^d_{ij}\overline{d_{Li}}d_{Rj} + M^u_{ij}\overline{u_{Li}}u_{Rj} + h.c. \end{aligned} \tag{2.49}$$

where the interaction terms have been omitted. In order to obtain proper mass terms, the matrices M^d_{ij} and M^u_{ij} must have diagonal form. This is achieved with the help of four unitary matrices $V^d_L, V^u_L, V^d_R, V^u_R$ such as

$$\begin{aligned} M^d_{diagonal} &= V^d_L M^d V^{d\dagger}_R, \\ M^u_{diagonal} &= V^u_L M^u V^{u\dagger}_R. \end{aligned} \tag{2.50}$$

The following redefinition of the quark states can be then performed to make the transformation from the flavor eigenstates to the mass eigenstates

$$\begin{aligned} d_{Li} &\to (V^d_L)_{ij}d_{Lj}, \quad & d_{Ri} &\to (V^d_R)_{ij}d_{Rj}, \\ u_{Li} &\to (V^u_L)_{ij}u_{Lj}, \quad & u_{Ri} &\to (V^u_R)_{ij}u_{Rj}. \end{aligned} \tag{2.51}$$

The flavor eigenstates are the states that couple to the $W^\pm$ bosons (where the $W^\pm$ interaction is diagonal) while the mass eigenstates are the states with definite masses and lifetimes which are measured in experiments (where the masses are diagonal). The Yukawa Lagrangian for quarks now contains proper mass terms for the three up and down quark generations

$$\mathscr{L}^{quarks}_{Yukawa} = (M^d_{ij})_{diagonal}\overline{d_{Li}}d_{Rj} + (M^u_{ij})_{diagonal}\overline{u_{Li}}u_{Rj} + h.c. \tag{2.52}$$

The consequence of the redefinition in Eq. 2.51 is that if the quarks are expressed in their mass eigenstates instead of the flavor eigenstates, quark mixing between different generations appears in the charged current interactions. In other words, by making the Yukawa matrices diagonal in order to obtain proper mass terms for the quarks, the price to pay is that off-diagonal terms will appear in the charged currents.

Due to the unitarity of the matrices used in Eq. 2.51, introducing the mass eigenstates in the weak neutral current, which only involves terms like $\overline{u}u$ and $\overline{d}d$, does not lead to off-diagonal terms. This means that transitions between up or down quarks of different generations (such as b to s transitions) do not take place at tree level in the SM. In literature, these transitions are known as flavor changing neutral currents (FCNC) and they can only occur via loop diagrams, being highly suppressed in the SM. This suppression is known as the GIM mechanism [39].

The quark charged current part of Eq. 2.45 written in the flavor and mass eigenspaces is given by

$$\begin{aligned}
\mathscr{L}^{int}_{CC,flavor} &= \frac{g_W}{\sqrt{2}}\overline{u_{Li}}\gamma^{\mu}W^{-}_{\mu}d_{Li} + \frac{g_W}{\sqrt{2}}\overline{d_{Li}}\gamma^{\mu}W^{+}_{\mu}u_{Li}, \\
\mathscr{L}^{int}_{CC,mass} &= \frac{g_W}{\sqrt{2}}\overline{u_{Li}}(V^{u}_{L}V^{d\dagger}_{L})_{ij}\gamma^{\mu}W^{-}_{\mu}d_{Li} + \frac{g_W}{\sqrt{2}}\overline{d_{Li}}(V^{d}_{L}V^{u\dagger}_{L})_{ij}\gamma^{\mu}W^{+}_{\mu}u_{Li}.
\end{aligned} \tag{2.53}$$

The matrix $V^{u}_{L}V^{d\dagger}_{L} = V^{d}_{L}V^{u\dagger}_{L}$ in Eq. 2.53 is the Cabibbo-Kobayashi-Maskawa (CKM) matrix [40, 41] and it is given by

$$V_{CKM} = \begin{pmatrix} V_{ud} & V_{us} & V_{ub} \\ V_{cd} & V_{cs} & V_{cb} \\ V_{td} & V_{ts} & V_{tb} \end{pmatrix}. \tag{2.54}$$

The CKM matrix is a 3 × 3 unitary complex matrix, whose elements describe the probability of a transition from quark with flavor i to a quark with flavor j given by $|V_{ij}|^2$. In general, a $N \times N$ unitary complex matrix is described by $(N-1)^2$ parameters which can be divided into mixing angles and complex phases as follows

$$(N-1)^2 = \underbrace{\frac{1}{2}N(N-1)}_{\text{mixing angles}} + \underbrace{\frac{1}{2}(N-1)(N-2)}_{\text{complex phases}}. \tag{2.55}$$

In the case of $N = 3$ quark generations, the CKM matrix is described by three mixing angles and one complex phase. The CKM matrix can be parametrized in multiple ways and the so-called standard parametrization [42] in terms of three angles θ_{ij} and one complex phase δ is given by

$$v_{CKM} = \begin{pmatrix} c_{12}c_{13} & s_{12}c_{13} & s_{13}e^{-i\delta} \\ -s_{12}c_{23} - c_{12}s_{23}s_{13}e^{i\delta} & c_{12}c_{23} - s_{12}s_{23}s_{13}e^{i\delta} & s_{23}c_{13} \\ s_{12}s_{23} - c_{12}c_{23}s_{13}e^{i\delta} & -c_{12}s_{23} - s_{12}c_{23}s_{13}e^{i\delta} & c_{23}c_{13} \end{pmatrix} \tag{2.56}$$

where $s_{ij} \equiv \sin\theta_{ij}$, $c_{ij} \equiv \cos\theta_{ij}$, $i, j = 1, 2, 3$ and the complex phase δ is chosen to be between the first and third generation. The elements of the CKM matrix are not predicted by the SM and must be determined experimentally using decays that involve quark transitions which are sensitive to each particular element[7]. The most recent measurements of the CKM elements $|V_{ij}|$ are given by [43]

$$V_{CKM} = \begin{pmatrix} 0.974353^{+0.000049}_{-0.000056} & 0.22500^{+0.00024}_{-0.00021} & 0.003667^{+0.000088}_{-0.000073} \\ 0.22487^{+0.00024}_{-0.00021} & 0.973521^{+0.000057}_{-0.000062} & 0.04145^{+0.00035}_{-0.00061} \\ 0.008519^{+0.000075}_{-0.000146} & 0.04065^{+0.00040}_{-0.00055} & 0.999142^{+0.000018}_{-0.000023} \end{pmatrix}. \tag{2.57}$$

The diagonal elements are all very close to one meaning that the couplings to the same generation are stronger than to different generations. A popular parametrization that takes advantage of this CKM hierarchy is the Wolfenstein parametrization [44] which describes the CKM matrix in terms of the four parameters A, λ, ρ and η. These parameters are related to the standard parametrization as

$$\begin{aligned} \sin\theta_{12} &= \lambda, \\ \sin\theta_{23} &= A\lambda^2, \\ \sin\theta_{13} e^{-i\delta} &= A\lambda^3(\rho - i\eta). \end{aligned} \tag{2.58}$$

The CKM matrix in the Wolfenstein parametrization thus becomes

$$V_{CKM} = \begin{pmatrix} 1-\frac{\lambda^2}{2} & \lambda & A\lambda^3(\rho - i\eta) \\ -\lambda & 1-\frac{\lambda^2}{2} & A\lambda^2 \\ A\lambda^3(1-\rho-i\eta) & -A\lambda^2 & 1 \end{pmatrix} + \mathcal{O}(\lambda^4). \tag{2.59}$$

Instead of the parameters ρ and η, the generalized parameters are usually used and they are defined as

$$\begin{aligned} \overline{\rho} &= \rho(1 - \frac{1}{2}\lambda^2), \\ \overline{\eta} &= \eta(1 - \frac{1}{2}\lambda^2). \end{aligned} \tag{2.60}$$

The measured values of the Wolfenstein parameters are [43]

$$\begin{aligned} \lambda &= 0.22500^{+0.00024}_{-0.00022}, \\ A &= 0.8132^{+0.0119}_{-0.0060}, \\ \overline{\rho} &= 0.1566^{+0.0085}_{-0.0048}, \\ \overline{\eta} &= 0.3475^{+0.0118}_{-0.0054}. \end{aligned} \tag{2.61}$$

---

[7] For example, the elemeent V_{cb} can be measured using tree level processes of b to c decays

It is easy to see that with this parametrization the CKM matrix retains its unitarity and the hierarchical structure is emphasized. The unitarity of the CKM matrix, i.e. $V_{CKM} V_{CKM}^{\dagger} = 1$, imposes the following relations

$$\sum_k |V_{ik}|^2 = 1, \tag{2.62}$$

$$\sum_k V_{ik} V_{jk}^* = 0. \tag{2.63}$$

There are six constraints in Eq. 2.63 which can be interpreted as sides of a triangle in the complex plane. For $i = 1$ and $j = 3$, Eq. 2.63 becomes

$$V_{ud} V_{ub}^* + V_{cd} V_{cb}^* + V_{td} V_{tb}^* = 0. \tag{2.64}$$

Eq. 2.64 represents the so-called *unitarity triangle* shown in Fig. 2.4. The apex of the triangle lies in the complex plane at the point $(\overline{\rho}, \overline{\eta})$ given by

$$\overline{\rho} + i\overline{\eta} = -\frac{V_{ud} V_{ub}^*}{V_{cd} V_{cb}^*} = 1 - \frac{V_{td} V_{tb}^*}{V_{cd} V_{cb}^*}. \tag{2.65}$$

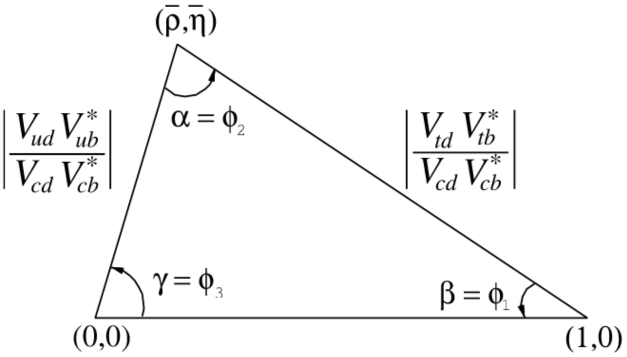

Figure 2.4: The unitarity triangle shown in the complex plane [45].

The three angles of the unitarity triangle are given by

$$\begin{aligned} \alpha = \phi_1 &= \arg\left(\frac{V_{td} V_{tb}^*}{V_{ud} V_{ub}^*} -\right), \\ \beta = \phi_2 &= \arg\left(\frac{V_{cd} V_{cb}^*}{V_{td} V_{tb}^*} -\right), \\ \gamma = \phi_3 &= \arg\left(\frac{V_{ud} V_{ub}^*}{V_{cd} V_{cb}^*} -\right), \end{aligned} \tag{2.66}$$

and their experimental values are measured to be $\alpha = 91.98^{+0.82o}_{-1.40}$, $\beta = 22.42^{+0.64o}_{-0.37}$,

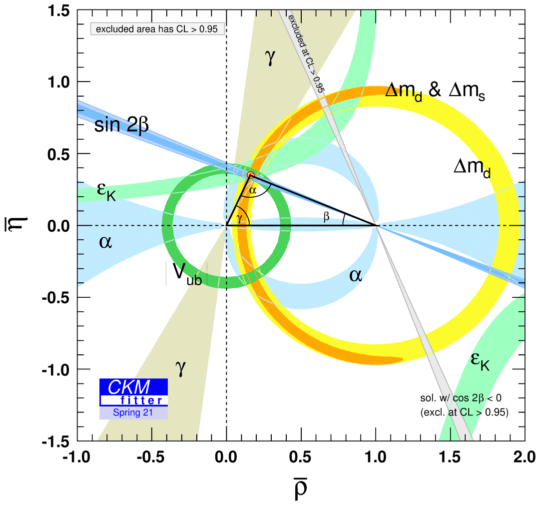

Figure 2.5: Measurements of the CKM unitarity triangle as of spring 2021. [43]

$\gamma = 65.5^{+1.3o}_{-1.2}$ [43]. The CKM unitarity triangle as measured by the CKM fitter group is shown in Fig. 2.5.

In the lepton sector mixing between families does not occur in the SM since there is no Yukawa term in the Lagrangian for the neutrino masses (as there are no right-handed neutrinos). Therefore, for the charged leptons there exists a mass basis which is the same as the flavor basis in which the mass matrix is diagonal. Nonzero masses for neutrinos would require introducing a Yukawa mass term and this would allow for lepton flavor mixing in the charged current interaction in analogy to the up and down quarks. The equivalent of the CKM matrix in the lepton sector is known as the Pontecorvo-Maki-Nakagawa-Sakata (PMNS) matrix [46].

2.1.6 *CP* violation

The charge-conjugation and parity operations were introduced in Sec. 2.1.4 and it was shown that the weak interaction maximally violates both. The *CP* operation combines charge-conjugation with parity and changes simultaneously the quantum numbers and the handedness of a particle. For instance, a left-handed electron e^-_L is transformed under *CP* to a right-handed positron e^+_R. The *CP* operation was still considered to be a good symmetry in the early stages of the SM. The first evidence of *CP* violation was established in neutral kaon decays from the Cronin-Fitch experiment [47] in 1964.

The origin of *CP* violation in the SM lies in the complex entries Y_{ij} of the Yukawa matrices and consequently the complex entries of the CKM matrix. In fact, the third generation of quarks was predicted in order to explain the observed *CP* violation. The SM with only two generations of quarks implies a 2×2 real mixing matrix which has only one free parameter known as the Cabibbo angle θ_C. In order for *CP* violation to occur in the SM, three generations are needed and thus the 3 × 3 CKM matrix is described by three real parameters and one complex phase, as shown in the previous section. It is this complex phase that allows for *CP* violation.

In order to see how *CP* violation arises, a generic Yukawa term can be written as

$$\mathscr{L}_{Yukawa} = Y_{ij}\overline{\psi_{Li}}\phi\psi_{Rj} + Y^*_{ij}\overline{\psi_{Rj}}\phi^\dagger\psi_{Li}, \tag{2.67}$$

and performing a *CP* transformation of the spinor fields gives

$$CP(\overline{\psi_{Li}}\phi\psi_{Rj}) = \overline{\psi_{Rj}}\phi^\dagger\psi_{Li}, \tag{2.68}$$

so that the Yukawa Lagrangian stays invariant under CP if $Y_{ij} = Y^*_{ij}$. Alternatively, performing a CP operation on the mass basis charged current Lagrangian of Eq. 2.53 gives

$$\begin{aligned} \mathscr{L}_{CC} &= \frac{g_W}{\sqrt{2}}\overline{u_{Li}}(V_{CKM})_{ij}\gamma^\mu W^-_\mu d_{Li} + \frac{g_W}{\sqrt{2}}\overline{d_{Li}}(V^*_{CKM})_{ij}\gamma^\mu W^+_\mu u_{Li}, \\ \mathscr{L}^{CP}_{CC} &= \frac{g_W}{\sqrt{2}}\overline{d_{Li}}(V_{CKM})_{ij}\gamma^\mu W^+_\mu u_{Li} + \frac{g_W}{\sqrt{2}}\overline{u_{Li}}(V^*_{CKM})_{ij}\gamma^\mu W^-_\mu d_{Li}, \end{aligned} \tag{2.69}$$

where again the Lagrangian stays invariant under CP if $V_{CKM} = V^*_{CKM}$. This condition is not satisfied since the CKM matrix is not real but has one complex phase. Therefore the CP symmetry of the Lagrangian is not conserved.

CP violation was first observed in neutral kaon decays and has since been observed and well measured in both neutral B^0 meson decays and charged $B^\pm$ meson decays. More recently, *CP* violation in neutral D^0 charm meson decays has been observed [48]. In the SM, *CP* violation can be classified into the three different categories described below.

2.1.6.1 *CP* violation in decay

This type of *CP* violation is also known as *direct CP* violation. It takes place when the decay rate of a particle P to a final state F is not the same as the decay rate of the antiparticle $\overline{P}$ to the *CP* conjugated final state $\overline{F}$, i.e.

$$\Gamma(P \to F) \neq \Gamma(\overline{P} \to \overline{F}), \tag{2.70}$$

and the associated CP-violating observable is

$$\mathscr{A}_{CP} = \frac{\Gamma(P \to F) - \Gamma(\overline{P} \to \overline{F})}{\Gamma(P \to F) + \Gamma(\overline{P} \to \overline{F})}. \tag{2.71}$$

The total decay amplitudes which describe the $\Gamma(P \to F)$ process and the *CP* conjugated process $\Gamma(\overline{P} \to \overline{F})$ can be denoted as A_f and $\overline{A}_{\overline{f}}$, respectively. From Eq. 2.69 it is seen that under *CP* conjugation the complex coupling of the weak charged current is turned into its complex conjugate. This means that the two amplitudes will have a phase that changes sign under *CP*. Since this phase comes from the complex coupling of the weak interaction, it is referred to as weak phase. The amplitudes can also have a different strong phase coming from gluon exchange in the final state. However, since the strong interaction is *CP*-conserving, the strong phase does not change sign under *CP*. Besides the weak and strong phases, the other key ingredient for direct *CP* violation is the existence of two interfering amplitudes (a_1 and a_2) for the same $P \to F$ process. Thus, the final amplitude for the process will be given by the vector sum of the two amplitudes. Because of the weak phase that changes sign, the amplitudes for the process and antiprocess will differ. This mechanism that generates *CP* violation is illustrated in Fig. 2.6.

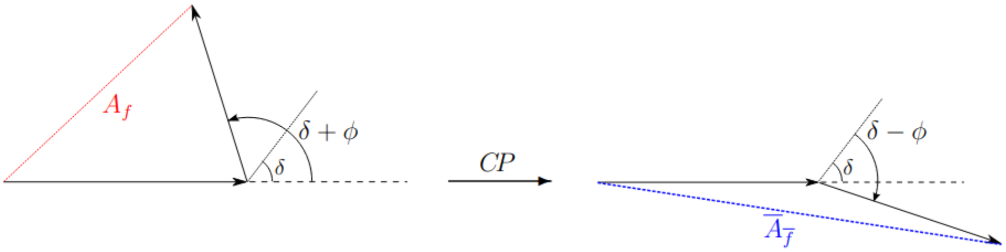

Figure 2.6: Schematic of *CP* violation. The weak phase ϕ changes sign under *CP*, while the strong phase δ stays invariant. The resulting vector sum of the two amplitudes for the process and antiprocess are thus different, i.e. $A_f \neq \overline{A}_{\overline{f}}$.

The total amplitudes A_f and $\overline{A}_{\overline{f}}$ can then be written as

$$\begin{aligned} A_f &= |a_1| e^{i(\delta_1 + \phi_1)} + |a_2| e^{i(\delta_2 + \phi_2)}, \\ \overline{A}_{\overline{f}} &= |a_1| e^{i(\delta_1 - \phi_1)} + |a_2| e^{i(\delta_2 - \phi_2)}, \end{aligned} \tag{2.72}$$

and knowing that $\Gamma(P \to F) \propto |A_f|^2$ the numerator of Eq. 2.71 becomes

$$\mathcal{A}_{CP} \propto -2|a_1||a_2| \sin(\delta_2 - \delta_1) \sin\big(\phi_2 - \phi_1\big). \tag{2.73}$$

From Eq. 2.73 it is evident that for direct *CP* violation there must be two interfering amplitudes with different weak and strong phases. The condition for *CP* violation can also be expressed as a ratio of the magnitudes of the two amplitudes

$$\left| \frac{A_f}{\overline{A}_{\overline{f}}} \right| \neq 1. \tag{2.74}$$

The condition implies that the decay rates for the process and antiprocess are different. The condition would not be satisfied in case of vanishing weak phase, i.e. real weak coupling. Direct *CP* violation can occur for both neutral and charged meson decays and was observed for example in the $B^0 \to K^+\pi^-$ channel [49].

2.1.6.2 *CP* violation in mixing

The phenomenon of neutral meson oscillation gives rise to the second mechanism that generates *CP* violation. A generic neutral meson P^0 can turn into its antiparticle $\overline{P^0}$ while propagating, which can then turn back into the particle P^0 and this process repeats over time. This process is called *mixing*. This is because the particle propagates as a mass eigenstate which is a linear combination of *CP* eigenstates P^0 and $\overline{P^0}$ and can oscillate between the two states as it propagates. In other words, the mass eigenstates are not exact *CP* eigenstates. The heavy and light mass eigenstates as functions of time can be written then as

$$\begin{aligned} |P_H(t)\rangle =& p\left|P^0(t)\right\rangle - q\left|\overline{P^0}(t)\right\rangle, \\ |P_L(t)\rangle =& p\left|P^0(t)\right\rangle + q\left|\overline{P^0}(t)\right\rangle, \end{aligned} \tag{2.75}$$

where the complex coefficients q and p must satisfy $|q|^2 + |p|^2 = 1$. *CP* violation in mixing occurs when the probability of oscillating from particle to antiparticle is different than the probability for the reverse process, i.e.

$$\Gamma(P^0 \to \overline{P^0}) \neq \Gamma(\overline{P^0} \to P^0). \tag{2.76}$$

These probabilities are functions of time and are given by the following expressions of squared amplitudes

$$\begin{aligned} \left|\left\langle\overline{P^0}\middle|P^0(t)\right\rangle\right|^2 =& |g_-(t)|^2\left|\frac{p}{q}\right|^2, \\ \left|\left\langle P^0\middle|\overline{P^0}(t)\right\rangle\right|^2 =& |g_+(t)|^2\left|\frac{q}{p}\right|^2. \end{aligned} \tag{2.77}$$

where the functions $g_\pm(t)$ depend on the masses and decay constants (lifetimes) of the two mass eigenstates of the neutral meson system [15]. The condition for *CP* violation in mixing can then be expressed as

$$\left|\frac{q}{p}\right| \neq \left|\frac{p}{q}\right| \neq 1. \tag{2.78}$$

CP violation in mixing is also known as *indirect CP* violation and it was first observed in $K^0 - \overline{K}^0$ mixing by the Cronin-Fitch experiment via neutral kaon decays to two charged pions.

2.1.6.3 *CP* violation in interference between a decay with and without mixing

The other possibility for indirect *CP* violation to occur is as a consequence of the interference between the amplitude of a decay $P^0 \to F$ and the amplitude of the same decay, but with mixing $P^0 \to \overline{P^0} \to F$. This implies that the final state F has to be a common CP eigenstate for both the particle P^0 and the antiparticle $\overline{P^0}$.

The condition for CP violation in this case is given by

$$\Gamma(P^0 \to \overline{P^0} \to F) \neq \Gamma(\overline{P^0} \to P^0 \to F). \tag{2.79}$$

The two amplitudes that interfere in this case are the ones associated to the $P^0 \to F$ and $P^0 \to \overline{P^0} \to F$ processes. In order for CP violation to happen, there must be a phase between the mixing and decay amplitudes. This phase, denoted by ϕ_I, is given by [15]

$$\phi_I = \arg\left(\frac{q}{p}\frac{\overline{A}_{\overline{f}}}{A_f}\right), \tag{2.80}$$

therefore the condition for CP violation in interference of mixing and decay can be expressed as

$$\phi_I \neq 0. \tag{2.81}$$

A good example of observed CP violation in the interference between mixing and decay is in the so-called 'golden channel' $B^0 \to J/\psi K^0_S$ [50].

2.2 Semileptonic B decays

2.2.1 Lepton flavor universality

In the SM, the gauge bosons of the electroweak interaction have the same coupling to all three lepton generations. In other words, the interactions of the electroweak bosons with the leptons are independent of the lepton flavor. This means that particle decays to any of the three lepton generations do not depend on the lepton flavor and the only difference in branching ratios is due to a phase space factor accounting for the different masses of the charged leptons. This property is known as *lepton flavor universality* (LFU). Since the SM does not allow for LFU violation, any observation of lepton flavor non-universality implies the existence of New Physics (NP).

Several experiments including LHCb, Belle, Belle2 and BaBar have been performing tests of LFU in various b-hadron decays with leptons in the final state. A detailed description of the LHCb experiment and a brief description of the other experiments also known as B Factories is given in Chapter 3. The two main classes of decays where LFU tests are performed are the $b \to s\ell^+\ell^-$ and $b \to c\ell\nu_\ell$ transitions. There are multiple results coming from all these experiments which show tensions of $2-3\sigma$ with respect to the SM predictions of LFU. Collectively, all the recently measured deviations from the SM in $b-$hadron decays are known as the *b-anomalies*.

2.2.1.1 LFU tests in $b \to s\ell^+\ell^-$

Transitions where a B hadron decays into another hadron containing an s quark and a pair of charged leptons, i.e. $B \to X_s\ell^+\ell^-$ or at quark level $b \to s\ell^+\ell^-$, are FCNC processes and are therefore highly suppressed in the SM by the GIM mechanism. These transitions are not allowed to occur at tree level in the SM and thus can only occur via loop diagrams such as the ones shown in Fig. 2.7.

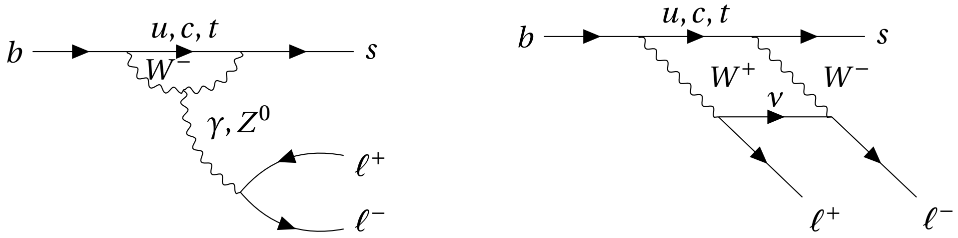

Figure 2.7: SM Feynman diagrams for the $b \to s\ell^+\ell^-$ process showing a penguin loop diagram (left) and a box diagram (right).

Typically, LFU tests are performed by measuring ratios of branching fractions of B hadron decays where only the final state leptons differ. The advantage of defining ratio observables is that most of the theoretical and experimental uncertainties are cancelled out. These ratios are known as $\mathscr{R}_X$ and are generically defined as

$$\mathscr{R}_X = \frac{\mathscr{B}(H_b \to X\ell_1^+\ell_1^-)}{\mathscr{B}(H_b \to X\ell_2^+\ell_2^-)}, \tag{2.82}$$

where H_b is the $b-$hadron, X is a hadron containing a strange quark and ℓ_1, ℓ_2 are leptons from different generations. Two of the most important such ratios are the $\mathscr{R}_{\mathscr{K}^{*\prime}}$ and $\mathscr{R}_K$

$$\begin{aligned} \mathscr{R}_{K^{*0}} &= \frac{\mathscr{B}(B^0 \to K^{*0}\mu^+\mu^-)}{\mathscr{B}(B^0 \to K^{*0}e^+e^-)}, \\ \mathscr{R}_K &= \frac{\mathscr{B}(B^+ \to K^+\mu^+\mu^-)}{\mathscr{B}(B^+ \to K^+e^+e^-)}. \end{aligned} \tag{2.83}$$

The SM prediction for these ratios is equal to one with uncertainties at the percent level [51]. These ratios depend on the q^2 quantity which is the invariant mass squared of the two leptons and typically the measurements are performed in bins of q^2. The measurements of the $\mathscr{R}_K$ and $\mathscr{R}_{K^{*0}}$ ratios from the LHCb, Belle and BaBar experiments are given in Fig. 2.8 in bins of q^2.

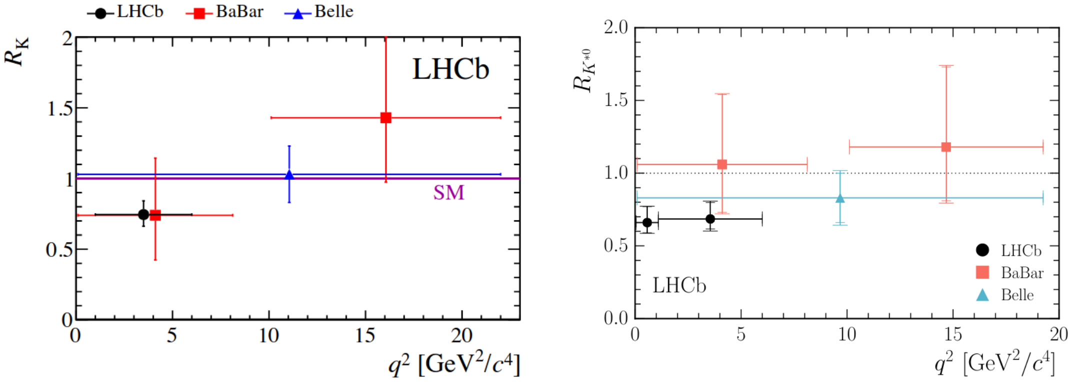

Figure 2.8: Measurements of $\mathscr{R}_K$ [52] (left) and $\mathscr{R}_{K^{*0}}$ [53] (right) in bins of q^2 from the LHCb, Belle and BaBar experiments.

The values measured by the LHCb experiment using Run 1 data collected in 2011 and 2012 for $\mathscr{R}_{K^{*0}}$ are compatible with the SM prediction at the level of ~ 2.1 and ~ 2.4 standard deviations for the two q^2 regions as shown below [53]

$$\begin{aligned} \mathscr{R}_{K^{*0}}(0.045 < q^2 < 1.1\,\text{GeV}^2) =& 0.66^{+0.11}_{-0.07} \pm 0.03, \\ \mathscr{R}_{K^{*0}}(1.1 < q^2 < 6.0\,\text{GeV}^2) =& 0.69^{+0.11}_{-0.07} \pm 0.05. \end{aligned} \tag{2.84}$$

The $\mathscr{R}_K$ ratio was measured by LHCb using Run 1 and first half of Run 2 (2015 and 2016) data and the measurement is 3.1 standard deviations away from the SM prediction. The measured value is given by [54]

$$\mathscr{R}_K(1.1 < q^2 < 6.0\,\text{GeV}^2) = 0.846^{+0.044}_{-0.041}. \tag{2.85}$$

An updated combined measurement of $\mathscr{R}_K$ and $\mathscr{R}_{K^{*0}}$ using the full Run 1 and Run 2 data was performed more recently by LHCb in two q^2 regions. These measurements supersede the previous LHCb measurements and are all in agreement with the SM. The values are given by [55, 56]

$$\begin{aligned} \mathscr{R}_{K^{*0}}(0.1 < q^2 < 1.1\,\text{GeV}^2) =& 0.927^{+0.093}_{-0.087}(\text{stat})^{+0.036}_{-0.035}(\text{syst}), \\ \mathscr{R}_{K^{*0}}(1.1 < q^2 < 6.0\,\text{GeV}^2) =& 1.027^{+0.072}_{-0.068}(\text{stat})^{+0.027}_{-0.026}(\text{syst}), \\ \\ \mathscr{R}_{K}(0.1 < q^2 < 1.1\,\text{GeV}^2) =& 0.994^{+0.090}_{-0.082}(\text{stat})^{+0.029}_{-0.027}(\text{syst}), \\ \mathscr{R}_{K}(1.1 < q^2 < 6.0\,\text{GeV}^2) =& 0.949^{+0.042}_{-0.041}(\text{stat})^{+0.022}_{-0.022}(\text{syst}). \end{aligned} \tag{2.86}$$

Other LFU tests in $b \to s\ell^+\ell^-$ meson decays are performed in the $B^0 \to K^0_{\text{S}}\ell^+\ell^-$ and $B^+ \to K^{*+}\ell^+\ell^-$ channels and the measured ratios $\mathscr{R}_{K^0_{\text{S}}}$ and $\mathscr{R}_{K^{*+}}$ are compatible with the SM at 1.5 and 1.4 standard deviations, respectively [57]. The first LFU test with baryon decays was performed at the LHCb experiment with the $\Lambda^0_b \to pK^-\ell^+\ell^-$

modes [58].

An alternative approach to study the anomalies in $b \to s\ell^+\ell^-$ transitions is given by the angular analyses and certain observables related to the angular distribution of the decay are good probes for NP. In general, the angular distribution depends on q^2 and a set of decay angles. An important set of angular observables are the so-called optimized observables $P_a^{(\prime)}$ whose definition is chosen in order to minimize the hadronic uncertainties. The definitions and descriptions of these angular observables can be found in [59]. A deviation from the SM prediction of almost 3σ in some q^2 bins was observed by the LHCb experiment in the P_5' observable related to the angular distribution of the $B^0 \to K^{*0}\mu^+\mu^-$ decay [60]. Similarly, LHCb has observed a deviation of 3σ with respect to the SM predictions in the same q^2 region for the P_2 angular observable in the $B^+ \to K^*\mu^+\mu^-$ decay [61]. The measurements of the two angular observables P_2 and P_5' are shown in Fig. 2.9.

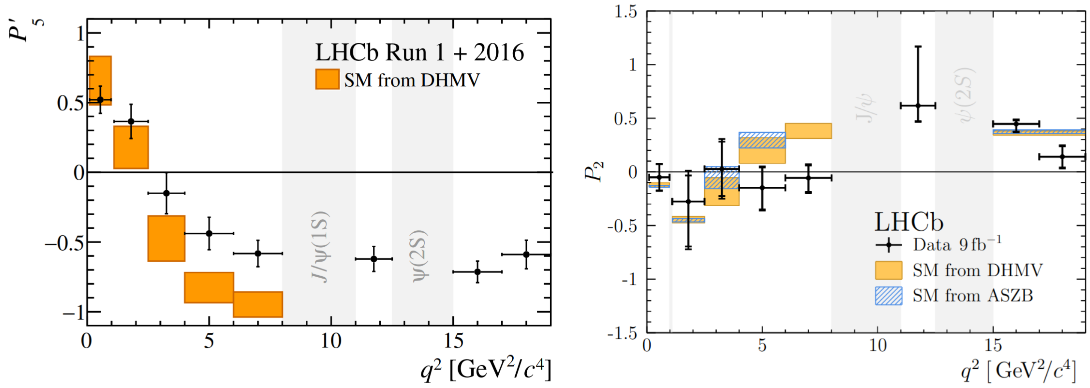

Figure 2.9: Measurements of the P_2 angular observable in $B^+ \to K^{*+}\mu^+\mu^-$ (right) [61] and the P_5' angular observable in $B^0 \to K^{*0}\mu^+\mu^-$ (left) [60]. The 2.9 (3)σ deviations from SM in the $P_5'(P_2)$ observables are found in the same q^2 region of 6.0 – 8.0 GeV^2

2.2.1.2 LFU tests in $b \to c\ell\nu_\ell$

Decays where a b-hadron decays into a c-hadron and a lepton neutrino pair, generically denoted by $H_b \to H_c\ell\nu_\ell$, are commonly referred to as semileptonic decays since only one lepton is visible in the final state. The quark level transition is $b \to c\ell\nu_\ell$ where the lepton can be either an electron (e), a muon (μ) or a tau lepton (τ). In the SM these are tree-level FCCC transitions mediated by the $W^\pm$ bosons. The Feynman diagram of the quark-level SM $b \to c\ell\nu_\ell$ process is given in Fig. 2.10.

Lepton flavor universality tests are performed in these transitions using observables defined as the following ratio

$$\mathscr{R}(H_c) = \frac{\mathscr{B}(H_b \to H_c\ell_1\nu_{\ell_1})}{\mathscr{B}(H_b \to H_c\ell_2\nu_{\ell_2})}, \tag{2.87}$$

where ℓ_1 and ℓ_2 are leptons from different generations. The two main observables

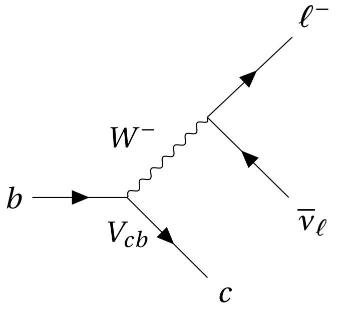

Figure 2.10: Feynman diagram of the $b \to c\ell\nu_\ell$ transition in the SM mediated by a W^- boson. The probability of the transition is given by $|V_{cb}|^2$.

that generated a large amount of interest in the recent years are the so-called $\mathscr{R}(D)$ and $\mathscr{R}(D^*)$ given by

$$\begin{aligned}\mathscr{R}(D) &= \frac{\mathscr{B}(B \to D\tau\nu_\tau)}{\mathscr{B}(B \to D\ell\nu_\ell)},\ \ell = \mu, e,\\ \mathscr{R}(D^*) &= \frac{\mathscr{B}(B \to D^*\tau\nu_\tau)}{\mathscr{B}(B \to D^*\ell\nu_\ell)},\ \ell = \mu, e.\end{aligned} \tag{2.88}$$

By taking the ratio of the two branching fractions the uncertainties related to the hadronic transition as well as the contribution of the CKM matrix element $|V_{cb}|$ cancel out. Therefore, these ratio observables are in principle theoretically clean. The most recent average SM prediction based on several calculations for these ratios is [1]

$$\begin{aligned}\mathscr{R}(D) &= 0.298 \pm 0.004,\\ \mathscr{R}(D^*) &= 0.254 \pm 0.005.\end{aligned} \tag{2.89}$$

On the experimental side so far Belle, BaBar and LHCb have performed combined measurements of $\mathscr{R}(D)$ and $\mathscr{R}(D^*)$. The LHCb experiment has measured $\mathscr{R}(D^*)$ using two of the τ lepton decay modes, the so-called hadronic $\tau \to \pi\pi\pi\nu$ and muonic $\tau \to \mu\nu\overline{\nu}$ channel. The most recent measurements performed by these three experiments so far are listed in Tab. 2.4 [1, 62–67].

Experiment	τ decay mode	Measurement	Value
BaBar	$\tau \to \ell\nu\overline{\nu}$	$\mathscr{R}(D)$	$0.440 \pm 0.058(\text{stat}) \pm 0.042(\text{syst})$
		$\mathscr{R}(D^*)$	$0.332 \pm 0.024(\text{stat}) \pm 0.018(\text{syst})$
Belle	$\tau \to \ell\nu\overline{\nu}$	$\mathscr{R}(D)$	$0.375 \pm 0.064(\text{stat}) \pm 0.026(\text{syst})$
		$\mathscr{R}(D^*)$	$0.293 \pm 0.038(\text{stat}) \pm 0.015(\text{syst})$
Belle	$\tau \to \ell\nu\overline{\nu}$	$\mathscr{R}(D)$	$0.307 \pm 0.037(\text{stat}) \pm 0.016(\text{syst})$
		$\mathscr{R}(D^*)$	$0.283 \pm 0.018(\text{stat}) \pm 0.014(\text{syst})$
Belle	$\tau \to \pi\nu, \tau \to \rho\nu$	$\mathscr{R}(D^*)$	$0.270 \pm 0.035(\text{stat})^{+0.028}_{-0.025}(\text{syst})$
LHCb	$\tau \to \mu\nu\overline{\nu}$	$\mathscr{R}(D)$	$0.441 \pm 0.060(\text{stat}) \pm 0.066(\text{syst})$
		$\mathscr{R}(D^*)$	$0.281 \pm 0.018(\text{stat}) \pm 0.024(\text{syst})$
LHCb	$\tau \to \pi\pi\pi\nu$	$\mathscr{R}(D^*)$	$0.257 \pm 0.012(\text{stat}) \pm 0.014(\text{syst})$ $\pm 0.012(\text{BF})$

Table 2.4: Measured values of $\mathscr{R}(D)$ and $\mathscr{R}(D^*)$. In the measurements performed by BaBar and Belle using the leptonic τ decay mode, the tau is reconstructed in both $\tau^- \to e^-\overline{\nu}_e\nu_\tau$ and $\tau^- \to \mu^-\overline{\nu}_\mu\nu_\tau$ while the LHCb measurement uses only the muonic mode.

All the experimental results along with their averages and correlations as well as the theoretical SM predictions are shown graphically in the plot given in Fig. 2.11. The average experimental result for the combined $\mathscr{R}(D)$ and $\mathscr{R}(D^*)$ measurements is more than 3σ away from the SM prediction. More precise measurements of these ratios are being performed in order to confirm or infirm the presence of NP in these decays.

In addition to $\mathscr{R}(D)$ and $\mathscr{R}(D^*)$, recently the LHCb experiment has performed LFU tests in semileptonic decays of heavier b-hadrons which are not accessible at the other B Factories. More specifically, LHCb measured the ratios $\mathscr{R}(J/\psi)$ and $\mathscr{R}(\Lambda_c^+)$ defined as

$$\begin{aligned} \mathscr{R}(J/\psi) &= \frac{\mathscr{B}(B_c^+ \to J/\psi\tau^+\nu_\tau)}{\mathscr{B}(B_c^+ \to J/\psi\mu^+\nu_\mu)}, \\ \mathscr{R}(\Lambda_c^+) &= \frac{\mathscr{B}(\Lambda_b^0 \to \Lambda_c^+\tau^-\overline{\nu}_\tau)}{\mathscr{B}(\Lambda_b^0 \to \Lambda_c^+\mu^-\overline{\nu}_\mu)}, \end{aligned} \tag{2.90}$$

for which the measured values are [68, 69]:

$$\begin{aligned}\mathscr{R}(J/\psi) =& 0.71 \pm 0.17(\text{stat}) \pm 0.18(\text{syst}),\\ \mathscr{R}(\Lambda_c^+) =& 0.242 \pm 0.026(\text{stat}) \pm 0.040(\text{syst}) \pm 0.059(\text{ext}).\end{aligned} \tag{2.91}$$

The $\mathscr{R}(J/\psi)$ experimental result lies about 2σ away from the SM prediction given by [70], while the $\mathscr{R}(\Lambda_c^+)$ result is in agreement with the SM prediction from [71].

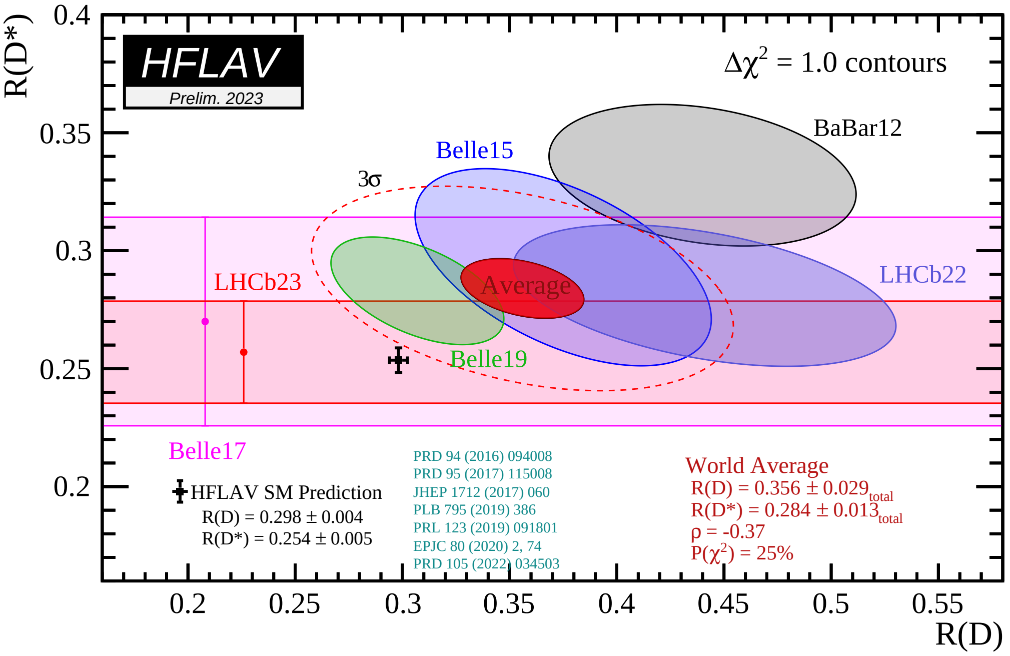

Figure 2.11: Combined measurement of the $\mathscr{R}(D)$ and $\mathscr{R}(D^*)$ ratios. The black point with errors shows the SM prediction. The various measurements of $\mathscr{R}(D^*)$ by LHCb and Belle are shown as points while the combined $\mathscr{R}(D)$-$\mathscr{R}(D^*)$ measurements from LHCb, BaBar and Belle are shown as ellipses. The average combined value over all measurements is given by the red ellipse. The dashed red line indicates the 3σ contour. The average SM prediction lies at about 3.2σ with respect to the experimental average [1]

Collectively, these ratio measurements which serve as direct LFU tests show significant tensions between theory and experiment and thus point to NP in $b \to c\ell\nu_\ell$ charged current transitions. To complement the direct search for lepton flavor non-universality, other observables sensitive to NP effects in $b \to c\ell\nu_\ell$ have been proposed, such as the longitudinal D^* polarisation F_L [72], τ lepton polarisation [65, 73], forward-backward asymmetry [74, 75] and full angular distributions [3, 9, 76, 77].

2.2.2 Effective field theory and New Physics in $b \to c\ell\nu_\ell$

Typically, semileptonic B decays are treated theoretically in terms of an *effective field theory* (EFT). This approach treats the SM as a low-energy (effective) field theory of a more complete NP theory, where NP is heavier than SM. A parallel can be made with respect to the Fermi weak theory of the beta decay, i.e. $n \to pe^-\overline{\nu}_e$, which takes place at an energy scale ~ 1 MeV much lower than the electroweak scale $m_W \sim 100$ GeV. The degrees of freedom of the heavy electroweak W boson are integrated out and encoded into an effective weak coupling constant G_F (the Fermi constant). Thus, the low-energy weak decay is effectively described by a point-like four-fermion interaction which concerns the light particles only. The short distance effects of the heavy electroweak bosons were discovered only when the SPS reached the required energy scale, i.e. the electroweak energy scale.

So far the SM provided an accurate description of the particle interactions probed at the energies up to the electroweak scale. However, various measurements such as the ones described in the previous section indicate that the SM might not be the complete underlying theory. Therefore, the SM can be considered the low-energy (long distance) approximation of a NP theory at a scale Λ larger than the electroweak scale, i.e. $\Lambda \gg m_W$ [8], where the new degrees of freedom appear. The effects of these new (heavy) degrees of freedom can be parametrized at the electroweak scale by adding NP terms to the SM Lagrangian, i.e.

$$\mathscr{L}_{eff} = \mathscr{L}_{SM} + \frac{1}{\Lambda}\mathscr{L}_5 + \frac{1}{\Lambda^2}\mathscr{L}_6 + \frac{1}{\Lambda^3}\mathscr{L}_7 + \ldots, \tag{2.92}$$

where Λ is the characteristic scale of the NP and $\mathscr{L}_n$ represent NP terms in the Lagrangian given by

$$\mathscr{L}_n = \sum_i g_i^{(n)} \mathscr{O}_i^{(n)}. \tag{2.93}$$

In Eq. 2.93, $\mathscr{O}_i^{(n)}$ are gauge invariant operators of mass dimension $n > 4$ constructed from the SM fields only and the $g_i^{(n)}$ are constant dimensionless effective couplings, also known as Wilson coefficients, that incorporate the short distance effects of the heavy NP contributions. Therefore, in general the EFT at low energies ignores the short distance heavy degrees of freedom and keeps only the light degrees of freedom which propagate over long distances. The effects of the heavy degrees of freedom are incorporated in the short distance effective couplings that multiply the operators. This method has the advantage that any NP contributions may be parametrized by just adding new operators (and their coefficients) in the Lagrangian.

The SM Lagrangian $\mathscr{L}_{SM}$ in Eq. 2.92 is of mass dimension four such that the factors $\frac{1}{\Lambda^k}$, where $n - k = 4$, are needed to preserve the correct dimension of the Lagrangian. It can be shown that the dominant corrections to $\mathscr{L}_{SM}$ come from the dimension-six term such that only correction to the SM Lagrangian given by the term $\frac{1}{\Lambda^2}\mathscr{L}_6$ is considered further [78]. A complete set of dimension-six operators is given in [79].

---

[8] Typically the Λ scale of NP of the order of 1 TeV

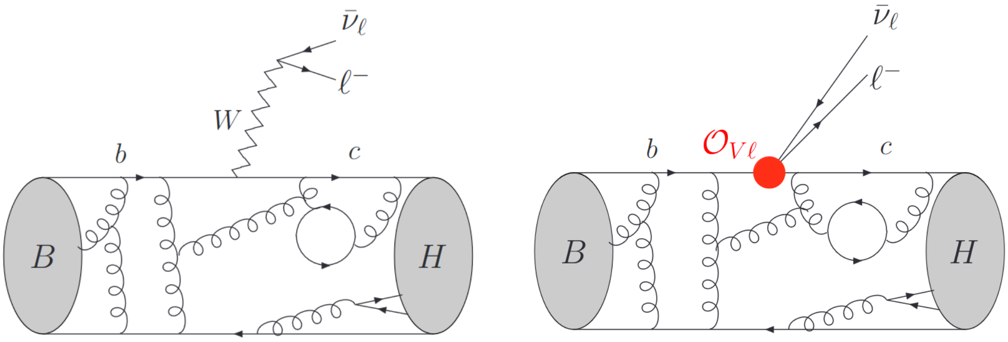

Figure 2.12: Illustration of a $b \to c\ell^-\overline{\nu}_\ell$ transition in the SM (left) and effective field theory approach (right), as seen at the hadronic level, in the case of a B meson decaying into an unspecified H meson [80]. In the effective (low energy) approach, the degrees of freedom associated with the (heavy) W boson are integrated out.

This approach can be employed in the case of $b \to c\ell\overline{\nu}_\ell$ FCCC transitions which can thus be described at low energies in terms of an effective Hamiltonian consisting of a dominant SM contribution and corrections from NP contributions. An illustration of the effective theory approach in the SM is shown in Fig. 2.12. The total effective Hamiltonian reads

$$\mathcal{H}_{eff} = \mathcal{H}_{SM} + \mathcal{H}_{NP} = \frac{4G_F}{\sqrt{2}} V_{cb} \left(\mathcal{O}_{SM} + \sum_i g_i \mathcal{O}_i \right), \tag{2.94}$$

where $G_F = 1.662787 \times 10^{-5}\,\text{GeV}^{-2}$ is the Fermi constant, V_{cb} is the CKM matrix element, g_i are the Wilson coefficients and $\mathcal{O}_i$ their associated four-fermion dimension-six Wilson operators which account for NP corrections. $\mathcal{O}_{SM}$ is the dominant SM Wilson operator defined as the left-handed vector operator:

$$\mathcal{O}_{SM} = (\overline{c}\gamma^\mu P_L b)(\overline{\ell}\gamma_\mu P_L \nu_\ell) = (\overline{c}_L \gamma^\mu b_L)(\overline{\ell}_L \gamma_\mu \nu_{\ell L}), \tag{2.95}$$

where P_L is the left-handed projection operator defined in Eq. 2.23. The normalisation in Eq. 2.94 is chosen such that the Wilson coefficient of the SM operator is 1. The structure of $\mathcal{O}_{SM}$ operator in Eq. 2.95 reflects the $(V-A) \times (V-A)$ nature of the weak interaction in the SM. The complete set of operators that can contribute to $b \to c\ell\nu$ weak decays is restricted by the requirement of Lorentz invariance and is limited to the Lorentz structures given in Table 2.2. The NP effective Hamiltonian that includes these four-fermion operators has the general structure [81]

$$\mathcal{H}_{NP} = \frac{4G_F}{\sqrt{2}} V_{cb} \sum_{\gamma,\mu,\epsilon} g^{\gamma}_{\mu\epsilon} (\overline{c}\Gamma^\gamma b_\mu)(\overline{\ell}_\epsilon \Gamma^\gamma \nu_\ell) + h.c., \tag{2.96}$$

where the index γ represents scalar (S), vector (V) or tensor (T) interactions according to

$$\begin{aligned}\Gamma^S &= 1, \\ \Gamma^V &= \gamma^\mu, \\ \Gamma^T &= \sigma^{\mu\nu} = \frac{i}{2}\left[\gamma^\mu, \gamma^\nu\right],\end{aligned} \tag{2.97}$$

and the indices $\mu, \epsilon \in \{L, R\}$ represent the chirality of the fermion fields. For a given γ, the chirality of $\bar{c}$ is fixed by μ while the chirality of ν_ℓ is fixed by ϵ. Summing over the three indices γ, μ, ϵ gives a total 12 independent dimension six four-fermion Wilson operators. Assuming that there are no right-handed neutrinos, i.e. $g^S_{\mu L} = g^V_{\mu R} = g^T_{\mu L} = 0$, only six possible operators are left. Furthermore, the tensor operator with opposite quark and neutrino set of chiralities vanishes, i.e. $\mathcal{O}^T_{RR} = (\bar{c}_L \sigma^{\mu\nu} b_R)(\bar{\ell}_R \sigma_{\mu\nu} \nu_{\ell L}) = 0$, and thus only one tensor operator contributes [82]. Within these assumptions, there are thus five Wilson operators that contribute to the total effective Hamiltonian for $b \to c\ell\nu_\ell$ weak decays, namely

$$\mathcal{H}_{eff} = \frac{4G_F}{\sqrt{2}} V_{cb}\left[(1+g^V_{LL})\mathcal{O}^V_{LL} + g^V_{RL}\mathcal{O}^V_{RL} + g^S_{LR}\mathcal{O}^S_{LR} + g^S_{RR}\mathcal{O}^S_{RR} + g^T_{LR}\mathcal{O}^T_{LR} + h.c.\right]. \tag{2.98}$$

Explicitly, the five Wilson operators in the equation above are given by

$$\begin{aligned}\mathcal{O}^V_{LL} &= (\bar{c}_L \gamma^\mu b_L)(\bar{\ell}_L \gamma_\mu \nu_{\ell L}) = (\bar{c}\gamma^\mu P_L b)(\bar{\ell}\gamma_\mu P_L \nu_\ell), \\ \mathcal{O}^V_{RL} &= (\bar{c}_R \gamma^\mu b_R)(\bar{\ell}_L \gamma_\mu \nu_{\ell L}) = (\bar{c}\gamma^\mu P_R b)(\bar{\ell}\gamma_\mu P_L \nu_\ell), \\ \mathcal{O}^S_{LR} &= (\bar{c}_R b_L)(\bar{\ell}_R \nu_{\ell L}) = (\bar{c} P_L b)(\bar{\ell} P_L \nu_\ell), \\ \mathcal{O}^S_{RR} &= (\bar{c}_L b_R)(\bar{\ell}_R \nu_{\ell L}) = (\bar{c} P_R b)(\bar{\ell} P_L \nu_\ell), \\ \mathcal{O}^T_{LR} &= (\bar{c}_R \sigma^{\mu\nu} b_L)(\bar{\ell}_R \sigma_{\mu\nu} \nu_{\ell L}) = (\bar{c}\sigma^{\mu\nu} P_L b)(\bar{\ell}\sigma_{\mu\nu} P_L \nu_\ell).\end{aligned} \tag{2.99}$$

Using the following simplified notation: $g_L \equiv g^V_{LL}$, $g_R \equiv g^V_{RL}$, $g_{S_L} \equiv g^S_{LR}$, $g_{S_R} \equiv g^S_{RR}$, $g_T \equiv g^T_{LR}$ and using the relation $g_{S,P} = g_{S_L} \pm g_{S_R}$ it is possible to write Eq. 2.98 as

$$\begin{aligned}\mathcal{H}_{eff} = \frac{4G_F}{\sqrt{2}} V_{cb}\{&\left[(1+g_L)\bar{c}\gamma^\mu P_L b + g_R \bar{c}\gamma^\mu P_R b\right]\bar{\ell}\gamma_\mu P_L \nu_\ell \\ &+ \left[g_S \bar{c} b + g_P \bar{c}\gamma^5 b\right]\bar{\ell} P_L \nu_\ell + g_T \bar{c}\sigma^{\mu\nu} P_L b \bar{\ell}\sigma_{\mu\nu} P_L \nu_\ell + h.c.\},\end{aligned} \tag{2.100}$$

where the contributing operators are the left-handed vector (L), right-handed vector (R), scalar (S), pseudoscalar (P) and tensor (T). The SM corresponds to the case where $g_L = g_R = g_S = g_P = g_T = 0$.

2.2.3 *CP* violation in $b \to c\ell\nu_\ell$

The experimental results discussed in Sec. 2.2.1.2, such as $\mathscr{R}(D^*)$, $\mathscr{R}(D)$ and $\mathscr{R}(J/\psi)$ indicate the possible presence of NP in $b \to c\ell\nu_\ell$ decays. Up to date, there is a wide variety of theory papers and observables proposed to probe the nature of the NP in these decays. In this thesis, we follow the approach given in [2] and focus on the measurement of *CP* violating observables as means to constrain and distinguish different NP scenarios.

As discussed in Sec. 2.1.6, any *CP* violation requires the presence of at least two interfering amplitudes with different weak and strong phases. In the case of $b \to c\ell\nu_\ell$ transitions, there is only one tree level SM amplitude which is shown in Fig. 2.13 for the $B^0 \to D^{*-}\ell^+\nu_\ell$ decay. Since *CP* violation requires at least two amplitudes, measuring nonzero *CP* violation automatically implies the existence of a second NP amplitude. Therefore, *CP* violation in $b \to c\ell\nu_\ell$ is a smoking-gun signal of NP.

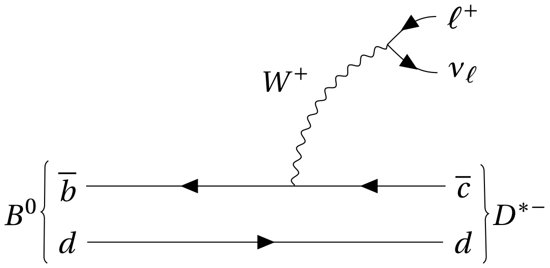

Figure 2.13: The Feynman diagram of the $B^0 \to D^{*-}\ell^+\nu_\ell$ decay in the SM, where $\ell = e, \mu$ or τ. The transition is mediated by a W^+ boson.

There are three classes of NP particles that can couple to both leptons and quarks and thus can mediate $b \to c\ell\nu_\ell$ decays at tree-level. These are charged Higgs $H^\pm$ bosons, $W'^\pm$ bosons and leptoquarks (LQ). Feynman diagrams of $b \to c\ell\nu_\ell$ decays mediated by W'^+ and a leptoquark are shown in Fig. 2.14. A list of references of NP models that can contribute to $b \to c\ell\nu_\ell$ is given in [2].

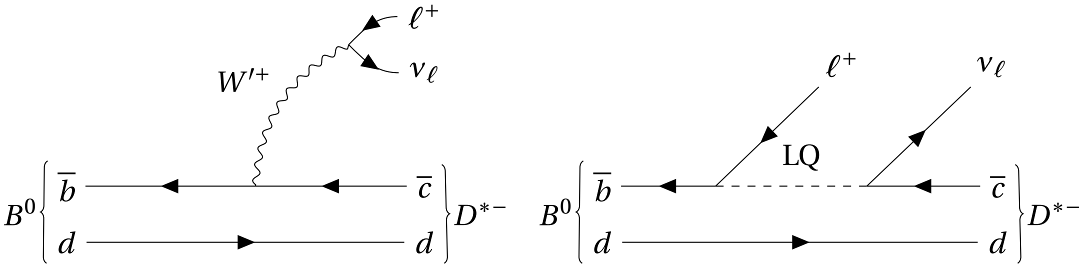

Figure 2.14: Possible NP Feynman diagrams of the $B^0 \to D^{*-}\ell^+\nu_\ell$ decay, where $\ell = e, \mu$ or τ. The $b \to c\ell\nu_\ell$ transition is mediated by a W'^+ (left) and a leptoquark (right).

Regarding the *CP*-violating observables, the most common one is the direct *CP* asymmetry defined in Eq. 2.71. In order for this observable to deviate from zero, there need to be (at least) two amplitudes with different weak and strong phases. However, since strong phases originate from hadronic transitions (as can be seen in Fig. 2.12), in the case of $B^0 \to D^{*-}\ell^+\nu_\ell$ decays the *only* underlying hadronic transition is the $B \to D^*$ (or $b \to c$ at quark level) transition for any amplitude regardless of it being SM or NP. As a consequence, there can be no strong phase difference between any amplitudes in the $b \to c\ell\nu_\ell$ mode [9]. The implication of the vanishing strong phase difference is that the direct CP-violating observable is zero, i.e.

$$\mathscr{A}_{dir}^{CP} = \frac{\Gamma(\overline{B}^0 \to D^{*+}\ell^-\overline{\nu}_\ell) - \Gamma(B^0 \to D^{*-}\ell^+\nu_\ell)}{\Gamma(\overline{B}^0 \to D^{*+}\ell^-\overline{\nu}_\ell) + \Gamma(B^0 \to D^{*-}\ell^+\nu_\ell)} = 0. \tag{2.101}$$

As a consequence, if there are NP amplitudes with different weak phases (but no strong phase difference) than the SM one, the CP violating effects will not appear as a decay rate asymmetry but instead will appear as kinematical effects in the decay angular distribution. These effects are generally known as *triple product asymmetries* [9, 83, 84]. Since these are kinematic observables, in order to produce such effects, the NP amplitude must have a different Lorentz structure than the left-handed vector structure of the SM (Eq. 2.95). In general, the NP models that contribute only to g_L in Eq. 2.100, i.e. same Lorentz structure as the SM, are preferred to explain the b-anomalies [10]. Therefore, the measurement of nonzero CP-violating effects in $b \to c\ell\nu_\ell$ decays would immediately rule out all NP models that contribute only to g_L.

The b-anomalies of $\mathscr{R}(D)$, $\mathscr{R}(D^*)$ and $\mathscr{R}(J/\psi)$ together with the fact that there are no tensions with respect to the SM in the measurement of $\mathscr{R}(D^*)_{\mu/e}$ [85] indicate that the NP may be present in $b \to c\tau\nu_\tau$ decays. The study of CP-violating effects would require the experimental reconstruction of the angular distribution of $B^0 \to D^{*-}\tau^+\nu_\tau$. However, since the τ decays into final states that include one or two neutrinos which are not reconstructable in experiment, these decays are very difficult to deal with and the τ momentum, $\vec{p}_\tau$, cannot be reconstructed with good precision. Therefore, it is logical to start by measuring the CP-violating effects in $B^0 \to D^{*-}\mu^+\nu_\mu$ since its angular distribution is fully reconstructable. Even though the b-anomalies are preferably explained by NP in $b \to c\tau\nu_\tau$, the same NP may affect $b \to c\mu\nu_\mu$ and may lead to measurable deviations from the SM in the angular distribution of $B^0 \to D^{*-}\mu^+\nu_\mu$.

2.2.3.1 Angular distribution

The kinematics of the $B^0 \to D^{*-}\mu^+\nu_\mu$ are described within the formalism of helicity angles. The decay is treated as $B^0 \to D^{*-}W^{*+}$ where the on-shell $D^{*-} \to \overline{D}^0\pi^-$ while the off-shell $W^{*+} \to \mu^+\nu_\mu$. The decay is fully described by four kinematic quantities,

---

[9] Strong phases coming from higher-order amplitudes are considered negligible

[10] In the SM case, the total decay rate is proportional to $|g_{SM}|^2$. In the NP case with same Lorentz structure as SM, the NP coupling simply adds to the SM coupling and the total decay rate is then proportional to $(|g_{SM}|^2 + 2Re(g_{SM}g_{NP}^*) + |g_{NP}|^2)$. In the case where NP has different Lorentz structure than SM, there is no SM-NP interference and the correction to the total decay rate is just $|g_{NP}|^2$. Since NP effects are generally expected to be small, i.e. $|g_{NP}| < |g_{SM}|$, the largest correction to the decay rate comes from the interference term $2Re(g_{SM}g_{NP}^*)$

the invariant mass squared of the lepton system q^2 defined as

$$q^2 = (p_B - p_{D^*})^2, \tag{2.102}$$

and the three helicity angles shown in Fig. 2.15. The angles are defined in the rest frames of their respective intermediate parent particle. The z-axis is chosen such that it is aligned with the direction of the D^{*-} in the rest frame of the B^0. The angles have the following definitions

- $\boldsymbol{\theta_D}$ is the polar angle between the direction of the $\overline{D}^0$ meson and the opposite direction of the B^0 meson in the D^{*-} meson rest frame ($\theta_D \in [0, \pi]$)
- $\boldsymbol{\theta_\ell}$ is the polar angle between the direction of the $\boldsymbol{\mu}^+$ and the opposite direction of the B^0 meson in the W^{*+} rest frame ($\theta_\ell \in [0, \pi]$)
- $\boldsymbol{\chi}$ is the azimuthal angle between the plane containing the μ^+ and ν_μ coming from the W^{*+} and the plane containing the $\overline{D}^0$ and π^- coming from the D^{*-} ($\chi \in [0, 2\pi]$)

Formally, the angles are defined as

$$\cos\theta_D = \left(\hat{p}_{D^0}^{(D^{*-})}\right) \cdot \left(\hat{p}_{D^{*-}}^{(B^0)}\right) = \left(\hat{p}_{D^0}^{(D^{*-})}\right) \cdot \left(-\hat{p}_{B^0}^{(D^{*-})}\right), \tag{2.103}$$

$$\cos\theta_\ell = \left(\hat{p}_{\mu^+}^{(W^{*+})}\right) \cdot \left(\hat{p}_{W^{*+}}^{(B^0)}\right) = \left(\hat{p}_{\mu^+}^{(W^{*+})}\right) \cdot \left(-\hat{p}_{B^0}^{(W^{*+})}\right), \tag{2.104}$$

$$\cos\chi = \left(\hat{p}_{\mu^+}^{(B^0)} \times \hat{p}_{\nu_\mu}^{(B^0)}\right) \cdot \left(\hat{p}_{D^0}^{(B^0)} \times \hat{p}_{\pi^-}^{B^0}\right), \tag{2.105}$$

where $\hat{p}_X^{(Y)}$ are unit vectors of the direction of particle X in the rest frame of Y.

We note that the convention where the angles are defined in the same way for the CP conjugated decay is used, i.e. $\overline{\theta_D} = \theta_D, \overline{\theta_\ell} = \theta_\ell, \overline{\chi} = \chi$.

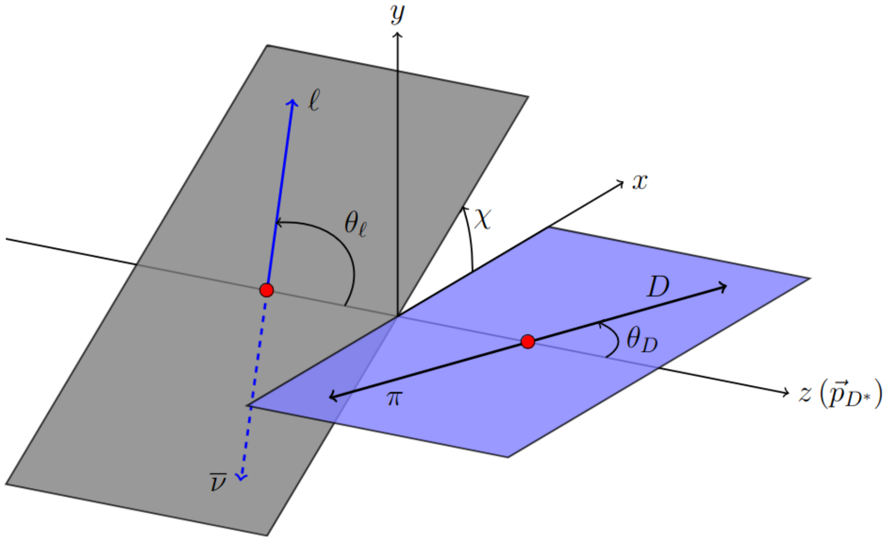

Figure 2.15: Helicity angles of the $\overline{B} \to D^*(\to D\pi)\ell\overline{\nu}_\ell$ decay. Figure taken from [3].

In order to calculate the angular distribution, the total amplitude of the $B^0 \to D^{*-}\mu^+\nu_\mu$ decay is needed. In the SM, this amplitude can be written as

$$\mathcal{M}_{(m;n)} = \epsilon^{\mu}_{D^*}(m) M_{\mu\nu} \epsilon^{\nu}_{W^*}(n), \tag{2.106}$$

where $\epsilon^{\mu}_{D^*}$ and $\epsilon^{\nu}_{W^*}$ are the polarization vectors of the real D^{*-} meson and of the virtual intermediate W^{*+} boson. There are three polarization states for the D^{*-}, namely $m = +,-,0$ and four polarization states for the W^{*+}, $n = +,-,0,t$. Since the B^0 meson is spin-0 particle, out the 12 possible polarization combinations, only four are nonzero due to conservation of angular momentum. These are $++, --, 00, 0t$ and they correspond to four helicity amplitudes $\mathscr{A}_+, \mathscr{A}_-, \mathscr{A}_0, \mathscr{A}_t$. The total amplitude in the SM takes the form

$$\mathcal{M}^{SM} = \sum_{m=\pm,0,t} g_{mm} \mathscr{H}_{D^*}(m) \mathscr{A}_m \mathscr{L}_{W^*}(m), \tag{2.107}$$

where $\mathscr{H}_{D^*}$ and $\mathscr{L}_{W^*}$ are the hadronic and leptonic matrix elements, respectively, and are functions of the kinematics. In the NP case, the decay becomes $B^0 \to D^{*-}(\to \overline{D}^0\pi^-)N^{*+}(\to \mu^+\nu_\mu)$ since the W^{*+} boson mediator is replaced by a new particle N^{*+} with a different interaction and coupling. As no RH neutrinos are assumed, the NP in the leptonic piece can only have three structures as seen in Eq. 2.100, namely $V-A$ (left-handed vector), $S-P$ (left-handed scalar) and T (tensor). This leads to four more helicity amplitudes, one from the $S-P$ interaction, $\mathscr{A}_{SP}$, and three from the T interaction, $\mathscr{A}_{0,T}, \mathscr{A}_{+,T}, \mathscr{A}_{-,T}$. With regards to the hadronic current, there are more NP contributions, as seen from Eq. 2.100. The total amplitude in the NP case is

$$\mathcal{M}^{NP} = \mathcal{M}^{SP} + \mathcal{M}^{VA} + \mathcal{M}^{T}, \tag{2.108}$$

where the SM contribution is included in $\mathscr{M}^{VA}$. Each term in $\mathscr{M}^{NP}$ has a structure similar to the SM one in Eq. 2.107 and can be written as a product of a hadronic piece, a leptonic piece and a helicity amplitude, summed over the possible polarizations of D^{*-} and N^{*+}. The eight helicity amplitudes that govern the decay in the NP case are given by [2]

$$
\begin{aligned}
\mathscr{A}_{SP} &= -g_P \frac{\sqrt{\lambda(m_B^2, m_{D^*}^2, q^2)}}{m_b + m_c} A_0(q^2), \\
\mathscr{A}_0 &= -(1+g_L-g_R)\,\frac{(m_B+m_{D^*})(m_B^2-m_{D^*}^2-q^2)}{2m_{D^*}\sqrt{q^2}} A_1(q^2) \\
&\quad + (1+g_L-g_R)\,\frac{\lambda(m_B^2, m_{D^*}^2, q^2)}{2m_{D^*}(m_B+m_{D^*})\sqrt{q^2}} A_2(q^2), \\
\mathscr{A}_t &= -(1+g_L-g_R)\,\frac{\sqrt{\lambda(m_B^2, m_{D^*}^2, q^2)}}{\sqrt{q^2}} A_0(q^2), \\
\mathscr{A}_+ &= (1+g_L-g_R)\,(m_B+m_{D^*})A_1(q^2) - (1+g_L+g_R)\frac{\sqrt{\lambda(m_B^2, m_{D^*}^2, q^2)}}{m_B+m_{D^*}} V(q^2), \\
\mathscr{A}_- &= (1+g_L-g_R)\,(m_B+m_{D^*})A_1(q^2) + (1+g_L+g_R)\frac{\sqrt{\lambda(m_B^2, m_{D^*}^2, q^2)}}{m_B+m_{D^*}} V(q^2)\,, \\
\mathscr{A}_{0,T} &= g_T\,\frac{1}{2m_{D^*}(m_B^2-m_{D^*}^2)}\Big((m_B^2-m_{D^*}^2)(m_B^2+3m_{D^*}^2-q^2)T_2(q^2) - \lambda(m_B^2, m_{D^*}^2, q^2)T_3(q^2)\Big), \\
\mathscr{A}_{\pm,T} &= g_T\,\frac{\sqrt{\lambda(m_B^2, m_{D^*}^2, q^2)}\,T_1(q^2) \pm (m_B^2-m_{D^*}^2)T_2(q^2)}{\sqrt{q^2}},
\end{aligned}
\tag{2.109}
$$

where $\lambda(a,b,c) = a^2+b^2+c^2-2ab-2ac-2bc$. The helicity amplitudes in Eq. 2.109 are quantities that describe the hadronic interactions and are parametrized in terms of the functions $A_0, A_1, A_2, V, T_1, T_2, T_3$ which are all functions of q^2 and are generally referred to as *Form Factors*. There are several parametrizations widely used in literature to model the form factors. Some of the best known are the ISGW2 parametrization [86], the CLN parametrization [87], the BGL parametrization [88] and the more recent BLPR parametrization [89]. In addition, it can be seen that various NP couplings contribute to various helicity amplitudes and if all NP couplings are set to zero, the eight amplitudes are reduced to the four ones present in the SM.

The angular distribution is proportional to the square of the total amplitude $|\mathscr{M}^{NP}|^2$. The full derivation of the angular distribution is given in [2] and the result is

$$\begin{aligned}\frac{d\Gamma}{dq^2 d\cos\theta_D d\cos\theta_\ell d\chi} = \frac{3}{8\pi}\frac{G_F^2|V_{cb}|^2(q^2-m_\ell^2)^2|p_{D^*}|}{2^8\pi^3 m_{B^0}^2 q^2} \\ \times \mathscr{B}(D^{*-}\to D^0\pi^-)\left(N_1+\frac{m_\ell}{\sqrt{q^2}}N_2+\frac{m_\ell^2}{q^2}N_3\right),\end{aligned} \tag{2.110}$$

where $|p_{D^*}| = \sqrt{\lambda(m_{B^0}^2, m_{D^*}^2, q^2)}/(2m_{B^0})$ is the D^* 3-momentum in the B^0 rest frame. The angular functions N_1, N_2 and N_3 are given in [2] and include both CP-conserving and CP-violating terms. It can be seen that N_2 and N_3 terms have significant suppression factors since $m_\ell << q$. In Tab. 2.5 only the unsuppressed (corresponding to N_1) CP-violating terms are reported.

Coefficient	Coupling	Angular function
$\mathrm{Im}(\mathscr{A}_\perp\mathscr{A}_0^*)$	$\mathrm{Im}[(1+g_L+g_R)(1+g_L-g_R)^*]$	$-\sqrt{2}\sin 2\theta_\ell \sin 2\theta_D \sin\chi$
$\mathrm{Im}(\mathscr{A}_\parallel\mathscr{A}_\perp^*)$	$\mathrm{Im}[(1+g_L-g_R)(1+g_L+g_R)^*]$	$2\sin^2\theta_\ell \sin^2\theta_D \sin 2\chi$
$\mathrm{Im}(\mathscr{A}_{SP}\mathscr{A}_{\perp,T}^*)$	$\mathrm{Im}(g_P g_T^*)$	$-8\sqrt{2}\sin\theta_\ell \sin 2\theta_D \sin\chi$
$\mathrm{Im}(\mathscr{A}_0\mathscr{A}_\parallel^*)$	$\mathrm{Im}[(1+g_L-g_R)(1+g_L+g_R)^*]$	$-2\sqrt{2}\sin\theta_\ell \sin 2\theta_D \sin\chi$

Table 2.5: Unsuppressed CP-violating terms in the angular distribution, their couplings and the angular functions they contribute to [2]

The three distinct angular terms given in Tab. 2.5 correspond to the terms usually denoted by I_7, I_8, I_9 in other derivations of the full angular distribution, e.g. in [3]. We note that all CP-violating terms are proportional to $\sin\chi$ or $\sin 2\chi$ and that their coefficients are all given by $\mathrm{Im}(\mathscr{A}_i\mathscr{A}_j^*)$ [11]. Here $\mathrm{Im}(\mathscr{A}_i\mathscr{A}_j^*)$ can only be nonzero if the two helicity amplitudes $\mathscr{A}_i$ and $\mathscr{A}_j$ have different phases. If there is a different strong phase but no weak phase between the pairs of amplitudes this would mean only parity violation and not CP violation [12]. Alternatively, if there is a different weak phase but no strong phase between the pairs of amplitudes, this truly means CP violation.

This idea is illustrated in Eq. 2.111 where $\phi_{i,j}$ and $\delta_{i,j}$ are weak and strong phases of the helicity amplitudes $\mathscr{A}_i, \mathscr{A}_j$, respectively, i.e. $\mathscr{A}_{i,j} = |\mathscr{A}|e^{i\phi_{i,j}}e^{i\delta_{i,j}}$

$$\mathrm{Im}(\mathscr{A}_i\mathscr{A}_j^*) = |\mathscr{A}_i||\mathscr{A}_j|\left(\underbrace{\sin\big(\phi_i-\phi_j\big)\cos\big(\delta_i-\delta_j\big)}_{CP\text{ violation}}+\underbrace{\cos\big(\phi_i-\phi_j\big)\sin\big(\delta_i-\delta_j\big)}_{\text{parity violation}}\right). \tag{2.111}$$

Since $\delta_i = \delta_j$ is true for any i, j, any terms in the angular distribution proportional to $\mathrm{Im}(\mathscr{A}_i\mathscr{A}_j^*)$ are therefore truly CP-violating.

---

[11] In Tab. 2.5, the transversity basis is used for the amplitudes, i.e. $\mathscr{A}_{\|,\perp(,T)} = (\mathscr{A}_{+(,T)} \pm \mathscr{A}_{-(,T)})/\sqrt{2}$

[12] Alternatively, this scenario can be referred to as *fake* CP-violation

In order to distinguish between parity- and *CP* violation, the same angular term must be compared in the decay and the *CP*-conjugated decay, i.e. in $B^0 \to D^{*-}\mu^+\nu_\mu$ and $\overline{B}^0 \to D^{*+}\mu^-\overline{\nu}_\mu$ decays. When going from decay to *CP* conjugated decay, the charge conjugation flips the sign of the weak phase and the parity conjugation flips the sign of the azimuthal angle χ. Therefore, for *CP*-odd processes the sign of the angular term stays the same while for parity odd processes, the sign of the angular term changes.

As discussed previously, in $B^0 \to D^{*-}\ell^+\nu_\ell$ decays there is only one $B^0 \to D^{*-}$ hadronic transition and all amplitudes must have the same strong phase. Therefore, the parity violation must be zero in these decays. In practice, this can serve as a good consistency check that is independent of NP.

In Tab. 2.5 it is seen that the *CP*-violating terms are sensitive to different NP couplings. In particular, two of the angular functions are sensitive to the imaginary part of the right-handed vector coupling $\text{Im}(g_R)$ while only one term is sensitive to the imaginary part of the product of the pseudoscalar and tensor couplings $\text{Im}(g_P g_T^*)$. Therefore, a measurement of these angular terms will give information on these specific NP couplings. A discussion on which NP models are excluded and which are favored if either of g_R or $g_P g_T^*$ is measured to be nonzero is given in [2].

3 The LHCb detector at the LHC

The work presented in this thesis is based on data from proton-proton collisions collected by the LHCb experiment at the LHC in Run 2, specifically during the 2016-2018 period.

The LHC accelerator complex at CERN and an overview of the four main experiments that collect the proton-proton colission data is given in Sec. 3.1. The main objective of the LHCb detector is to study the decays of hadrons containing b and c quarks. In order to address the challenges of these decays, the LHCb detector makes use of multiple detection systems. The vertexing and tracking system has the role to reconstruct the trajectories of charged particles and to reconstruct their momentum using the curvature of the trajectory. The tracking system and its performance are discussed in Sec. 3.2.1. A particle identification (PID) system is used at LHCb to efficiently distinguish between the different final state particles such as kaons, pions and muons. The PID system and its performance are discussed in Sec. 3.2.2. Finally, a trigger system is needed in order to reduce the collision rate to a lower rate that can be saved on disk while rejecting background events and saving only interesting events. The trigger system is discussed in Sec. 3.2.3.

3.1 The Large Hadron Collider

The Large Hadron Collider (LHC) [90] is the largest particle accelerator and collider ever built, installed in a tunnel with a circumference of approximately 27 km. It is located about 100m underground near Geneva, Switzerland and it is operated by the European Organization for Nuclear Research (CERN). The tunnel was previously built to host the Large Electron-Positron (LEP) collider which ran from 1989 to 2000 and which is, to date, the most powerful lepton accelerator ever built. In the early 2000's, the LEP was dismantled such that the construction of the LHC could begin.

The CERN accelerators complex is shown in Fig. 3.1, where the LHC is the last acceleration step. Protons are extracted from hydrogen gas in which the electrons are removed from the hydrogen atoms by means of an electric field. The protons are first sent to the LINAC2 linear accelerator and accelerated to 50 MeV. They are then sent to a series of three circular accelerators of increasing size. Firstly, the protons are injected in the Proton Synchrotron Booster (PSB), which consists of four superimposed rings of radius 25 m, where the they are accelerated to 1.4 GeV. They then enter the Proton Synchrotron (PS) with a circumference of 628 m, where the protons are accelerated to 25 GeV and finally the Super Proton Synchrotron (SPS) with a circumference of 7 km, where the protons reach 450 GeV. Only at this point the protons are injected into the LHC, where they are further accelerated in two beampipes that circulate in opposite directions. The heavy ions take a slightly different route. They are produced by electron cyclotron resonance, they are sent first to the LINAC3 linear accelerator, then to the Low Energy Ion Ring (LEIR). From there, they are injected in the PS along with the protons, following the same chain to the LHC.

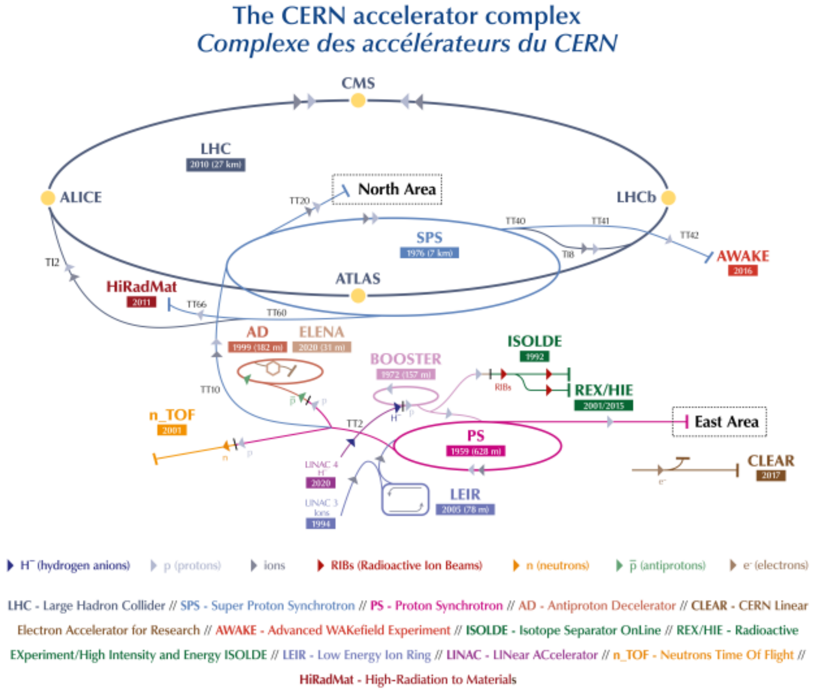

Figure 3.1: Schematic view of the CERN accelerator complex as of 2019 [91]

The LHC is a two-ring hadron accelerator where the proton (or heavy ion) beams are accelerated in opposite directions in the two rings. It consists of 8 arcs of about 2.8 km and 8 straight segments of 500 m. The beams are accelerated by means of radio-frequency cavities and are curved at the 8 arcs by 1232 superconducting dipole magnets, each providing a strong magnetic field of up to 8.3 T. A very high intensity current is needed to reach this magnetic field, therefore the magnets are made out of superconducting material (NbTi) that needs to be cooled at 1.9 K. This is achieved via a liquid helium cryogenic system. In order to have the protons focused in a beam and reduce the transverse beam size, 392 quadrupole magnets are used.

The LHC beams are composed of up to 2808 bunches per ring with $\sim 10^{11}$ protons per bunch. The period of time of about 20h between the beam injection and beam dump is called *fill*. The proton bunches cross at 40 MHz, corresponding to a collision each 25 ns. When the two beams cross, the protons in bunches collide and convert their kinetic energy into massive particles. The beams are collided at four different points along the LHC ring and where experiments are installed to study the results of the collisions. The four main experiments at the LHC have different physics programmes:

- **ATLAS**: A Toroidal LHC Apparatus [92] is one of the two general purpose detectors and the largest at the LHC. It has a cylindrical shape, covering the full 4π solid angle around the beampipe. The detector measures the momentum of particles via a strong magnetic field produced by a toroidal magnet configuration, hence its name. Its physics programme includes SM studies such as Higgs boson, $W^{\pm}$ and Z bosons, top and bottom quarks as well as Beyond the Standard Model (BSM) physics such as suppersymmetry, dark matter candidates and long-lived particles. One of the most important goals of ATLAS was to study the Higgs boson, leading to its famous discovery in 2012 [18].

- **CMS**: Compact Muon Solenoid [93] is the second general purpose detector at the LHC with a physics programme similar to ATLAS. Its geometry is the same as ATLAS, while the main difference is that the magnetic field at CMS is produced by a superconducting solenoidal magnet. The magnetic field is stronger than the one at ATLAS, allowing for better momentum resolution. Together with ATLAS, CMS shared the discovery of the Higgs boson in 2012 [19].

- **ALICE**: A Large Ion Collider Experiment [94] is the LHC experiment dedicated to the study of ultrarelativistc heavy ion collisions. The aim of this experiment is to study the strong interaction by studying Quark-Gluon Plasma (QGP), a special state of matter that can offer information about the early Universe.

- **LHCb**: Large Hadron Collider beauty [4] is the experiment dedicated to flavor physics. It is designed to study b-hadron and c-hadron decays. It will be described in detail in the following section.

The performance of the LHC is expressed in terms of luminosity. Luminosity links the number (N) of events of a certain process with the cross-section of the process (σ) as shown in Eq. 3.1, where $\mathscr{L}(t)$ is the instantaneous luminosity.

$$\frac{dN}{dt} = \mathscr{L}(t)\sigma. \tag{3.1}$$

The instantaneous luminosity describes the number of collisions per unit time that the LHC can achieve and is given as

$$\mathscr{L} = \frac{n^2 N_b f \gamma}{4\pi\sigma_{xy}} F, \tag{3.2}$$

where n is the number of protons in a bunch, N_b is the number of bunches, f is the revolution frequency of the proton bunches, γ is the relativistic factor, F is a geometrical factor that accounts for the beam crossing angle, σ_{xy} is the size of a bunch in the transverse XY plane, which can be written as $\sigma_{xy} = \varepsilon\beta$, where ε is the normalized transverse beam emittance and β is the beta function. From Eq. 3.2 we see that luminosity is inversely proportional with the transverse beam size σ_{xy}, such that the highest luminosity occurs for the minimum value of β which is denoted by β^*. Minimization of the β function is achieved by a special magnet at the interaction point, called low-β triplet. The nominal instantaneous luminosity of the LHC at the beggining of each fill is $\mathscr{L} = 10^{34}$ cm^{-2}s^{-1}. The number of collisions recorded at each experiment at the LHC is given by the integrated luminosity $\mathscr{L}_{int} = \int \mathscr{L}(t)dt$.

The instantaneous luminosity at ATLAS and CMS compared with the one at LHCb is shown in Fig. 3.2. ATLAS and CMS operate at the maximum luminosity of 10^{34} cm^{-2}s^{-1} delivered by the LHC, i.e. the beams are squeezed as much as possible are collided head-on. As a consequence, the number of proton interactions (PVs) per bunch crossing is around 10-100. That is because ATLAS and CMS study heavier particles with large transverse momentum decay products and lower production cross-sections, and in order to deal with the very busy particle environment, very tight trigger selections are employed. Instead, at LHCb, the luminosity is artificially limited to 4×10^{32} cm^{-2}s^{-1} in order to have only 1-2 proton interactions (PVs) per bunch crossing. This is because a larger number of PVs would be difficult to reconstruct and the performance of the detector would be degraded by the large particle rates. Therefore, at LHCb the beams are less focused and are spatially separated at the beggining of the fill, such that they do not collide head-on. Over the fill duration, as the number of protons in the beams decreases, the spatial separation of the two beams is constantly adjusted such that the instantaneous luminosity is kept constant within 5% [4]. This procedure, illustrated in Fig. 3.2, is called *luminosity leveling*.

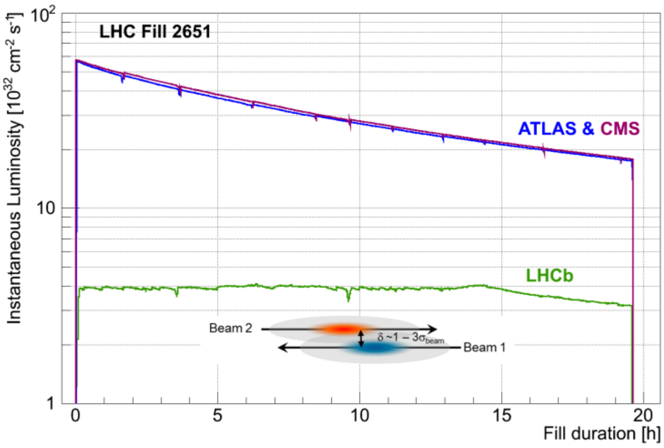

Figure 3.2: Instantaneous luminosity compared for ATLAS, CMS and LHCb during one fill. The luminosity at LHCb is kept approximately constant for the duration of the fill. [4]

The LHC ran during several periods of time with long shutdowns between the data-taking periods. The first data-taking period is called *Run 1*, which took place between 2010-2012. The center-of-mass energy ($\sqrt{s}$) during Run 1 was 7 TeV for 2010 and 2011, and 8 TeV for 2012. After Run 1, a shutdown called *Long Shutdown 1*(LS1) between 2013-2015 took place in order to upgrade the detectors and the accelerator. The second period of data-taking is called *Run 2* and it lasted between 2015-2018 with the center-of-mass energy increased to 13 TeV. After 2018, another shutdown called *Long Shutdown 2* (LS2) took place until 2022 in order to further upgrade the LHC experiments and increase the centre-of-mass energy to 14 TeV. The integrated luminosities recorded at ATLAS, CMS and LHCb experiments during Run 1 and Run 2, by year, are given in Tab. 3.1. The integrated luminosities recorded at LHCb are significantly lower than ATLAS and CMS.

		Integrated luminosity (fb^{-1})		
Year	$\sqrt(s)$ (TeV)	ATLAS	CMS	LHCb
2010	7	0.0450	0.0415	0.0377
2011	7	5.08	5.55	1.11
2012	8	21.3	21.8	2.08
2015	13	3.9	3.87	0.328
2016	13	35.6	38.3	1.67
2017	13	46.9	45.0	1.71
2018	13	60.6	63.7	2.19

Table 3.1: Center-of-mass energy $\sqrt{s}$ and integrated luminosity recorded during the several years of data-taking in Run 1 and Run 2 at ATLAS, CMS and LHCb. [95–97]

3.2 The LHCb experiment

The LHCb detector was designed to study primarily decays of particles containing b-quarks. Before discussing the LHCb detector and its features, it is useful to understand how b-quarks are produced in particle colliders. There are two types of accelerators that can produce large numbers of b-quarks: electron-positron (e^-e^+) colliders, also called B Factories, and proton-proton (pp) colliders.

In the B Factories, electrons are collided with positrons at a centre-of-mass energy of 10.58 GeV, the mass of the $\Upsilon(4S)$ resonance. This resonance decays exclusively to $b\overline{b}$ ($B^0\overline{B}^0$ or B^+B^-) pairs, making it very suitable to study decays of B mesons. The big advantages of the B Factories are a high luminosity and a very low amount of physics backgrounds due to the nature of the collided particles, i.e. e^- and e^+ are elementary particles. The drawback is the low $b\overline{b}$ production cross-section of $\sigma(e^+e^- \to \Upsilon(4S)) \approx$ 1.1 nb [98]. Another limitation is the centre-of-mass energy that can be achieved with a e^-e^+ collider, due to photon radiation by the light charged particle beams. In this type of colliders, the b-quarks are produced isotropically such that the detectors have a full solid angle geometry. The B Factories were the Belle experiment [99] at the KEKB accelerator located in Japan which took collision data between 1999-2010 and the BaBar [98]experiment at the PEP-II accelerator at SLAC in the United States. The Belle II experiment [100], the succesor of Belle, installed at the SuperKEKB upgraded accelerator, has been running and collecting collision data since 2019.

In pp colliders, such as the LHC, the cross section for $b\bar{b}$ production is about 10^5 larger than at B Factories. That is because the cross section increases linearly with $\sqrt{s}$. The $\sigma(pp \to H_b X)$ cross section, where H_b is a hadron containing a b-quark, as measured by the LHCb experiment is $(72 \pm 0.3 \pm 6.8)$ μb for $\sqrt{s} = 7$ TeV and $(144 \pm 1 \pm 21)$ for $\sqrt{s} = 13$ TeV [101]. Due to the larger cross-section, despite the larger luminosity at the B Factories, more $b\bar{b}$ pairs are produced at LHCb, about 10^{12} pairs in one year of data taking. The main production mechanisms of $b\bar{b}$ pairs in pp collisions are called gluon-gluon fusion ($gg \to b\bar{b}$) and quark-quark fusion ($qq \to b\bar{b}$). The Feynman diagrams of these processes are shown in Fig. 3.3.

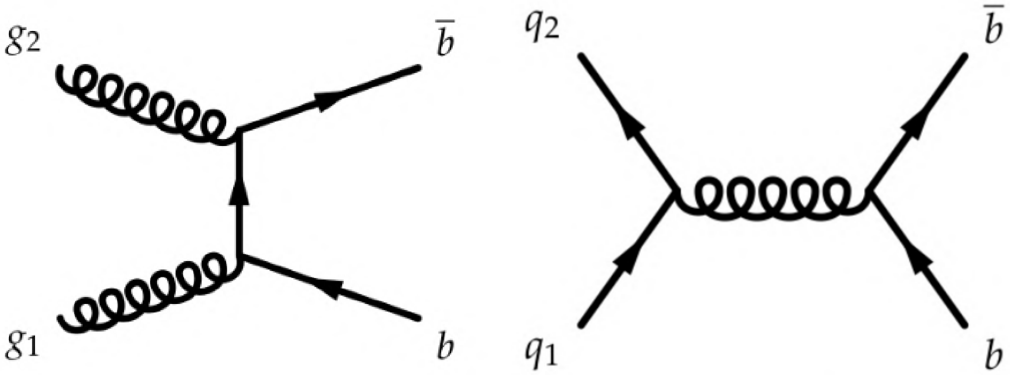

Figure 3.3: Feynman diagrams for the gluon-gluon (left) and quark-quark (right) fusion processes

After they are produced, the b-quarks undergo a process called *hadronization*, i.e. the formation of hadrons out of quarks and gluons. In comparison with the B Factories, due to the larger energy of the $b\bar{b}$ pairs at the LHC, b-hadrons with larger masses than the B mesons (B^0, $B^{\pm}$) can be produced, such as B_c^+ mesons or Λ_b^0 baryons. However, due to the composite nature of the protons, many particles are produced in the collisions, giving rise to much higher amounts of backgrounds at LHCb than at the B Factories.

The dominant $b\bar{b}$ production mechanisms in pp collisions give rise to $b\bar{b}$ quark pairs that are heavily boosted along the LHC beamline in the same forward or backward cone, i.e. the two b quarks are produced at small angles with respect to the beam axis. The cross-section of $b\bar{b}$ production is shown in Fig. 3.4 as a function of the beam axis angles and, equivalently, as a function of the pseudorapidities. Pseudorapidity is a quantity commonly used in particle physics to describe the angle of a particle with respect to the beam axis and is defined as:

$$\eta = \text{-}\ln(\tan\frac{\theta}{2}). \tag{3.3}$$

As seen from Eq. 3.3, at large η, particles are very close to the beam axis, i.e. $\theta = 0^o$, while for small η particles are produced almost perpendicular to the beam axis, i.e. $\theta = 90°$.

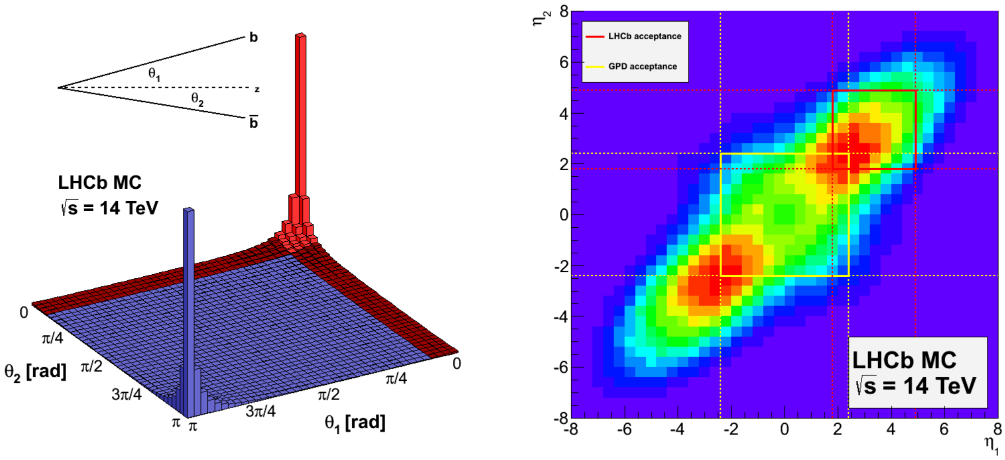

Figure 3.4: Left: simulated $b\bar{b}$ production cross-section as a function of beam direction for $\sqrt{s} = 14$ TeV. Most of the $b\bar{b}$ pairs are produced at $\theta_1 = \theta_2 = 0$ and $\theta_1 = \theta_2 = \pi$, where θ_1 and θ_2 are the angles with respect to the beam axis. The acceptance of the LHCb detector is shown in red. Right: simulated $b\bar{b}$ production cross-section as a function of the pseudorapidity η for $\sqrt{s} =$ 14 TeV. The region indicated by the yellow square is the CMS and ATLAS acceptance while the region indicated by the red square is the LHCb acceptance [102].

It is for this reason that LHCb detector was designed to have a forward geometry, namely it has a forward conical shape with the apex at the interaction point. A transverse view of the LHCb detector is shown in Fig. 3.5, where the coordinate system is defined such that the origin is the interaction point, the z-axis is along the beam direction and the y-axis is the vertical axis. LHCb is a *single-arm forward spectrometer* that covers the angular acceptance of 10-250 mrad in the $x-z$ plane and 10-300 mrad in the $y-z$ plane. This is equivalent to a pseudorapidity coverage of f $2 < \eta < 5$. While LHCb only has about 4% angular acceptace, and does not have full angular coverage like ATLAS, CMS or the B Factories, about 25 % of the $b\bar{b}$ pairs fall into the acceptance of the detector [102].

The main purpose of the LHCb detector is to study b- and c-hadron decays. During the pp collisions, $b\bar{b}$ and $c\bar{c}$ quark pairs are produced and they immediately hadronize, forming bound states such as b- and c- mesons and baryons. The point in space where the proton beams interacted and produced the b-hadron is called primary vertex (PV). The b-hadrons typically have a lifetime of the order of $\sim$ 1 ps so they travel a few mm before decaying into other particles. The point where the b-hadron decays is called secondary vertex (SV). The b-hadron is then reconstructed by its charged or neutral decay products which can be either stable or unstable. In LHCb jargon, stable particles are the ones that can travel through most or all of the detector, while the unstable particles are the ones that decay before crossing the detector and need to be reconstructed too from their decay products. Some examples of stable particles at

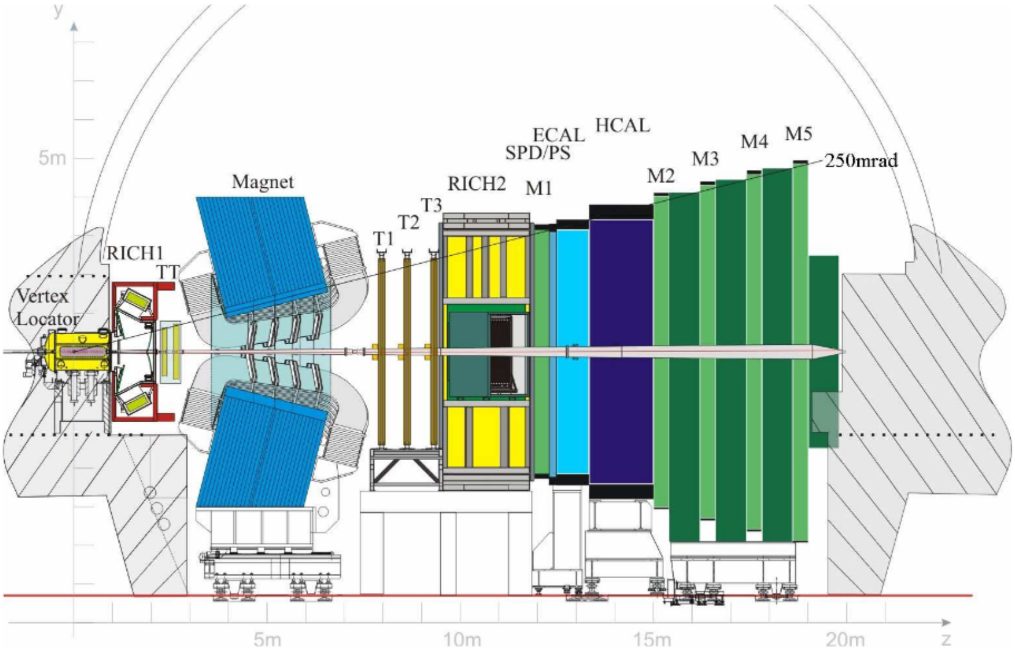

Figure 3.5: Layout of the LHCb detector in the $y-z$ plane [4]

LHCb are muons ($\mu^{\pm}$), charged kaons ($K^{\pm}$) and charged pions ($\pi^{\pm}$). Neutrinos (ν) are not directly detectable at LHCb.

In order to address the challenges of b-hadron decays, the LHCb detector must meet certain requirements:

- Since b-hadrons have decay vertices displaced by a few mm from the PV, LHCb must be able to detect these vertices and distinguish between PVs and SVs. As such, a very precise vertexing system is needed.
- The momentum of charged particles must be measured very precisely in order to obtain an accurate invariant mass of the b-hadron. This allows to distinguish between b-hadron decays and other decays and thus reduce the combinatorics. It also helps to distinguish between decays of b-hadrons with similar masses. A precise tracking system with good momentum resolution is needed.
- In order to study the wide range of b-hadron decays and to distinguish between different decays with the same topology, LHCb must be able to identify very well different particles such as muons, kaons and pions and distinguish between. An excellent particle identification system is needed.
- A good trigger system is needed to cope with the large instantaneous luminosity in order to select the signal events in an efficient manner while rejecting the background and keeping the data within a reasonable size.

The LHCb detector is composed of many individual subdetectors and components, as seen in Fig. 3.5. A brief summary of the subdetectors roughly following the z-axis is as follows. At the origin ($z = 0$), the VErtex LOcator (VELO) is installed around the interaction point. Its job is to measure very precisely and to distinguish between the 3D positions of primary vertices and displaced (secondary) vertices. A magnet is used to curve the trajectories of charged particles in order to determine their momentum. The other tracking stations are the Tracker Turicensis (TT) and the T1-T3 trackers, placed before and after the magnet, respectively. There are two detectors used for charged hadron identification, namely the RICH1 and RICH2, placed before and after the magnet. Next, there is the Electromagnetic CALorimeter (ECAL) and Hadronic CALorimeter (HCAL) which help identify and measure the energy of both charged and neutral particles. Finally, there are 5 muon stations (M1-M5) used to measure the muons, where the M1 station is placed before the calorimeters.

All LHCb components can be organized into three main systems: a tracking and vertexing system, a particle identification system and a trigger system. Each component and its features, as in Run 2, will be presented individually in detail in the following sections.

3.2.1 The vertexing and tracking system

Many of the b-hadrons of interest at LHCb decay to final states with multiple charged particles. The purpose of the tracking system is to reconstruct the trajectories of charged particles by using the information that the particles leave in the tracking detectors, called *hits*. It consists of the VELO, the TT and the T1-T3 tracking stations. A dipole magnet is also placed in the detector in addition to the tracking stations. The magnet has the role to deflect the charged particles and curve their trajectories. The trajectory is reconstructed by connecting particle hits in the different tracking stations. The curvature of the trajectory is then used to infer the momentum of the charged particle.

Vertex Locator

Displaced vertices are a distinctive feature of b- and c-hadron decays. The purpose of the VELO subdetector [103, 104] is to measure track coordinates close to the interaction point. These tracks are then used to locate and distinguish between primary vertices and displaced vertices, i.e. production and decay vertices of b- and c-hadrons and to provide a measurement of their lifetimes. An accurate knowledge of the 3D coordinates of the primary and secondary vertices is important to LHCb analyses and is essential in the analysis presented in this thesis. The separation between PVs and SVs is done based on tracks *Impact Parameter* (IP), which is the minimum distance between the track and a vertex, here the PV.

The VELO consists of a series of parallel silicon modules situated along and perpendicular to the beam axis and surrounding the interaction region, as shown in the top part of Fig. 3.6. The silicon modules are placed only 7 mm away from the beams. Since this distance is smaller than the beam injection requirements, the VELO modules are designed in two retractable halves which can be opened during each beam injection and can be closed when the beams are stable, as shown in the bottom part of Fig. 3.6. In this way, radiation damage that would be caused by the unfocused beam is avoided. There is a small overlap between the two halves when VELO is closed. The two halves of the VELO are called A and C side. Because of this movable system, the VELO halves are subject to alignment imprecisions of up to 10 μm [104]. The VELO alignment precision is very important for the measurement performed in this analysis.

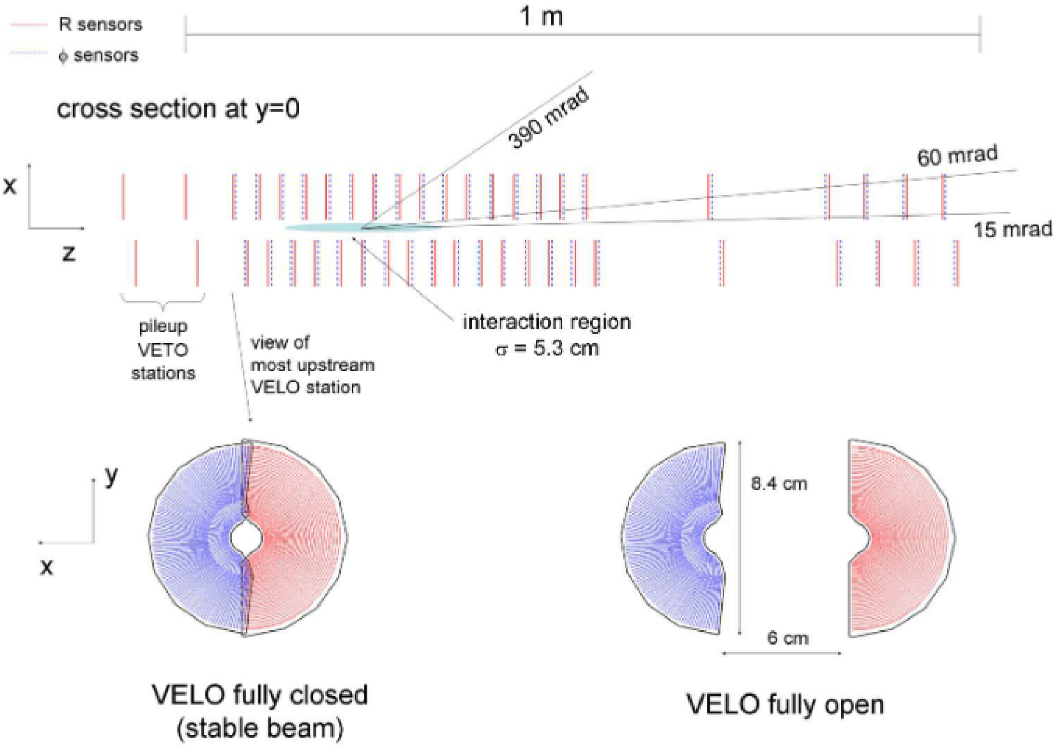

Figure 3.6: Cross section of the VELO modules in the $x-z$ plane (top) and $x-y$ plane (bottom) [4]

Each half of the VELO is made of 21 silicon modules, where each module consists of two semicircular silicon strip sensors, called R and Φ sensors, which measure the radial distance from the beam and the azimuthal angle around the beam, respectively. The third coordinate is determined by knowing the position of each module on the z axis. The sensors are made of silicon microstrips of 300 μm thickness. An illustration of the sensors is given in Fig. 3.7 (left). The sensors have an outer radius of 41.9 mm. In the case of the R sensors, the silicon strips are arranged concentrically with the center given by the LHC beam, and the pitch of the strip varies between 38 μm and 102 μm along the radius. Each strip is subdivided into four 45^o regions. In the case of the Φ sensor which measures the coordinate orthogonal to the R sensor, the strips are arranged radially, and are split into an inner and outer region. The outer region starts at a radius of 17.25 mm and its pitch is set to be roughly half (39.3 μm) that of the inner region (78.3 μm), which ends at the same radius. Besides the arrangement of the strips, the technology used for the two sensors is the same, and it was chosen due to its radiation tolerance. The R and Φ sensors are placed in a back-to-back manner on the modules, as shown in Fig. 3.7 (right).

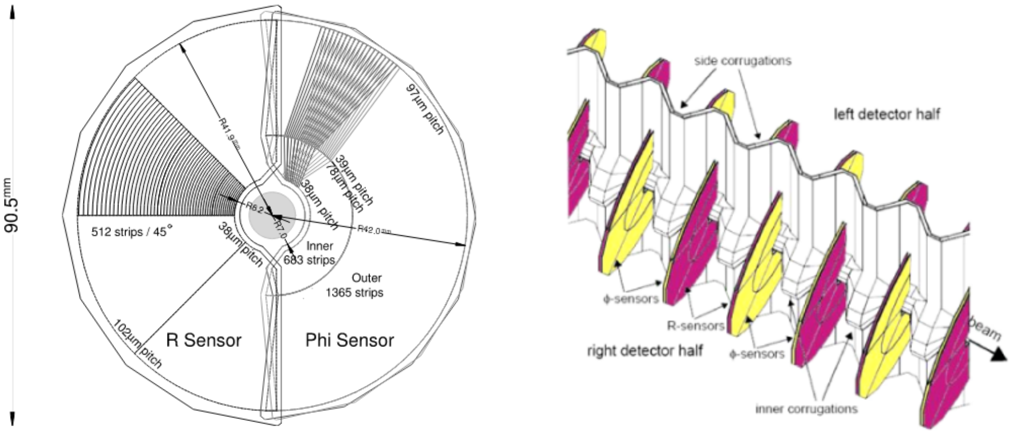

Figure 3.7: Left: VELO R and Φ sensor geometry. The silicon strip arrangement on R and Φ sensors is illustrated [4]. Right:

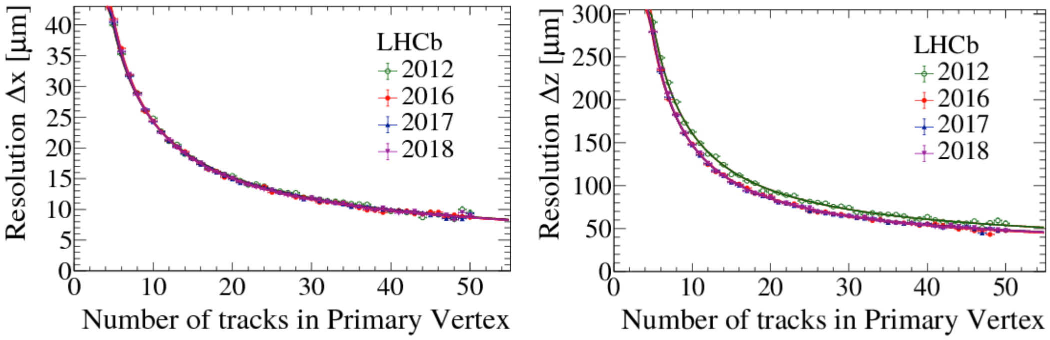

Figure 3.8: Primary vertex resolution on the x (left) and z (right) coordinate as a function of the track multiplicity [105]

The VELO is kept in a vacuum environment and it is enveloped in thin aluminium foil in order to minimize the material that particles travel through and protect the vacuum of the VELO container from the vacuum of the LHC. Additionally, the aluminum foil, also called RF foil, is used to protect the VELO sensors from electromagnetic radiation coming from the beam. Since it is so close to the interaction region, the VELO is subject to a high radiation environment. For this reason, a special CO_2 cooling system maintains the sensors between -10° C and 0° C.

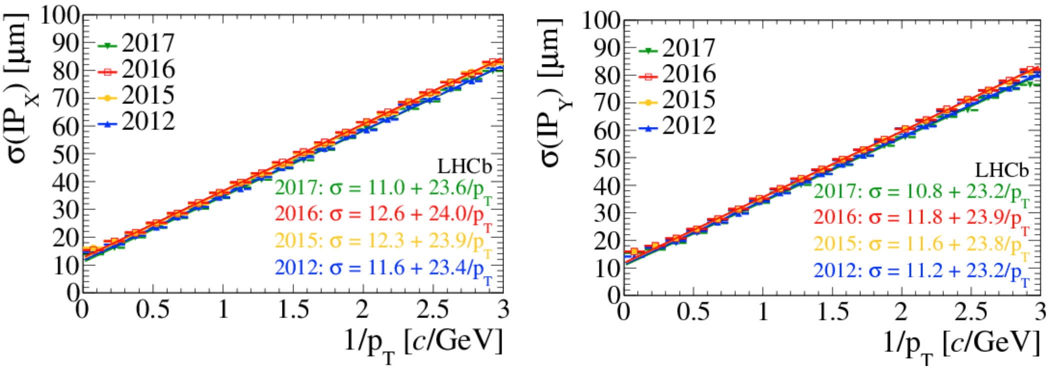

Figure 3.9: Resolution on the x (left) and y (right) coordinates of the IP as a function of the inverse transverse momentum [105]

The performance of the VELO can be expressed in terms of vertexing and IP resolution. For 2011 data, the resolution for a 25-track vertex was found to be 13 μm in the transverse plane and 71 μm along the z-axis. This resolution is dependent on the number of tracks in the vertex and it degrades as the number of tracks decreases. The resolution on the x and z coordinates of the PV can be seen in the plots shown in Fig. 3.8. However, the resolution is much better then the typical flight distance of b- and c-hadrons of about 10 mm, meaning that the VELO can achieve a good separation between PVs and SVs. The track IP can be measured with a precision of up to 15 μm for high transverse momentum tracks and it degrades as the transverse momentum decreases.The resolution on the x and y coordinates of the IP of a track is shown in the plots in Fig. 3.9.

The magnet

A dipole magnet [106] is used at LHCb to curve charged particles trajectories in order to measure their curvature radius and hence their momentum. The magnet is made out of two trapezoidal coils bent at 45° placed inside an iron yoke which weighs 1500 tons, while the coils together weigh 54 tons. A perspective view of the magnet is shown in Fig. 3.10 (left). The magnet is also referred to as a warm magnet due to the fact that it is not superconducting. The design of the magnet and its position at about 5 m from the interaction point was chosen in order to have a magnetic field inside the RICH stations of less than 2 mT and the largest possible field in the region between VELO and the last tracking station (T3). The strength of the magnetic field along the z-axis is shown in Fig. 3.10 (right). The magnet provides an integrated magnetic field of $\int B dl = 4$ Tm. The magnet bends charged particles trajectories in the horizontal $(x-z)$ plane. At LHCb, the tracking stations are required to have a momentum resolution on charged particle tracks of 0.4% for momenta up to 200 GeV/c. In order to achieve this resolution, the strength of the magnetic field is known with a precision of a few times 10^{-4} Tm and the position of the field peak with a precision of a few mm [107].

The magnet polarity is switched regularly such that at the end of each data-taking period, equal amounts of data with `MagUp` and `MagDown` configurations are collected

[108]. This is to ensure that any systematic asymmetric effects of the magnet polarity are cancelled out and it is especially important for *CP* violation analyses.

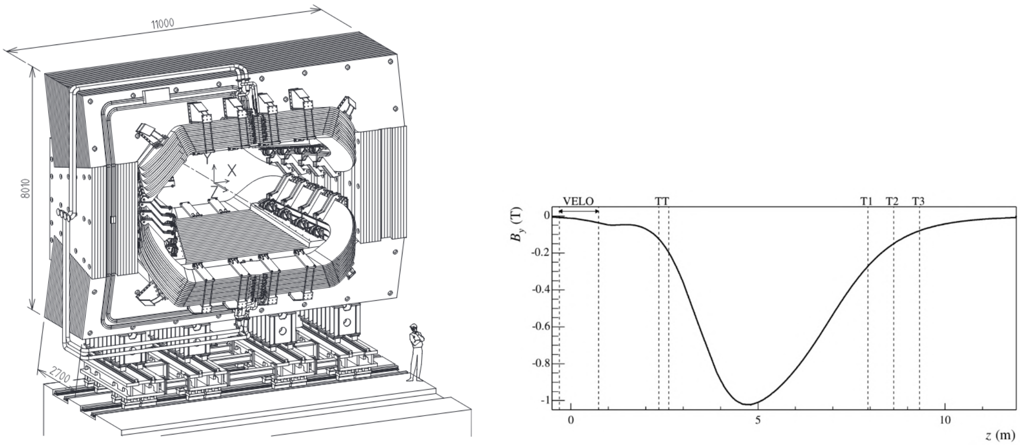

Figure 3.10: Left: Perspective view of the dipole magnet [4]. Right: Scan of the magnetic field along the z-axis. The positions along z of the VELO, TT and T1-T3 stations are also shown. The integrated magnetic field is 4 Tm.

Tracking stations

There are four main tracking stations at LHCb, the TT and the T1-T3 stations [109, 110]. The TT is separated from the T1-T3 and it is located before the magnet. A layout of the tracking stations is shown in Fig. 3.11.

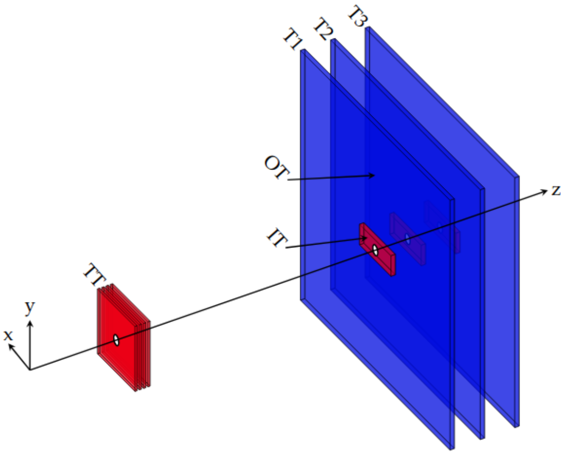

Figure 3.11: Layout of the tracking system [111]

The TT measures 140 cm in width and 120 cm in height and is covered entirely by silicon microstrip detectors. It is situated around the beampipe, and it covers the full angular acceptance of LHCb. The total active area of the TT is about 8.4 m^2.

The particles that travel through are detected by creating electron-hole pairs in the silicon and the electric signal which is generated is read out by the electronics. The TT consists of four detection layers configured in a $x-u-v-x$ geometry, where the two layers in the middle (u and v) are tilted at a stereo angle of $\pm 5^o$ with respect to the vertical. This arrangement allows the determination of the 3D coordinates of the track. The four layers are grouped in two pairs, TTa (x and u) and TTb (v and x), as seen in Fig. 3.12 (left), separated by a gap of 30 cm. Each of the four layers is covered with sensors that are 500 μm thick, 9.64 cm wide and 9.44 cm long. The sensors have a strip pitch of 183 μm which achieves a resolution on the track reconstruction of 50 μm. The main role of the TT is to reconstruct trajectories of charged particles with low momentum, i.e. particles whose trajectories are not bent enough by the magnet and would otherwise escape the acceptance of the other tracking stations.

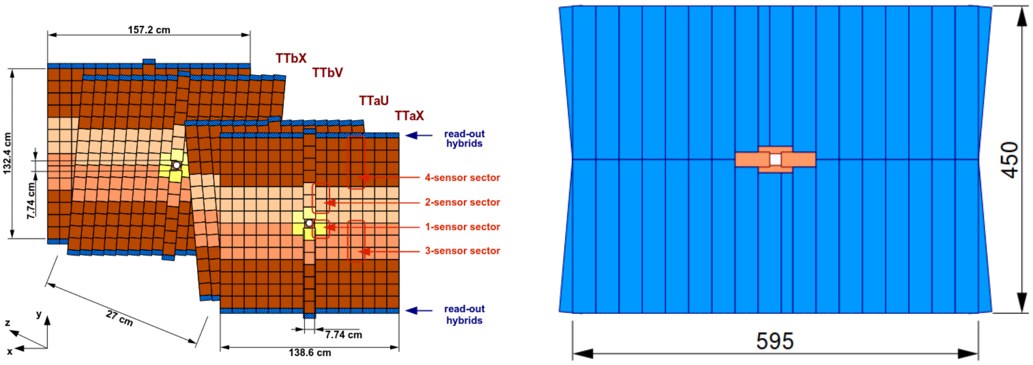

Figure 3.12: Left: Layout of the four layers of the TT station. [112]. Right: Overview of a tracking station. The IT is shown in orange while the OT is shown in blue [109]

The T1-T3 stations, located after the magnet, consist of two sections: the Inner Tracker (IT) and the Outer Tracker (OT). A front view of a tracking station showing the IT and OT is given in Fig. 3.12 (right). The tracking stations are about 600 cm wide and 450 cm tall.

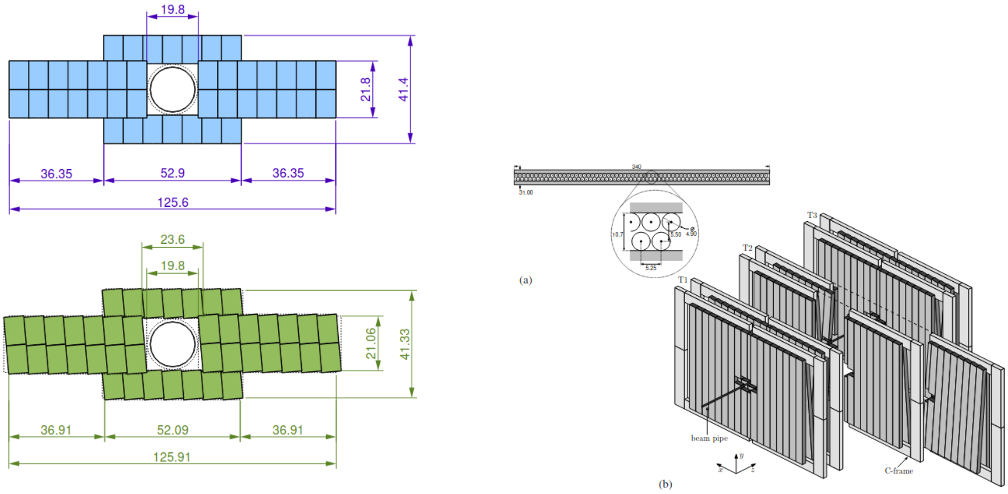

Figure 3.13: Left: Layout of an x (stereo) layer of one IT station is shown on the top (bottom) [109]. Right: Layout of the OT [113]

The IT covers the area around the beampipe, having a cross shape surface of 120 × 40 cm^2. It consists of four detection layers, with the same $x-u-v-x$ configuration as for the TT, where the two middle layers are tilted by ±5° with respect to the vertical. The total active area of the IT is about 4.0 m^2. The layers are covered by silicon strip sensors 7.6 cm wide, 11 cm long and 320 μm thick with a strip pitch of 198 μm, giving a similar 50μm resolution as for the TT. The layout of the first layer and a stereo layer of the IT is shown in Fig. 3.13 (left). Since they have the same sensors of silicon technology, the TT and IT are referred to as the Silicon Tracker (ST). Since the TT and IT cover the area close to the beampipe, the silicon technology was chosen to deal with the high hit density and to provide the required spatial resolution.

The OT covers the rest of the 600×450 cm^2 tracking station surface. As the hit density decreases in areas farther away from the beampipe, the constraints for the spatial resolution are not so stringent. Because of this, and the fact that silicon technology is more expensive, the straw drift tube technology was chosen for the OT.

The tubes have an inner diameter of 5 mm and a wall thickness of 75 μm with a tube pitch in a layer of 5.25 mm. The distance between the two layer planes is 5.5 mm. Each station consists of four modules with the same $x-u-v-x$ configuration as the IT and TT, where the u and v layers are tilted by ±5° with respect to the vertical. Each module consists of two layers of 64 straw tubes. A schematic of the OT stations is given in Fig. 3.13 (right). The straw tubes are filled with a mixture of Ar (70 %) and CO_2 (30%). Particle that cross the tubes ionize the gas inside them and the liberated electrons are collected by the metallic wire generating an electric pulse that is then read out. The drift time of the gas combination is about 50 ns which gives a spatial resolution of about 200 μm.

Track reconstruction

The distribution of the magnetic field within the LHCb experiment is such that the tracks are approximately straight lines in the VELO, TT and tracking stations, i.e. the magnetic field is weak both upstream and downstream of the magnet, where the tracking detectors are located. Different types of tracks are classified based on the tracking detectors they hit along their trajectories. An overview of different track categories at LHCb is shown in Fig. 3.14.

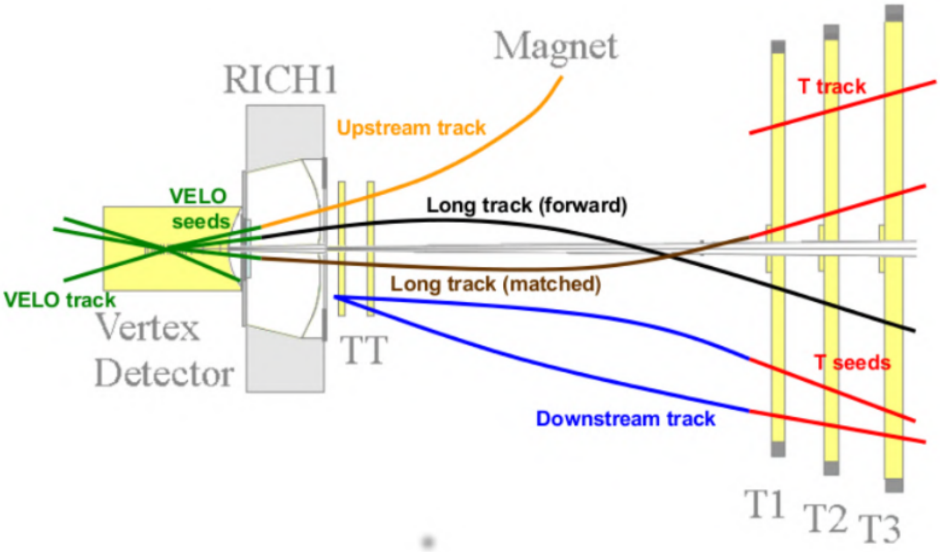

Figure 3.14: Different track types reconstructed at LHCb [114]

- **Long Tracks** are tracks that leave hits in all tracking detectors and thus have the best momentum resolution. For this reason, in most LHCb analyses, and in this analysis, long tracks are used.
- **Upstream Tracks** are tracks that leave hits in the VELO and TT station. These are tracks with low momentum that have their trajectories significantly bent by the magnet and thus do not reach the other tracking stations.
- **Downstream Tracks** are tracks that have hits only in the TT and T1-T3 stations. These are tracks of decay products of particles that decay outside the VELO, such as K^0_S and Λ.
- **T Tracks** are tracks with hits only in the T1-T3 stations. They are typically produced in secondary interactions.
- **VELO Tracks** are tracks that leave hits in the VELO only. They are useful for primary vertices reconstruction

The reconstruction of long tracks is performed by two algorithms, known as *forward tracking* and *track matching* [115]. In the case of forward tracking, the algorithms starts by creating VELO track segments, also known as *seeds*, and combines them with hits in the T stations. The algorithm uses one VELO track and one hit in a T station to form a trajectory, fix the momentum of the track and project this trajectory in the other T stations. Hits in the T stations that are consistent with the projection are included in the final long track. Additionally, in order to increase the momentum resolution of the track, hits in the TT that are consistent with the projected track are included. The track matching algorithm starts again with VELO seeds, but instead combines them with T track segments. The T tracks are found by a separate algorithm. Hits in the TT consistent with the projected trajectory are added in the same way. A Kalman filter [116, 117] is run on each track to account for multiple scattering and energy losses to the detector and thus improve the precision on the momentum of the track. The quality of the track is determined by means of a χ^2 test which helps to remove fake tracks, also known as ghost tracks. Ghost tracks do not correspond to real particle trajectories and appear due to incorrect matching of VELO and T tracks. A machine learning algorithm is used to reject a large fraction of ghost tracks while keeping 99% of real tracks [118].

The final relative momentum resolution on long tracks varies between 0.4% and 1.1%, depending on the track momentum, as shown in Fig. 3.15 (left). The track reconstruction efficiency at LHCb is determined using data driven methods, such as the tag and probe method which uses $J/\psi \to \mu^+\mu^-$ decays [115]. A comparison of the track reconstruction efficiency between Run 1 and Run 2 is given in Fig. 3.15 (right). The efficiency exceeds 95% in the region $5\,\text{GeV}/c < p < 200\,\text{GeV}/c$.

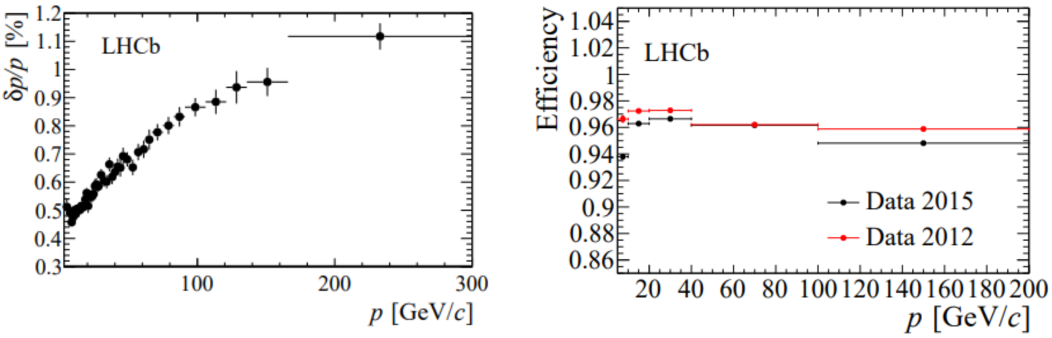

Figure 3.15: Left: Relative momentum resolution as function of the momentum of the track [119] Right: Track reconstruction efficiency compared between Run 1 and Run 2 [120]

3.2.2 The particle identification system

Since the *b*- and *c*-hadron decays studied at LHCb decay into a variety of both charged and neutral final state stable particles, an efficient particle identification (PID) system is needed to distinguish between the different particles and perform the precision studies that LHCb is designed for.

The PID system at LHCb allows to distinguish between charged hadrons such as pions, kaons and protons, charged leptons, i.e. muons and electrons as well as neutral particles such as neutral pions, neutral kaons and photons.

The PID system at LHCb consists of the Ring Imaging Cherenkov (RICH) detectors which identify charged hadrons, the calorimeters which identify and measure the energy of electrons, photons and neutral hadrons and the muon stations which measure the momentum of muons.

RICH detectors

A pair of RICH (RICH1 and RICH2) detectors are used in LHCb to separate the charged hadrons, pions, kaons and protons over the full momentum range [121]. The RICH detectors provide particle identification based on Cherenkov light. This light is emitted when a particle travels through a medium with a speed greater than the speed of light in that medium. The Cherenkov light is emitted in a cone with the direction given by the angle θ according to the following equation:

$$\cos\theta = \frac{1}{n\beta} \tag{3.4}$$

Here n is the refractive index of the medium and $\beta = v/c$, where v is the speed of the particle. Cherenkov light is emitted when $v > c/n$. In this way, by measuring the angle θ the speed of the particle is inferred. The identification of a particle is achieved by knowing its mass. This is done by combining the information of its momentum from the tracking system with the velocity measured by the RICH according to the following equation:

$$m = \frac{p}{\beta\gamma c} = \frac{pn\cos\theta}{c\gamma}, \tag{3.5}$$

where γ is the relativistic factor. In both RICH detectors, a system of spherical and flat mirrors are used to to reflect the Cherenkov light out of the RICH acceptance. Hybrid Photon Detectors (HPD) are then used to detect the Cherenkov photons in the wavelength range of 200-600 nm. Since HPDs operate efficiently only in magnetic fields of up 3 mT, they are protected by a MuMetal cylinder which allows the HPDs to operate in magnetic fields of up to 50 mT [4].

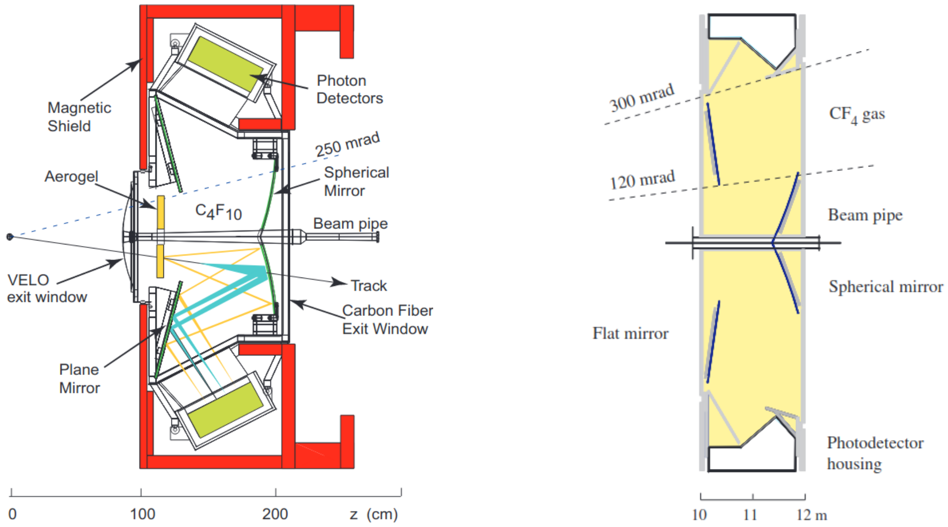

Figure 3.16: Left: Side view of the RICH1 detector [4] Right: Top view of the RICH2 detector

The RICH1 detector is placed upstream of the magnet and covers the full LHCb acceptance. Its role is to identify particles at larger polar angles with lower momenta and thus covers the low momentum range at about 1-60 GeV/c. The RICH1 detector layout is given in in Fig. 3.16 (left). The radiative medium is aerogel and flurobutane gas (C_4F_{10}). In Run 2, the aerogel was removed [122]. The distribution of Cherenkov angles for different particles as measured by the C_4F_{10} radiator in RICH1 is shown in Fig. 3.17.

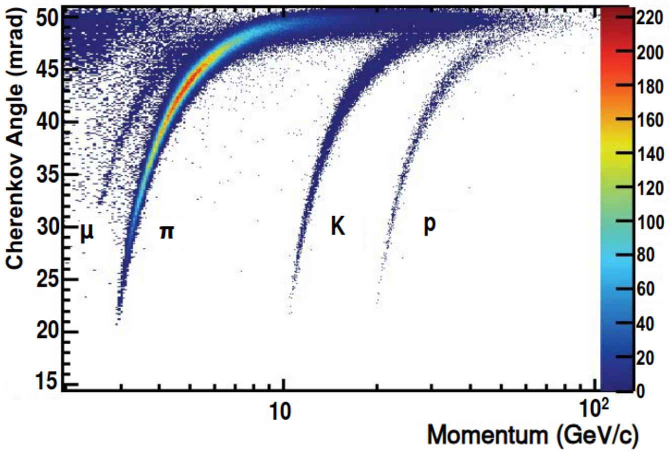

Figure 3.17: Cherenkov angles from data for different particles as function of the track momentum for the RICH1 radiator of C_4F_{10} gas [119]. At high momentum the separation of particle identity is challenging.

The RICH2 detector is located downstream of the magnet and it has a reduced angular acceptance of about ±120 mrad horizontally and about ±100 mrad vertically. This is because RICH2 is designed to identify particles with larger momentum, from 15 GeV/c up to 100 GeV/c, therefore it covers the region where particles with a harder momentum spectrum are expected. A schematic of the RICH2 detector is shown in Fig. 3.16 (right). The RICH2 uses a CF_4 gas radiator which has a smaller refractive index than the C_4F_{10} radiator of RICH1, meaning that particles need to have larger speed in order to produce Cherenkov light.

The Calorimeters

The main goal of the calorimeter system [123] is to provide identification for electrons, photons and hadrons and to measure their energy as well as their position. The energy information needs to be provided very fast, in a time window of 4 μs, as it is used in the trigger system. The other essential function of the calorimeter system is to measure photons as precisely as possible in order to study b-hadron decays that contain prompt photons or neutral pions which decay to two photons. The calorimeter system is the only system at LHCb capable of detecting photons.

The calorimeter system consists of two main components: the ECAL followed by the HCAL. The ECAL has the role to detect and measure the energy of particles that interact electromagnetically, i.e. electrons and photons, while the HCAL has the role to detect and measure the energy of particles that interact hadronically (weakly or strongly). Both calorimeters consist of alternating layers of a heavy material and a scintillating material, thus the principle of particle detection is the same: the passage of a charged particle through the heavy material produces particle showers that in turn produce light in the scintillating material. The amount of light produced by scintillations is measured and it is proportional to the energy of the incident particle.

Upstream of the ECAL, the PreShower (PS) detector and the Scintillating Pad Detector (SPD) are placed, with the SPD being the most upstream. The SPD/PS system consists of two planes of scintillating pads with high granularity separated by a 12 mm thick lead wall. The scintillating light is transmitted by wavelength shifting fibers (WLS) to photomultiplier tubes (PMTs). The thickness of the wall is equivalent to $2.5X_0$, where X_0 is the radiation length, i.e. the distance that an electron can travel in a material before its energy is reduced by $1/e$. The purpose of the SPD/PS system is to distinguish between electrons, photons and neutral pions. An electron, being a charged particle, will produce a signal in the SPD whereas a neutral photon will not. This information is used in the trigger system to separate electrons from photons. Both particles will then produce showers in the lead wall and their energy will be measured by the ECAL. The PS helps distinguish between electrons and hadrons (such as pions) as the hadron will not produce a shower in the lead wall, and will only interact later in the HCAL. Together, the four components of the calorimeter system can effectively separate electrons, photons, charged and neutral hadrons, as shown in Fig. 3.18.

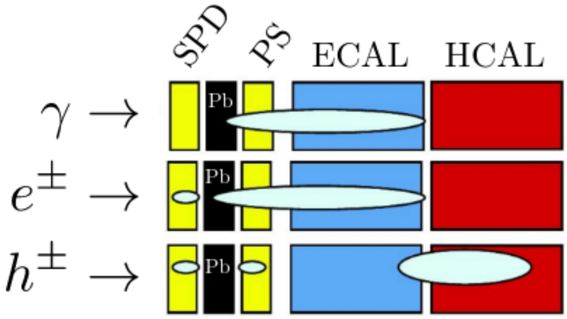

Figure 3.18: Schematic of the calorimeter system showing the four components. The principle of distinguishing between electrons, photons and hadrons is shown [124]

The reconstruction of electrons at LHCb is more challenging than for the other charged particles and it requires information from both the ECAL and the tracking system. This is due to *bremsstrahlung* emission, which is an effect where a fraction of the kinetic energy of a charged particle is released as a photon when it passes close to a nucleus. This process is inversely proportional to the mass squared of the particle such that it is much more significant for electrons than for muons or pions. Therefore, the emission of bremsstrahlung photons during the passage of electrons through the detector material degrades the momentum and energy resolution of electrons with respect to other charged particles. For this reason, special algorithms have been implemented to measure the electrons momentum and improve the resolution [125, 126].

The ECAL consists of 66 layers of 2 mm thick lead absorber and 4 mm think scintillator tiles arranged in a so-called shashlik structure. The total thickness of the ECAL is 42 cm. This is equivalent to $25X_0$ and is enough to contain the full high energy electromagnetic shower. It covers an area of 7.6×6.2 m^2 and covers the angular acceptance of 300 (250) mrad in the horizontal (vertical) plane. The light produced in the scintillator tiles is transmitted by WLS fibers to PMTs in the same way as for the SPD/PS. The resolution of the ECAL is parametrised by [127]:

$$\frac{\sigma(E)}{E} = \frac{(9.0 \pm 0.5)\%}{\sqrt{E}} \oplus (0.8 \pm 0.2)\% \oplus \frac{0.003}{E \sin\theta}, \tag{3.6}$$

where E is the particle energy (in GeV) and θ is the angle between the beam axis and a line from the interaction point to the centre of the ECAL cell. The second term is a constant term coming from mis-calibrations and non-linearities while the third term is a noise term.

The HCAL consists of 6 layers of 16 mm thick iron absorber and 4 mm thick scintillator tiles arranged similarly in a shashlik structure. It has a total thickness of 1.65 m and is equivalent to 5.6 hadronic interaction lengths. The hadronic interaction length is the mean distance before a hadron interacts with a nucleus of the material it traverses and is proportional to $N^{1/3}$ of the material, where N is the number of nucleons. This is why the material used for the HCAL is iron which has a lower atomic number than lead. The thickness of the HCAL is not enough to capture the full hadronic showers and thus it has a worse resolution than the ECAL. The information from the HCAL on the hadron energy would not be accurate enough and thus it is used only for triggering purposes, i.e. to decide on keeping an event if it is above a certain E_{T} threshold. The resolution of the HCAL is parametrised by [127]:

$$\frac{\sigma(E)}{E} = \frac{(67 \pm 5)\%}{\sqrt{E}} \oplus (9 \pm 2)\%, \tag{3.7}$$

where E is the deposited energy in GeV.

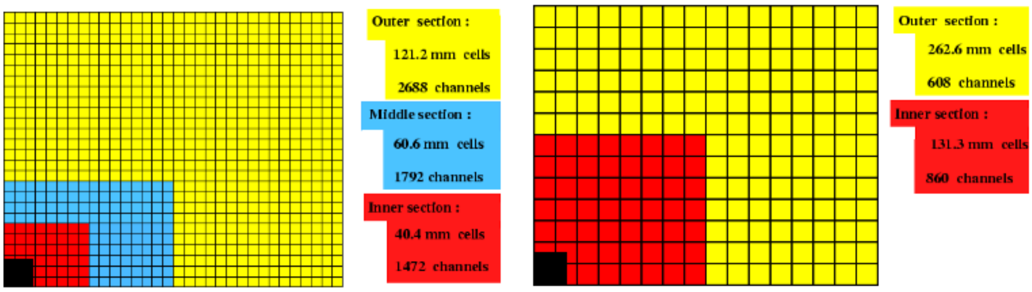

Figure 3.19: Cross section of the SPD/PS and ECAL (left) and HCAL (right), showing the calorimeter cells segmentation [127]

Since the density of particle hits changes by about 2 orders of magnitude over the calorimeter surface, the calorimeters have variable segmentation depending on the distance from the beam pipe. The ECAL is designed to have three regions with differenct cell sizes, as shown in Fig. 3.19 (left). The cells are smaller in size in the region closest to the beampipe, where the particle hit density is high, and have increasingly larger sizes in the regions farther away from the beam pipe. The same segmentation has been chosen for the SPD/PS system. Due to the dimensions of the hadronic showers, the HCAL cells are larger than the ECAL cells and are divided in only two regions with different cell sizes, as shown in Fig. 3.19 (right).

The muon stations

Many of the b-hadron decays studied by LHCb decay to final states containing muons, such as the 'gold-plated' channels $B^0 \rightarrow J/\psi K^0_{\mathrm{S}}$ and $B^0 \rightarrow J/\psi\phi$, where $J/\psi \rightarrow \mu^+\mu^-$, or the very rare flavor changing neutral current decay $B^0_s \rightarrow \mu^+\mu^-$. In the case of semileptonic decays such as the one studied in this analysis, $B^0 \rightarrow D^{*-}\mu^+\nu_\mu$, muons provide a tag on the flavor of the initial state of the B meson. Muon identification and triggering is therefore essential for LHCb. The muon system delivers information regarding the transverse momentum of the muons in a 4 μs time window. This information is used at the first level (hardware) L0 trigger to take a binary decision on saving the event. The information from the muon system along with the calorimeters constitutes the basis of the L0 trigger.

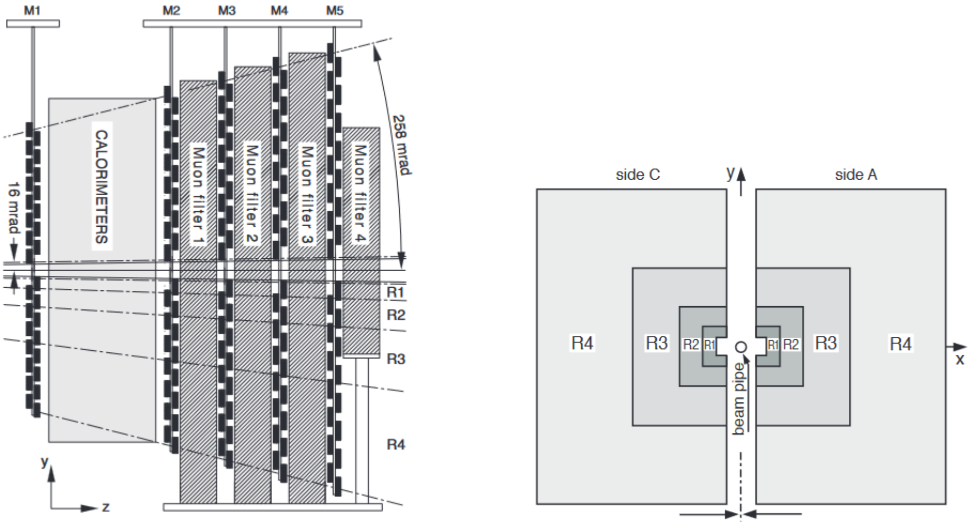

Figure 3.20: Left: Side view of the muon system Right: Layout of one muon station [128]

The muon system at LHCb consists of five muon stations [129] M1-M5, shown in Fig. 3.20 (left). The muon stations M2-M5 are the last subdetectors along the z-axis, downstream of the calorimeters, farthest away from the interaction point. Their exploits the fact that muons are not affected by bremsstrahlung and do not interact hadronically such that they are not stopped neither in the ECAL nor in the HCAL and are the only particles able to reach the muon stations.

The inner and outer angular acceptances of the muon system are 20 (16) mrad and 306 (258) mrad in the bending (non-bending) plane respectively. They cover a total area of 435 m^2. This results in an acceptance of about 20 % for muons from inclusive b-hadron semileptonic decays. Each of the five station is divided into four regions R1-R4, as shown in Fig. 3.20 (right). The granularity is increased for the regions closer to the beampipe where the occupancy is higher. This segmentation provides a similar occupancy over the whole detector.

The M2-M5 stations are located downstream of the HCAL. Between each two consecutive stations, an iron absorber with a thickness of 80 cm is placed. The total thickness of the muon system is equivalent to 20 radiation lenghts. Therefore, only muons with a momentum greater than 6 GeV/c can reach the last muon station. The iron blocks stop any other particles that may have traversed the calorimeters. In all four regions, the M2-M5 stations consist of multi wire proportional chambers (MWPCs). The gas mixture used in the MWPCs is Ar/CO_2/CF4 (40:55:5 %).

The M1 station is placed upstream of the ECAL. Its role is to provide a more accurate transverse momentum measurement which is used it the hardware trigger. Due to a larger particle density, the inner R1 region of the M1 station uses a different detector technology, namely triple gas electron multiplier detectors (triple-GEM) which are filled with Ar/CO_2/CF4 (45:15:40 %). The entire muon system has a total of 1380 MWPCs, which covers more than 99% of the system area. Each region of the muon stations is designed to have an efficiency of more than 99 % in order to have a global hit reconstruction efficiency of 95 %. This is demonstrated in Fig. 3.21

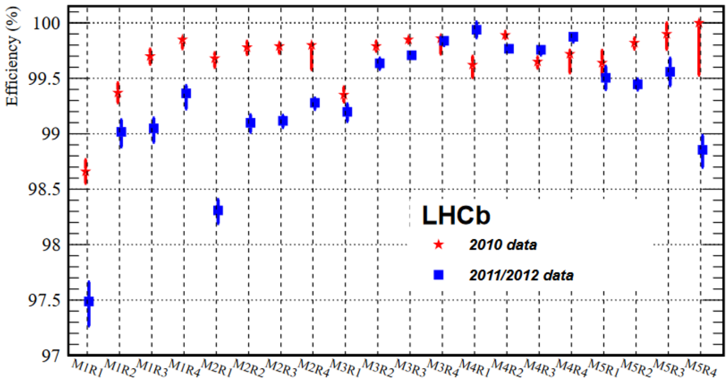

Figure 3.21: Hit reconstruction efficiency of each of the four regions of the five muon stations [119]

Performance of the PID system

The information provided by the PID system at LHCb is used to identify a wide range of particles. Information from RICH, calorimeters and muon stations is used to identify electrons, muons, protons, kaons and charged pions. Information from ECAL is used to identify photons and neutral pions. Thus, the Cherenkov angle measured by the RICH system, the energy deposits in the calorimeters and the hits in the muon stations are combined into a set of PID variables that can be used offline in analyses to reject misidentified particles.

For each particle track, a likelihood $\mathscr{L}_x$ is computed. This quantity reflects how likely the particle is of species x, where x can be electron, muon, proton, kaon or pion. Usually the logarithm of this likelihood is used, i.e. $\log \mathscr{L}_x$. Due to the large number of pions at LHCb, the likelihood is usually expressed as a *difference log likelihood* (DLL) with respect to the pion hypothesis:

$$DLL_x = \log \mathscr{L}_x - \log \mathscr{L}_\pi, \tag{3.8}$$

where a larger DLL_x implies that the particle is more likely to be of species x.

The information from the RICH detectors provide the log likelihood of electron, muon, proton and kaon relative to pion hypothesis. The calorimeters provide the log likelihood of electrons relative to pions while the muon system provides the likelihood of the (non) muon hypothesis. The likelihoods coming from all three PID subdetector systems are added linearly to create a *combined differential log likelihood* (CombDLL). This constitues the first class of PID variables at LHCb and are used at the trigger level and in offline analyses to perform selections. In particular, in the analysis performed in this thesis, variables such as CombDLL_K and CombDLL_μ are used to reject cases where kaons or muons are misidentified as pions as well as pions misidentified as kaons.

The second class of PID variables use machine learning algorithms (neural networks) to improve the likelihoods presented above. The likelihoods are combined with information from the tracking system and other information from the PID subdetector not used in the likelihood computation to create an improved set of PID variables. These are known as $ProbNN$ variables and they provide a single probability for the particle hypothesis [130].

The third type of PID variable is the `isMuon` binary variable [131], which is used to decide whether a particle track is a muon or not. The identification of muons is based on the hits in the muon stations and information from tracking system. Depending on the track momentum, the `isMuon` decision is triggered by hits in certain muon stations, as shown in Tab. 3.2.

Momentum range	Muon stations
$3\,\mathrm{GeV}/c < p < 6\,\mathrm{GeV}/c$	M2 and M3
$6\,\mathrm{GeV}/c < p < 10\,\mathrm{GeV}/c$	M2 and M3 and (M4 or M5)
$p > 10\,\mathrm{GeV}/c$	M2 and M3 and M4 and M5

Table 3.2: Muon stations needed to be hit in order to trigger `isMuon` [131]

The particle identification performance of the RICH system is studied using large data samples with genuine pion, kaon and proton tracks. The data samples consist of decays with large branching fractions such as $K^0_S \to \pi^+\pi^-$, $\Lambda \to p\pi^-$ and $D^{*+} \to (D^0 \to K^-\pi^+)\pi^+$. These decays cover the hadron tracks needed to estimate the performance of hadron PID. The kaon identification efficiency, i.e. kaons identified as kaons over the momentum range $2-100\,\mathrm{GeV}/c$ is about 95% in Run 1 data, as shown in Fig. 3.22 (left). The pion misidentification efficiency, i.e. pions misidentified as kaons is also shown and is on average about 10%. The plot shows the kaon ID efficiency and pion mis-ID efficiency in two cases: where $\log\mathscr{L}_K - \log\mathscr{L}_\pi > 0$ is required and where $\log\mathscr{L}_K - \log\mathscr{L}_\pi > 5$ is required. The more stringent requirement of $\log\mathscr{L}_K - \log\mathscr{L}_\pi > 5$ decreases the pion mis-ID efficiency to an average of about 3% while losing only about 10% of the kaon ID efficiency [119]. This demonstrates the ability of LHCb to efficiently separate kaons and pions.

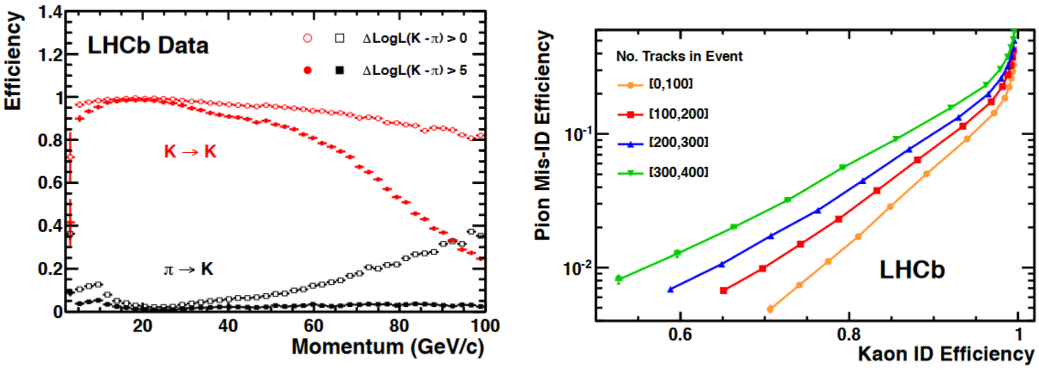

Figure 3.22: Left: Kaon ID efficiency and pion mis-ID efficiency as a function of the track momentum. The two efficiencies are shown for two different requirements of $DLL_K - DLL_\pi > 0$ (empty dots) and $DLL_K - DLL_\pi > 5$ (full dots) Right: Pion mis-ID efficiency versus kaon ID efficiency as measured in Run 1 as a function of track multiplicity [119]

The pion mis-ID efficiency versus the kaon ID efficiency for different numbers of tracks in the event is shown in Fig. 3.22 (right). The PID performance is slightly degraded with increasing track multiplicity.

The particle identification performance of the muon system is studied with the high statistics data samples of $J/\psi \to \mu^+\mu^-$, $\Lambda \to p\pi^-$ and $D^0 \to K^-\pi^+$ decays. The muon identification (`isMuon` criteria) efficiency as a function of the track momentum, as well as the proton, pion and kaon mis-ID, i..e protons, pions and kaons misidentified as muons, efficiencies are shown in Fig. 3.23. The muon ID efficiency is, on average over the momentum range, about 98 % while the proton, pion and kaon mis-ID efficincies are all, on average, at about 1 %. This demonstrates the ability of LHCb to efficienctly identify muons and separate muons from hadrons.

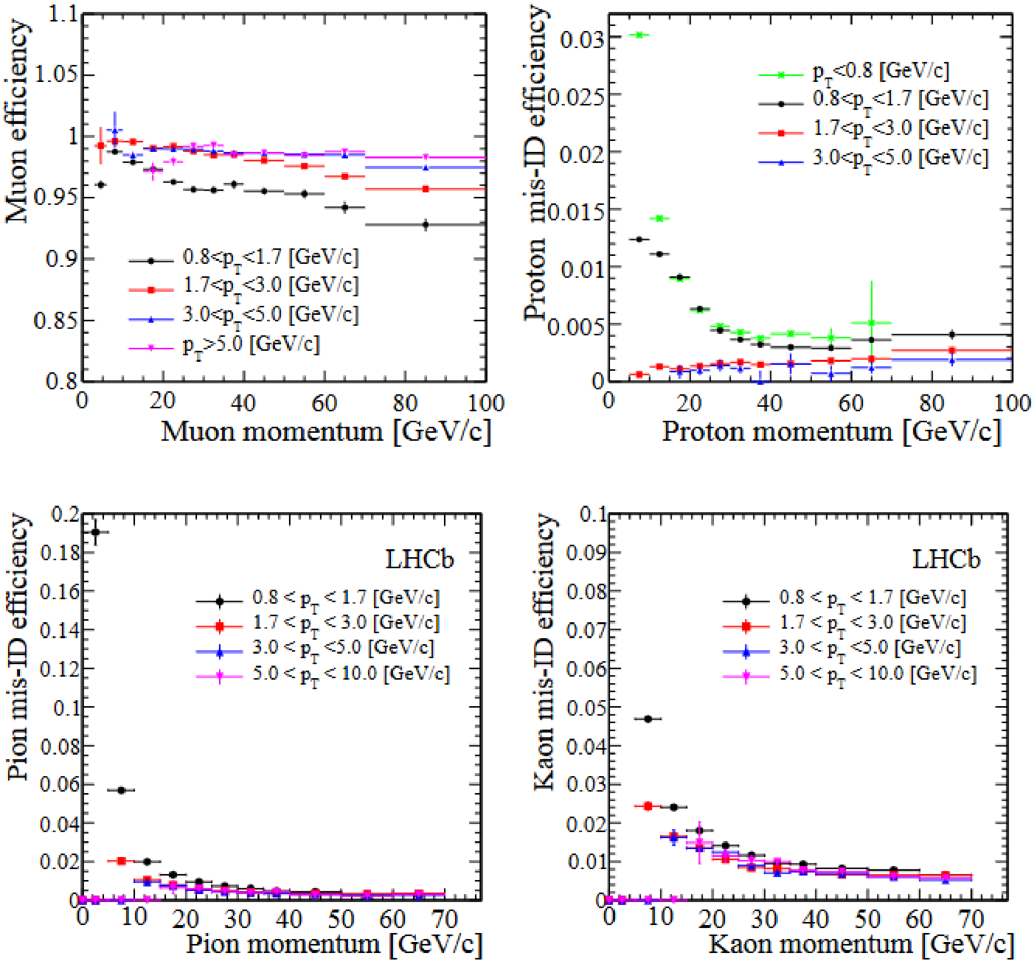

Figure 3.23: Top left: Muon ID efficiency as function of the muon momentum. Top right: Proton mis-ID efficiency as function of the proton momentum. Bottom left: Pion mis-ID efficiency as function of pion momentum. Bottom right: Kaon mis-ID efficiency as function of kaon momentum. All plots show the efficiencies for different ranges of transverse momenta of the tracks. [119]

3.2.3 The trigger system

The nominal bunch crossing rate at the LHC is 40 MHz, corresponding to a collision each 25 ns. However, in practice at LHCb the collision rate visible at LHCb is about 30 MHz due to empty bunches and inelastic pp collisions. At an operating luminosity of 2×10^{32} cm^{-2}s^{-1} and a center-of-mass energy of 7 TeV, the visible pp interaction have a rate of producing $b\bar{b}$ pairs of only about 100 kHz. Only 15 % of these will produce a b-hadron that will actually fall into the detector acceptance. Furthermore, the interesting decays studied at LHCb typically have low branching fractions. For this reason, most of the events in a pp collision are not interesting for LHCb and thus saving the full 40 MHz on disk would be unnecessary. Furthermore, the 40 MHz rate is equivalent to about 1.9 TBytes/s which would require an unreasonable amount of space. The trigger system of LHCb [105, 132–135] has the purpose to reduce the nominal 40 MHz of collision rate to a lower rate of a few kHz that can be saved on disk while keeping the interesting events and rejecting background events.

The trigger system at LHCb consists of two stages, the hardware level trigger, known as Level-0 (L0) trigger, and a software level trigger known as high level trigger (HLT). The software trigger is further divided into HLT1 and HLT2. This trigger system reduced the data rate from 40 MHz to 5 kHz in Run 1 (2012) and to 12.5 kHz in the whole Run 2. The trigger schemes at LHCb of 2012 and 2015 are shown in Fig. 3.24. The rest of this section will describe the trigger conditions of Run 2. The L0 trigger has the role to reduce the data rate from 40 MHz to 1 MHz, which is the rate at which the full LHCb detector can be read out. The constraint on the readout rate comes from the bandwidth and frequency of the front-end electronics operating at a $\mu = 1.1$ visible interactions per bunch crossing. The 1 MHz output rate of L0 is then passed to the software trigger, where HLT1 reduces the rate to 150 kHz and HLT2 finally reduces the rate to 12.5 kHz which is stored on disk. The trigger system consists of multiple algorithms that are used to take the decision on whether an event is interesting or not and to save it. These algorithms are conventionally referred to as *trigger lines*.

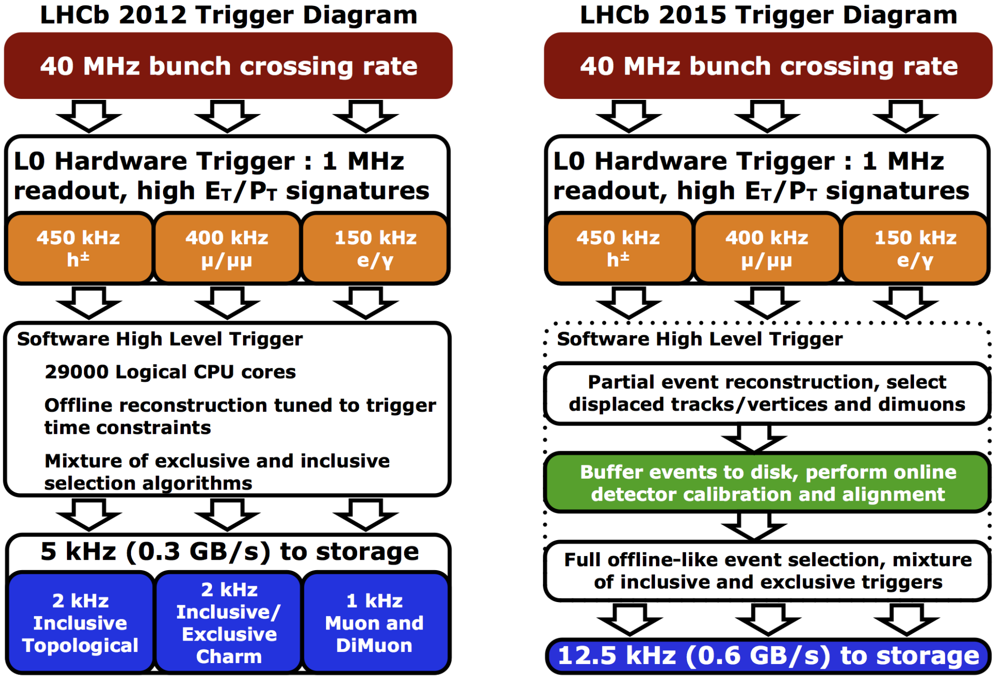

Figure 3.24: Left: Trigger scheme in Run 1. Right: Trigger scheme in Run 2 [136].

L0 trigger

The L0 trigger is based on a system of field programmable gate arrays (FPGAs) that have a latency of 4 μs. The L0 system uses mainly information from the two calorimeters and muon stations which are the only subdetectors that can provide the information fast enough. The information from these subdetectors is used in separate L0 trigger lines which look for particles with large transverse momentum and transverse energy as these are signatures of b-hadron decays due to their large mass.

The L0-calorimeter trigger line (`L0Calo`) selects events based on information from the PS, SPD, ECAL and HCAL. The `L0Calo` line is divided into `L0Hadron`, `L0Photon` and `L0Electron`. These lines are used to select hadrons, photons and electrons based on their transverse energy (E_{T}) deposited in clusters of 2×2 calorimeter cells. The transverse energy is defined as:

$$E_{\mathrm{T}} = \sum_{i=1}^{4} E_i \sin\theta_i, \tag{3.9}$$

where E_i is the energy deposited in cell i and θ_i is the angle between the cell i and the beam axis. The SPD and PS allow to distinguish between hadrons, electrons and photons. The E_{T} thresholds for passing the `L0Calo` trigger line for hadrons, electrons and photons are not the same in different data-taking periods. The thresholds of 2016 and 2017 are given in Tab. 3.3.

The L0-muon trigger line (`L0Muon`) selects events based on the existence of straight line tracks in the M1-M5 muon stations and chooses pairs of muon tracks with the largest p_{T} in the event. The two muon trigger lines are `L0Muon` and `L0DiMuon`. The `L0Muon` line selects events where either of the two tracks is above the p_{T} threshold and the `L0DiMuon` selects events with the product of the two p_{T} above the threshold. The p_{T} thresholds for the L0 muon trigger lines are given in Tab. 3.3 for 2016 and 2017 years of data-taking. The thresholds were looser in 2017 due to some difficulties with the beam injection that caused the collision rate to be lower [105].

	$E_{\mathrm{T}}/p_{\mathrm{T}}$ thresholds		
L0 trigger	2016	2017	SPD hits
Hadron	> 3.7 GeV	> 3.46 GeV	< 450
Photon	> 2.78 GeV	> 2.47 GeV	< 450
Electron	> 2.4 GeV	> 2.11 GeV	< 450
Muon	> 1.8 GeV	> 1.35 GeV	< 450
DiMuon	$> 2.25\ \mathrm{GeV}^2$	$> 1.69\ \mathrm{GeV}^2$	< 900

Table 3.3: The L0 trigger thresholds for p_{T} and E_{T} in 2016 and 2017 years of data-taking in Run 2 [105]

In addition to the E_{T} and p_{T} thresholds, a requirement on the number of hits in the SPD is placed in the L0 trigger in order to reject events with high occupancy in the detector that would be difficult to process. In Run 2, this requirement was always that the number of SPD hits is smaller than 450. All L0 trigger lines decisions are transferred to the *L0 Decision Unit* which performs a logical `OR` operation between them. If the L0 trigger decision is passed then the whole detector is read out and the event is passed further to the software trigger.

High level trigger

The first L0 trigger passes the reduced 1 MHz to the second level HLT trigger which further reduces this rate in two steps, at the HLT1 and HLT2 levels. The HLT is implemented as a software application in `C++` and it runs on the event filter farm (EFF) which consists of 1700 processors with 27000 physical cores.

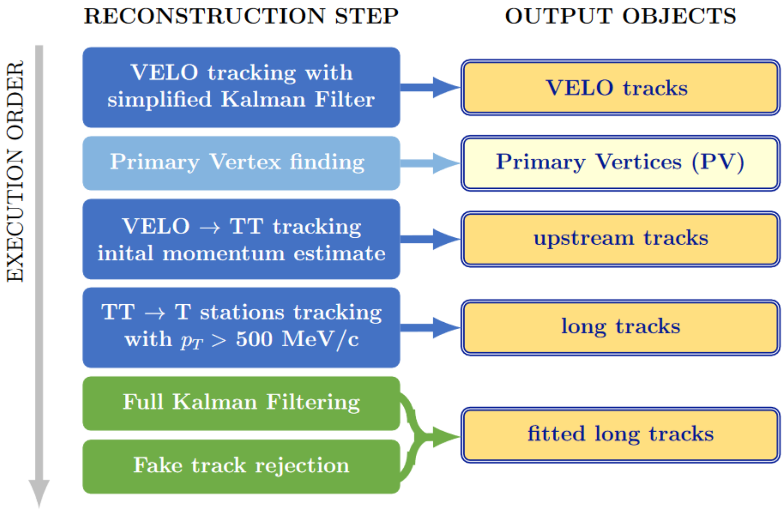

Figure 3.25: HLT1 track and vertex reconstruction sequence [105]

At the HLT1 level a partial event reconstruction is performed and long tracks, i.e. tracks that with hits in the entire tracking system, of charged particles with a p_{T} larger than 500 MeV/c are reconstructed. At the same time, a reconstruction of the primary vertex is performed.

First, the hits in the VELO are combined to form a straight line which is fitted with a simplified Kalmar filter. This VELO track is then extrapolated and hits in the TT are matched to it to form upstream tracks. This provides an initial momentum estimate with a precision of about 20 % which is used to reject tracks with low p_{T}. Hits in the IT and OT consistent with the extrapolation of a track with a p_{T} larger than 500 MeV/c are then added to form the long track. The long tracks are then fitted with a Kalmar filter and fake tracks are rejected. The PV is reconstructed at the same time using the fitted VELO tracks only. A schematic of the algorithm sequence for track reconstruction performed in HLT1 is shown in Fig. 3.25.

Muon identification also takes place in the HLT1. Fully fitted tracks are extrapolated to the muon stations and hits in the muon stations consistent with the extrapolation are searched for. The muon identification is performed by the `isMuon` algorithm based on the number of hits in the different muon stations.

The HLT1 consists of a few different trigger lines which exploit the features of b- and c-hadrons to select the events. There are two inclusive lines, which run on the output of the whole L0 trigger, that look for events with displaced decay vertices from the PV: a line that selects a single high p_{T} track and a line that selects a high p_{T} two-track vertex. These lines are based on multivariate algorithms [137]. There are also HLT1 muon lines used to select muons from b- and c-hadrons as well as muons coming from W and Z boson decays. The muon lines run on the output of the `L0Muon` and `L0DiMuon` lines. Additionally, there are calibration lines which select $D^0 \to K^-\pi^+$ and $J/\psi \to \mu^+\mu^-$ candidates and are used for the alignment of the tracking system and the muon system, respectively. A procedure of real time alignment and calibration of the LHCb subdetectors, specific to Run 2, is performed in HLT1 and it allows HLT2 to achieve a better performance on the reconstruction, similar to the offline reconstruction performance. This is possible because the output of HLT1 is buffered to disk and can be used for online alignment and calibration.

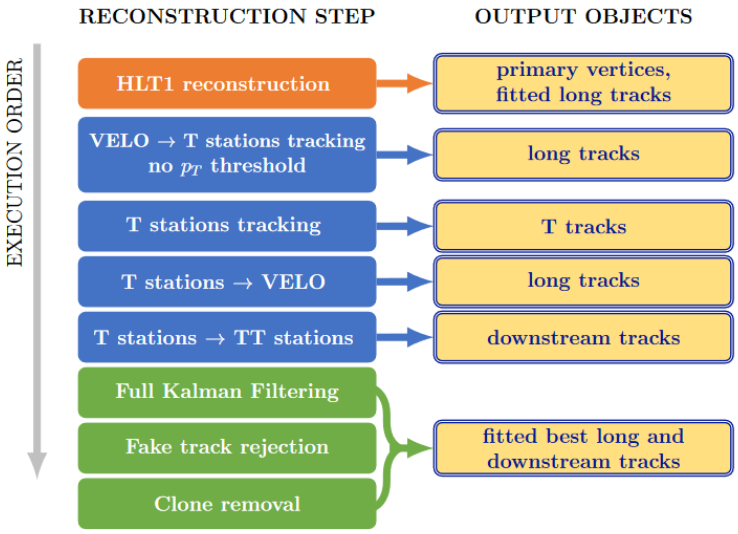

Figure 3.26: HLT2 track reconstruction sequence [105]

The HLT2 runs on the output of HLT1. HLT2 performs a full reconstruction of the event and reduces the event rate to the final value of 12.5 kHz. The HLT2 performs an improved track reconstruction of charged particles by making use of a more advanced pattern recognition than the one in HLT1. The final precision on the momentum resolution of long and downstream tracks is thus obtained. Besides the information from the muon system, HLT2 also uses the PID information from the RICH system and calorimeters, which was not used in HLT1 due to time constraints, to reconstruct neutral particles and perform particle identification.

The charged track reconstruction steps are shown in Fig. 3.26. The sequence begins with the same reconstruction performed in HLT1. However, at this stage the p_{T}

requirement on the track is dropped and low p_{T} tracks can be also reconstructed. All tracks are then reconstructed, including long tracks, which were also reconstructed in HLT1, T tracks and downstream tracks for particles that decay outside the VELO. The tracks are once again fitted with a Kalman filter and fake tracks are rejected with neural network algorithms.

The HLT2 lines are more exclusive than the HLT1 ones and they are designed to select decays with specific decay topologies and decay products.

Software and simulation

The data collected by the LHCb detector is subject to a series of processing steps performed by different software applications [138]. The general C++ framework on which all LHCb software is based is called `GAUDI` [139, 140]. The first processing step of data is the trigger, described in the previous section, which at the software level is run by the `MOORE` application. The output of the trigger is saved on disk and the offline event reconstruction is performed by the `BRUNEL` application. The output of the offline reconstruction is stored in so-called *data summary type* (DST) files.

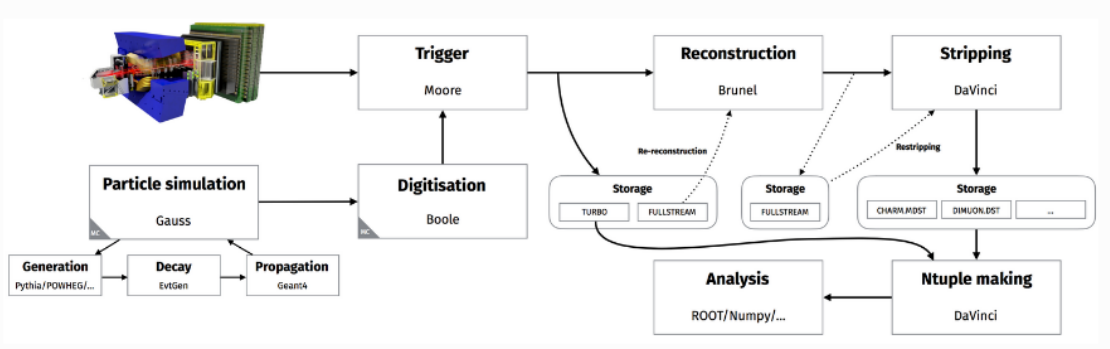

Figure 3.27: Schematic of the LHCb data flow [141]

The final processing step of data is performed with the `DaVinci` application. During `DaVinci` the reconstructed tracks from `BRUNEL` are used to fit decay vertices and reconstruct candidates, i.e. sets of tracks assumed to come from a specific decay chain hypothesis. Based on the information from the subdetectors, various kinematic and geometric quantities (variables) useful for offline analyses are computed. Since the data size at this point is still too large for offline analysis, another filtering step known as *stripping* is performed during `DaVinci`. The stripping process is organised in *stripping lines*. These lines define a set of loose requirements based on variables computed during `DaVinci` and are dedicated to select specific decays and reject backgrounds in an efficient manner. The analysts can then choose a convenient stripping line based on their decay of interest. Therefore, `DaVinci` is run on stripped DST files and the output is stored as a `ROOT` [142] file, known as an *NTuple*, which is used for further analysis. A schematic of the whole data processing sequence at LHCb is shown in Fig. 3.27.

Monte-Carlo (MC) simulation of particle data is widely used in high energy physics and is essential to most of LHCb analyses. Simulations can be produced for any process and particle decay of interest, also known as signal decay. At LHCb simulation is realised with `GAUSS` [143]. The pp collisions and the hadronisations of the quarks produced in the collisions are simulated with the `PYHTIA` package [144]. The resulting particles are forced to decay to specific final states of interest. Hadronic decays are simulated with `EvtGen` [145] and `PHOTOS` [146] is used to account for final state radiations. The passage of the final state particles through the LHCb detector is simulated with the `GEANT4` package [147]. The `BOOLE` application simulates the digitised responses of the LHCb subdetectors. These responses are then passed to `MOORE` to run the software trigger on the simulation. The MC data is then subject to the same data processing steps as real data, as shown in Fig. 3.27.

3.2.4 LHCb in Run 3

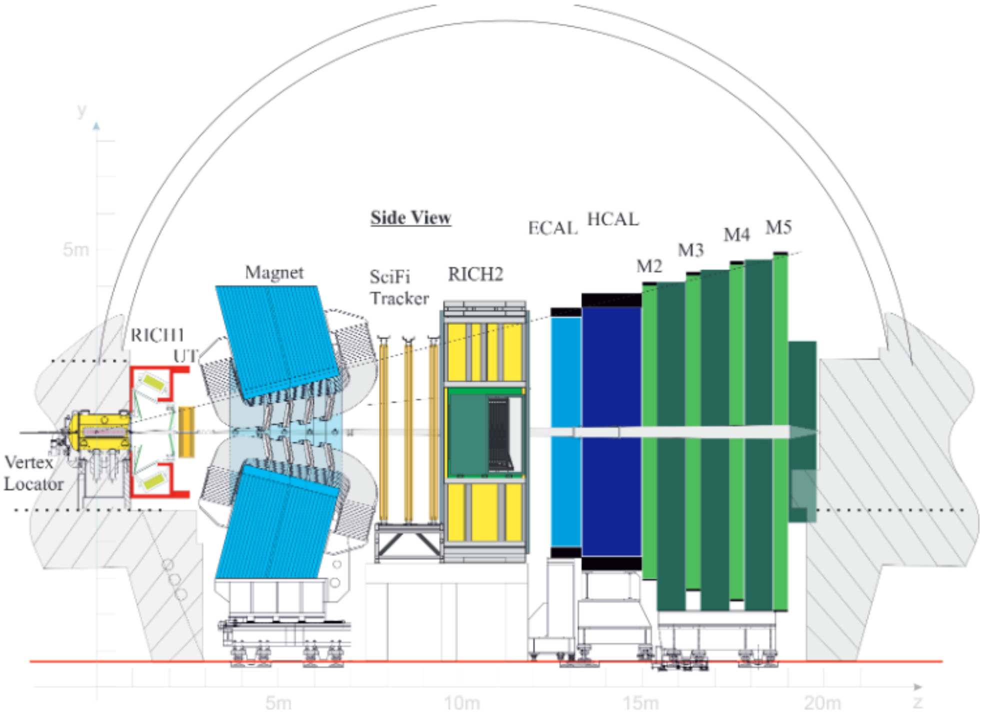

Figure 3.28: Cross section of the upgraded LHCb detector [148]

Although the analysis presented in this thesis is based on data collected in Run 2, it is worth mentioning the upgrade of the LHCb detector for Run 3 [149]. After the end of Run 2, the LHC entered the LS2 phase during 2018-2021 in order to increase the center-of-mass energy and the luminosity. The LHCb detector suffered major upgrades in order to profit from these changes. The instantaneous luminosity at LHCb will be increased by a factor of 5, from 4×10^{32} cm^{-2}s^{-1} to 2×10^{33} cm^{-2}s^{-1} thus increasing the number of interactions per bunch crossing from 1-2 to an average of about 5. In order to deal with this higher luminosity, a new trigger system has been implemented. During Run 2, the `L0` trigger limited the data acquisition rate from 40 MHz to 1 MHz. For Run 3, the hardware `L0` trigger was removed and replaced by a full software trigger that can process every single bunch crossing at 25 ns allowing for the full readout of the detector at 40 MHz [133, 150]. Furthermore, most of the subdetectors at LHCb were upgraded to deal with higher luminosity and endure a higher radiation environment. The TT station upstream of the magnet was removed and replaced by a high granularity silicon micro-strip detector with better coverage called the *Upstream Tracker* (UT). The T1-T3 tracking stations downstream of the magnet will be replaced by three *Scintillating Fibre Tracker* (SFT) stations which consists of scintillating fibres 2.5 m long and are read out by Silicon Photomultipliers [148]. The SPD and PS in front of the calorimeteres are removed while the ECAL and HCAL were kept in place. The RICH and muon systems were upgraded to operate at a 40 MHz data rate and the M1 station was removed since it was only providing information to the `L0` trigger which does not exist anymore [151]. Finally, the VELO was upgraded to cope with the higher readout rate and luminosity. For this reason, the silicon sensors and the electronics were completely changed. [152]. A view of the upgraded LHCb detector is given in Fig. 3.28.

4 Search for *CP* violation in $B^0 \to D^{*-}\mu^+\nu_\mu$

Semileptonic decays such as $B^0 \to D^{*-}\mu^+\nu_\mu$ ($b \to c\ell\nu_\ell$ at quark level) are mediated in the SM by the W boson with a left-handed vector ($V-A$) interaction. The W boson has the same coupling to all three lepton generations e, μ and τ, property which is known as lepton flavor universality. As discussed in Sec. 2.2.1, several LFU tests such as $\mathscr{R}(D)$ and $\mathscr{R}(D^*)$ were performed by various collaborations and tensions $\sim 3\sigma$ are observed between the theoretical predictions and the experimental measurements. These tensions suggest the presence of NP in semileptonic decays and are the motivation for any measurements complementary to the $\mathscr{R}(Hc)$ ones. To explain the tensions, several theoretical models where hypothetical particles such as charged Higgs ($H^\pm$), prime W' bosons or leptoquarks (LQ) may mediate the $b \to c\ell\nu_\ell$ decay in addition to the SM W boson. These NP particles can interact via Lorentz structures different than the left-handed vector one of the SM such as right-handed vector, scalar, pseudoscalar or tensor. To complement the search for NP in semileptonic decays, *CP*-violating observables have been proposed as means to constrain and distinguish different NP scenarios, as discussed in Sec. 2.2.3. Since there is only one amplitude in the SM at tree level for $b \to c\ell\nu_\ell$ decays, *CP* violation is zero to a good approximation in these decays as any *CP*-violating effects require (at least) two interfering amplitudes. Measuring nonzero *CP* violation in these decays is thus a clean probe of NP. The standard direct *CP* violation, defined as the difference in the rates between process and *CP* conjugated process, requires the presence of a weak phase and strong phase difference between two interfering amplitudes. In the $b \to c\ell\nu_\ell$ case, the strong phase difference vanishes since any amplitude either SM or NP will have the same $b \to c$ hadronic transition and consequently *CP* violation in these decays can appear only as a kinematic effect in the angular distribution.

Since the tensions with respect to the SM are seen in $\mathscr{R}(D)$ and $\mathscr{R}(D^*)$, i.e. ratios involving tau leptons, the NP is generally considered to contribute in the $b \to c\tau\nu_\tau$ mode. The reconstruction of the τ at LHCb is problematic due to having two missing neutrinos in the final state such that the reconstruction of the angular distribution in this mode is heavily affected by detector resolution effects. Instead, the angular distribution in the $b \to c\mu\nu$ mode is accessible and may be subject to the same NP as the τ mode. In particular, the NP scenarios for which the *CP* asymmetry is nonzero are the right-handed vector current and the interference between pseudoscalar and tensor currents with couplings given by g_R and $g_P g_T^*$, respectively.

The $B^0 \to D^{*-}\mu^+\nu_\mu$ decay is fully described by four kinematic parameters, i.e q^2

and the three helicity angles shown in Fig. 2.15, namely θ_ℓ, θ_D and χ. The analysis presented in this thesis aims to perform a measurement of CP violation in $B^0 \to D^{*-}\mu^+\nu_\mu$ decays by measuring the P-odd part of its angular distribution which consists of terms proportional to $\sin\chi$ or $\sin 2\chi$. Several angular analyses of semileptonic decays are currently being carried out at LHCb, however in order to obtain the required precision on the P-odd part, a dedicated analysis is needed where specific P-odd systematic effects are considered. At LHCb, $D^*\mu$ combinations are reconstructed from the final state particles and since the neutrino is not detectable, its momentum is reconstructed from the B meson line of flight between the primary and secondary vertices.

The LHCb dataset used to reconstruct the $B^0 \to D^{*-}\mu^+\nu_\mu$ decays and the simulation samples used in the analysis are described in Sec. 4.1. Details on the neutrino reconstruction procedure and reconstruction of the helicity angles can be found in Sec. 4.2.

A background template fit is performed to data using templates derived from simulation in order to estimate the various background contributions and determine the signal fraction. This step is important as an estimation of the background fractions are needed in order to assign any systematic uncertainties arising from P-odd effects in backgrounds. The fit procedure is described in Sec. 4.3.

The symmetry properties of the angular distribution are exploited in order to extract the P-odd part and cancel out the P-even part in a model independent way. The method is described in Sec. 4.5. The P-odd part is extracted in 2D bins of $\cos\theta_D$ vs $\cos\theta_\ell$ with $\sin\chi$ or $\sin 2\chi$ weights. The CP asymmetry is proportional to the NP couplings such that a linear fit can be performed to extract the values of the NP couplings. The fit uses NP templates obtained from SM simulation reweighted to the two NP possible cases, i.e. complex values for g_R and $g_P g_T^*$. The NP reweighting is performed using the `Hammer` software. The reweighting procedure and the NP CP asymmetry templates are discussed in Sec. 4.4.

The two sources of systematic uncertainties due to P-odd effects in backgrounds and potential P-odd effects in the track reconstruction efficiency are discussed and estimated in Sec. 4.6.

4.1 Datasets and event selection

This section introduces the data and simulation samples used in this analysis and the event selection procedure used to obtain the final sample with which the CP asymmetry measurement is performed. The data sample consists of the data taken by LHCb during the years 2016, 2017 and 2018 of the Run 2 period of the LHC at a centre of mass energy $\sqrt{s} = 13\,\text{TeV}$. The total dataset corresponds to an integrated luminosity of $5.4\,\text{fb}^{-1}$.

The $B^0 \to D^{*-}\mu^+\nu_\mu$ decay at LHCb is reconstructed as a $D^0\mu^\pm$ combination where an additional $\pi^\pm$ is added to the D^0 to form the D^* candidate. Subsequently, the D^0 meson is reconstructed with the $D^0 \to K^-\pi^+$ mode. The following three orthogonal samples can be obtained from data:

- Correct-sign. This sample consists of $D^{*-}\mu^{+}$ combinations. The particles have the correct charges to be coming from a real B meson decay. This is the data sample used for the measurement of the CP asymmetries.

- True-D^{*}. This sample consists of $D^{*-}\mu^{-}$ combinations. The particles have the same charges so they do not come from a true B meson decay. The sample is used to model combinatorial background where a true D^{*-} and a μ^{+} coming from different decay chains are combined.

- Fake-D^{*}. This sample consists of wrong sign D^{*} combinations, i.e $D^{0}\pi^{-}\mu^{-}$ combinations. The flavor of the D^{0} and the charge of the π^{-} are wrong such that they do not form a legitimate D^{*} meson. The sample is used to model the fake D^{*} combinatorial background where random D^{0} and pions are combined.

An additional sample is derived from data to model the background where another particle, typically a hadron, is misidentified as a muon. This is referred to as the muon misID sample. This sample is obtained by imposing specific particle identification requirements on the muon candidate.

Finally, simulation samples are used to model the signal decay and all the partially reconstructed backgrounds, i.e. other decays with the same final state signature as the signal that may contribute in the data sample. The following sections discuss the reconstruction and selection procedure applied to both data and simulation.

Event selection

The data sample is subject to a series of filtering steps where at each step events are removed based on certain selection criteria designed to maximize the signal yield and remove backgrounds. The three steps of this selection chain are applied in the following order: the online filtering, i.e. the trigger, a central offline filtering referred to as “stripping” and finally an analysis specific offline selection. Each step removes events based on the values of various reconstructed quantities known as variables. A list with all variables used in the selection procedure is given below.

- p. Momentum of the particle track.
- p_{T}. Transverse momentum of the particle track.
- η. Pseudorapidity of the particle track
- `nVeloClusters`. Number of hit clusters in the VELO
- `nITClusters`. Number of hit clusters in the IT.
- `nOTClusters`. Number of hit clusters in the OT.
- `nSPDHits`. Number of hits in the SPD detector.

- `nPV`. Number of primary vertices.
- track χ^2. χ^2 score of the track fitted by the tracking algorithm
- track χ^2/ndf. χ^2 score of the track divided by the number of degrees of freedom
- χ^2_{IP}. χ^2 score of the PV reconstruction with and without the track
- χ^2_{vtx}. χ^2 score of the fitted vertex of a particle.
- χ^2_{vtx}/ndf. χ^2_{vtx} divided by the number of degrees of freedom
- DOCA. Distance of closest approach between two particle tracks.
- DIRA. Cosine of angle between the direction of flight of a particle and a vector that connects the PV and the decay vertex of the particle.
- FD. Flight distance between the primary vertex and the particle decay vertex.
- χ^2_{FD}. χ^2 score of the FD. This variable indicates how well a track can be separated from the PV.
- m_{corr}. Variable defined as $\sqrt{m^2_{D^*\mu} + p^2_\perp} + p_\perp$ where $m_{D^*\mu}$ is the invariant mass of the $D^*\mu$ combination and $p_\perp$ is the $D^*\mu$ momentum transverse to the B^0 flight direction
- GhostProb. Variable which describes the probability of a track to be a ghost track. A ghost track is a random combination of segment tracks in the tracking stations.
- PIDx. The combined log likelihood for the given (x) particle hypothesis with respect to the pion hypothesis. The definition of these variables is given in Eq. 3.8.
- IP. Impact parameter, i.e. distance of a particle track to the primary vertex

Trigger selection

At LHCb each event must pass the trigger decision before being saved for further offline analysis. The trigger consists of the L0, HLT1 and HLT2 levels described in Sec. 3.2.3. The trigger system response can be placed in one of the following categories [153]:

- Triggerred On Signal (TOS). The presence of the signal in the event is sufficient to fire the trigger
- Triggerred Independent of Signal (TIS). The “rest of the event” is sufficient to fire the trigger

- Triggerred on Both (TOB). Neither TIS nor TOS is sufficient, but both are necessary to fire the trigger

This analysis implements a trigger strategy similar to the ones designed for semileptonic analyses with final state muons. The trigger lines used for L0, HLT1 and HLT2 levels are given in Tab. 4.1.

Trigger level	Lines
L0	(D^0 `L0Hadron_TOS` || B^0 `L0Global_TIS`)
HLT1	(D^0 `Hlt1TrackMVA_TOS` || D^0 `Hlt1TwoTrackMVA_TOS`)
HLT2	B^0 `Hlt2XcMuXForTauB2XcMu_TOS`

Table 4.1: Trigger line requirements

At the L0 trigger all events have to pass either the `L0Hadron` line (TOS on the hadronic part of the event) or the `L0Global` requirement (TIS on the whole event). The `L0Global` requires that at least one of the L0 trigger lines (Tab. 3.3) have been passed. L0 trigger requirements for muons are not used in order to not cause any biases in the shapes of their kinematic variables.

Before the HLT1 reconstruction takes place, some cuts are placed to remove events with high occupancy in the tracking stations. These are called Global Event Cuts (GEC) and are given in Tab. 4.2.

`Global Event Cuts`
$50 <$ `nVeloClusters` < 6000
$50 <$ `nITClusters` < 3000
$50 <$ `nOTClusters` < 15000

Table 4.2: Cuts applied before the HLT1 reconstruction

The HLT1 trigger lines `Hlt1TrackMVA` and `Hlt1TwoTrackMVA` select one track or two-track combinations with large momentum and decay vertex displaced from the PV. At least one of the two lines is required to be TOS on the D^0. The requirements of the two HLT1 trigger lines for 2016 conditions are given in Tab. 4.3 and Tab. 4.4. The displacement from the PV requirement is implemented with a multivariate analysis (MVA) classifier. However, in the case of `Hlt1TrackMVA` line, the MVA output is approximated by the analytical formula shown in Tab. 4.3.

The HLT2 trigger makes use of the line `Hlt2XcMuXForTauB2XcMu` which was designed for the muonic $\mathcal{R}(D)$ and $\mathcal{R}(D^*)$ analyses. It selects events with large-p_{T} D^0 detached from the PV and it avoids cuts on the muon kinematics [1]. The selection criteria imposed by the `Hlt2XcMuXForTauB2XcMu` trigger line are given in Tab. 4.5.

In addition, the trigger line `Hlt2XcFakeMuXForTauB2XcMu` is used for the muon misID sample. This trigger line has the same selection as the regular one, except that

---

[1] In these analyses any biases in the shapes of muon kinematics may cause difficulties in distinguishing between the tauonic and muonic modes

`Hlt1TrackMVA`
Input track selections
$p_{\mathrm{T}} > 600\,\mathrm{MeV}$ $p > 3\,\mathrm{GeV}$ track $\chi^2/\mathrm{ndf} < 2.5$
$(p_{\mathrm{T}} > 25\,\mathrm{GeV} \wedge \chi^2_{\mathrm{IP}} > 7.4) \vee [(1\,\mathrm{GeV} < p_{\mathrm{T}} < 25\,\mathrm{GeV}) \wedge \log(\chi^2_{\mathrm{IP}}) > (\frac{1}{p_{\mathrm{T}}[\mathrm{GeV}]-1})^2 + (\frac{1.1}{25\,\mathrm{GeV}})(25\,\mathrm{GeV} - p_{\mathrm{T}}) + \log(7.4)]$

Table 4.3: Requirements of the `Hlt1TrackMVA` trigger line in 2016

`Hlt1TwoTrackMVA`	
Single tracks	$p_{\mathrm{T}} > 500\,\mathrm{MeV}$ $p > 5.0\,\mathrm{GeV}$ track $\chi^2/\mathrm{ndf} < 2.5$ GhostProb < 0.2
Track pair before vertexing	$(p_1 + p_2)_T > 2.0\,\mathrm{GeV}$
Track pair combination	$\chi^2_{\mathrm{vtx}} < 10$ $m_{corr} > 1\,\mathrm{GeV}$ $2 < \eta < 5$ DIRA > 0
MVA requirement	MVA output > 0.95
MVA training variables	χ^2_{vtx} Vertex distance χ^2 $p_{T1} + p_{T2}$ Nr. of tracks with $\chi^2_{\mathrm{IP}} < 16$

Table 4.4: Requirements of the `Hlt1TwoTrackMVA` trigger line in 2016

the muon candidates are required to fail the `isMuon` requirement but still pass the `inMuon` requirement. This means that the muon tracks are required to not have any hits in the muon stations but still be in the muon stations acceptance.

Stripping selection

After the data passed the trigger selection, a central offline selection is performed at LHCb for data reduction purposes. The stripping line `b2D0MuXB2DMuForTauMuLine` is used in this analysis to combine D^0 and μ candidates of both signs and apply cuts on this combination. The selections required for this stripping line are given in Tab. 4.5 and they closely follow the HLT2 trigger selection with additional PID cuts on the final state tracks.

In addition, the stripping line `b2D0MuXFakeB2DMuForTauMuLine` is used to construct the muon misID sample. This stripping line exactly matches the selections in the nominal line except that the μ candidates have to follow the same particle identification requirements as the misID HLT2 line.

Event-level cuts	**Variable**	**Stripping**	**HLT2**
GEC	nSPDHits	< 600	—
PV Cut	nPV	> 0	—
Particle Cuts	**Variable**	**Stripping**	**Hlt2**
μ	χ^2_{IP}	> 16.0	> 16.0
	GhostProb	< 0.5	—
	p	> 3.0 GeV	—
	PIDμ	> -200	—
K, π	p_{T}	> 300 MeV	> 200 MeV
	p	> 2.0 GeV	> 5.0 GeV
	χ^2_{IP}	> 9.0	> 9.0
	GhostProb	< 0.5	—
	K PIDK	> 4	> 2
	π PIDK	< 2	< 4
	$\lvert p_{\mathrm{T}}(\pi)\rvert + \lvert p_{\mathrm{T}}(K)\rvert$	> 2.5 GeV	> 2.5 GeV
	$\geq$1 track p_{T}	—	> 800 MeV
D^0	$\chi^2_{\mathrm{vtx}}/\mathrm{ndf}$	< 4.0	< 10.0
	DIRA	> 0.999	> 0.999
	χ^2_{FD}	> 25.0	> 25.0
	mass window (MeV)	$1790 - 1950$	$1830 - 1910$
	p_{T}	—	> 2 GeV
	Child pair DOCA	—	< 0.10 mm
$D^0\mu$	m	< 10 GeV	< 10.5 GeV
	m (before vertexing)	< 10.2 GeV	< 11 GeV
	$\chi^2_{\mathrm{vtx}}/\mathrm{ndf}$	< 6.0	< 15.0
	DIRA	> 0.999	> 0.999
	DOCA	—	< 0.50 mm
	χ^2_{FD}	—	> 50

Table 4.5: `b2D0MuXB2DMuForTauMuLine` stripping line and `Hlt2XcMuXForTauB2XcMu` trigger line cuts

Offline selection

An analysis specific offline selection is implemented in order to suppress various backgrounds. The offline selection follows the one in the muonic $\mathscr{R}(D^*)$ analysis [67] and it is shown in Tab. 4.6. In the $\mathscr{R}(D^*)$ analysis, complex MVA classifiers, such as isolation Boosted Decision Trees (BDTs) are trained and their response is cut on to reject specific backgrounds. In this analysis, these procedures are avoided since they may lead to parity-odd systematic effects that could be difficult to control.

Particle	Variable	Selection
μ	p	$<$ 100 GeV
	PIDμ	$>$ 2
	$\log_{10}(1 - \vec{p}_\mu \cdot \vec{p}_i / \lvert p_\mu \rvert p_i \rvert)_{i=K,\pi,\pi_S}$	$>$ -5
D^0	p_T	$>$ 2 GeV
	χ^2_IP	$>$ 9
	lnIP	$>$ -3.5
	mass window	1842-1888 MeV
D^*	$\lvert\Delta m$-$\Delta m_{PDG}\rvert$	$<$ 2.5 MeV
	π_S GhostProb	$<$ 0.25
$D^0\mu$	DIRA	$>$ 0.999
$D^*\mu$	mass window	$<$ 5280 MeV
	DIRA	$>$ 0.999
	d_{XY} (transverse FD)	$<$ 7 mm
	χ^2_vtx/ndf	$<$ 6

Table 4.6: Offline selection

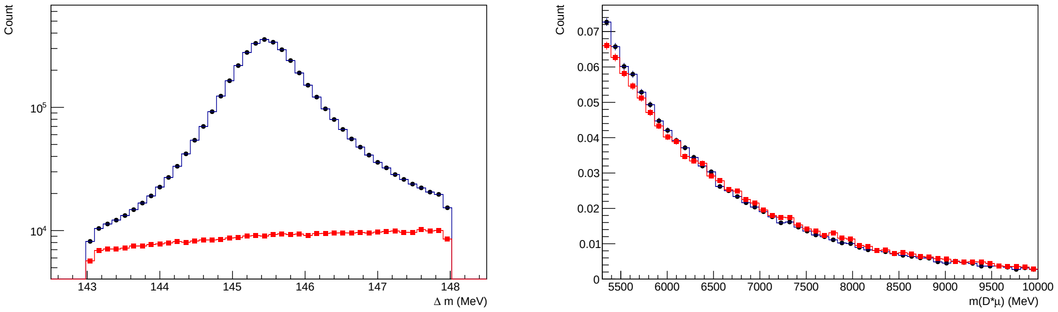

Figure 4.1: Left: Δm variable distribution. Correct sign data in black and wrong sign data in red. The sidebands of the distribution are cut away around the signal D^* peak. Right: Upper side-band of the $D^*\mu$ mass variable. Correct sign data in black and same sign data in red.

The cut on the Δm variable is meant to reduce the contribution of the fake D^* combinatorial background by removing the events that are outside of the signal region. Fig.

4.1 (left) shows the Δm distribution for the correct sign and wrong sign data samples. The wrong sign events form the fake D^* combinatorial background sample which is further used in the analysis to check whether these events introduce any bias in the CP-violating observables. The upper side band of the $D^*\mu$ mass variable is shown in Fig. 4.1 (right) for correct sign and same sign data. In this region there are no true B meson decays and only combinatorial background contributes. The plot shows a good agreement between the correct sign combinatorial and same sign combinatorial which is evidence that the two samples are kinematically equivalent. This motivates the use of the same sign data sample to model combinatorial background in the signal region.

The final data sample of the combined 2016, 2017 and 2018 years after all selection criteria have been passed consists of 2748185 events and this is the sample that will be used for the measurement of the CP-violating observables.

Simulation samples

The $B^0 \to D^{*-}\mu^+\nu_\mu$ signal and all physical backgrounds are modelled using Monte Carlo simulation. The MC sample for a specific decay is identified by an unique number called the `EvtType`. The MC is produced at in both `MagUp` and `MagDown` configurations of the magnet.

After the events are generated a set of loose cuts is applied to discard events that would not pass the detection tresholds or would not be in the geometric acceptance of the detector. These are referred to as generator level cuts and their efficiencies are available and come together with each MC sample. The generator cuts are given in Tab. 4.7. In addition to the generator level selection, before the events are saved on disk, another step of selection called *MC filtering* is performed on the MC samples in order to reduce the storage size. The selection used by the filtering closely resembles the stripping selection such that events that would otherwise not pass the stripping requirements are not saved on disk.

Particle	Variable	Selection
K,π	p_x/p_z	-0.38-0.38
	p_y/p_z	-0.28-0.28
	θ	> 0.01 rad
	p_T	> 250 MeV
μ	p_x/p_z	-0.38-0.38
	p_y/p_z	-0.28-0.28
	θ	> 0.01 rad
	p	> 2950 MeV
D^0	$\lvert p(\pi)\rvert + \lvert p(K)\rvert$	> 15 GeV
	$\lvert p_\mathrm{T}(\pi)\rvert + \lvert p_\mathrm{T}(K)\rvert$	> 2450 MeV

Table 4.7: MC generator level cuts

A procedure called *truth matching* is performed on the final state particles in the

MC samples to ensure that the reconstructed particles are matched to the true generated ones. This procedure helps remove any misidentified tracks, ghost tracks and combinatorial backgrounds.

A list of all MC samples used in this analysis is given in Tab. 4.8. The numbers of events saved on disk, i.e. passing generator and filter cuts are reported separately for the three years. The samples are either single modes such as $B^0 \to D^{*-}\mu^+\nu_\mu$ or $B^0 \to D^{*-}\tau^+\nu_\tau$ or so-called cocktail modes such as the D^{**} states or the double charm decays. The cocktail modes consist of several decay modes with the appropriate relative branching fractions. More details about the composition of each cocktail sample can be found in Sec. 4.3 and in [154].

Sample	**EvtType**	2016	2017	2018
$B^0 \to D^{*-}\mu^+\nu_\mu$	11574021	85470057	81975745	103168826
$B^0 \to D^{*-}\tau^+\nu_\tau$	11574011	17217664	18008069	25341935
$B^0 \to (D^{**-} \to D^{*-}\pi^0)\mu^+\nu_\mu$	11874430	46653556	45469066	58082278
$B^0 \to (D^{**-} \to D^{*-}\pi^0)\tau^+\nu_\tau$	11874440	375581	519245	561800
$B^+ \to (D^{**0} \to D^{*-}\pi^+)\mu^+\nu_\mu$	12873450	37417148	117729837	48051754
$B^+ \to (D^{**0} \to D^{*-}\pi^+)\tau^+\nu_\tau$	12873460	618529	598526	744330
$B^+ \to D^{**0}[\to D^{*+}\pi^0\pi^+]\mu^+\nu_\mu$	12675402	5560586	4739776	6162695
$B^0 \to D^{**-}[\to D^{*-}\pi^+\pi^-]\mu^+\nu_\mu$	11676012	4824507	4834264	8353204
$B_s^0 \to D_s^{**-}\mu^+\nu_\mu$	13674000	1498067	1531966	2070074
$B^0 \to D^{*-}D_{(s)}^+X, D_{(s)}^+ \to X\mu^+\nu_\mu$	11894610	16188308	13480119	16837410
$B^0 \to D^{*-}D_{(s)}^+X, D_{(s)}^+ \to X\tau^+\nu_\tau$	11894210	1678170	1283823	1283823
$B^+ \to D^{*-}D_{(s)}^+X, D_{(s)}^+ \to X\mu^+\nu_\mu$	12895400	7000178	7459109	6798676
$B^+ \to D^{*-}D_{(s)}^+X, D_{(s)}^+ \to X\tau^+\nu_\tau$	12895000	899320	1555844	1282503

Table 4.8: Tracker-Only MC samples. The numbers shown are the numbers of events saved on disk, i.e. events passing generator and filtering cuts.

The MC samples used in this analysis were generated for the $\mathcal{R}(D)$ and $\mathcal{R}(D^*)$ analyses where the dominating systematic uncertainties are due to the statistics of the MC samples. For this reason, very large numbers of events, especially for the signal $B^0 \to D^{*-}\mu^+\nu_\mu$ sample, are generated. In order to reduce the time of the simulation by a factor of ~ 8, so called Tracker-Only (TO) MC samples were produced. For the production of the samples, only the tracking system was simulated with `Geant4` while completely removing the simulated response of all other subdetectors such as the RICH system or the calorimeters. As a consequence, trigger and PID information is missing in the TO MC samples. In order to have the MC aligned with data in terms of event selection, the trigger and PID responses have to be emulated offline.

The trigger emulation is implemented with dedicated software tools developed for the TO samples used in this analysis. More details about the tools can be found in [155]. The tools are based on the procedures given in [156].

The L0 trigger lines used in the analysis are the `L0Hadron` TOS on the D^0 and the `L0Global` TIS on the B^0 candidate. The `L0Hadron` line is triggered if the transverse energy passes a certain threshold, as shown in Tab. 3.3. The emulation of the `L0Hadron` line is realized using an `XGBoost` regressor to predict the ratio of events passing this line. A set of variables related to E_{T} and available in the TO MC, as well as the trigger response from a fully simulated sample are used to train the regressor. This results in a set of weights that can be then applied to the TO samples. In the case of the `L0Global` TIS decision, since the trigger decision is independent of the tracks that form the candidate and there are many more particle tracks per event than the final state tracks of the signal decay, it can be argued that the rest of event is the same for all B meson decays. Therefore, the efficiency of the `L0Global` TIS decision can be measured in data for a particular B meson decay and can then be ported to the TO samples. This efficiency was measured with a $B \to J/\psi K$ data sample in bins of kinematic variables p_{T} and p_z of the B. A weight for each event in the TO is assigned based on which B^0 p_{T}-p_z bin it falls in. The true information on the p_{T} and p_z is used.

The `Hlt1TrackMVA` and `Hlt1TwoTrackMVA` trigger lines are required to be TOS on the D^0 or its daughters. The candidates have to pass a set of requirements on the single and two-track combinations and the score of the MVA classifier has to pass a threshold, as shown in Tab. 4.3 and 4.4. All the variables needed for the selection and training of the MVA are available in the TO simulation [2] such that the response of the HLT1 trigger can be emulated by applying all the selection offline. The `Hlt2XcMuXForTauB2XcMu` trigger line is emulated by directly applying the selection shown in Tab. 4.5.

The PID selection used in this analysis consists of the two cuts on the K PIDK and π PIDK variables in the stripping and the μ PIDμ requirement in the offline selection. Their purpose is to remove events with misidentified final state particles. These PID variables are not present in the TO simulation and need to be emulated offline. The `PIDGen2` package [157] is used to generate the PID variables needed for the selection. The `PIDGen2` tool uses sWeighted[3] calibration data samples to generate a 4D PDF in the PID variable, two kinematic variables p_{T} and η, and one multiplicity variable n_{Tracks}. This 4D PDF is then smeared using a Gaussian filter. Finally, for each MC event in $(p_{\mathrm{T}}, \eta, n_{Tracks})$ the PID variable is drawn from the 4D PDF, this approach is also referred to as PID resampling.

4.2 Neutrino reconstruction

The decay studied in this analysis, $B^0 \to D^{*-}\mu^+\nu_\mu$, has a neutrino in the final state that can not be detected at LHCb. In order to reconstruct the kinematic quantities which are essential for this analysis, i.e. the three angles described in Sec. 2.2.3.1 and q^2, as well as other important variables needed for the template fit described in Sec. 4.3, some approximation on the neutrino momentum has to be made. There are two approaches to approximate the momentum of the undetected neutrino, the first one

---

[2] These variables are extracted using a specific tool in the event reconstruction during `DaVinci`

[3] The sWeight method is based on the sPlot technique [158] and is a way to obtain the unfolded signal distribution in a control variable by using other independent discriminating variables to remove the background.

is based on an approximation of the B meson rest frame, while the second one makes use of topological information to solve a quadratic equation and obtain the neutrino momentum up to a two-fold ambiguity.

4.2.1 Rest frame approximation

In the rest frame approximation, in order to estimate the four-momentum of the B meson, the following assumption is made: the proper velocity in the lab frame ($\gamma\beta$) of the B meson along the z-axis (beam axis) is equal to the proper velocity of the partially reconstructed B meson, i.e. $D^*\mu$ combination, along the z-axis. This approximation is valid because of the large boost of the B mesons along the z-axis in the LHCb detector which is much larger than the boost of the B decay products in the B rest frame. Thus, the following relation can be written

$$(p_B)_z = \frac{m_B}{m_{D^*\mu}}(p_{D^*\mu})_z, \tag{4.1}$$

where m_B is the (PDG) mass of the B meson and $m_{D^*\mu}$ and $p_{D^*\mu}$ are the mass and momentum of the reconstructed $D^*\mu$ system. Using information provided by the VELO subdetector at LHCb, the B meson direction vector can be computed as

$$\begin{aligned} B_{DX} &= (SV)_x - (PV)_x, \\ B_{DY} &= (SV)_y - (PV)_y, \\ B_{DZ} &= (SV)_z - (PV)_z, \end{aligned} \tag{4.2}$$

where $(PV)_{x,y,z}$ and $(SV)_{x,y,z}$ are the 3D coordinates of the primary vertex and B decay vertex (secondary vertex), respectively, as measured by VELO. The topology of the decay is illustrated in Fig. 4.2 where the red dotted line represents the direction of the B meson determined by the measured positions of the PV and SV.

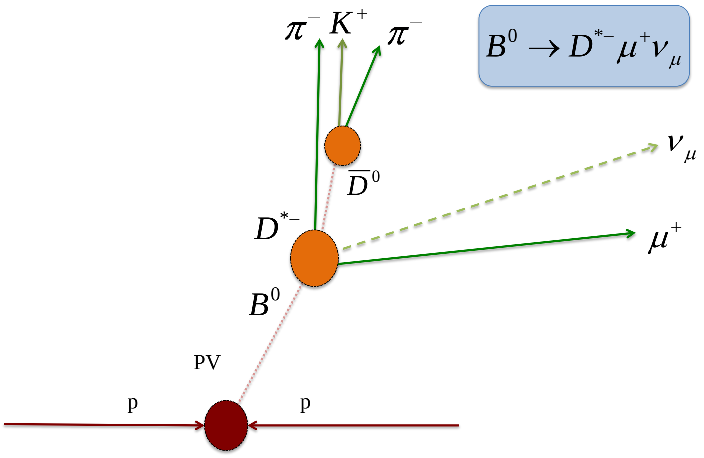

Figure 4.2: Topology of the signal $B^0 \to D^{*-}\mu^+\nu_\mu$ decay. The coordinates of the PV and of the SV, i.e. B decay vertex are measured by VELO.

The angles that the B direction makes with the X, Y, Z axes are given by

$$\begin{aligned}\cos(\alpha_x) &= \frac{B_{DX}}{|\vec{B_D}|},\\ \cos(\alpha_y) &= \frac{B_{DY}}{|\vec{B_D}|},\\ \cos(\alpha_z) &= \frac{B_{DZ}}{|\vec{B_D}|}.\end{aligned} \tag{4.3}$$

The absolute value of the B meson three-momentum can be expressed as

$$p_B = \frac{m_B}{m_{D^*\mu}}(p_{D^*\mu})_z\sqrt{1+\tan^2(\alpha_z)}. \tag{4.4}$$

The components of the B meson four-momentum can then be expressed as

$$\begin{aligned}(p_B)_x &= p_B\cos(\alpha_x),\\ (p_B)_y &= p_B\cos(\alpha_y),\\ (p_B)_z &= p_B\cos(\alpha_z),\\ (p_B)_E &= \sqrt{m_B^2+(p_B)_x^2+(p_B)_y^2+(p_B)_z^2}.\end{aligned} \tag{4.5}$$

A single estimate for the four-momentum of the B meson, and consequently of the neutrino, is thus obtained. This approach is used to compute the m^2_{miss} and E^*_μ variables used in the template fit described in Sec. 4.3.

4.2.2 Quadratic equation approach

In the quadratic equation approach, the B meson momentum is estimated using the topological information of the position of the primary and secondary vertices up to a two-fold ambiguity [159]. The absolute value of the B meson momentum can be computed in terms of kinematic variables of the $B^0 \to D^{*-}\mu^+\nu_\mu$ candidate according to the following equation

$$p_B = \frac{\left(m_B^2 + m_{D^*\mu}^2\right) p_{D^*\mu}\cos\theta \pm E_{D^*\mu}\sqrt{(m_B^2 - m_{D^*\mu}^2)^2 - 4m_B^2 p_{D^*\mu}^2 \sin^2\theta}}{2(m_{D^*\mu}^2 + p_{D^*\mu}^2 \sin^2\theta)}, \tag{4.6}$$

where $m_{D^*\mu}$, $p_{D^*\mu}$ and $E_{D^*\mu}$ are the invariant mass, momentum, and energy of the reconstructed $D^{*+}\mu^-$ system , m_B is the mass of the B meson, and θ is the angle between the direction of the B meson and the $D^*\mu$ system. The angle θ is given by

$$\cos\theta = \frac{\vec{B_D} \cdot \vec{p_{D^*\mu}}}{|\vec{B_D}||\vec{p_{D^*\mu}}|}, \tag{4.7}$$

where $\vec{B_D}$ is the vector defined in Eq. 4.2. The events where $\cos\theta < 0$, i.e. $\theta > 90°$, are unphysical since the $p_{D^*\mu}$ and B_D point in opposite directions and these events are removed. We note that Eq. 4.6 yields two solutions which are referred to as solution "+" and solution "−". Because of detector resolution effects, in about 28 % of events the expression under the square root in Eq. 4.6 becomes negative. In those cases, the closest solution to the "physical" one is obtained by setting the square root to zero. These events are included in both solutions. In this analysis, by always choosing either solution "+" or solution "-" the correct choice rate would be 50% if there would be no inefficiencies in reconstruction. However, since efficiency in general depends on the momentum of the decay products (which in turn are different for the neutrino flying forward or backward, i.e. solution "−" and solution "+") the ratio can differ from 50%. Several approaches to increase this rate can be used, such as using a multivariate regression algorithm based on the decay flight information [160].

Once the absolute value p_B is computed, the four-momentum of the B meson is calculated using the knowledge of its flight direction vector, i.e. Eqs. 4.2 - 4.5. Finally, the kinematic quantities of interest $q^2, \cos\theta_\ell, \cos\theta_D$ and χ are reconstructed for both solutions $p_B^\pm$. The residual distributions of the four kinematic variables for the two solutions are shown in Fig. 4.3.

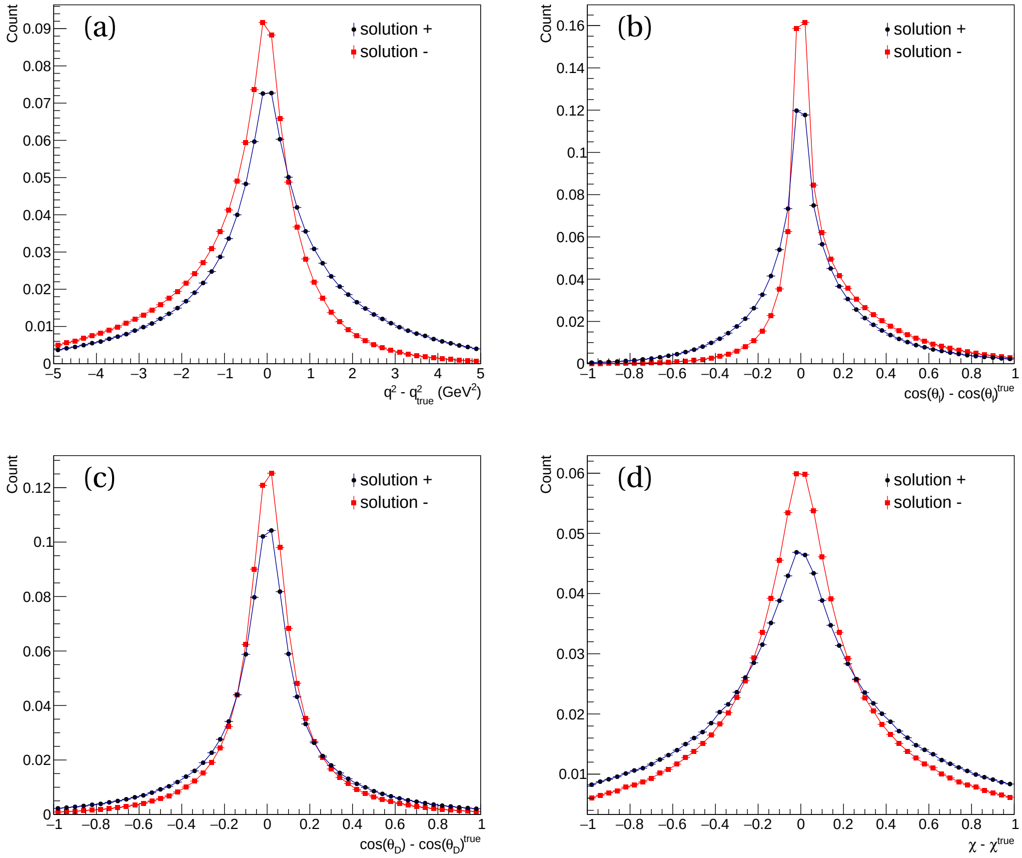

Figure 4.3: Residual distributions for the two solutions of the reconstructed $\overline{B}^0 \to D^{*+}\mu^-\overline{\nu}_\mu$ kinematic parameters from MC simulation (a) q^2, (b) θ_ℓ, (c) θ_D and (d) χ

It is clear that solution "-" offers a better resolution than solution "+". The reason for this can be understood from the following argument. Solution "+" corresponds to the case where the muon and the neutrino fly in the same direction, while solution "-" corresponds to the case where the muon and neutrino fly in opposite directions. Effectively, the resolution function in this case is a mixture of the "true" and "fake" resolution functions. The ratio of this mixture depends on the reconstruction efficiency of solutions "+" and "-". But the efficiency of the two solutions (when they are the true one) is different due to different kinematics. Therefore, the resolutions of the two solutions are different and it appears to be better for solution "-" such that in all subsequent studies only solution "-" is used.

After the first approximation of the B meson four-momentum is obtained, a kinematic refit of the track parameters is performed in order to improve the resolution on the kinematic variables. This refit is done with `DecayTreeFitter` [161] [4] which is an algorithm that can provide better estimates for the track parameters of the final state

---

[4] `DecayTreeFitter` is a LHCb specific tool based on code originally developed at BaBar

particles by imposing hypothesis-driven mass constraints and/or vertex constraints.

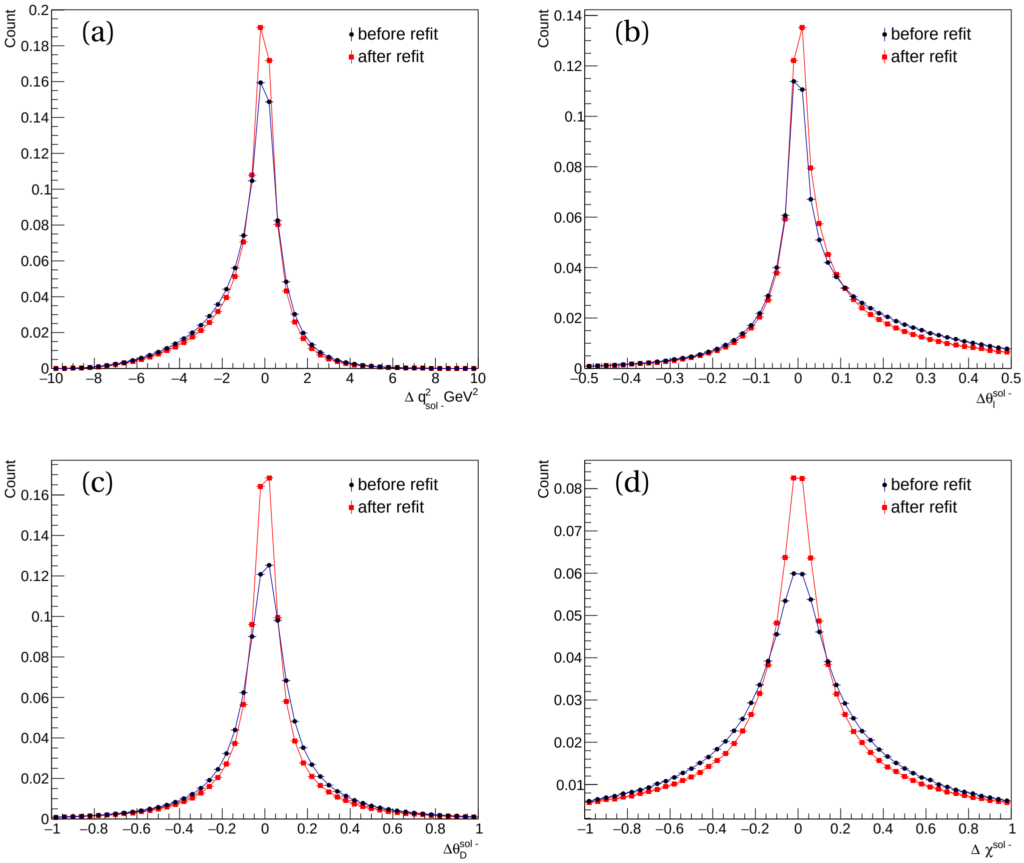

Figure 4.4: Residual distributions for solution "-" of the reconstructed $\overline{B}^0 \to D^{*+}\mu^-\overline{\nu}_\mu$ decay parameters before and after the kinematic refit (a) q^2, (b) θ_ℓ, (c) θ_D and (d) χ

By knowing the full decay chain that leads to the final state, the additional information that comes with this hypothesis (mass or vertex constraints) can help to provide a better estimate on the final state four-momenta. In this analysis, `DecayTreeFitter` is used to perform a full kinematic refit of the $B^0 \to D^{*-}\mu^+\nu_\mu$ decay tree that includes all possible kinematic information (including the missing neutrino with first momentum estimation from Eq. 4.6) and all correlations. The neutrino, D^0 meson and B^0 meson masses are constrained to their PDG values. Fig. 4.4 shows the residual distributions of the four kinematic parameters before and after the kinematic refit obtained using MC simulation. The effect of the kinematic refit on improving the resolution is clearly visible, especially in the θ_D and χ variables.

The distributions of the four kinematic variables $q^2, \cos\theta_\ell, \cos\theta_D$ and χ for solution "-" are shown in Fig. 4.5. Since the true information is accessible in simulation, the 2D correlations between the true variables and the reconstructed variables after the kinematic refit are shown in Fig. 4.6. A high correlation is visible in all four kinematic variables.

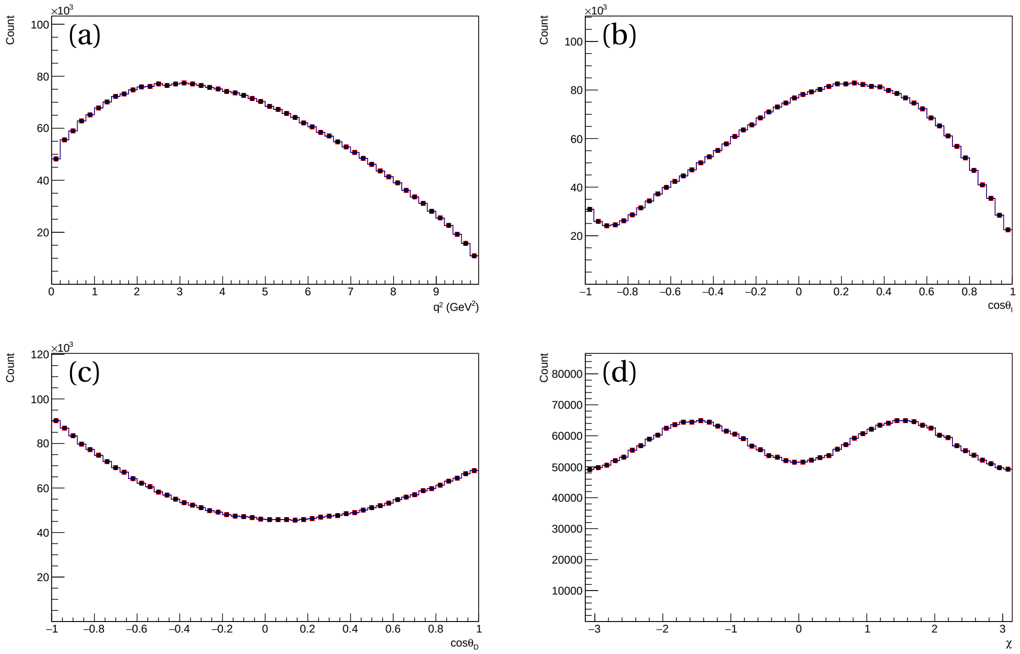

Figure 4.5: Distributions of the kinematic variables for solution “-” after the kinematic refit (a) q^2, (b) $\cos\theta_\ell$, (c) $\cos\theta_D$ and (d) χ.

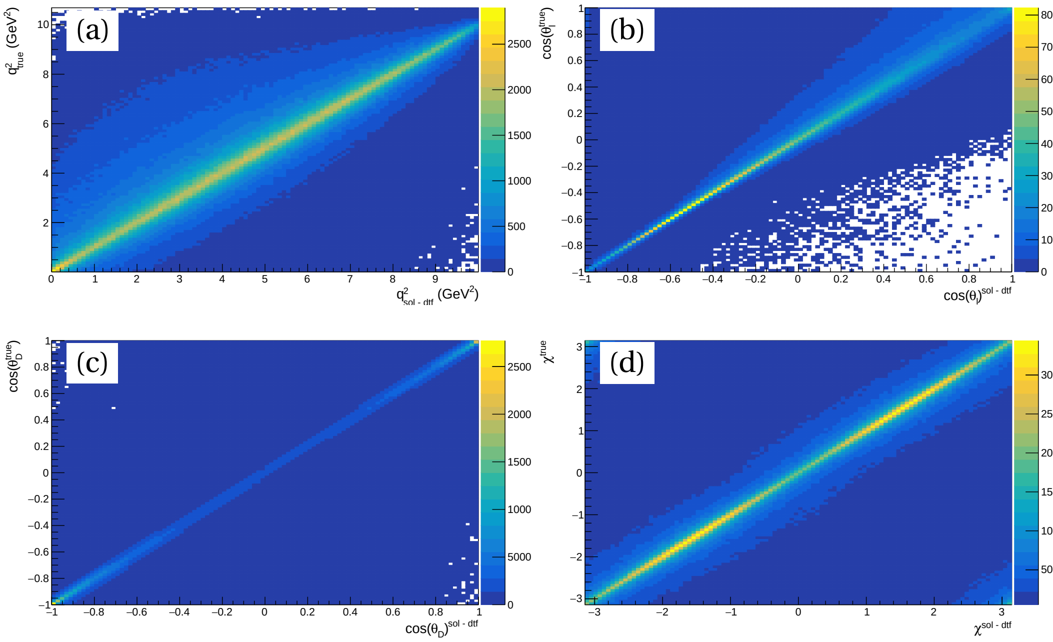

Figure 4.6: Correlations for solution “-” between the true and the reconstructed $B^0 \to D^{*-}\mu^+\nu_\mu$ decay parameters after the kinematic refit (a) q^2, (b) $\cos\theta_\ell$, (c) $\cos\theta_D$ and (d) χ. Lighter colors indicate larger density of events.

4.3 Background template fit

A template fit is implemented in the data sample to estimate the fraction of signal decays and the contributions of various backgrounds with the same final state signature as the $B^0 \to D^{*-}\mu^+\nu_\mu$ signal. The partially reconstructed backgrounds can be split in two categories: semileptonic and double charm backgrounds. Semileptonic backgrounds consist of decays of other B mesons that result in a D^{*-} and a primary μ^+ or a secondary muon coming from a $\tau^+ \to \mu^+\nu_\mu\overline{\nu}_\tau$ decay. Double charm backgrounds are B meson decays to a D^{*-} and another charm hadron that decays semileptonically. The templates of the signal and all physics backgrounds are constructed from MC simulations of each process. A third background category exists due to LHCb reconstruction effects for which the templates are constructed in a data-driven way: combinatorial background and background with hadrons misidentified as muons. A description of all backgrounds is given in the following sections.

The fit is a binned extended maximum likelihood template fit and is implemented using the `RooFit` data modelling package [162]. The templates are three-dimensional histograms in the variables q^2, m^2_{miss} and E^*_μ. These kinematic variables were chosen as they have a large discriminating power between signal and various background processes [163]. The three variables are all defined in the B meson rest frame and their definitions are the following

- $q^2 = (p_B - p_{D^*})^2$ is the invariant mass squared of the lepton system
- $m^2_{miss} = (p_B - p_{D^*} - p_\mu)^2$ is the squared missing mass due to the missing neutrino
- E^*_μ is the muon energy in the B rest frame

where p_B, p_{D^*} and p_μ are the four momenta of the B meson, of the D^* meson and of the muon, respectively. The binning schemes used in the fit are given in Tab.4.9

Variable	Nr of bins	Range
q^2 (GeV^2)	4	[0, 10]
m^2_{miss} (GeV^2)	10	[-2, 8]
E^*_μ (GeV)	10	[0.2, 2.2]

Table 4.9: Bin schemes of the three variables used in the fit

Since the B meson rest frame can not be exactly reconstructed at LHCb, the approximation methods described in Sec. 4.2 are used to compute these kinematic variables. In particular, E^*_μ, m^2_{miss} are computed using the rest frame approximation while the q^2 variable is computed using the quadratic equation approach and solution “-” is used. Most of the templates are derived from simulation, while only three are derived from data.

For most of the simulation derived templates, knowledge on the branching ratios is used to constrain their contribution in the fit relative to the signal mode. Their fraction with respect to signal is constrained via a Gaussian added to the likelihood centered around the expected fraction which is given by

$$f_{\mathrm{bkg}}^{\mathrm{exp}} = \frac{N_{\mathrm{bkg}}}{N_{\mathrm{sig}}} = \frac{\mathscr{B}_{\mathrm{bkg}}\epsilon_{\mathrm{bkg}}}{\mathscr{B}_{\mathrm{sig}}\epsilon_{\mathrm{sig}}}, \tag{4.8}$$

where $\mathscr{B}_{\mathrm{bkg,\,sig}}$ are the branching ratios and $\epsilon_{\mathrm{bkg,\,sig}}$ are the efficiencies taken from simulation of the background and signal modes, respectively. The next sections introduce all the templates included in the fit and their constraints. The projections of the templates for the signal and largest expected backgrounds are also shown.

4.3.1 Simulation derived templates

Signal

The signal template consists of reconstructed $B^0 \to D^{*-}\mu^+\nu_\mu$ decays. The three projections are shown in Fig. 4.7. The signal yield is unconstrained and allowed to float freely in the fit.

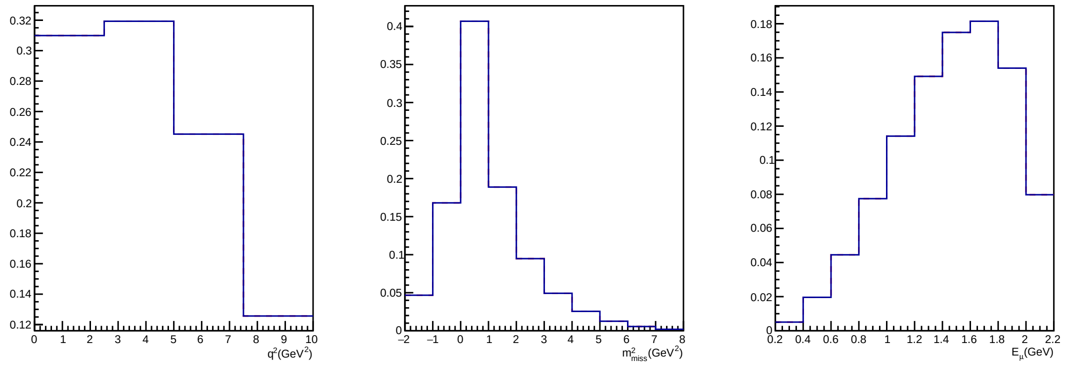

Figure 4.7: Projections of the 3D template in q^2, m^2_{miss} and E^*_μ for the $B^0 \to D^{*-}\mu^+\nu_\mu$ signal sample

Feed down from $B^0 \to D^{*-}\tau^+\nu_\tau$

The relative contribution of this background is constrained by its relative branching ratio and efficiency correction factor, introduced in the total PDF as a Gaussian constraint. The reported branching ratio is $\mathscr{B}(B^0 \to D^*\tau\nu) = (1.58 \pm 0.09)\%$ where the $\mathscr{B}(\tau \to \mu\nu\nu) = (17.39 \pm 0.04)\%$ needs to also be taken into account [164]. The resulting combined branching ratio used as a constraint in the fit is $(2.74 \pm 0.15) \times 10^{-3}$. The expected size of this background is about 5% of the signal mode. The projections of the 3D template for this mode are shown in Fig. 4.8

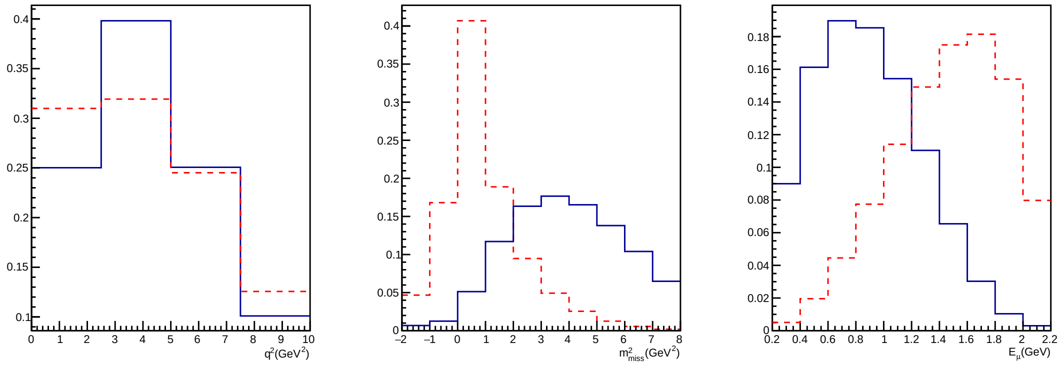

Figure 4.8: Projections of the 3D template in q^2, m^2_{miss} and E^*_μ for the $B^0 \to D^{*-}\tau^+\nu_\tau$ sample in blue. The signal projections are shown in red for comparison

Feed down from $B^0 \to D^{**-}\mu^+\nu_\mu$

This template consists of $B^0 \to D^{**-}[\to D^{*-}\pi^0]\mu^+\nu_\mu$ decays where the D^{*-} candidate comes from the decay of a charged excited charm meson resonance state. There are three dominant resonances that can contribute, namely $D_1(2420)^-$, $D_1'(2430)^-$ and $D_2^*(2460)^-$, which are all included in a single template. The projections of the 3D template are shown in Fig. 4.9.

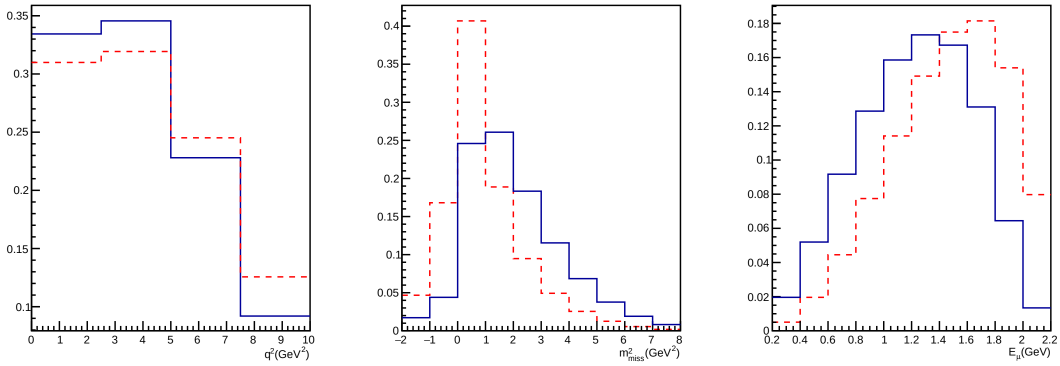

Figure 4.9: Projections of the 3D template in q^2, m^2_{miss} and E^*_μ for the $B^0 \to D^{**-}\mu^+\nu_\mu$ sample in blue. The signal projections are shown in red for comparison.

The relative contribution of this background is constrained by the sum of branching fractions of the three D^{**} modes. The separate branching ratios are given in Tab. 4.10. However, these branching ratios are given as the product $\mathscr{B}(B^0 \to D^{**-}\ell^+\nu_\ell) \times \mathscr{B}(D^{**-} \to \overline{D}^{*0}\pi^-)$. In order to correct this branching ratio, the following exact isospin symmetry relationship is used: $(\mathscr{B}(D^{**-} \to D^{*-}\pi^0))/(\mathscr{B}(D^{**0} \to D^{*-}\pi^+)) = 1/2$. Therefore, the branching ratios are taken as half of the values reported in Table

4.10, such that the total branching ratio used as a Gaussian constraint is $(3.29 \pm 0.47) \times 10^{-3}$. The size of this background is expected to be about 6.5% of the signal mode.

Decay	$\mathscr{B}(10^{-3})$	$\sigma(10^{-3})$
$B^0 \to D_1(2420)^- \mu^+ \nu_\mu$	2.80	0.28
$B^0 \to D_1^{'}(2430)^- \mu^+ \nu_\mu$	3.1	0.9
$B^0 \to D_2^*(2460)^- \mu^+ \nu_\mu$	0.68	0.12

Table 4.10: Semileptonic branching ratios of B^0 to excited charm states [164]

Feed down from $B^+ \to D^{**0} \mu^+ \nu_\mu$

This template consists of $B^+ \to D^{**0}[\to D^{*-}\pi^+]\mu^+\nu_\mu$ decays where the D^{*-} candidate comes from the decay of a neutral excited charm meson resonance state. There are three resonance that can contribute, namely $D_1(2420)^0$, $D_1'(2430)^0$ and $D*_2(2460)^0$, which are all included in a single template. The projections of the 3D template are shown in Fig. 4.10.

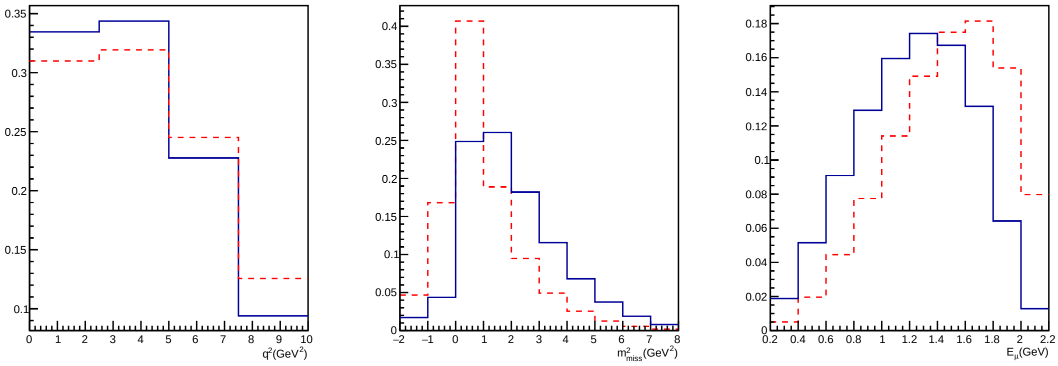

Figure 4.10: Projections of the 3D template in q^2, m^2_{miss} and E^*_μ for the $B^+ \to D^{**0}\mu^+\nu_\mu$ sample in blue. The signal projections are shown in red for comparison.

The contribution of this background is treated in the same way as for the $B^0 \to D^{**-}\mu^+\nu_\mu$ mode. The branching ratios of the three modes are given in Table 4.11. In this case, the branching ratios do not need to be adjusted since they are reported as the product $\mathscr{B}(B^+ \to D^{**0}\mu^+\nu_\mu) \times \mathscr{B}(D^{**0} \to D^{*+}\pi^-)$.

The total branching ratio used to constrain this background is $(6.74 \pm 0.67) \times 10^{-3}$. This size of this background is expected to be about 13% of the signal mode.

Feed down from $B^0 \to D^{**-}\tau^+\nu_\tau$ and $B^+ \to D^{**0}\tau^+\nu_\tau$

The contributions of these backgrounds are constrained to be the same as the corresponding muon modes times an overall factor composed of the $\mathscr{B}(\tau \to \mu\nu\nu) =$

Decay	$\mathscr{B}(10^{-3})$	$\sigma(10^{-3})$
$B^+ \to D_1(2420)^0\mu^+\nu_\mu$	3.03	0.20
$B^+ \to D_1^{'}(2430)^0\mu^+\nu_\mu$	2.7	0.6
$B^+ \to D_2^*(2460)^0\mu^+\nu_\mu$	1.01	0.24

Table 4.11: Semileptonic branching ratios of B^+ to excited charm states [164]

$(17.39 \pm 0.04)\%$ and a phase space factor of 0.3 [165]. Thus, the resulting branching ratios used to constrain these modes are $(1.71 \pm 0.24) \times 10^{-4}$ and $(3.51 \pm 0.11) \times 10^{-4}$. The sizes of these backgrounds are expected to be about 0.3% and 0.7% of the signal mode, respectively.

Higher D^{**} states

This background is due to B decays to heavier $D^*\pi\pi$ resonances rather than $D^*\pi$. Two templates corresponding to $B^0 \to D^{**-}[\to D^{*-}\pi^+\pi^-]\mu^+\nu_\mu$ and $B^+ \to D^{**0}[\to D^{*+}\pi^0\pi^+]\mu^+\nu_\mu$ decays are included in the fit. Since the branching ratios of these higher states are not measured, the contributions of these backgrounds are allowed to float freely.

Feed down from $B_s^0 \to D_s^{**-}\mu^+\nu_\mu$

This background is composed of the two following modes: $B_s^0 \to D_{s1}^{-'}\mu^+\nu_\mu$ and $B_s^0 \to D_{s2}^{*-}\mu^+\nu_\mu$. The following branching ratio was measured to be $\mathscr{B}(B_s^0 \to D_{s1}(2536)^-\mu\nu) \times \mathscr{B}(D_{s1}^- \to D^{*-}K_S^0) = (2.7 \pm 0.7) \times 10^{-3}$ [164]. This branching ratio is corrected by the fragmentation ratio f_s/f_d [166]. The branching ratio of decays to the D_{s2}^{*+} mode is adjusted by an additional factor of 0.3 taken from the ratio of branching fractions of B^0 to D_1^- and D_2^{*-}. The total branching fraction used to constrain this background is $(9.1 \pm 2.3) \times 10^{-4}$. The size of this background is expected to be about 2% of the signal mode.

Double charm with secondary muon $B^0 \to D^{*-}D_{(s)}^+X, D_{(s)}^+ \to X\mu^+\nu_\mu$

This template consists of a cocktail of B^0 decay modes to a D^{*-} and another ground state or excited charm meson (and possibly another particle), where the charm meson decays semileptonically. The projections of the 3D template are shown in Fig. 4.11.

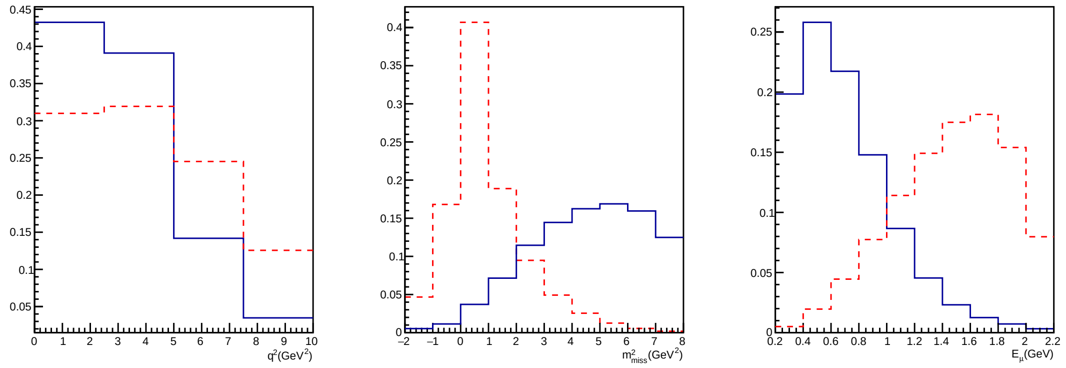

Figure 4.11: Projections of the 3D template in q^2, m^2_{miss} and E^*_μ for the $B^0 \to D^{*-}D^+_{(s)}X, D^+_{(s)} \to X\mu^+\nu_\mu$ sample in blue. The signal projections are shown in red for comparison.

The leading modes present in this cocktail along with the appropriate subsequent semileptonic branching ratios are reported in in Tab. 4.12. In particular, for the secondary semileptonic decays, the branching ratio $\mathscr{B}(D^0 \to X^-\mu^+\nu_\mu)$ is taken as the sum of the two leading decay modes present in the cocktail simulation where X^- is either a K^- or a K^{*-} giving a value of $5.30 \pm 0.24\%$. In the case of $\mathscr{B}(D^+_s \to X^0\mu^+\nu_\mu)$ the branching ratio is obtained as the sum of the leading decay modes where X^0 can be a ϕ^0, η^0 or η'^0 particle with a value of $5.40 \pm 0.87\%$.

The secondary semileptonic branching ratios $\mathscr{B}(D^+_s \to X^0\mu^+\nu_\mu)$ and $\mathscr{B}(D^0 \to X^-\mu^+\nu_\mu)$ are taken as the sum of their leading modes. The total branching ratio used to constrain this background is $(2.46 \pm 0.22) \times 10^{-3}$. The size of this background is expected to be about 5% of the signal mode.

Decay	Additional $\mathscr{B}$	Final $\mathscr{B}$
$B^0 \to D^{*-}D^{*+}_s$ $(1.77 \pm 0.14)\%$	$\mathscr{B}(D^{*+}_s \to D^+_s\pi^0/\gamma) \times \mathscr{B}(D^+_s \to X^0\mu^+\nu_\mu)$ $1 \times (5.40 \pm 0.87)\%$	$(9.56 \pm 1.72) \times 10^{-4}$
$B^0 \to D^{*-}D^{*0}K^+$ $(1.06 \pm 0.09)\%$	$\mathscr{B}(D^{*0} \to D^0\pi^0/\gamma) \times B(D^0 \to X^-\mu^+\nu_\mu)$ $1 \times (5.30 \pm 0.24)\%$	$(5.62 \pm 0.54) \times 10^{-4}$
$B^0 \to D^{*-}D^+_{s1}(2460)$ $(9.3 \pm 2.2) \times 10^{-3}$	$\mathscr{B}(D^+_{s1} \to D^{*+}_s\pi^0) \times \mathscr{B}(D^{*+}_s \to D^+_s\gamma)\times$ $\times\mathscr{B}(D^+_s \to X^0\mu^+\nu_\mu)$ $(48 \pm 11)\% \times (93.5 \pm 0.7)\%$ $\times(5.40 \pm 0.87)\%$	$(2.25 \pm 0.82) \times 10^{-4}$
$B^0 \to D^{*-}D^+_s$ $(8.0 \pm 1.1) \times 10^{-3}$	$\mathscr{B}(D^+_s \to X^0\mu^+\nu_\mu)$ $(5.30 \pm 0.87)\%$	$(4.24 \pm 0.91) \times 10^{-4}$
$B^0 \to D^{*-}D^{*+}K^0$ $(8.1 \pm 0.7) \times 10^{-3}$	$\mathscr{B}(D^{*-} \to D^0\pi^-) \times \mathscr{B}(D^0 \to X^-\mu^+\nu_\mu)$ $(67.7 \pm 0.5)\% \times (5.30 \pm 0.24)\%$	$(2.91 \pm 0.28) \times 10^{-4}$

Table 4.12: Leading B^0 to double charm branching ratios with secondary muons [164]

Double charm with secondary muon $B^+ \to D^{*-}D^+_{(s)}X, D^+_{(s)} \to X\mu^+\nu_\mu$

This template consists of a cocktail of $B^\pm$ decay modes to two charm mesons (and another particle), where one of the charm mesons decays semileptonically. The projections of the 3D template are shown in Fig. 4.12.

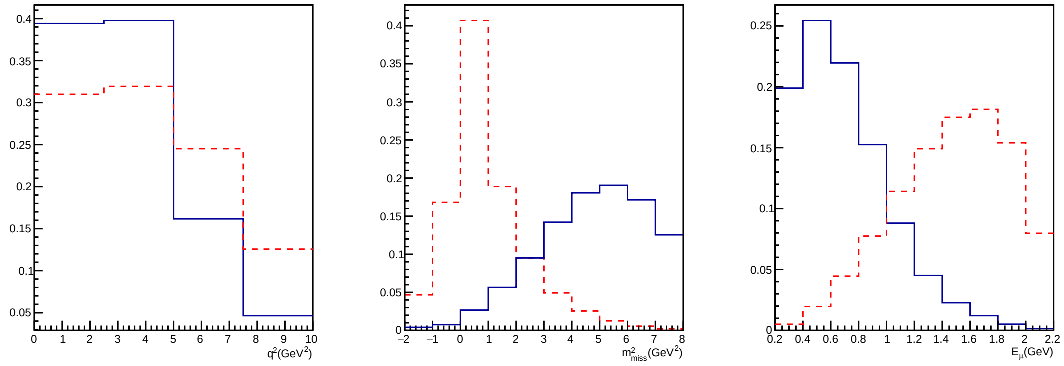

Figure 4.12: Projections of the 3D template in q^2, m^2_{miss} and E^*_μ for the $B^+ \to D^{*-}D^+_{(s)}X, D^+_{(s)} \to X\mu^+\nu_\mu$ sample in blue. The signal projections are shown in red for comparison.

The two leading modes along with their appropriate semileptonic modes are given in Table 4.13. The sum of the modes shown in the table is $(5.34 \pm 0.67) \times 10^{-4}$. The size of this background is expected to be about 1% of the signal mode.

Decay	Additional $\mathscr{B}$	Final $\mathscr{B}$
$B^+ \to D^{*0}D^{*+}K^0$ $(9.2 \pm 1.2) \times 10^{-3}$	$\mathscr{B}(D^{*0} \to D^0\pi^0/\gamma) \times \mathscr{B}(D^0 \to X^-\mu^+\nu_\mu)$ $1 \times (5.30 \pm 0.24)\%$	$(4.87 \pm 0.67) \times 10^{-4}$
$B^+ \to D^{*+}D^{*-}K^+$ $(1.32 \pm 0.18) \times 10^{-3}$	$\mathscr{B}(D^{*-} \to D^0\pi^-) \times \mathscr{B}(D^0 \to X^-\mu^+\nu_\mu)$ $(67.7 \pm 0.5)\% \times (5.30 \pm 0.24)\%$	$(0.47 \pm 0.07) \times 10^{-4}$

Table 4.13: Leading B^+ to double charm branching ratios with secondary muons [164]

Double charm with tertiary muon $B^0/B^- \to D^*D_{(s)}X, D_{(s)} \to X\tau\nu, \tau \to \mu\nu\nu$

The two templates consist of B^0 and B^- decay modes to two charm mesons, where one of them decays semileptonically via the τ mode. In the case of B^0 decays, the leading modes amount for a branching ratio of $(2.79 \pm 0.36) \times 10^{-4}$ which is used as a constraint. The size of this background is expected to be about 0.5% of the signal mode. In the case of B^- decays, since there are no values in the PDG for these decay modes, their contribution is taken to be 10 times smaller than the corresponding muon case. The final branching ratio used to constrain it is $(0.53 \pm 0.07) \times 10^{-4}$. This background is about 0.1% of the signal mode.

All the branching ratios used to constrain the various simulation derived background templates as well as the fractions with respect to signal are summarized in Tab. 4.14. The table is split in two parts, first the semileptonic backgrounds and second the doublecharm backgrounds.

Decay mode	$\mathscr{B}$ estimate	Fraction
$B^0 \to D^{*-}\mu^+\nu_\mu$ (signal)	$(4.97 \pm 0.12)\%$	1
$B^+ \to (D^{**0} \to D^{*-}\pi^+)\mu^+\nu_\mu$	$(6.74 \pm 0.67) \times 10^{-3}$	0.130
$B^0 \to (D^{**-} \to D^{*-}\pi^0)\mu^+\nu_\mu$	$(3.29 \pm 0.47) \times 10^{-3}$	0.065
$B^0 \to D^{*-}\tau^+\nu_\tau$	$(2.74 \pm 0.15) \times 10^{-3}$	0.050
$B_s^0 \to D_s^{**-}\mu^+\nu_\mu$	$(9.10 \pm 2.30) \times 10^{-4}$	0.020
$B^0 \to (D^{**-} \to D^{*-}\pi^0)\tau^+\nu_\tau$	$(1.71 \pm 0.24) \times 10^{-4}$	0.003
$B^+ \to (D^{**0} \to D^{*-}\pi^+)\tau^+\nu_\tau$	$(3.51 \pm 0.11) \times 10^{-4}$	0.007
$B^0 \to D^{*-}D^+_{(s)}X, D^+_{(s)} \to X\mu^+\nu_\mu$	$(2.46 \pm 0.22) \times 10^{-3}$	0.050
$B^+ \to D^{*-}D^+_{(s)}X, D^+_{(s)} \to X\mu^+\nu_\mu$	$(5.34 \pm 0.67) \times 10^{-4}$	0.010
$B^0 \to D^{*-}D^+_{(s)}X, D^+_{(s)} \to X\tau^+\nu_\tau$	$(2.79 \pm 0.36) \times 10^{-4}$	0.005
$B^+ \to D^{*-}D^+_{(s)}X, D^+_{(s)} \to X\tau^+\nu_\tau$	$(0.53 \pm 0.07) \times 10^{-4}$	0.001

Table 4.14: The most significant expected backgrounds for the $\overline{B}^0 \to D^{*+}\mu^-\overline{\nu}_\mu$ decay mode, estimates of their branching ratios ($\mathscr{B}$) [164] and estimated yield fractions with respect to signal.

4.3.2 Data driven templates

Combinatorial background

In the reconstruction procedure, random particles coming from different decay chains may be combined to form particle candidates. This results in events where the candidates are fake ones coming from these random combinations. These events are generally referred to as combinatorial background. In this analysis we deal with two types of combinatorial backgrounds:

- True D^* combinatorial. True D^{*-} particles and μ^+ coming from different decay chains are combined
- Fake D^* combinatorial. The D^{*-} candidates are not true but random combinations of D^0 and pions coming mainly from the primary vertex.

The true D^* combinatorial template is derived from data using same sign $D^{*+}\mu^+$ combinations. Since a D^{*+} and a μ^+ cannot come from the same B^0 decay these events form a sample that is representative random $D^{*-}\mu^+$ combinations. In the fit, this background is constrained to the number of same sign events found in data with a standard deviation of 8%. The projections of the 3D template derived from data for the true D^* combinatorial background are shown in Fig. 4.13

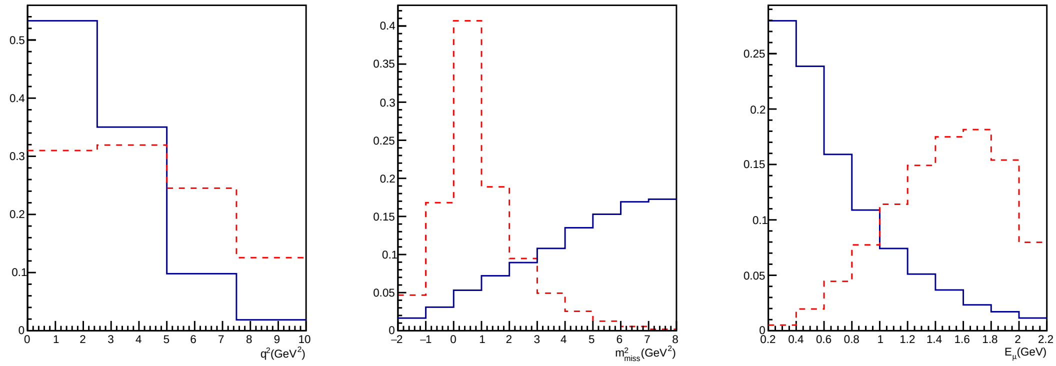

Figure 4.13: Projections of the 3D template in q^2, m^2_{miss} and E^*_μ for the true D^* combinatorial template in blue. The signal projections are shown in red for comparison.

The second type of combinatorial background is modelled from data using wrong sign $D^0\pi^-\mu^+$ combinations. This sample consists of events where D^0 and π^- come from different decay chains. In a similar way as for the other type of combinatorial, this background is constrained in the fit to the number of wrong sign events found in data with a standard deviation of 8%. The projections of the 3D template derived from data for the fake D^* combinatorial background are shown in Fig. 4.13

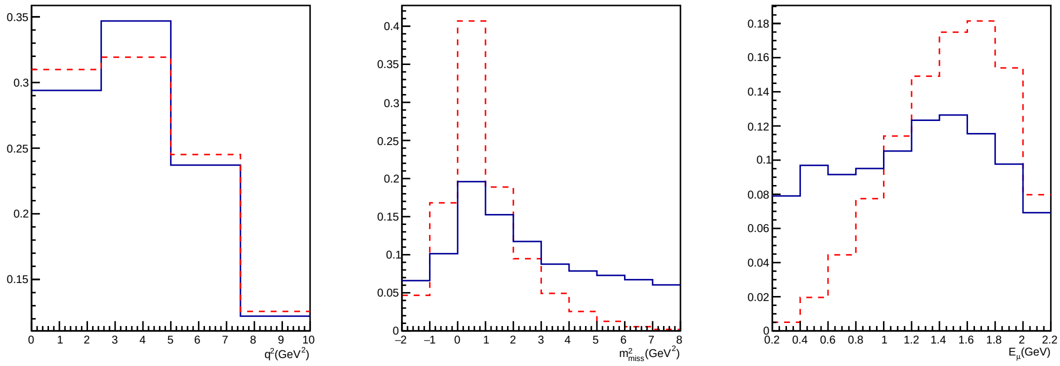

Figure 4.14: Projections of the 3D template in q^2, m^2_{miss} and E^*_μ for the fake D^* combinatorial template in blue. The signal projections are shown in red for comparison.

Muon misID

Another source of background in the $B^0 \to D^{*-}\mu^+\nu_\mu$ data sample consists of decays where other charged particles such as pions, kaons or protons (and to a less extent electrons) are misidentified as muons. This sample is obtained from data using the same selection except that the `IsMuon` requirement is not passed. Additionally, the selection criteria on the muon PID variable PIDmu is removed. This means the muon misID sample is made out of events where the muon candidate is within the muon chambers acceptance but is required to fail the muon identification requirement. The contribution of this background is unconstrained and allowed to float freely in the fit. The projections of the 3D template for the muon misID background are shown in Fig. 4.15.

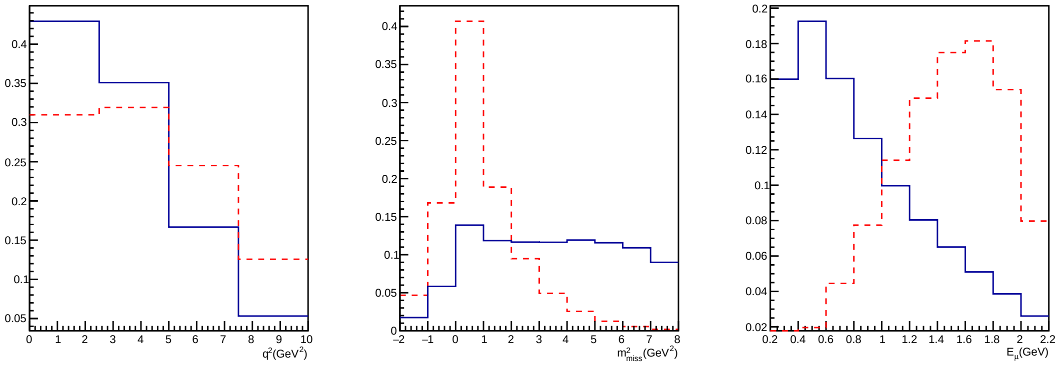

Figure 4.15: Projections of the 3D template in q^2, m^2_{miss} and E^*_μ for the muon misID template in blue. The signal projections are shown in red for comparison.

4.3.3 Fit results

The background template fit is performed separately for the three years included in the dataset i.e. 2016, 2017 and 2018. The fit projections in the case of the 2016 data sample are shown in Fig. 4.16 and the contribution of the signal and of each background mode are visible in different colors. The fit quality can be expressed in terms of χ^2 per number of degrees of freedom and for the 2016 fit its value is $\chi^2/384 = 4.79$. The agreement between the total PDF and data can be visualised also in terms of the unfolded (flattened) 3D PDF where each of the 400 bins are compared with data. This is shown in Fig. 4.17. Due to the chosen fit variables and binning scheme some bins in either data or simulation templates are kinematically forbiden and therefore are empty. In these cases, due to technical reasons the bin content is set to 1e-6, an arbitrarily small (but nonzero) number, such that effectively these bins do not contribute to the likelihood. The same approach is used in the $\mathscr{R}(D^*)$ analyses.

The large pulls in the 1D and 3D flattened projections, as well as the large χ^2/ndof value indicate that the agreement between the total PDF and the data is not ideal. However, this is accepted since known discrepancies between data and simulation are not accounted for and some of the templates included in the fit lack the proper treatment. As discussed in Sec. 4.1, the only corrections applied to the Tracker-Only MC samples are the trigger and PID response. Other corrections such as kinematic corrections (some kinematic and topological variables of the B meson and its daughters are not well reproduced in LHCb simulation) need to be applied. The hadronic model, i.e. form factors, used in generating the MC samples may also affect the template shapes and cause discrepancies with respect to data. The data driven templates are included in the fit directly as they are and their constraints are rough estimations. A more careful treatment of these templates is needed to ensure better modelling of the combinatorial and muon misID backgrounds. In particular, the μ misID template can be split in several templates for different particles misidentified as muons with the proper efficiencies. The fake D^* combinatorial can be estimated by a fit to the Δm variable in the correct sign sample and this yield can then be used to rescale the shape of the wrong sign template. The μ misID contribution should be subtracted from these samples in order to get the combinatorial for real muons only. The true D^* combinatorial contribution can be estimated by fitting the upper-sideband of the $m(D^*\mu)$ variable ($m(D^*\mu) > 5280\,\text{MeV}$) in the correct sign data sample since in this region there are no decays from real B mesons and only combinatorial background is present. The contributions of the fake D^* combinatorial and μ misID backgrounds then have to be subtracted in order to avoid double counting. All these procedures would ensure a much better agreement between data and the fit model and are needed in order to reach sub-percent level precision on the background fractions in analyses that measure $\mathscr{R}(D)$ and $\mathscr{R}(D^*)$. However, for the purpose of this thesis, this level of precision is not needed and percent level precision on the background fractions is sufficient. The measurement of the NP observables in this analysis is affected by the fractions determined by the background fit results in the following way. The signal fraction in the data sample is needed since it enters the overall normalisation in the calculation of the NP couplings from the raw CP asymmetries (see Sec. 4.5). Since some of the backgrounds can manifest parity- or CP-odd effects that may bias the NP couplings measurement, upper limits on their fractions in data are needed in order to assign systematic uncertainties due to these effects. Therefore, even though some of the background components are over or underestimated, it will not impact the related systematic uncertainties in a significant way.

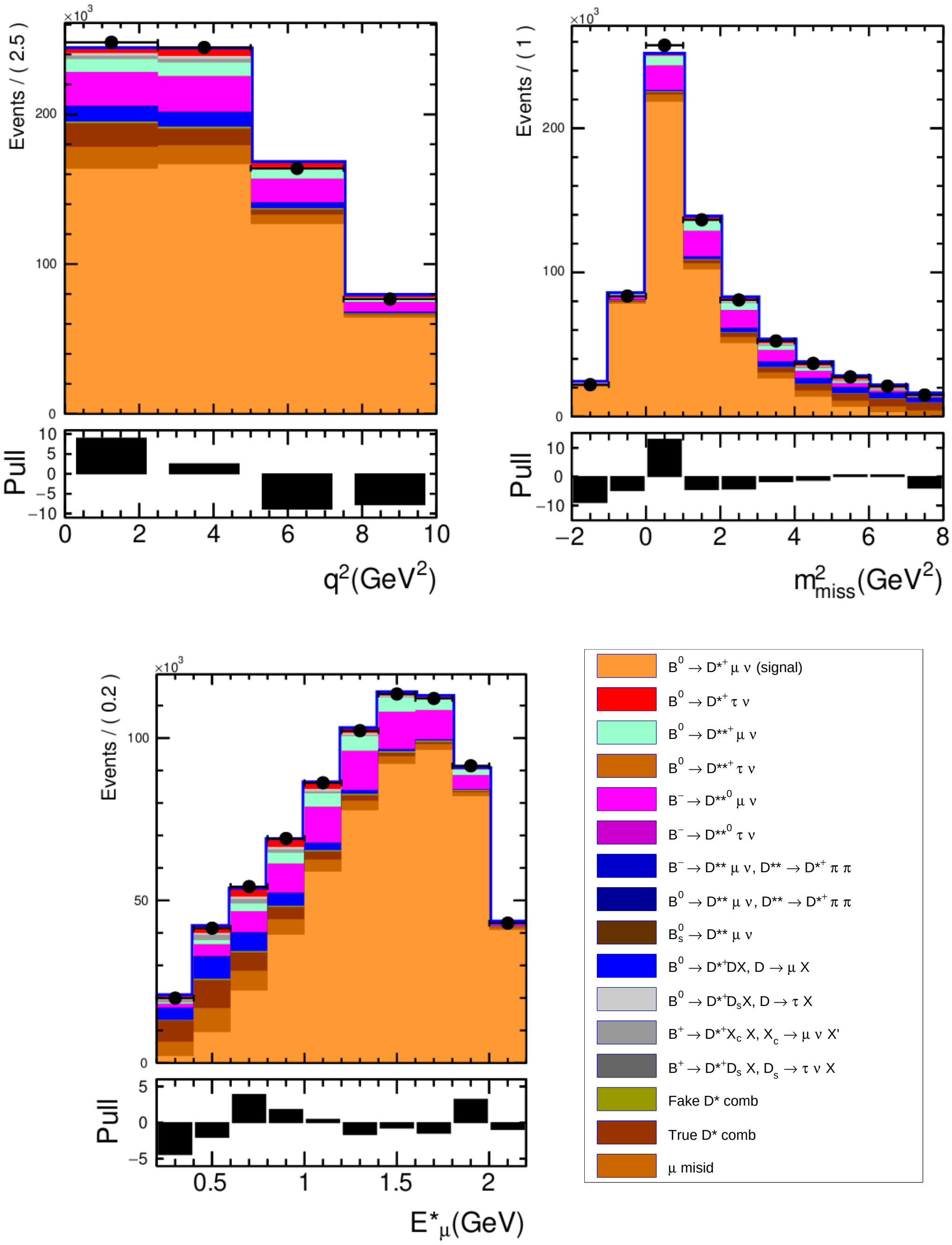

Figure 4.16: Fit projections of the three fit variables for the 2016 signal data sample.

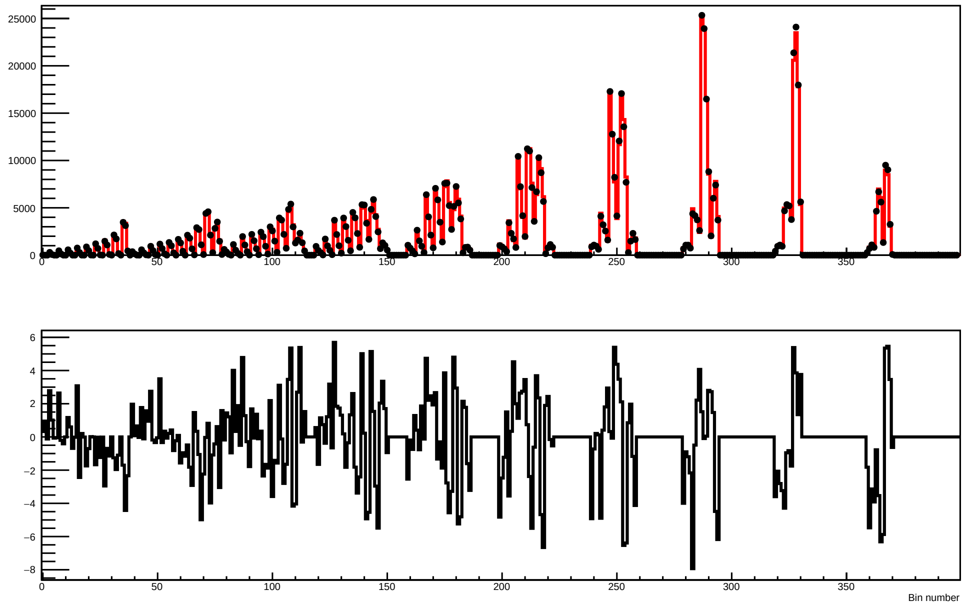

Figure 4.17: Flattened projection of the 3D PDF (red histogram) compared with data (black points) across the 400 bins (top) and its pull distribution (bottom) for the fit to the 2016 data sample.

The results of the fit are given in Tab. 4.15. The results for the different years are compatible with each other and the results summed over the three years are reported. The signal yield is found to be about 63% of the data sample. The largest partially reconstructed backgrounds are found to be as expected the two $B \to [D^{**} \to D^{*}\pi]\mu\nu$ modes which together are about 17% of the signal and the double charm background which is about 5% of the signal. The $B^0 \to D^{*-}\tau^{+}\nu_{\tau}$ background seems to be underestimated by the fit and a fraction of about 2% of the signal is found whereas a fraction of around 5% is expected. The true D^* combinatorial and μ misID backgrounds are likely to be overestimated by the fit and their fractions with respect to signal are found to be 5.5% and 6.5%, respectively. A discussion on which backgrounds can manifest P and CP odd effects, an estimation of the magnitude of these effects and the upper limits on the systematic uncertainties arising from these effects is given in Sec. 4.6.1.

Component	Yield	Signal fraction
$B^0 \to D^{*-}\mu^+\nu_\mu$	1777896 ± 3232	1
$B^0 \to D^{*-}\tau^+\nu_\tau$	36424 ± 2197	$2.04\% \pm 0.12\%$
$B^0 \to [D^{**-} \to D^{*-}\pi^0]\mu^+\nu_\mu$	80508 ± 15900	$4.52\% \pm 0.89\%$
$B^+ \to [D^{**0} \to D^{*-}\pi^+]\mu^+\nu_\mu$	223117 ± 16075	$12.54\% \pm 0.90\%$
$B^0 \to D^{**-}\tau^+\nu_\tau$	1690 ± 156	$0.09\% \pm 0.01\%$
$B^+ \to D^{**0}\tau^+\nu_\tau$	9326 ± 244	$0.52\% \pm 0.01\%$
$B^+ \to [D^{**0} \to D^{*+}\pi^0\pi^-]\mu^+\nu_\mu$	1 ± 662.59	$0.00\% \pm 0.03\%$
$B^0 \to [D^{**-} \to D^{*-}\pi^+\pi^-]\mu^+\nu_\mu$	1 ± 529	$0.00\% \pm 0.03\%$
$B_s^0 \to D_s^{**-}\mu^+\nu_\mu$	1 ± 265	$0.00\% \pm 0.01\%$
$B^0 \to D^{*-}D^+_{(s)}X, D^+_{(s)} \to X\mu^+\nu_\mu$	82888 ± 3188	$4.66\% \pm 0.18\%$
$B^+ \to D^{*-}D^+_{(s)}X, D^+_{(s)} \to X\mu^+\nu_\mu$	19397 ± 1289	$1.09\% \pm 0.07\%$
$B^0 \to D^{*-}D^+_{(s)}X, D^+_{(s)} \to X\tau^+\nu_\tau$	16691 ± 798	$0.93\% \pm 0.04\%$
$B^+ \to D^{*-}D^+_{(s)}X, D^+_{(s)} \to X\tau^+\nu_\tau$	1641 ± 124	$0.09\% \pm 0.01\%$
Fake D^* combinatorial	15124 ± 2592	$0.85\% \pm 0.14\%$
True D^* combinatorial	98871 ± 2084	$5.56\% \pm 0.11\%$
μ misid	116751 ± 4899	$6.56\% \pm 0.27\%$

Table 4.15: Values of the normalization parameters and their statistical uncertainty as determined by the fit. The numbers shown are the fit results summed over the three years of the data sample.

4.4 NP reweighting

Typically, analyses of semileptonic decays have to deal with the impossibility to measure the full kinematics due to missing neutrinos and resolution effects need to be acounted for. Additionally, significant backgrounds are present in the final states of most semileptonic decays and the shapes of these backrounds need to be studied and discriminated against the signal. For these reasons, large MC samples are needed to model these type of decays and templates based on these MC samples are typically used to fit certain observable variables in data. The distributions of these observables are affected by various NP scenarios. As a consequence, MC samples for each NP case that can contribute to a certain observable are needed to describe and directly fit the data. The simulation samples that are typically produced in experiments such as LHCb do not include NP effects and often use basic and outdated form factor models.

In this analysis, in order to generate the NP templates needed to fit the observed asymmetry in data, the software library `Hammer` (*Helicity Amplitude Model for Matrix Element Reweighting*) [5] is used to reweight the SM MC to the NP scenarios that the *CP*-violating observables are sensitive to. The reweighting procedure relies on efficient amplitude-level tensorial calculations and allows the user to control in detail the NP model as well as the hadronic form factor scheme. At the end, `Hammer` provides a set of weights that can be applied to change the shape of observable distributions to the desired NP and form factor cases. The only input required is the truth-level four-momenta of all the final state particles of the decay.

Considering a MC sample consisting of I events with weights w_I and truth level kinematics $\{q\}_I$ that we want to reweight from an ’old’ theory to a ’new’ theory, the first step is to compute the ratio of the differential decay rates

$$r_I = \frac{d\Gamma_I^{new}/dPS}{d\Gamma_I^{old}/dPS}, \tag{4.9}$$

where PS stands for phase-space and Γ is the decay rate. This ratio is then used to perform the event-by-event mapping $w_I \to r_I w_I$. In the typical case, the ’old’ theory is the SM with a specific form factor parametrization, while the ’new’ theory can include NP contributions, a different form factor scheme, or a combination of both.

In terms of NP reweighting possibilities, `Hammer` allows to reweight processes under theories with a Lagrangian of the form

$$\mathcal{L} = \sum_\alpha c_\alpha \mathcal{O}_\alpha, \tag{4.10}$$

where $\mathcal{O}_\alpha$ is a basis of Wilson operators and c_α their associated Wilson coefficients. The Wilson operator basis available in `Hammer` and their coefficients are given in Tab. 4.16. The χ^i_j coefficients represent the NP couplings to the quark currents, while the λ^i_j represent the NP couplings to the lepton currents. The lower indices represent the helicities of the neutrino and of the b-quark, while the upper indices represent the . All `Hammer` internal calculations are done in the operator basis given in [167] which are defined as $\bar{b}\Gamma c$ operators. However, the inputs are defined in the more conventional $\bar{c}\Gamma b$ operator basis.

Current	WC tag	Wilson Coefficient	4-Fermi/$(i2\sqrt{2}V_{cb}G_F)$
SM	SM	1	$[\bar{c}\gamma^\mu P_L b]\,[\bar{\ell}\gamma_\mu P_L \nu]$
Vector	V_{qLlL}	$\chi_L^V\lambda_L^V$	$[\bar{c}\chi_L^V\gamma^\mu P_L b]\,[\bar{\ell}\lambda_L^V\gamma_\mu P_L \nu]$
	V_{qRlL}	$\chi_R^V\lambda_L^V$	$[\bar{c}\chi_R^V\gamma^\mu P_R b]\,[\bar{\ell}\lambda_L^V\gamma_\mu P_L \nu]$
	V_{qLlR}	$\chi_L^V\lambda_R^V$	$[\bar{c}\chi_L^V\gamma^\mu P_L b]\,[\bar{\ell}\lambda_R^V\gamma_\mu P_R \nu]$
	V_{qRlR}	$\chi_R^V\lambda_R^V$	$[\bar{c}\chi_R^V\gamma^\mu P_R b]\,[\bar{\ell}\lambda_R^V\gamma_\mu P_R \nu]$
Scalar	S_{qLlL}	$\chi_L^S\lambda_L^S$	$[\bar{c}\chi_L^S P_L b]\,[\bar{\ell}\lambda_L^S P_L \nu]$
	S_{qRlL}	$\chi_R^S\lambda_L^S$	$[\bar{c}\chi_R^S P_R b]\,[\bar{\ell}\lambda_L^S P_L \nu]$
	S_{qLlR}	$\chi_L^S\lambda_R^S$	$[\bar{c}\chi_L^S P_L b]\,[\bar{\ell}\lambda_R^S P_R \nu]$
	S_{qRlR}	$\chi_R^S\lambda_R^S$	$[\bar{c}\chi_R^S P_R b]\,[\bar{\ell}\lambda_R^S P_R \nu]$
Tensor	T_{qLlL}	$\chi_L^T\lambda_L^T$	$[\bar{c}\chi_L^T\sigma^{\mu\nu} P_L b]\,[\bar{\ell}\lambda_L^T\sigma_{\mu\nu} P_L \nu]$
	T_{qRlR}	$\chi_R^T\lambda_R^T$	$[\bar{c}\chi_R^T\sigma^{\mu\nu} P_R b]\,[\bar{\ell}\lambda_R^T\sigma_{\mu\nu} P_R \nu]$

Table 4.16: NP operator basis and coupling conventions used in `Hammer`.

Accounting also for the form factors F_i, the generic amplitude for a process can be written as

$$\mathcal{M}(\{q\}) = \sum_{\alpha,i} c_\alpha F_i(\{q\})\mathcal{A}_{\alpha i}(\{q\}), \tag{4.11}$$

where $\mathcal{A}_{\alpha i}$ is the NP- and FF- generalized amplitude tensor. The differential rate is then

$$\begin{aligned} \frac{d\Gamma}{dPS} &= \sum_{\alpha,i,\beta,j} c_\alpha c_\beta^\dagger F_i F_j^\dagger(\{q\})\mathcal{A}_{\alpha i}\mathcal{A}_{\beta j}^\dagger(\{q\}) \\ &= \sum_{\alpha,i,\beta,j} c_\alpha c_\beta^\dagger F_i F_j^\dagger(\{q\})\,\mathcal{W}_{\alpha i\beta j}. \end{aligned} \tag{4.12}$$

The quantity $\mathcal{W} = \mathcal{A}\mathcal{A}^\dagger$ defined as the product of the amplitude tesor is called the *weight tensor*. The quantity $\sum_{ij} F_i F_j^\dagger \mathcal{W}_{\alpha i\beta j}$ is independent of Wilson coefficients and is computed once for a given event $\{q\}$ and can be contracted with any NP to generate an event weight. The integrated rate over a generic region of phase space Ω is given by

$$\Gamma_\Omega = \sum_{\alpha,\beta} c_\alpha c_\beta^\dagger \int_\Omega dPS \sum_{ij} F_i F_j^\dagger(\{q\})\mathcal{W}_{\alpha i\beta_j}(\{q\}). \tag{4.13}$$

The integral in the above equation is a NP-generalized tensor since it is independent of the Wilson coefficients. Therefore, it is computed only once and can then be contracted with any choice of NP Wilson coefficients. The `Hammer` library thus provides very efficient reweighting of MC samples to any NP scenario by computing and storing large generalized tensorial objects which can be then contracted with any NP Wilson coefficients to generate an event weight.

With respect to form factor parametrizations, the form factor schemes available in `Hammer` for $b \to c\ell\nu_\ell$ transitions are ISGW2, CLN, BGL and BLPR parametrizations. While ISGW2, CLN and BGL are implemented as SM only, the BLPR form factor scheme is the only one that allows for NP reweighting.

In the case of $B^0 \to D^{*-}\mu^+\nu_\mu$ decays, the *CP*-violating observables are sensitive to two NP scenarios, the presence of the right-handed vector complex coupling g_R and the interference between the pseudoscalar and tensor complex couplings $g_P g_T^*$. These NP cases can be specified in `Hammer` by setting a nonzero complex value to the Wilson coefficients corresponding to the appropriate operators from Tab. 4.16, i.e. the V_{qRlL} operator for the right-handed vector case and a combination of the S_{qLlL}, S_{qRlL} and T_{qLlL} operators for the interference between pseudoscalar and tensor case [5].

The distributions of the `Hammer` weights generated for the two relevant NP cases are shown in Fig. 4.18. The LHCb simulation sample for $B^0 \to D^{*-}\mu^+\nu_\mu$ decays is generated with SM coupling and with the HQET2 hadronic model of `EvtGen`[6]. The weights are generated with the BLPR form factor model (a form factor model in `Hammer` that supports NP in $b \to c\ell\nu_\ell$ decays) and with the inputs of NP Wilson operators and couplings as described above.

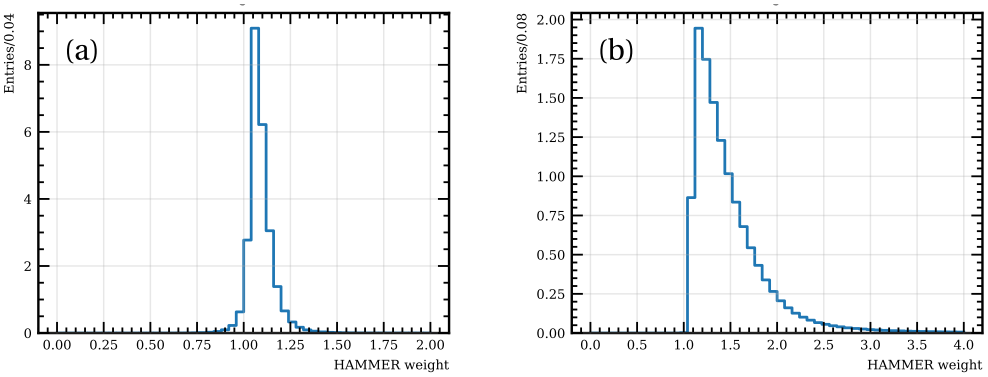

Figure 4.18: `Hammer` weights generated for the NP cases where $g_R = 0.1i$ (a) and $g_P g_T^* = 0.1i$ (b)

The weights are calculated by `Hammer` using the true four momenta of all the final state particles of the $B^0 \to D^{*-}\mu^+\nu_\mu$ decay, i.e. the K^+ and π^- from the $\overline{D}^0$ decay, the slow pion π^- coming from the D^{*-} decay and the lepton pair μ^+ and ν_μ. Although the LHCb MC simulation primarily concerns the reconstructed kinematic quantities of final state particles and simulates detector resolution effects and missing neutrinos, the true kinematic information of all particles as generated in the decay, i.e. before the particles pass through the detector, is also available.

---

[5] Since the *CP* asymmetry only depends on the imaginary part of the product $\mathrm{Im}(g_P g_T^*)$, g_P is set to be real and equal to 1 while g_T^* is set to be complex

[6] HQET2 hadronic model corresponds to CLN form factor scheme

4.5 Binned asymmetry fit

The analysis presented in this thesis studies the angular distribution in $B^0 \to D^{*-}\mu^+\nu_\mu$ decays and more specifically the P-odd part of the angular distribution. The total decay density given in Eq. 2.110 can be written as a sum of the P-even and P-odd components, i.e.

$$P(q^2,\theta_\ell,\theta_D,\chi) = P_{\rm even}(q^2,\theta_\ell,\theta_D,\chi) + P_{\rm odd}(q^2,\theta_\ell,\theta_D,\chi), \qquad (4.14)$$

where $P_{\rm odd}$ is the sum of the terms proportional to $\sin\chi$ and $\sin 2\chi$ shown in Tab. 2.5 and it can be written explicitly as

$$P_{\rm odd}(q^2,\theta_\ell,\theta_D,\chi) = P^{(1)}_{\rm odd}(q^2,\theta_\ell,\theta_D)\sin\chi + P^{(2)}_{\rm odd}(q^2,\theta_\ell,\theta_D)\sin 2\chi, \qquad (4.15)$$

where $P^{(1)}_{\rm odd}$ and $P^{(2)}_{\rm odd}$ are the angular functions which are now independent of χ. The symmetry properties of the total angular distribution can be exploited in order to cancel out the P-even part and extract only the P-odd component in a model independent way. The $P^{(1)}_{\rm odd}$ and $P^{(2)}_{\rm odd}$ terms can be obtained by integrating the total decay density with $\sin\chi$ and $\sin 2\chi$ weights in the following way[7]:

$$\begin{aligned} P^{(1)}_{\rm odd}(q^2,\theta_\ell,\theta_D) &= \frac{1}{\pi}\int_{-\pi}^{\pi} P(q^2,\theta_\ell,\theta_D,\chi)\sin\chi d\chi, \\ P^{(2)}_{\rm odd}(q^2,\theta_\ell,\theta_D) &= \frac{1}{\pi}\int_{-\pi}^{\pi} P(q^2,\theta_\ell,\theta_D,\chi)\sin 2\chi d\chi. \end{aligned} \qquad (4.16)$$

In this way, the $P^{(1)}_{\rm odd}$ and $P^{(2)}_{\rm odd}$ quantities which represent the P-odd components (in $\sin\chi$ and $\sin 2\chi$) of the total decay density are obtained separately and the rest of the (P-even) angular distribution along with its uncertanties is cancelled out.

According to Tab. 2.5, the $\sin\chi$ term has contributions from both the right-handed vector coupling g_R and the interference between the pseudoscalar and tensor currents $g_P g_T^*$ while the $\sin 2\chi$ term has contributions only from g_R. In the approximation where the NP couplings are small with respect to the SM coupling, i.e. $g_R \ll 1$ and $g_P g_T^* \ll 1$ the following relations can be written

$$\begin{aligned} P^{(1)}_{\rm odd}(q^2,\theta_D,\theta_\ell) &= {\rm Im}(g_R)F^{(1)}_{RH}(q^2,\theta_D,\theta_\ell) + {\rm Im}(g_P g_T^*)F^{(1)}_{PT}(q^2,\theta_D,\theta_\ell), \\ P^{(2)}_{\rm odd}(q^2,\theta_D,\theta_\ell) &= {\rm Im}(g_R)F^{(2)}_{RH}(q^2,\theta_D,\theta_\ell), \end{aligned} \qquad (4.17)$$

where the second order term proportional to ${\rm Im}(g_L g_R^*)$ in $P^{(1)}_{\rm odd}$ is omitted. We note that ${\rm Im}(g_P g_T^*)$ does not contribute to the $\sin 2\chi$ term and therefore does not contribute to $P^{(2)}_{\rm odd}$. The functions $F^{(1)}_{RH}$ and $F^{(2)}_{PT}$ are obtained from simulation and are referred to

---

[7] This is because $\int_{-\pi}^{\pi} f(x)\sin x dx \neq 0$ only if $f(x) = \sin x$. The same holds for $\sin 2\chi$. Therefore, since $P(q^2,\theta_\ell,\theta_D,\chi)$ is a sum of several angular terms, by integrating with $\sin\chi$ and $\sin 2\chi$ weights only the terms proportional to $\sin\chi$ and $\sin 2\chi$ survive.

as NP templates while $P_{\text{odd}}^{(1)}$ and $P_{\text{odd}}^{(1)}$ are extracted from data. The reweighting process to obtain the NP templates using `Hammer` was described in Sec. 4.4. Therefore, with the use of Eq. 4.17, the imaginary part of the NP couplings can be determined from data with NP templates.

In practice, where the experimental data is discrete rather than continuous, it is convenient to construct binned asymmetries. The asymmetry in the i-th bin A_i is given by

$$\begin{aligned} A_i^{(1)} &= \frac{N_{\text{bins}}}{N_{\text{signal}}} \sum_{n=1}^{N_i} \sin\chi_n, \\ A_i^{(2)} &= \frac{N_{\text{bins}}}{N_{\text{signal}}} \sum_{n=1}^{N_i} \sin 2\chi_n, \end{aligned} \tag{4.18}$$

where $N_{\text{signal}} = \sum_i N_i$ is the number of signal events in the sample and N_{bins} is the number of bins with $1 < i < N_{\text{bins}}$. The summation is performed over all the events in the i-th bin. The normalisation term $N_{\text{bins}}/N_{\text{signal}}$ ensures that the asymmetries are independent of the number of signal events in the sample as well as of the P-even component of the total density (as would be the case if the normalisation $1/N_i$ was used).

The binning is performed in two dimensions in $\cos\theta_D\, vs.\cos\theta_\ell$ in order to capture the whole phase space. The q^2 variable is not binned but integrated over thus the asymmetries are obtained over the whole q^2 range. A 2D scheme with 8×8 bins in $\cos\theta_{D,\ell}$ resulting in a total of 64 bins is chosen. A feasibility study of the method presented in this section can be found in [168] where it was shown that a finer binning does not impact the achieved statistical precision in a significant way. Consequently, the 8×8 bins in $\cos\theta_\ell\, vs.\cos\theta_D$ is considered to be sufficient. The asymmetries in Eq. 4.18 are the binned versions of the P-odd components of the decay density from Eq. 4.17 and are linearly proportional. The following linear relation holds:

$$A^{(i)} \propto P_{\text{odd}}^{(i)} \propto \text{Im}(g_{NP}). \tag{4.19}$$

The linearity holds because the two quantities $A^{(i)}$ and $P_{\text{odd}}^{(i)}$ are related via linear operations such as factoring detector efficiencies, resolution effects and calculation of integral over bin area. Therefore, a linear fit can be employed to extract the imaginary part of the NP couplings from the binned asymmetries observed in data.

Since the asymmetries in each bin are given by a sum of a large number of independent events, their fluctuations are Gaussian to a good degree of approximation and a χ^2 function can be implemented to fit simultaneously the binned versions of Eq. 4.17. Since the $\sin\chi$ and $\sin 2\chi$ terms are correlated as they are obtained from the same events in each bin i, their correlation is taken into account with the following χ^2_{corr} function

$$\chi^2_{\text{corr}} = \sum_i \sum_{a,b=1,2} \Delta A_i^{(a)} \left(\Sigma_i^{-1}\right)^{(ab)} \Delta A_i^{(b)}, \tag{4.20}$$

where the indices (a,b) represent the $\sin\chi$ and $\sin 2\chi$ terms and $\Delta A_i^{(a,b)}$ is the difference between the expected asymmetry determined from the NP templates and the asymmetry observed in data, i.e

$$\Delta A_i^{(a,b)} = \frac{\mathrm{Im}(g_R)_{\mathrm{fit}}}{\mathrm{Im}(g_R)_0} A_{RH,i}^{(a,b)} + \frac{\mathrm{Im}(g_P g_T^*)_{\mathrm{fit}}}{\mathrm{Im}(g_P g_T^*)_0} A_{PT,i}^{(a,b)} - A_i^{(a,b)}. \tag{4.21}$$

In Eq. 4.21 the quantities $A_{RH,i}^{(1,2)}$ and $A_{PT,i}^{(1,2)}$ are the $\sin\chi$ (denoted by the upper index $^{(1)}$ and $\sin 2\chi$ (denoted by the upper index $^{(2)}$ binned asymmetry templates obtained from the NP reweighting of the simulation with the right-handed current coupling $\mathrm{Im}(g_R)_0$ and with the interference between pseudoscalar and tensor current couplings $\mathrm{Im}(g_P g_T^*)_0$. The quantities $A_i^{(1,2)}$ are the binned asymmetries observed in data. Finally, the values of the NP couplings determined by minimizing the χ^2_{corr} function in the fit are denoted by $\mathrm{Im}(g_R)_{\mathrm{fit}}$ and $\mathrm{Im}(g_P g_T^*)_{\mathrm{fit}}$.

The covariance matrix Σ contains the information about the correlations between the $\sin\chi$ and $\sin 2\chi$ binned asymmetries and is given by the 2×2 matrix

$$\Sigma_i = \left(\frac{N_{\mathrm{bins}}}{N_{\mathrm{signal}}}\right)^2 \begin{pmatrix} \sum_{n=1}^{N_i} \sin^2\chi_n & \sum_{n=1}^{N_i} \sin\chi_n \sin 2\chi_n, \\ \sum_{n=1}^{N_i} \sin\chi_n \sin 2\chi_n & \sum_{n=1}^{N_i} \sin^2 2\chi_n, \end{pmatrix}, \tag{4.22}$$

where N_i is the number of events in each bin i.

The binned *CP* asymmetry templates in the SM case and in the two relevant NP cases using simulation are shown in Fig. 4.19, 4.20 and 4.21. The plot in the first row of each figure shows the total decay density in the 2D bins of $\cos\theta_D$ *vs.* $\cos\theta_\ell$ where the color indicates the number of events that fall into each bin. The first and second plots in the second row show the $\sin\chi$ and $\sin 2\chi$ weighted density, respectively. In each bin now the color indicates the magnitude of the asymmetry (the *P*-odd component of the density). In order to be able to visualize the uncertainties on the asymmetry, the 2D plots are flattened to 1D plots shown in the third row. The projection of the 2D bins is done from left to right, row by row, from bottom to top, i.e. from negative to positive values in both $\cos\theta_\ell$ and $\cos\theta_D$. In the SM case shown in Fig. 4.19, both the $\sin\chi$ and $\sin 2\chi$ asymmetries are consistent with zero. This is a trivial result since there are no weak phases in the generation of the SM simulation so the *CP* asymmetry is expected to be zero. Nevertheless, Fig. 4.19 demonstrates that there are no *P*-odd effects in the detection and reconstruction in the simulation. In the case of the same SM simulation reweighted with $\mathrm{Im}(g_R) = 0.1i$ shown in Fig. 4.20 the asymmetry has specific shapes in both $\sin\chi$ and $\sin 2\chi$ terms and its magnitude goes up to 1.5% and 2%, respectively. In the second NP case where $\mathrm{Im}(g_P g_T^*) = 0.1i$, the presence of the NP couplings contributes only to the $\sin\chi$ asymmetry shown in (b) and (d) in Fig. 4.21 where the shape of the asymmetry is different than the one generated by the right-handed vector coupling and its magnitude goes up to about 10%. Since the $\mathrm{Im}(g_P g_T^*)$ does not contribute to the $\sin 2\chi$ asymmetry, it is expected that this asymmetry is zero. However, Fig. 4.21 (c) and (e) show a statistically significant small (relative to the $\sin\chi$ term) asymmetry of magnitude up to 1%. This effect can be understood from the following argument. If the reconstruction efficiency contains terms proportional to $\cos\chi$, which is a parity-even quantity (parity-odd effects in the reconstruction efficiency and their consequences are discussed in Sec. 4.6.2) then this will cause a "leakage" of the $\sin\chi$ term into the $\sin 2\chi$ term and give rise to the effect seen in Fig. 4.21 (c).

The angular terms proportional to $\sin\chi$ (or $\sin 2\chi$) are parity-odd in nature and they reflect asymmetries between numbers of events with $\sin\chi > 0$ and $\sin\chi < 0$. These asymmetries can be either parity- or CP-odd depending on how they are related to the flavor of the B meson. As discussed in Sec. 2.2.3.1, for CP-odd processes, the sign of the angular term stays the same while for parity-odd processes, the sign changes between the decay and the CP conjugated decay. This is because the charge conjugation flips the sign of the weak phase and the parity conjugation flips the sign of angle χ, i.e. if there is no weak phase (parity-odd but not CP-odd) the CP operation will change the sign while for a true CP-odd process the angular term will flip sign twice and thus will not change. These two types of observable asymmetries can also be understood by defining the following quantities

$$\begin{aligned} a &= \frac{N(\sin\chi > 0) - N(\sin\chi < 0)}{N(\sin\chi > 0) + N(\sin\chi < 0)}, \\ \overline{a} &= \frac{\overline{N}(\sin\chi > 0) - \overline{N}(\sin\chi < 0)}{\overline{N}(\sin\chi > 0) + \overline{N}(\sin\chi < 0)}, \end{aligned} \tag{4.23}$$

where a and $\overline{a}$ are the asymmetries in numbers of events where $\sin\chi > 0$ and $\sin\chi < 0$ for the decay and the CP conjugated decay, respectively. Using Eq. 4.23, the parity and CP asymmetries can be defined formally as

$$\begin{aligned} a_P &= \frac{1}{2}(a - \overline{a}), \\ a_{CP} &= \frac{1}{2}(a + \overline{a}), \end{aligned} \tag{4.24}$$

where it is seen that in the parity-odd case, the angular term changes sign between B and $\overline{B}$ while in the CP-odd case it does not. In practice, when constructing the $\cos\theta_\ell$ *vs.* $\cos\theta_D$ 2D binned asymmetries, the CP asymmetries are obtained with $\sin\chi$ and $\sin 2\chi$ weights since in this case the sign does not change between B and $\overline{B}$ decays and the content in each bin is just the regular sum of $\sin\chi$ or $\sin 2\chi$ over all events. However, for parity asymmetries, an additional minus sign depending on the charge of the B meson in each event is assigned in addition to the $\sin\chi$ or $\sin 2\chi$ weight.

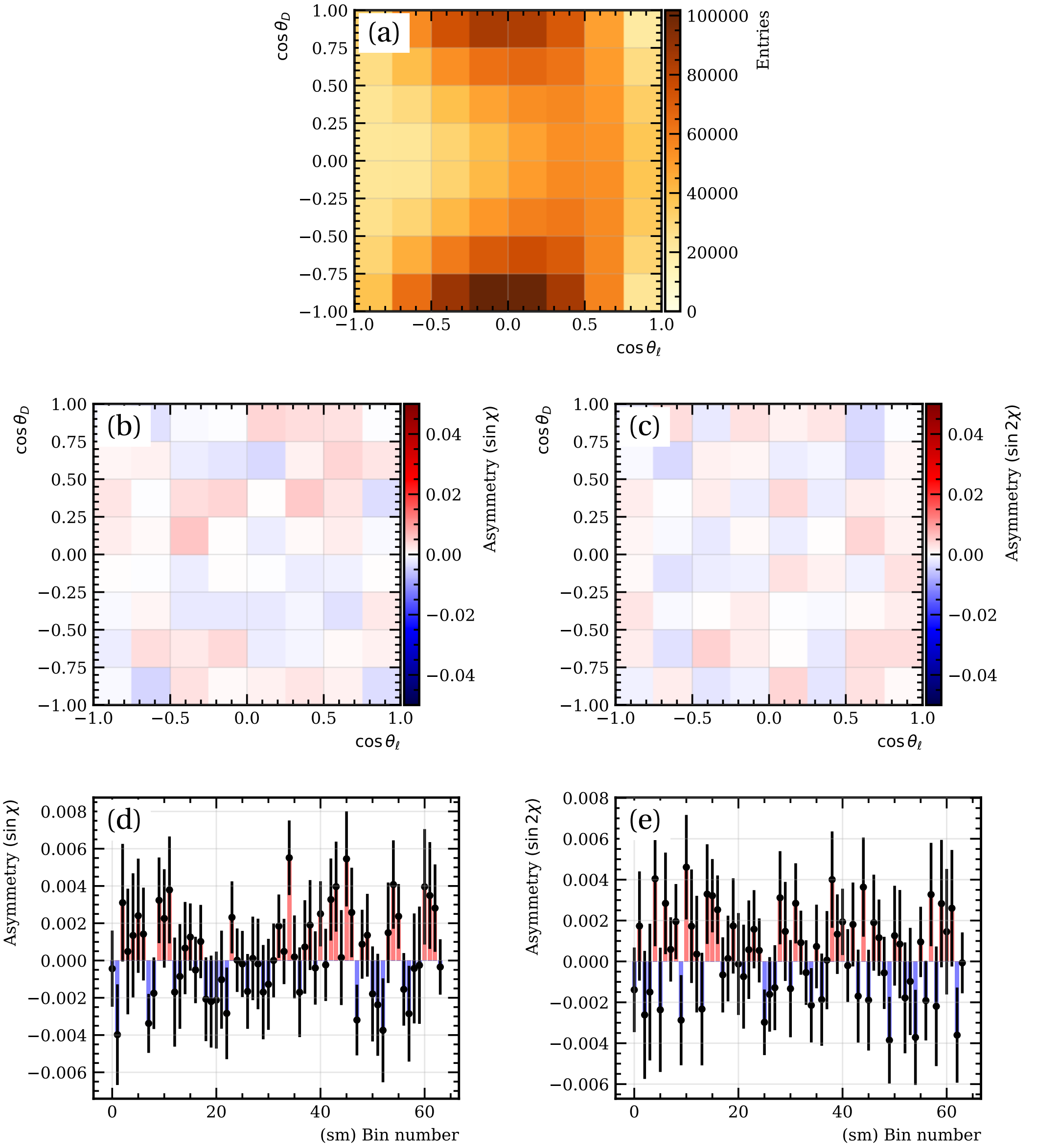

Figure 4.19: Binned density (a), binned 2D *CP* asymmetries (b,c) and flattened 1D *CP* asymmetries (d,e) of $\sin\chi$ and $\sin 2\chi$ terms in $(\cos\theta_D, \cos\theta_\ell)$ bins integrated over q^2 for the $B^0 \to D^{*-}\mu^+\nu_\mu$ SM simulation sample.

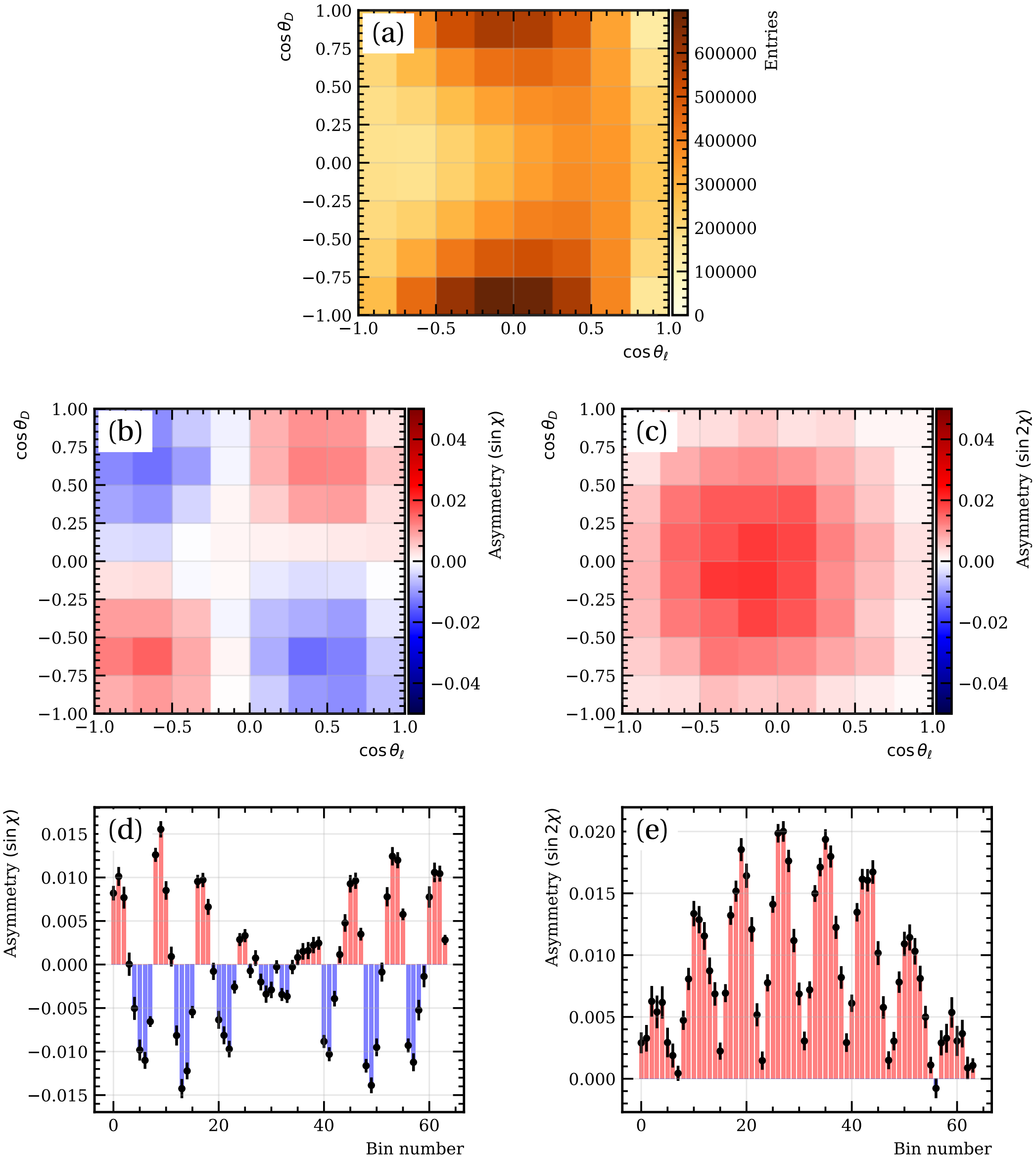

Figure 4.20: Binned density (a), binned 2D *CP* asymmetries (b,c) and flattened 1D *CP* asymmetries (d,e) of $\sin\chi$ and $\sin 2\chi$ terms in $(\cos\theta_D, \cos\theta_\ell)$ bins integrated over q^2 for the $B^0 \to D^{*-}\mu^+\nu_\mu$ simulation sample in the NP case of $\mathrm{Im}(g_R) = 0.1i$

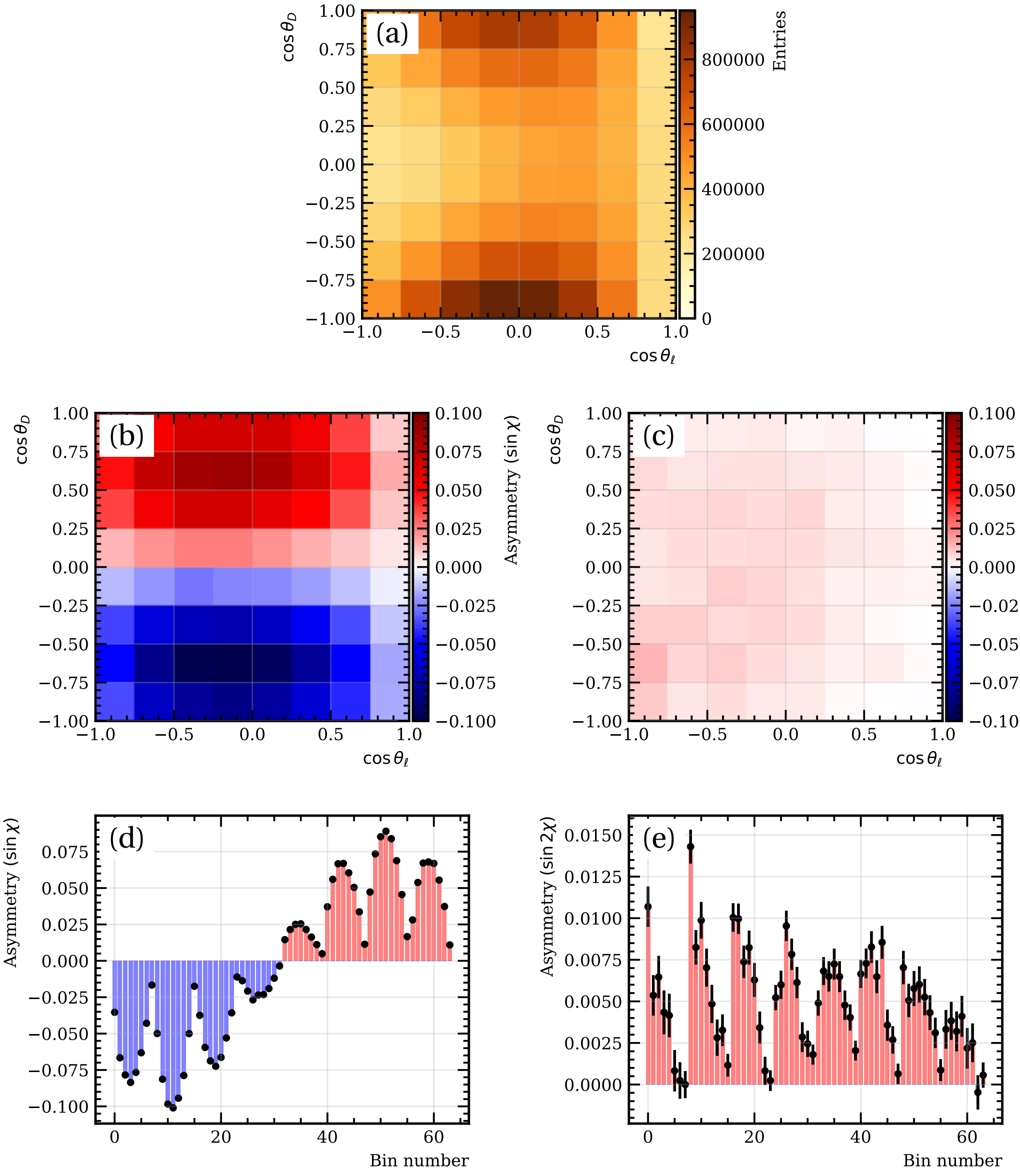

Figure 4.21: Binned density (a), binned 2D *CP* asymmetries (b,c) and flattened 1D *CP* asymmetries (d,e) of $\sin\chi$ and $\sin 2\chi$ terms in $(\cos\theta_D, \cos\theta_\ell)$ bins integrated over q^2 for the $B^0 \to D^{*-}\mu^+\nu_\mu$ simulation sample in the NP case of $\mathrm{Im}(g_P g_T^*) = 0.1i$

The linear relation shown in Eq. 4.19 is valid only in the assumption where the NP couplings are small with respect to the SM. If the NP contribution becomes large, the effects of quadratic terms in the NP couplings will become significant and the linearity will no longer hold. The NP couplings are fitted using the χ^2_{corr} function given in Eq. 4.20 in the interval $[-0.3i, 0.3i]$ in order to determine the region around zero where the linearity between the "true" and fitted couplings holds. Fig. 4.22 shows the dependence of the fitted couplings on the "true" couplings for both $\text{Im}(g_R)$ and $\text{Im}(g_P g_T^*)$. In both cases the linear regime occurs approximatively in the interval $[-0.1i, 0.1i]$. This result motivates the choice of $\text{Im}(g_R)_0 = 0.1i$ and $\text{Im}(g_P g_T^*)_0 = 0.1i$ for the NP templates used in Eq. 4.21 to fit the data, as these values lie within the linear region.

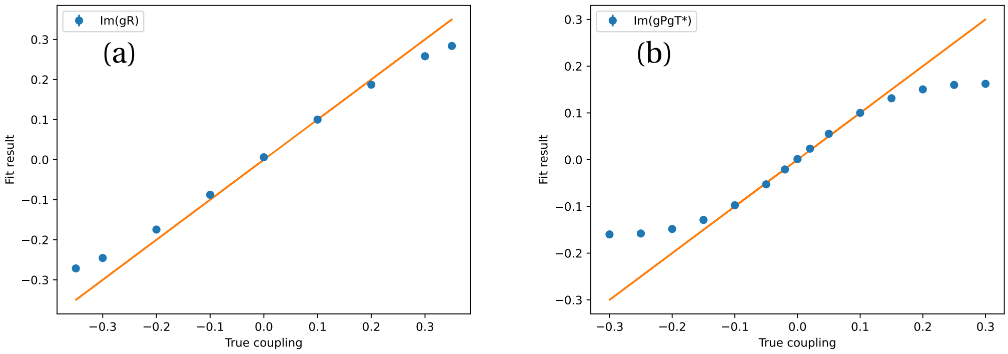

Figure 4.22: Dependence of the NP coupling obtained from the binned template fits on the "true" coupling used in the simulation for (a) right-handed current contribution and (b) interference of pseudoscalar and tensor currents. An $x = y$ line is also plotted in orange for a better visibility of the linear regime.

4.6 Systematic uncertainties

The systematic effects that can contribute to the asymmetries and introduce biases in the measurement of the NP couplings can be split into two categories: P-even effects and P-odd effects. The P-even ones can not produce fake P-odd terms in the angular distribution and can thus only affect the interpretation of the visible asymmetry in data in terms of the imaginary part of the NP couplings. Systematic effects coming from data sample composition (signal purity, background composition), form factor parametrisations, magnitudes of efficiencies of reconstruction and selection are examples of P-even effects. These types of systematic effects enter relative to the magnitude of the observed CP asymmetry and they become very small if the CP asymmetry in data is consistent with zero. The P-odd systematic effects are the ones that need to be carefully considered and are the main motivation for a dedicated analysis to measure the P-odd terms rather than the full angular distribution. This kind of effects can produce fake P-odd terms even in the SM-like (P-even) angular distribution and can be roughly split into two categories: P-odd background effects and instrumentation effects. A discussion of several of these effects and an estimation of their magnitude is given in the next sections.

4.6.1 P-odd effects in backgrounds

The physical backgrounds that can contribute in the $B^0 \to D^{*-}\mu^+\nu_\mu$ data sample can be split in two categories: semileptonic backgrounds and double charm backgrounds. The contributions of each particular mode was determined and the results were given and discussed in Sec. 4.3. A discussion on which of these backgrounds can manifest CP- and parity-odd effects and an estimation of their magnitudes is given in the next sections. In addition, the data-driven backgrounds (combinatoric and misID) may also introduce some bias in both CP and P asymmetries and their contributions are also checked and estimated.

Semileptonic backgrounds

CP-violating effects can appear in semileptonic decays only in NP scenarios and are zero in the SM. Therefore, systematic CP-odd effects in semileptonic backgrounds are not considered. On the other hand, parity-odd (but not CP-odd) effects can appear in the $B \to D^{**}\mu\nu$ decay (both charged and neutral D^{**} states) which is the dominant partially reconstructed semileptonic background in the $B^0 \to D^{*-}\mu^+\nu_\mu$ data sample. Together, the fraction of the charged and neutral D^{**} modes is about 17% of the signal mode. The dominant excited charm $D^{**} \to D^*\pi$ resonances consist of admixtures of the $D_1(2420)$, $D_1^{'}(2430)$ and $D_2^*(2460)$ states with different masses, widths, spin and parity quantum numbers. The properties of these states are given in Tab. 4.17. The contributions of other partially reconstructed semileptonic decays to the data sample are a few times smaller than the D^{**} modes and even if parity-violating effects appear in them, they would most likely be negligible and are therefore not considered here.

D^{**} state	Mass (MeV)	Width (MeV)	J^P
D_1	2421	31	1^+
$D_1^{'}$	2427	384	1^+
D_2^*	2461	47	2^+

Table 4.17: Mass, width, spin and parity of the D^{**} excited states

In these decays, strong phases can appear due to the interference of different excited charm resonances [6]. This mechanism would then generate CP violation in $B \to D^{**}\mu\nu$ decays provided that there is also a weak phase present in these decays (which can happen only with NP). However, in the absence the weak phase, the nonzero strong phase only produces parity violation.

In order to estimate the magnitude of the parity-odd effect coming from strong phases generated in this way, a simulation sample of $B^+ \to D^{**0}\mu^+\nu_\mu$ decays[8] was used (EvtType 12873450 in Tab. 4.8) and a strong phase difference δ_D was injected in the interference between the narrow $D_1(2420)$ and $D_2^*(2460)$ states. This procedure results in a set of weights that can then be applied to the asymmetry templates. As the value of the strong phase is not known, the injected δ_D was scanned in the interval 0°-360° in steps of 45° resulting in eight samples with different strong phase values. The implementation of this reweighting is similar in approach to the one in `Hammer` and it uses the true four momenta of the $B^+ \to D^{**0}\mu^+\nu_\mu$ final state particles to calculate the decay density with and without the strong phase and take the ratio as a weight. The amplitudes for the two resonances and the form factor model parameters are taken from [165]. The helicity angles and q^2 are then calculated from the partially reconstructed decay parameters as for the signal decay and the two asymmetry templates in $\sin\chi$ and $\sin 2\chi$ are obtained. The two asymmetries are then fitted using the function given in Eq. 4.20 to obtain the bias on the imaginary part of the two NP couplings. The 2D $\cos\theta_\ell \, vs. \cos\theta_D$ density, the 2D asymmetries and the fitted flattened 1D asymmetries for the $B^+ \to D^{**0}\mu^+\nu_\mu$ sample with no strong phase and for the sample with $\delta_D = 315°$ are shown in Fig. 4.23 and 4.24. The asymmetry plots for the samples corresponding to the other values of the strong phase can be found in Appendix *A*. It can be seen that for the unweighted sample the asymmetry is consistent with zero, while in the presence of a nonzero strong phase the asymmetry becomes significant in both $\sin\chi$ and $\sin 2\chi$ terms and their shapes are different than the asymmetries due to NP shown in Fig. 4.20 and 4.21. The results of the fits for the unweighted sample and for the different values of the injected strong phase δ_D are reported in Tab. 4.18. The largest bias for $\mathrm{Im}(g_R)$ is given by the case where $\delta_D = 315°$ while for $\mathrm{Im}(g_P g_T^*)$ the largest bias corresponds to the case where $\delta_D = 45°$. The values of the biases then have to be corrected by the fraction of this background with respect to the signal in order to assign an upper limit to the systematic bias coming from this effect. The final values for the bias and for the assigned systematic uncertainty for this background are given in Chapter 5.

---

[8] The $B^+ \to D^{**0}\mu^+\nu_\mu$ simulation sample is described with the ISGW2 hadronic model

Strong phase	$\Delta\,\mathrm{Im}(g_R)$	$\Delta\,\mathrm{Im}(g_P g_T^*)$
no δ_D	0.0023 ± 0.0019	0.0004 ± 0.0005
$\delta_D = 0°$	0.0237 ± 0.0022	0.0011 ± 0.0005
$\delta_D = 45°$	-0.0182 ± 0.0022	0.0015 ± 0.0005
$\delta_D = 90°$	-0.0483 ± 0.0023	0.0013 ± 0.0005
$\delta_D = 135°$	-0.0480 ± 0.0023	0.0005 ± 0.0005
$\delta_D = 180°$	-0.0200 ± 0.0022	-0.0002 ± 0.0005
$\delta_D = 225°$	0.0192 ± 0.0022	-0.0007 ± 0.0005
$\delta_D = 270°$	0.0485 ± 0.0023	-0.0005 ± 0.0005
$\delta_D = 315°$	0.0509 ± 0.0023	0.0002 ± 0.0005

Table 4.18: Fitted values of the NP couplings from the binned asymmetry fit to the $B^+ \to D^{**0}\mu^+\nu_\mu$ MC sample with different strong phase values.

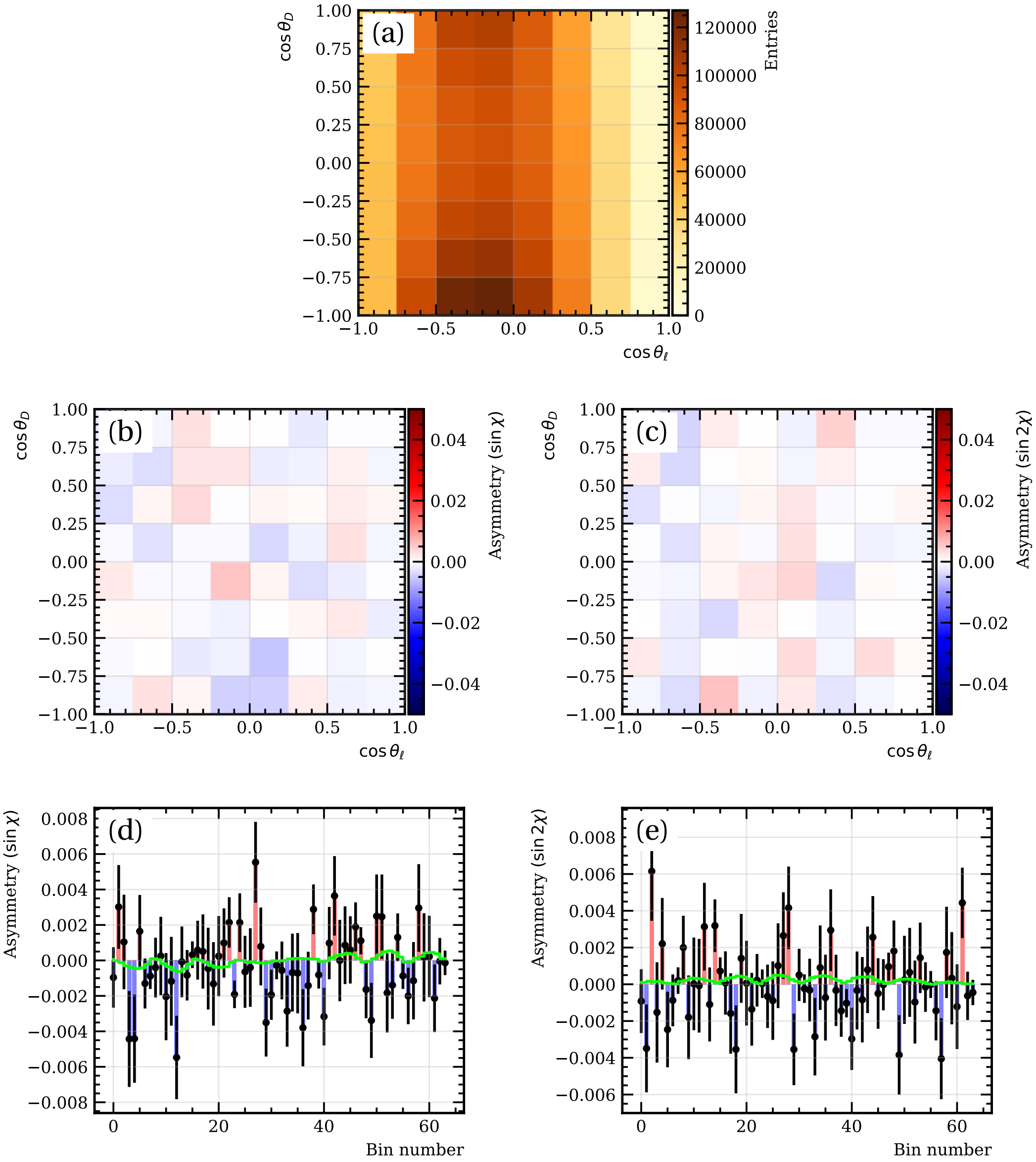

Figure 4.23: Binned density (a), binned 2D parity asymmetries (b,c) and flattened 1D parity asymmetries (d,e) of $\sin\chi$ and $\sin 2\chi$ terms in $(\cos\theta_D, \cos\theta_\ell)$ bins integrated over q^2 for the $B^+ \to D^{**0}\mu^+\nu_\mu$ simulation sample with no strong phase. Figures (d) and (e) also show the result of the best fit in green using the RH and PT templates.

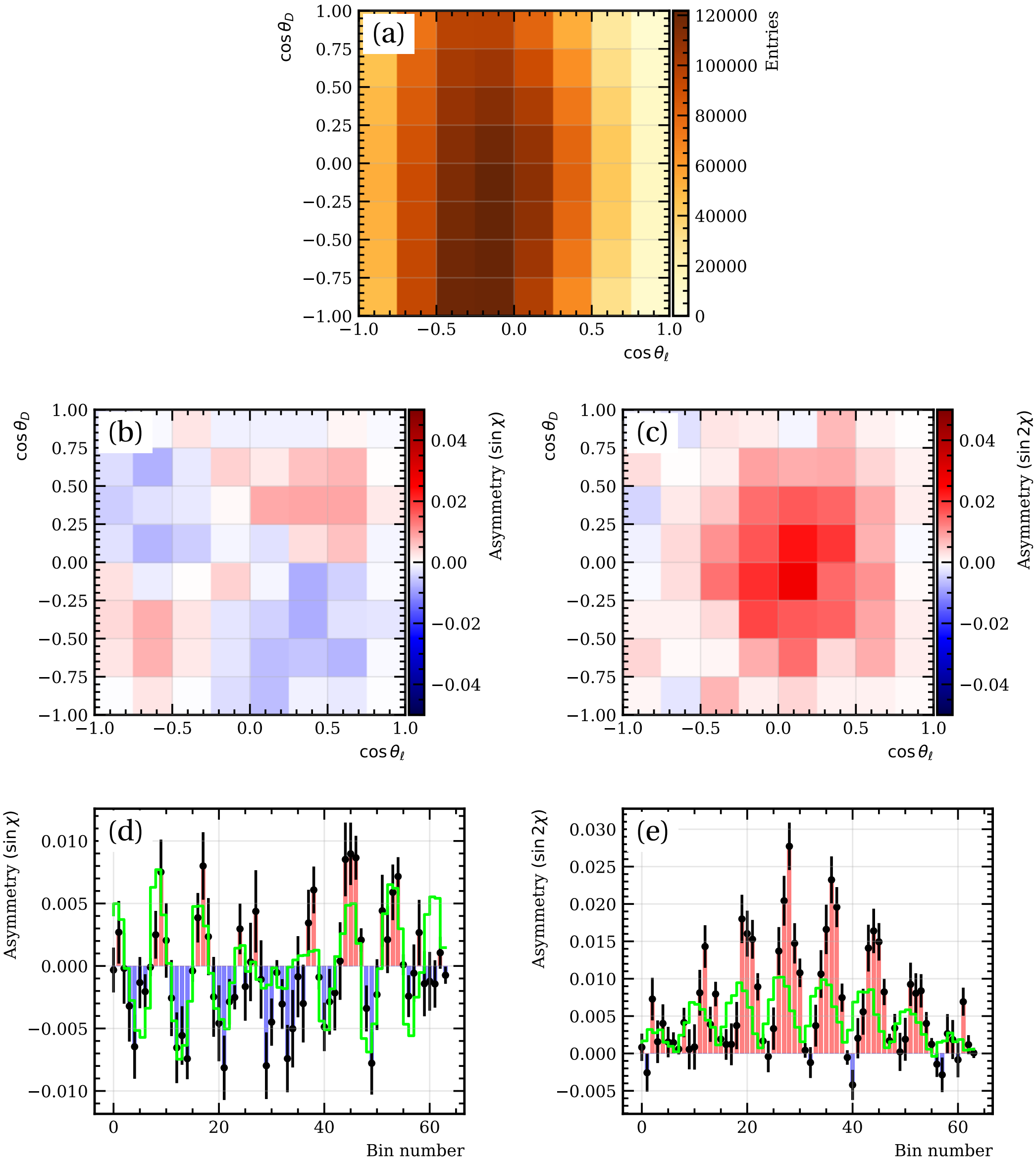

Figure 4.24: Binned density (a), binned 2D parity asymmetries (b,c) and flattened 1D parity asymmetries (d,e) of $\sin\chi$ and $\sin 2\chi$ terms in $(\cos\theta_D, \cos\theta_\ell)$ bins integrated over q^2 for the $B^+ \to D^{**0}\mu^+\nu_\mu$ simulation sample with strong phase $\delta_D = 315°$. Figures (d) and (e) also show the result of the best fit in green using the RH and PT templates.

Double charm backgrounds

It was shown in Sec. 4.3 that the largest double charm background contribution comes from the B^0 decays to two charm mesons, where one decays semileptonically. This template consists of a cocktail of B^0 decays to double charm, where the leading mode is given by the decay with the largest branching fraction $B^0 \to D^{*-} D_s^{*+}$ where $D^{*-} \to \overline{D}^0 \pi^-$, $D_s^{*+} \to D_s^+ \gamma / \pi^0$ and $D_s^+ \to X^0 \mu^+ \nu_\mu$. This is a decay to two vector charmed mesons with four final state particles and thus it can produce parity violation. Although *CP* violation in these decays is possible in the SM, the dominant amplitude is given by the $b \to c$ transition and as a consequence any *CP*-violating effect is suppressed by $|V_{ub}|/|V_{cb}|$ and is thus negligible. Therefore, only parity-violating effects in these decays are considered here.

The amplitude structure of the $B^0 \to D^{*-}[\to \overline{D}^0 \pi^-] D_s^{*+}[\to D_s^+ \gamma]$ was measured by the LHCb experiment [7] where the total decay rate is given by the interference of three helicity amplitudes H_0, H_- and H_+. These amplitudes describe the relative orientation of the polarisation vectors of the two vector mesons, i.e. H_0 is the longitudinal amplitude while $H_\pm$ are the two transverse amplitudes. The interference of these amplitudes is described by the strong phases ϕ_+ and ϕ_- of the two transverse amplitudes with respect to the longitudinal one. The values of these 5 parameters that fully describe the decay are measured to be

$$\begin{aligned}
|H_0| &= \ \ 0.760 \pm 0.007 \pm 0.007, \\
|H_-| &= \ \ 0.195 \pm 0.022 \pm 0.032, \\
|H_+| &= \ \ 0.620 \pm 0.011 \pm 0.013, \\
\phi_- &= -0.046 \pm 0.102 \pm 0.020 \text{ rad}, \\
\phi_+ &= \ \ 0.108 \pm 0.170 \pm 0.051 \text{ rad}.
\end{aligned} \tag{4.25}$$

The strong phases $\phi_\pm$ govern the degree of parity violation and the measured values are consistent with zero, i.e. no parity violation is expected. A study of the parity-violating effects in these decays was conducted using simulated $B^0 \to D^{*-}[\to \overline{D}^0 \pi^-] D_s^{*+}[\to D_s^+ \gamma]$ decays extracted from the cocktail sample (EvtType 11894610 in Tab. 4.8). The events are generated in `EvtGen` [145] with the following amplitude parameters

$$\begin{aligned}
|H_0| &= \ \ 0.7204, \\
|H_-| &= \ \ 0.4904, \\
|H_+| &= \ \ 0.4904, \\
\phi_- &= 0 \text{ rad}, \\
\phi_+ &= 0 \text{ rad}.
\end{aligned} \tag{4.26}$$

As a consequence, the parity asymmetry is expected to be zero in this simulation sample. However, maximal parity violation can be introduced by setting the strong phase values to $\phi_{\pm} = \pm\pi/2$. This is done in a similar way as in `Hammer`, by calculating the total decay rate using the truth level kinematics with and without the nonzero strong phase and taking the ratio as a weight. The background is then partially reconstructed as $B^0 \to D^{*-}\mu^+\nu_\mu$ signal and the asymmetry templates are obtained. Fig. 4.25 and 4.26 show the 2D density, 2D and flattened 1D $\sin\chi$ and $\sin 2\chi$ parity asymmetries together with the result of the fit with the RH and PT templates for the unweighted (zero parity violation) and the weighted (maximal parity violation) samples. We note that most of the events in this background are present in the low $\cos\theta_\ell$ region. The fitted values of the $\mathrm{Im}(g_R)$ and $\mathrm{Im}(g_P g_T^*)$ couplings for the two samples are given in Tab. 4.19.

Strong phase	$\Delta\,\mathrm{Im}(g_R)$	$\Delta\,\mathrm{Im}(g_P g_T^*)$
$\phi_{\pm} = 0$	-0.0027 ± 0.0045	0.00008 ± 0.00120
$\phi_{\pm} = \pm\frac{\pi}{2}$	0.0011 ± 0.0060	0.0017 ± 0.0017

Table 4.19: Fitted values of the NP couplings from the binned asymmetry fit to the $B^0 \to D^{*-}D_s^{*+}$ MC sample with different strong phase values.

The results of the fit show that there is no significant bias in the NP couplings coming from this background even in the case where maximal parity violation was introduced in the amplitude. This result could be explained by the fact that since the photon is not reconstructed and its degrees of freedom are integrated out, the parity violating effect coming from the two-body decays of the two vector mesons is cancelled out. Nevertheless, the numbers shown in Tab. 4.25 have to be corrected by the fraction of background double charm decays in the data sample. The final values for the bias and for the assigned systematic uncertainty for this background are given in Chapter 5.

Other double charm partially reconstructed backgrounds, such as $B \to D^* D_s \pi$ or $B \to D^{(*)} D^* K$ contribute at the percent or subpercent level and any P- or CP-violating effects coming from them are expected to be negligible and are therefore not considered.

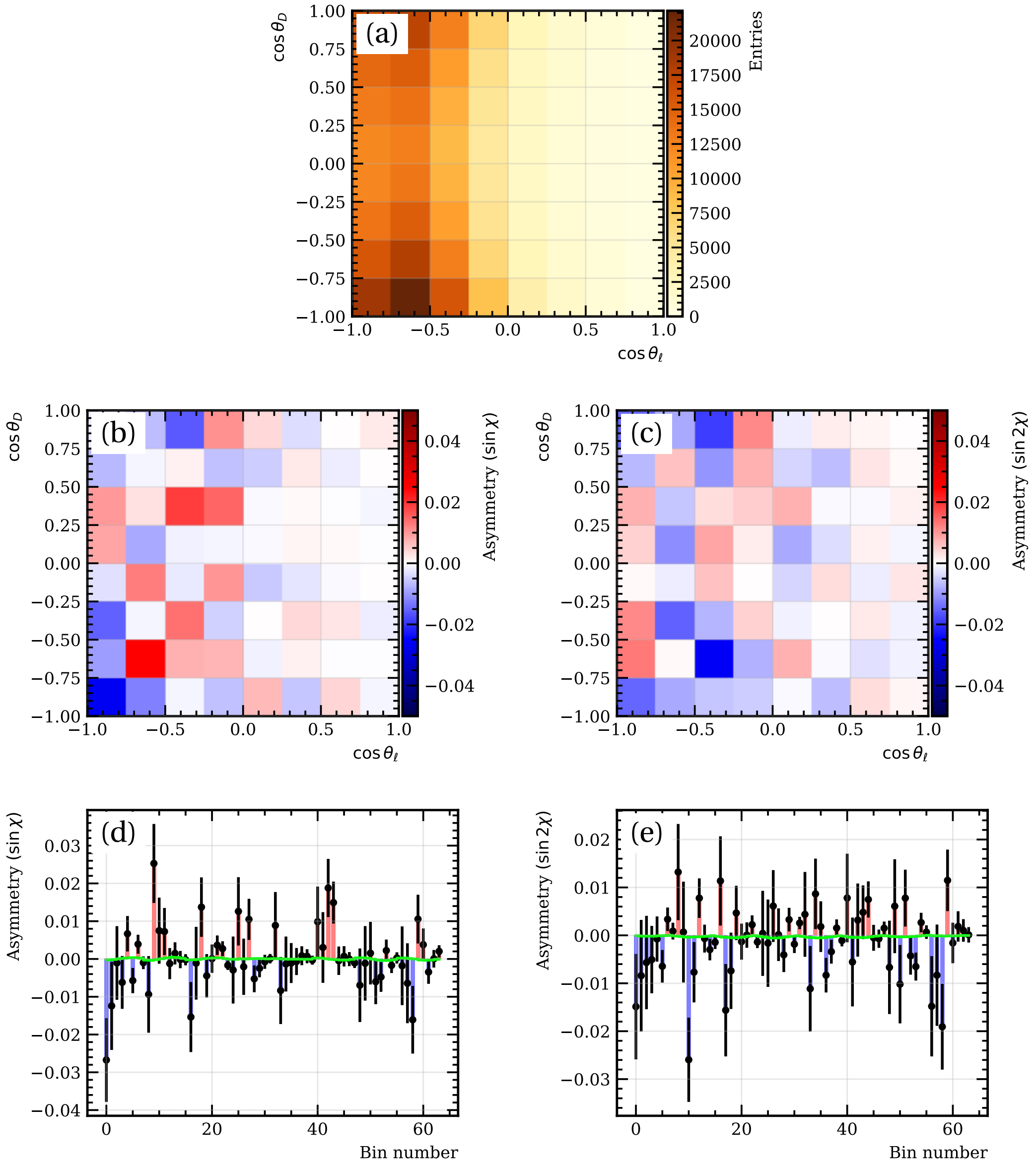

Figure 4.25: Binned density (a), binned 2D parity asymmetries (b,c) and flattened 1D parity asymmetries (d,e) of $\sin\chi$ and $\sin 2\chi$ terms in $(\cos\theta_D, \cos\theta_\ell)$ bins integrated over q^2 for the unweighted $B^0 \to D^{*-}D_s^{*+}$ simulation sample (no parity violation). Figures (d) and (e) also show the result of the best fit in green using the RH and PT templates.

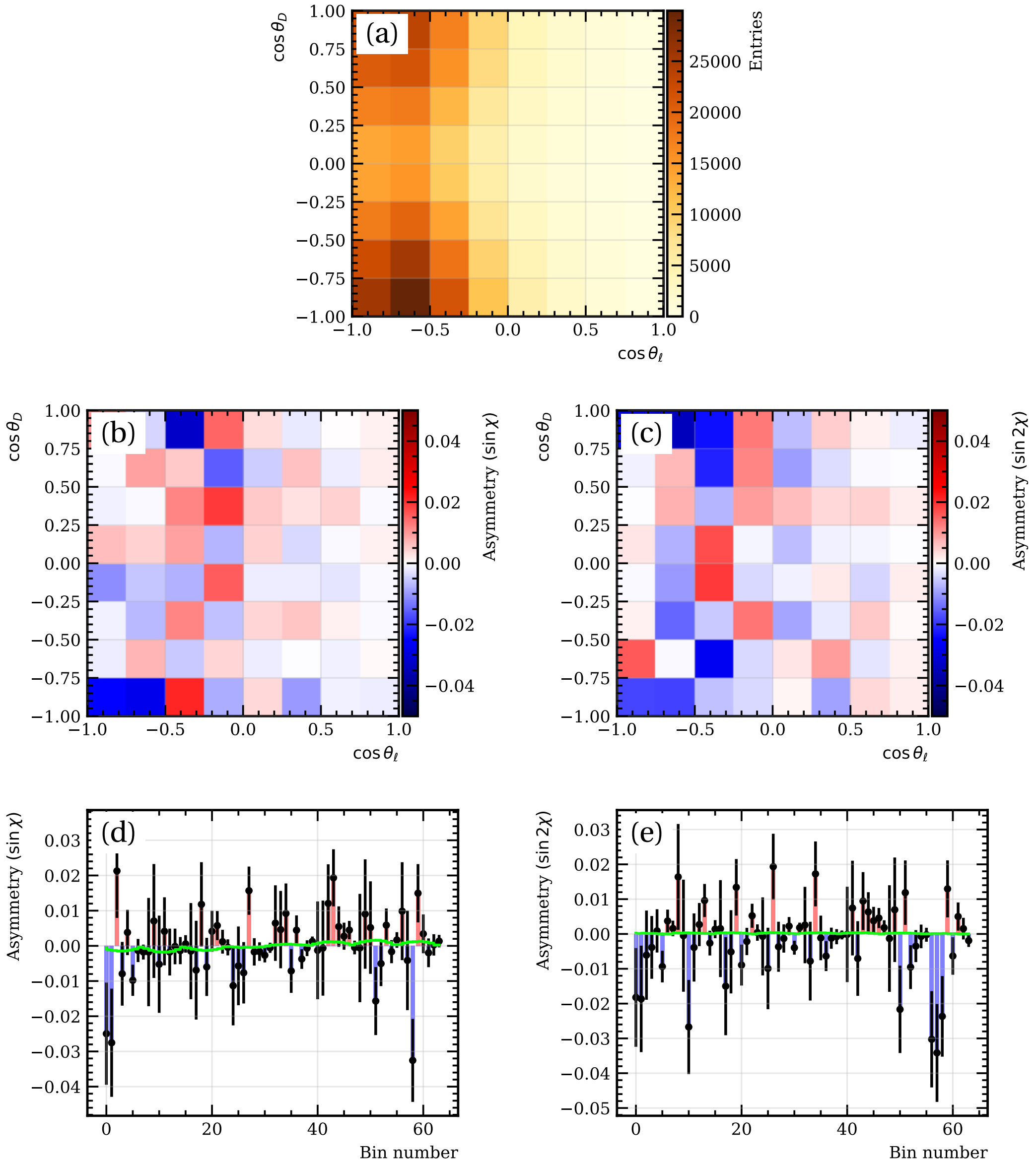

Figure 4.26: Binned density (a), binned 2D parity asymmetries (b,c) and flattened 1D parity asymmetries (d,e) of $\sin\chi$ and $\sin 2\chi$ terms in $(\cos\theta_D, \cos\theta_\ell)$ bins integrated over q^2 for the weighted $B^0 \to D^{*-} D_s^{*+}$ simulation sample (maximal parity violation). Figures (d) and (e) also show the result of the best fit in green using the RH and PT templates.

Data-driven backgrounds

In order to estimate the biases on the NP couplings that may arise from the non-physical backgrounds, the three samples derived from data described in Sec. 4.3.2, i.e. the misID and the true- and fake-D^* combinatorics, are used to build the $\sin\chi$ and $\sin 2\chi$ asymmetries and fit them with the RH and PT template model. Unlike the previously discussed backgrounds which only affected the parity asymmetry, since these are not physical backgrounds, they may contribute in both P and CP asymmetries. Fig. 4.27-4.32 show the 2D densities, 2D asymmetries and 1D flattened asymmetries for the three samples for both parity and CP templates. The results of the fit are given in Tab. 4.20 and Tab. 4.21. The misID sample shows a small bias of less than 2 sigma in both $\mathrm{Im}(g_R)$ and $\mathrm{Im}(g_P g_T^*)$ in the CP asymmetry case and in $\mathrm{Im}(g_R)$ only for the P asymmetry. In addition, the true D^* combinatorial sample shows a bias less than 2 sigma in $\mathrm{Im}(g_R)$ in both CP and P asymmetries with no bias seen in $\mathrm{Im}(g_P g_T^*)$. The fake D^* combinatorial shows no bias in either $\mathrm{Im}(g_R)$ or $\mathrm{Im}(g_P g_T^*)$. Nevertheless, the magnitudes of these biases have to be normalised to the number of background events found in the data sample. The contributions of these backgrounds were determined by the fit discussed in Sec. 4.3 and the measured fractions are used to place upper limit values on the systematic bias coming from them. The final values for the bias and for the assigned systematic uncertainties due to the three data-driven backgrounds are given in Chapter 5.

Bias source	$\Delta\,\mathrm{Im}(g_R)$	$\Delta\,\mathrm{Im}(g_P g_T^*)$
misID	-0.0105 ± 0.0046	0.0007 ± 0.0011
Fake D^* comb	-0.0008 ± 0.0208	0.0049 ± 0.0049
True D^* comb	0.0190 ± 0.0099	-0.0023 ± 0.0027

Table 4.20: Fitted values of the NP couplings from the binned parity asymmetry fit to the three data derived samples

Bias source	$\Delta\,\mathrm{Im}(g_R)$	$\Delta\,\mathrm{Im}(g_P g_T^*)$
misID	-0.0070 ± 0.0046	0.0022 ± 0.0012
Fake D^* comb	0.0198 ± 0.0208	0.0019 ± 0.0049
True D^* comb	0.0134 ± 0.0099	0.00006 ± 0.00273

Table 4.21: Fitted values of the NP couplings from the binned CP asymmetry fit to the three data derived samples

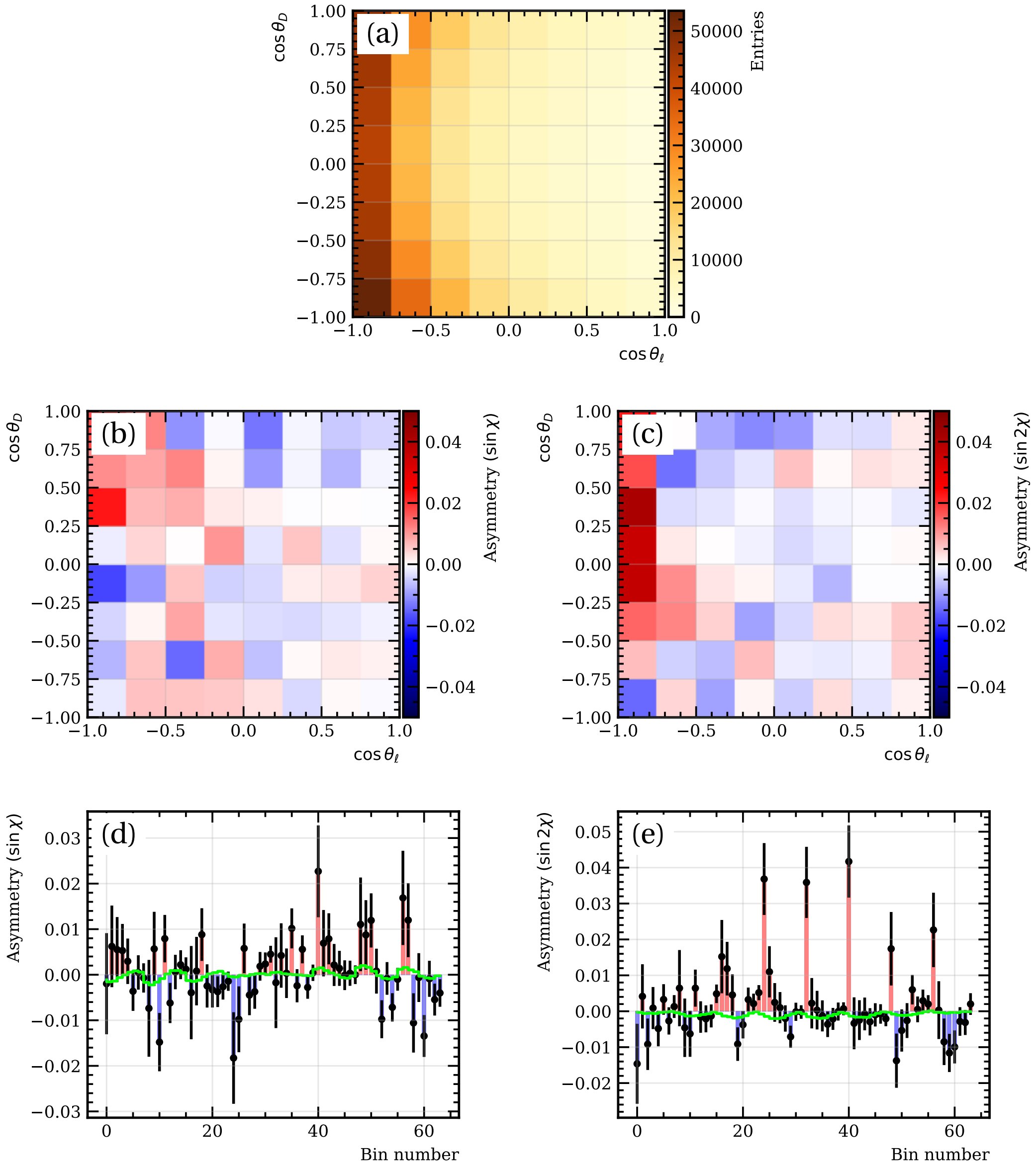

Figure 4.27: Binned density (a), binned 2D parity asymmetries (b,c) and flattened 1D parity asymmetries (d,e) of $\sin\chi$ and $\sin 2\chi$ terms in $(\cos\theta_D, \cos\theta_\ell)$ bins integrated over q^2 for the misID sample. Figures (d) and (e) also show the result of the best fit in green using the RH and PT templates.

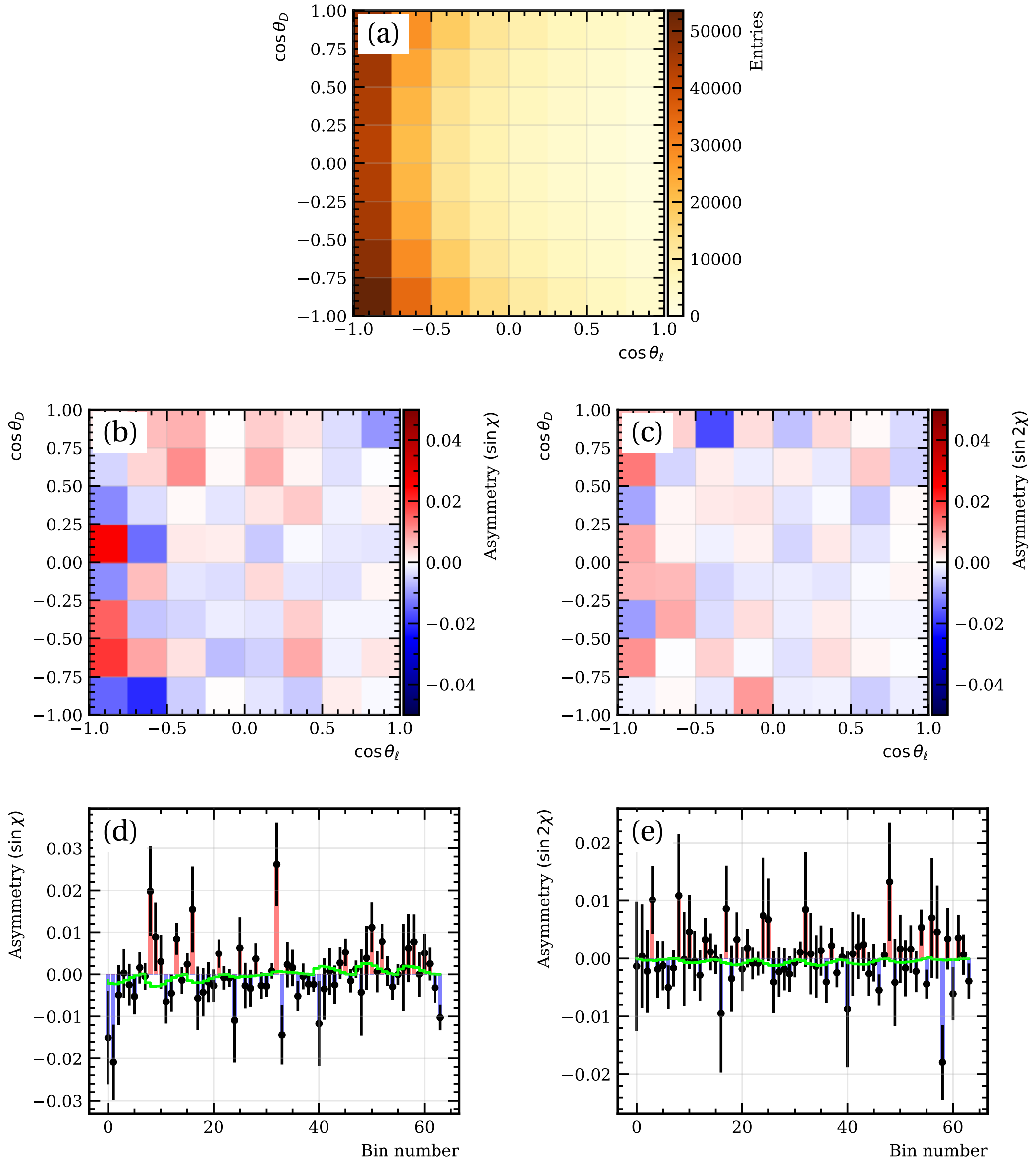

Figure 4.28: Binned density (a), binned 2D *CP* asymmetries (b,c) and flattened 1D *CP* asymmetries (d,e) of $\sin\chi$ and $\sin 2\chi$ terms in $(\cos\theta_D, \cos\theta_\ell)$ bins integrated over q^2 for the misID sample. Figures (d) and (e) also show the result of the best fit in green using the RH and PT templates.

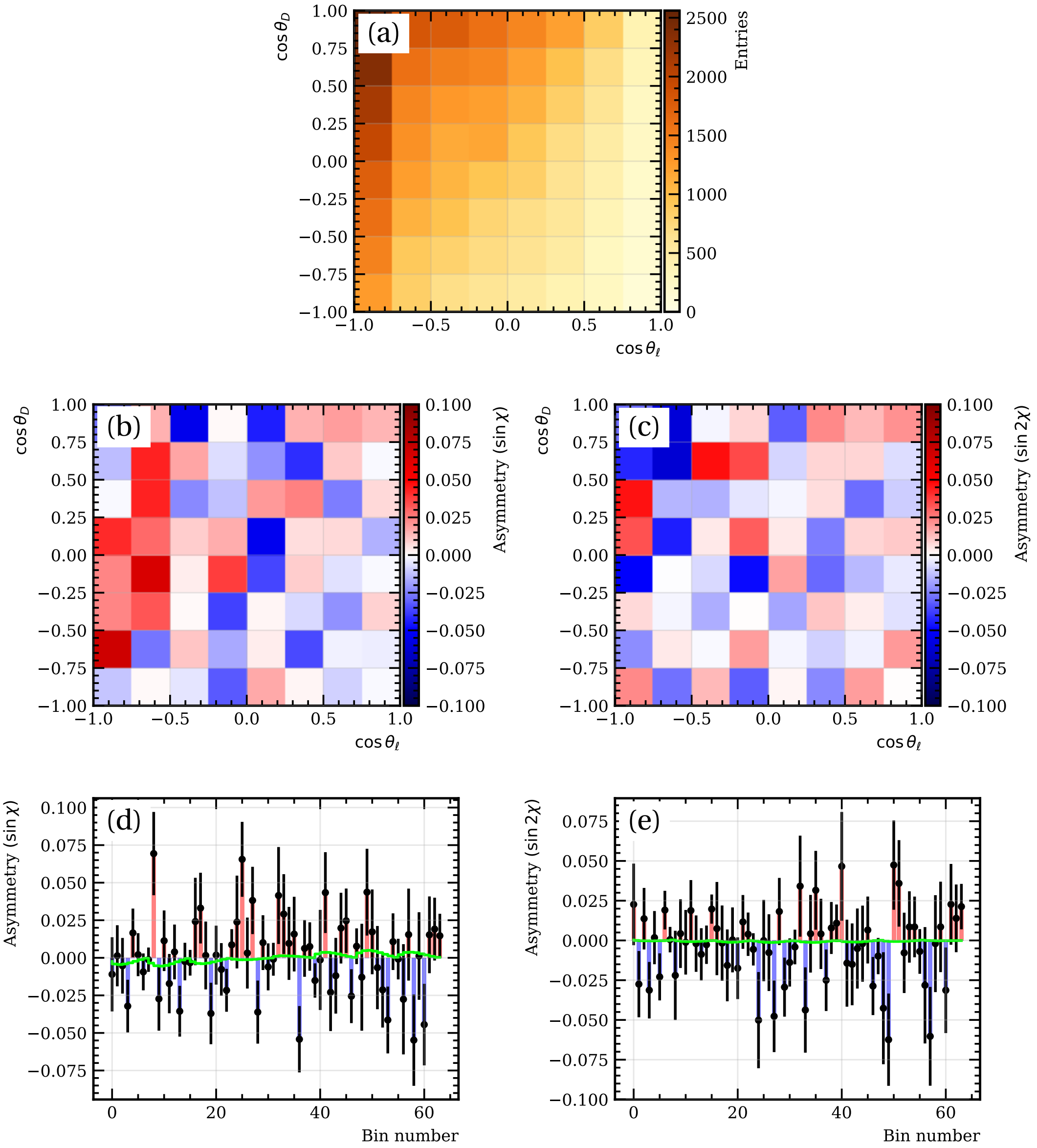

Figure 4.29: Binned density (a), binned 2D parity asymmetries (b,c) and flattened 1D parity asymmetries (d,e) of $\sin\chi$ and $\sin 2\chi$ terms in $(\cos\theta_D, \cos\theta_\ell)$ bins integrated over q^2 for the fake D^* sample. Figures (d) and (e) also show the result of the best fit in green using the RH and PT templates.

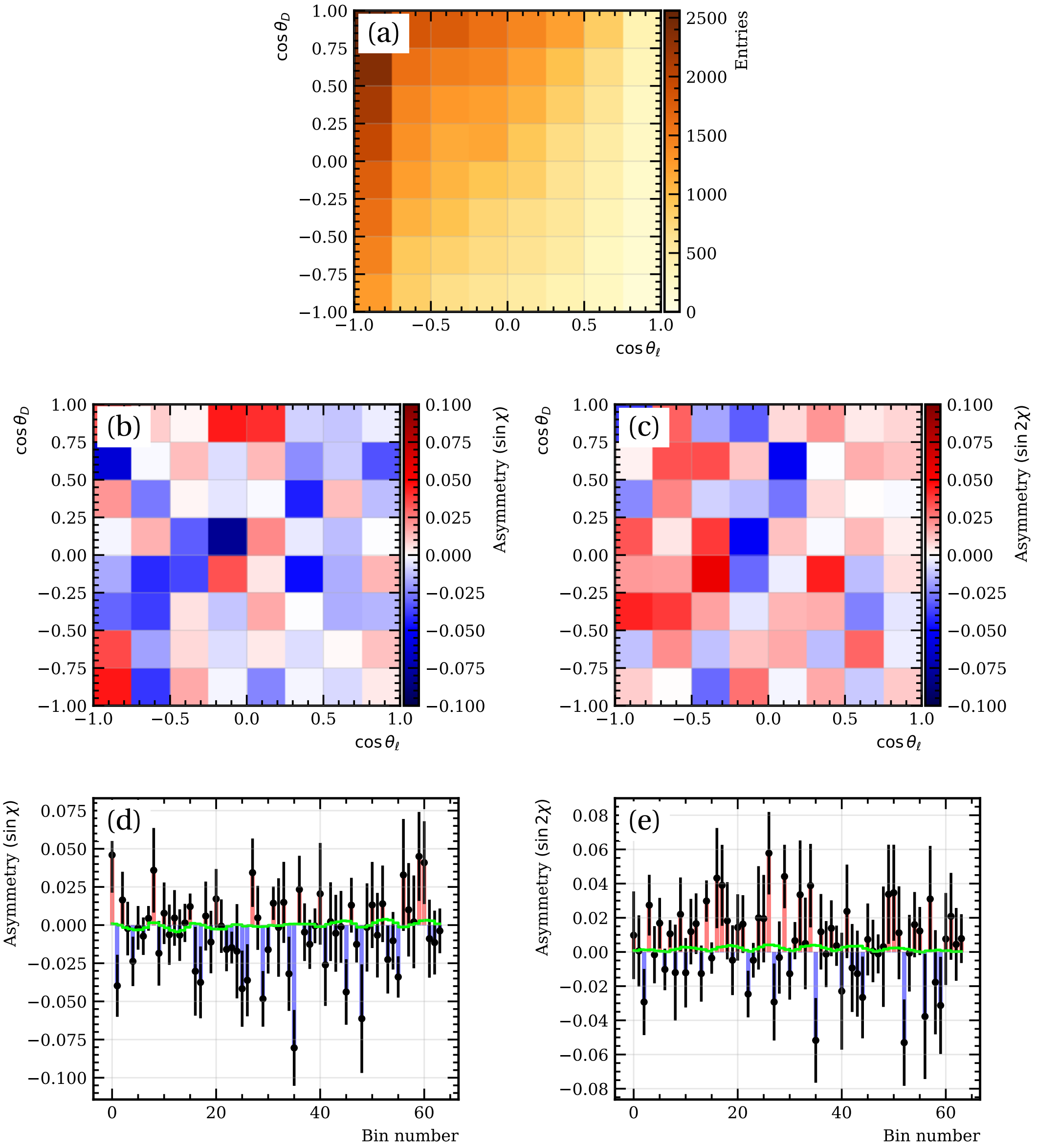

Figure 4.30: Binned density (a), binned 2D *CP* asymmetries (b,c) and flattened 1D *CP* asymmetries (d,e) of $\sin\chi$ and $\sin 2\chi$ terms in $(\cos\theta_D, \cos\theta_\ell)$ bins integrated over q^2 for the fake D^* sample. Figures (d) and (e) also show the result of the best fit in green using the RH and PT templates.

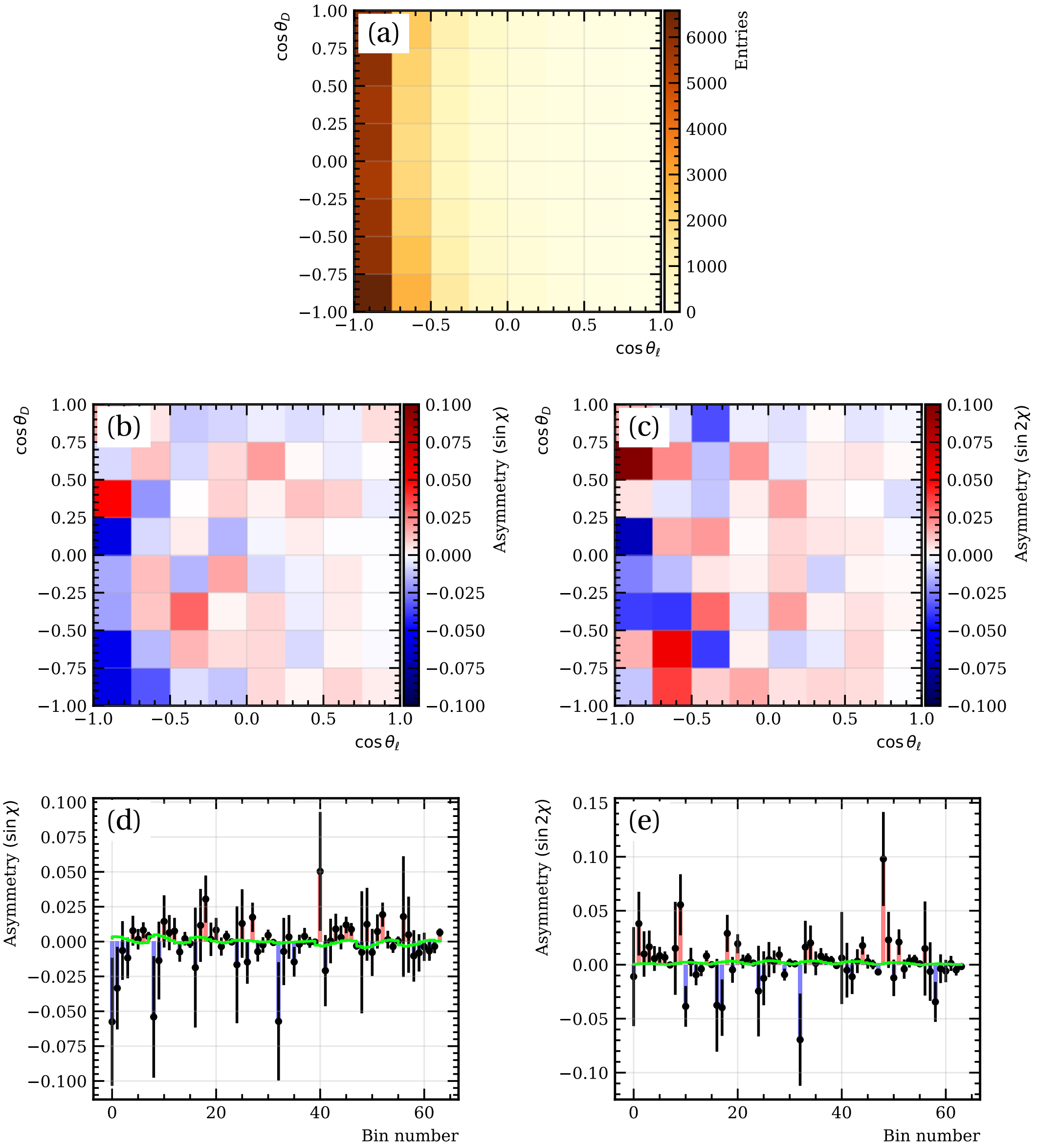

Figure 4.31: Binned density (a), binned 2D parity asymmetries (b,c) and flattened 1D parity asymmetries (d,e) of $\sin\chi$ and $\sin 2\chi$ terms in $(\cos\theta_D, \cos\theta_\ell)$ bins integrated over q^2 for the true D^* sample. Figures (d) and (e) also show the result of the best fit in green using the RH and PT templates.

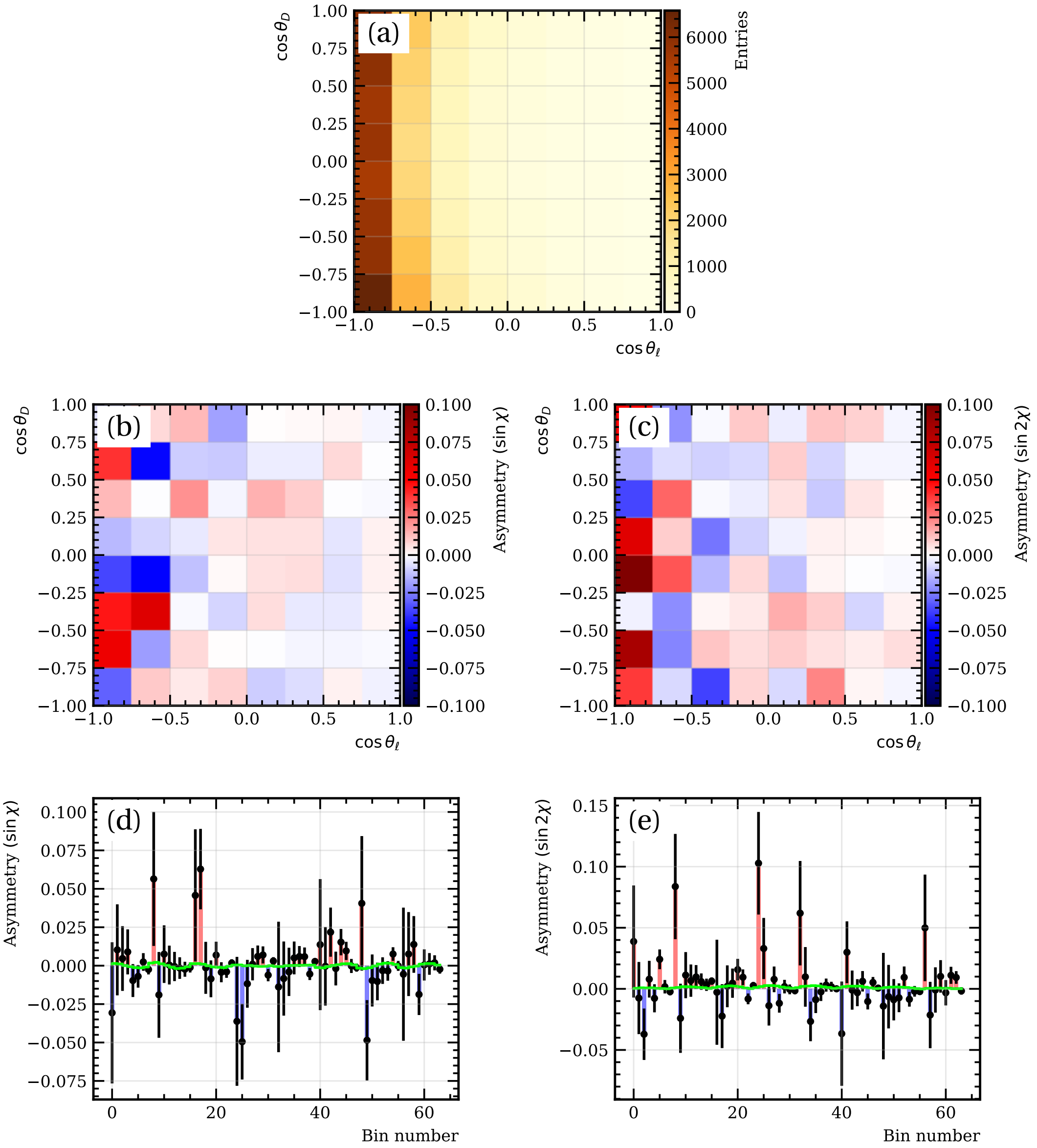

Figure 4.32: Binned density (a), binned 2D *CP* asymmetries (b,c) and flattened 1D *CP* asymmetries (d,e) of $\sin\chi$ and $\sin 2\chi$ terms in $(\cos\theta_D, \cos\theta_\ell)$ bins integrated over q^2 for the true D^* sample. Figures (d) and (e) also show the result of the best fit in green using the RH and PT templates.

4.6.2 P-odd instrumentation effects

The angular terms studied in this analysis are parity-odd in nature since they are proportional to $\sin\chi$ and $\sin 2\chi$ where the χ angle is intrinsically a parity-odd quantity. Therefore any chiral, i.e. asymmetric with respect to its mirror image, effect in the reconstruction procedure such as detector misalignments or reconstruction efficiencies that are not parity-even can introduce fake P-odd contributions in the reconstructed angular distribution. In particular, these effects can cause a bias in the χ angle and can therefore bias the measurement of the NP couplings.

The reconstructed distribution of events is given by the product of the total absolute amplitude squared which depends on kinematics and the total track reconstruction efficiency which depends on the track parameters, i.e. $|\mathcal{M}(\vec{\Theta}(\vec{\tau}^{(k)}))|^2\varepsilon(\vec{\tau}^{(k)})$[9] with k looping over the four final state charged tracks π, K, μ, π_S. Here the vector $\vec{\Theta} = (\theta_D, \theta_\ell, \chi, q^2)$ describes the kinematics and $\vec{\tau} = (x_0, y_0, t_x, t_y, 1/p)$ is the vector of reconstructed charged track parameters where x_0, y_0 are the track coordinates in the x-y plane at $z = 0$, t_x, t_y are the track slopes defined as $t_{x,y} = \frac{p_{x,y}}{p}$ and p is the momentum of the charged track. The total amplitude $\mathcal{M}(\vec{\tau}^{(k)})$ is invariant under rotations of the azmithual angle $\phi \in [-\pi, \pi]$ around the z-axis, i.e. rotations in the x-y plane, defined as

$$\phi = \arctan\frac{t_x}{t_y}. \tag{4.27}$$

However, if the efficiency $\varepsilon(\vec{\tau}^{(k)})$ contains terms that do not average out after integration over ϕ, this can influence the observable density and can give rise to fake parity-odd terms in the angular distribution. More specifically, the $\sin\chi$ angle can be expressed in the lab frame in spherical coordinates as

$$\sin\chi = \sum_{i \neq j} S_{ij} \cdot \sin\left(\phi_i - \phi_j\right), \tag{4.28}$$

where i, j label the B and the final state tracks $i, j \in \{B, K, \pi, \mu, \pi_S\}$, ϕ_i is the azimuthal angle of particle i as defined in Eq. 4.27 and S_{ij} are parity-even functions of the kinematics. Terms in the efficiency that are functions of $\sin\left(\phi_i - \phi_j\right)$ can thus give rise to a bias in $\sin\chi$. Possible instrumentation effects include:

- VELO misalignment or VELO efficiency can produce terms such as $\sin\left(\phi_B - \phi_i\right)$. These are single track efficiency terms.
- Tracking efficiency that has different dependence on ϕ for different particle species, i.e. PID efficiency, can produce terms such as $\sin\left(\phi_i - \phi_j\right)$ with $i \neq j \neq B$. These are two-track efficiency terms.

---

[9] The kinematic parameters are a function of the reconstructed track parameters so in principle we can write $\mathcal{M}(\vec{\Theta}(\vec{\tau}^{(k)})) = \mathcal{M}(\vec{\tau}^{(k)})$

These instrumentation effects are studied in the following sections, and the asymmetry bias arising from them is estimated and used to assign upper limit systematic uncertainties.

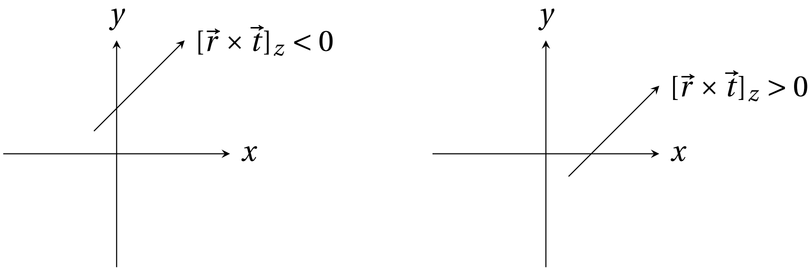

Figure 4.33: Illustration of“Left-handed” and “right-handed” bias in the track parameters relative to the original production point at $x = y = 0$.

4.6.2.1 VELO misalignment

Since the reconstruction of the kinematic parameters in the $B^0 \to D^{*-}\mu^+\nu_\mu$ decay at LHCb relies on the vertex position information from the VELO subdetector, misalignments of the VELO can introduce biases in the reconstructed parameters. The reconstruction procedure was discussed in Sec. 4.2. More specifically, these misalignments can systematically bias the tracks left and right with respect to their origin, i.e. bias the impact parameter of the tracks either left or right with respect to the PV, as illustrated in Fig. 4.33. This will induce a parity-odd effect in the reconstruction of the kinematic parameters, in particular in the χ angle which in turn will bias the asymmetries and the NP couplings.

A description of the VELO detector was given in Sec. 3.2.1. It consists of two movable halves that are retracted at each fill and then closed when the beams are stable. In Run 2, the VELO alignment procedure calibrates the positions of the two halves after each fill. The misalignment of the two halves with respect to each other can introduce a significant uncertainty in the relative positions between the secondary and primary vertex and consequently in the reconstruction of the P-odd quantity χ. Misalignments of the VELO as a whole do not affect the relative vertex position measurements and thus are not considered here.

The VELO alignment procedure calibrates the positions of the two VELO halves in terms of six degrees of freedom: three translations and three rotations around the x, y, z axes. These misalignment operations are illustrated in Fig. 4.34. The alignment of the VELO halves is mostly sensitive to T_x translations since this is the axis along which they are retracted and closed during each fill. An alignment precision of about 5 μm in T_x is reported in [104] using Run 1 data. Out of the six translations and rotations, the most dangerous ones are T_y and R_x, since they are the only ones that can produce parity-odd effects in the reconstruction.

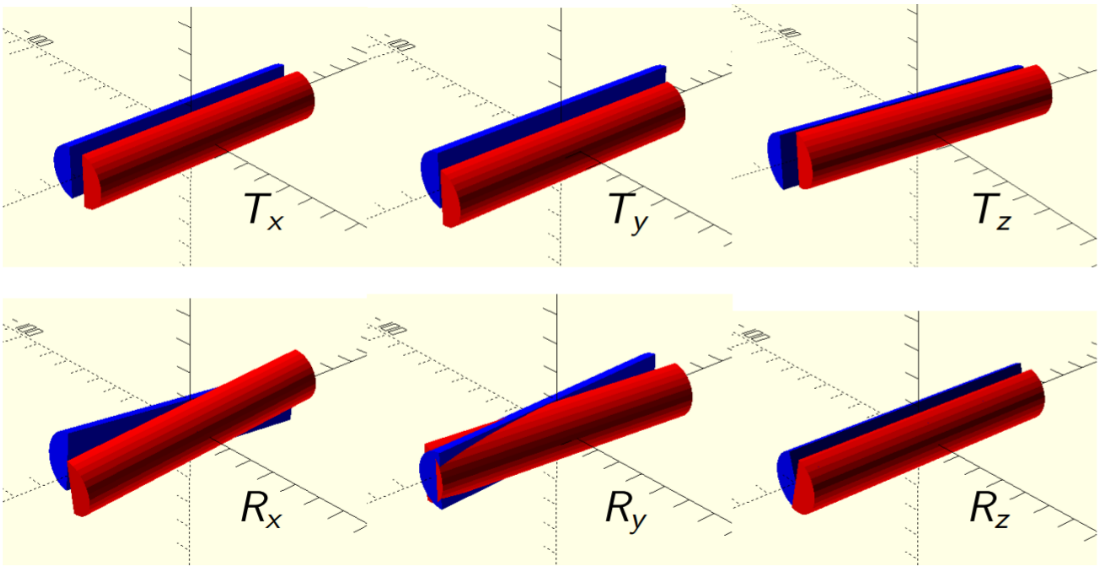

Figure 4.34: Illustration of the six misalignment operations between the two halves of the VELO, three translations T_x, T_y, T_z and three rotations R_x, R_y, R_z along the three axes.

The misalignment is applied in the signal simulation sample by translating or rotating the track parameters in opposite directions for $t_x > 0$ and $t_x < 0$ tracks, i.e. for tracks with positive and negative slopes. The displaced tracks are then fed to the kinematic refit algorithm discussed in Sec. 4.2.2 such that the vertices are refitted and the displacements are propagated to the reconstructed kinematic parameters. The misalignments introduce a bias in the paremeters such that the new parameters $\vec{\Theta}' = \vec{\Theta} + \delta\vec{\Theta}$ are reconstructed. Since the asymmetry templates are obtained by reweighting the $\cos\theta_\ell$ *vs.* $\cos\theta_D$ 2D binned density with the $\sin\chi$ and $\sin 2\chi$ weights, the bias in χ due to any of the six misalignments will introduce a bias in the asymmetry

$$\delta A = \frac{\partial P}{\partial \chi}\frac{\partial \chi}{\partial \rho_k}\rho_k, \tag{4.29}$$

where P is either $\sin\chi$ or $\sin 2\chi$ and ρ_k is the magnitude of one of the translation or rotation operations. As such, the following weights are used instead of $\sin\chi$ and $\sin 2\chi$ to obtain the 2D asymmetries

$$\begin{aligned} w_{\sin\chi} &= \cos\chi(\chi_{\rho_k} - \chi)\frac{\rho_k}{\Delta\rho_k}, \\ w_{\sin 2\chi} &= 2\cos 2\chi(\chi_{\rho_k} - \chi)\frac{\rho_k}{\Delta\rho_k}, \end{aligned} \tag{4.30}$$

where the $\cos\chi$ and $\cos 2\chi$ terms come from the $\partial P/\partial\chi$ term in Eq. 4.29, the $(\chi_{\rho_k} - \chi)/\Delta\rho_k$ term is the finite difference estimate of $\partial\chi/\partial\rho_k$ and χ_{ρ_k} is the misaligned χ angle due to operation k. Once $\partial\chi/\partial\rho_k$ is calculated in the simulation using an arbitrary small misalignment $\Delta\rho_k$, the effect of a misalignment with any magnitude can then be obtained by multiplying by ρ_k.

The effect of the misalignment on the asymmetries is evaluated using SM signal simulation where the misalignment values shown in Tab. 4.22 are applied and the weights given in Eq. 4.30 are used. The estimates of the T_x and T_y alignment precision given in 4.22 are obtained via a data-driven study using a $B^+ \to J/\psi K^+$ control sample which is described in the next section. In particular, for the dangerous parity-odd T_y operation, a misalignment of about 2 μm is found. Six misaligned simulation samples are thus obtained and used to construct the asymmetries, fit them with the NP template model and extract the bias on the NP couplings in the same way as for the various background samples in the previous sections.

The results of the fit to the six samples for parity and *CP* asymmetries are summarized in Tab. 4.24 and 4.23. The T_y and R_x are the only P-odd operations so it is expected that they will be the largest source of bias. Indeed, in the *CP* asymmetries case, the T_y misalignment shows the largest bias in both $\text{Im}(g_R)$ and $\text{Im}(g_P g_T^*)$ couplings, while the R_x misalignment shows no significant bias in either of the two NP couplings. In the case of parity asymmetries, no significant bias is observed due to any of the misalignment operations. The fact that the T_y misalignment bias in the *CP* case is one order of magnitude larger than in the parity case can be understood using the following argument. The *CP* asymmetry is the sum of the B and $\overline{B}$ components and does not keep track of the flavor of the B, while the parity asymmetry takes the flavor of the B into account. Since the tracking and vertexing in the VELO is insensitive to the charges of the tracks, i.e. there is no magnetic field inside the VELO, it is not surprising that the bias is more significant in the *CP* asymmetry case. Fig. 4.35 and 4.36 show the 2D and fitted 1D *CP* and parity asymmetries in the case of T_y misalignment of 2 μm. The asymmetry plots for the other five misalignment samples are given in Appendix *B*. The asymmetries due to T_y misalignment have a different pattern than the ones generated in the NP cases and their contribution can in principle be determined by including them as an independent component in the fit to data. However, for the purposes of this thesis, a systematic uncertainty is assigned based on the bias in the NP couplings determined by the fit.

Operation	Value (ρ_k)
T_x	5 μm
T_y	2 μm
T_z	10 μm
$R_{x,y}$	100 μrad
R_z	1 m rad

Table 4.22: Misalignment values applied in simulation

Translation/rotation	$\Delta\,\mathrm{Im}(g_R)$	$\Delta\,\mathrm{Im}(g_P g_T^*)$
T_x	-0.00049 ± 0.00084	0.00007 ± 0.00024
T_y	-0.00037 ± 0.00084	0.00002 ± 0.00024
T_z	-0.00062 ± 0.00085	0.00002 ± 0.00024
R_x	0.00022 ± 0.00084	0.00001 ± 0.00024
R_y	-0.00015 ± 0.00084	-0.00004 ± 0.00024
R_z	-0.00025 ± 0.00084	0.00002 ± 0.00024

Table 4.23: Fitted values of the NP couplings from the binned parity asymmetry fit for the translational and rotational components of VELO halves misalignment

Translation/rotation	$\Delta\,\mathrm{Im}(g_R)$	$\Delta\,\mathrm{Im}(g_P g_T^*)$
T_x	-0.00004 ± 0.00084	-0.00007 ± 0.00022
T_y	-0.00374 ± 0.00084	-0.00031 ± 0.00023
T_z	0.00019 ± 0.00084	-0.00007 ± 0.00023
R_x	-0.00022 ± 0.00084	-0.00004 ± 0.00023
R_y	-0.00026 ± 0.00085	-0.00005 ± 0.00023
R_z	-0.00152 ± 0.00084	-0.00021 ± 0.00023

Table 4.24: Fitted values of the NP couplings from the binned *CP* asymmetry fit for the translational and rotational components of VELO halves misalignment

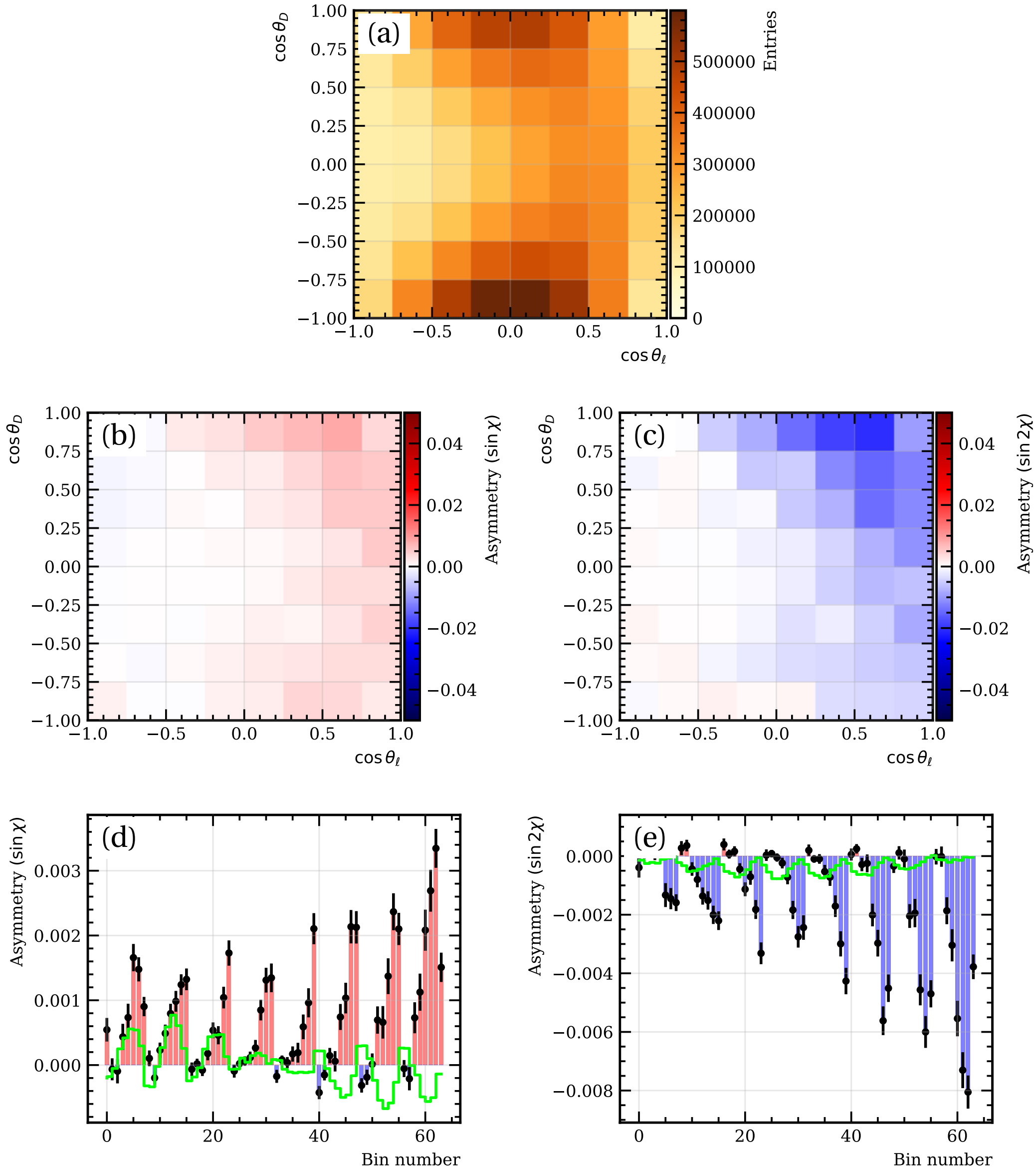

Figure 4.35: Binned density (a), binned 2D *CP* asymmetries (b,c) and flattened 1D *CP* asymmetries (d,e) of $\sin\chi$ and $\sin 2\chi$ terms in $(\cos\theta_D, \cos\theta_\ell)$ bins integrated over q^2 for the T_y misalignment $B^0 \to D^{*-}\mu^+\nu_\mu$ simulation sample. Figures (d) and (e) also show the result of the best fit in green using the RH and PT templates.

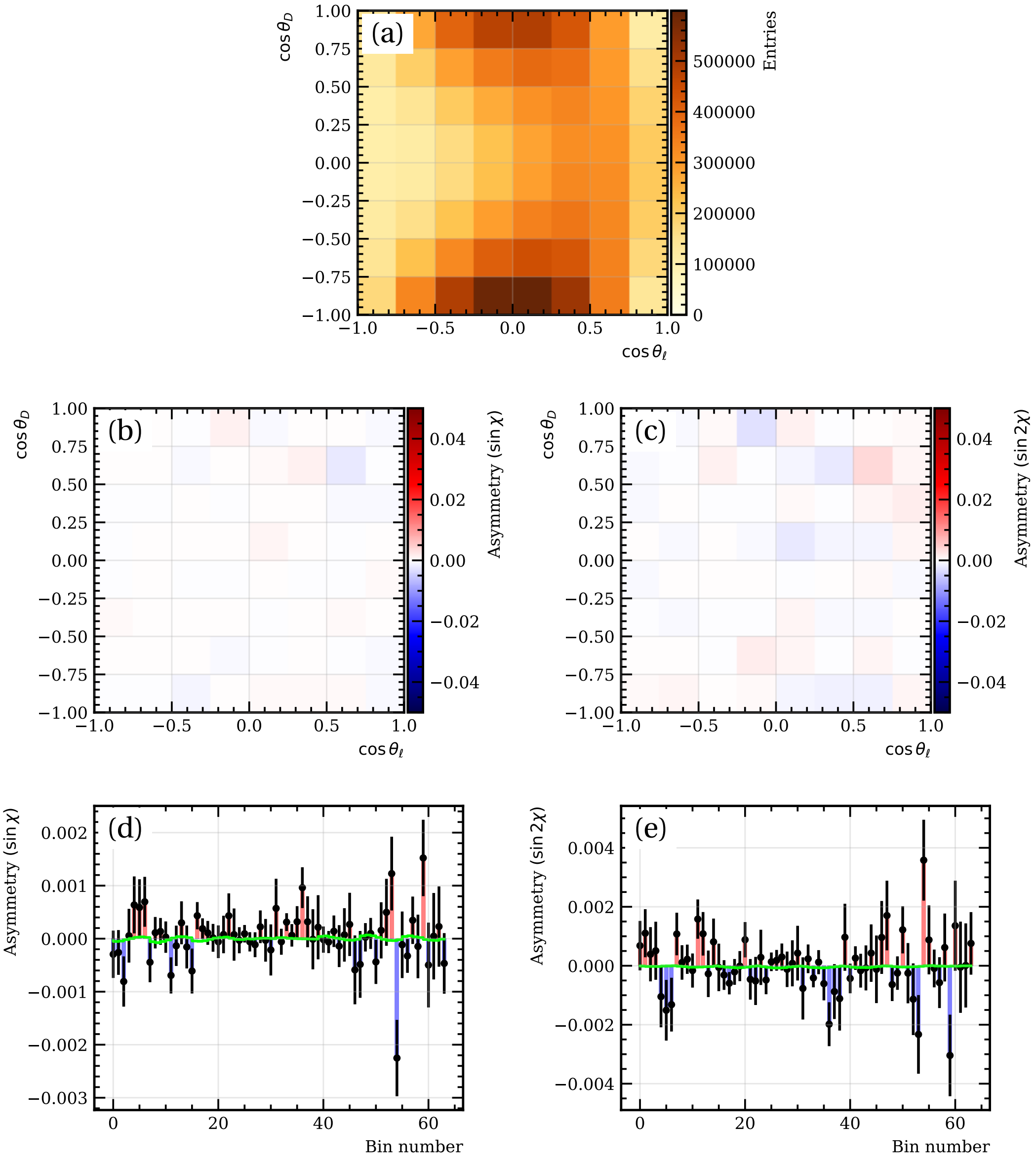

Figure 4.36: Binned density (a), binned 2D parity asymmetries (b,c) and flattened 1D parity asymmetries (d,e) of $\sin\chi$ and $\sin 2\chi$ terms in $(\cos\theta_D, \cos\theta_\ell)$ bins integrated over q^2 for the T_y misalignment $B^0 \to D^{*-}\mu^+\nu_\mu$ simulation sample. Figures (d) and (e) also show the result of the best fit in green using the RH and PT templates.

VELO misalignment calibration

In order to understand the magnitude of the VELO misalignments and correct for them, in particular with respect to the (parity-odd) T_y translation, a fully reconstructed, high-statistics data control sample of $B^+ \to J/\psi[\to \mu^+\mu^-]K^+$ decays is used. The misalignment of the two VELO halves with respect to each other in the x-y plane can introduce a "left-right" asymmetry in the vertex positions, which can introduce a parity-odd effect in the reconstruction of the kinematic parameters and will ultimately bias the measurement of the CP-violating variables, as discussed in the previous section. The bias in the position of the PV reconstructed using tracks passing entirely through either the left of the right VELO halves introduced by the misalignment of the two VELO halves along the x-axis is illustrated in Fig. 4.37.

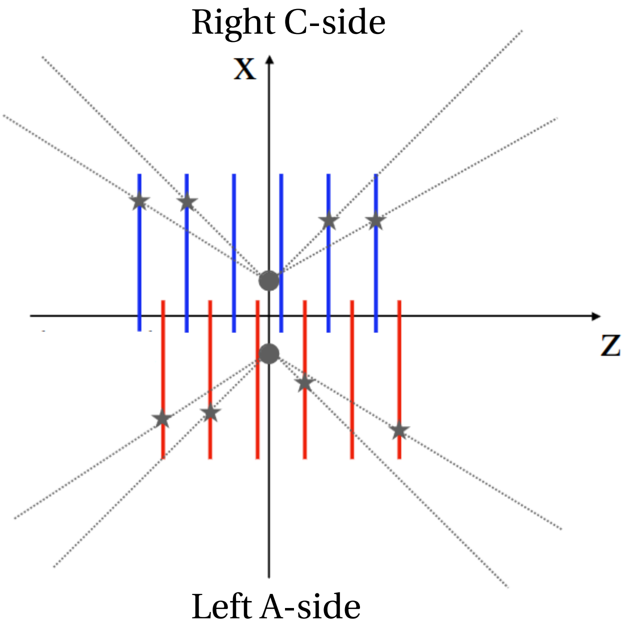

Figure 4.37: Reconstruction of the same PV using tracks flying separately in each VELO half. The misalignment along the x-axis introduces a bias in the vertex position.

The signed impact parameter (SIP) of the B in the $x-y$ plane, i.e. its z-component, can be used as a measure of the systematic bias either left or right with respect to the PV and is defined as:

$$SIP = [\vec{r} \times \vec{n}]_z = (x_{BV} - x_{PV})\frac{p_y}{p_T} - (y_{BV} - y_{PV})\frac{p_x}{p_T}, \tag{4.31}$$

where $\vec{r} = (x_{BV} - x_{PV}, y_{BV} - y_{PV}, z_{BV} - z_{PV})$, $\vec{n} = (\frac{p_x}{p_\mathrm{T}}, \frac{p_y}{p_\mathrm{T}}, \frac{p_z}{p_\mathrm{T}})$ and (x_{BV}, y_{BV}) are the coordinates of the B decay vertex, (x_{PV}, y_{PV}) are the coordinates of the primary vertex and (p_T, p_x, p_y) are the B meson transverse momentum and its $x-y$ components. The SIP defined in Eq. 4.31 is a parity-odd quantity and in the ideal case of no misalignments or any other parity-odd effects in reconstruction efficiency, this quantity is expected to be zero on average. The dependence of the SIP parameter on the angle ϕ of the B candidate (defined in Eq. 4.27) consists of two sinusoids with different phases and amplitudes in general, for $\phi > 0$ and $\phi < 0$. In addition, there exists a transitional region between the two sinusoids which consists of B decays where tracks are reconstructed in both VELO halves. The dependence is shown in Fig. 4.38 using all events for the 2016 `MagDown` data sample.

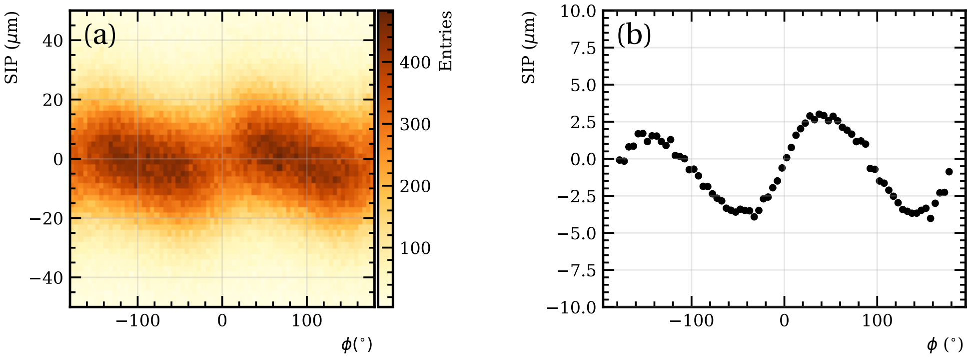

Figure 4.38: 2D event density in SIP *vs.* ϕ (a) and SIP as a function of ϕ (b) for the 2016 `MagDown` $B^+ \to J/\psi K^+$ data sample

Although after averaging out over ϕ only a small bias remains in $\langle SIP \rangle$ (up to 1 μm), large variations with ϕ of up to 5 μm are observed in data. This result indicates the misalignment of the two VELO halves with respect to the axes of the x-y plane. In the case of the $B^+ \to J/\psi K^+$ simulation sample, the SIP as a function of ϕ shows no significant bias indicating that there is no misalignment present in simulation, i.e. simulation and reconstruction use the same VELO coordinates. This is shown in Fig. 4.39 for the 2016 `MagDown` simulation sample.

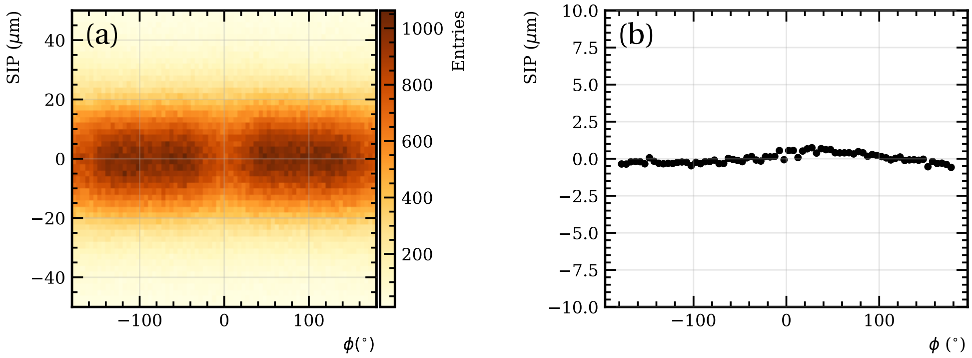

Figure 4.39: 2D event density in SIP *vs.* ϕ (a) and SIP as a function of ϕ (b) for the 2016 `MagDown` $B^+ \to J/\psi K^+$ simulation sample

Since the SIP has a sinusoidal dependence on the angle ϕ of B candidate, the dependence can be parametrized in the following way

$$SIP(\phi;\Delta x,\Delta y) = \sqrt{\Delta x^2 + \Delta y^2}\cos\big(\phi - \mathrm{atan2}(\Delta y, -\Delta x)\big), \tag{4.32}$$

where the Δx and Δy parameters are the misalignment biases of the VELO halves along the x and y axes. A fit is performed in order to determine these bias parameters by minimizing the following χ^2 function

$$\chi^2 = \sum_i \frac{(y_i - SIP(\phi;\Delta x,\Delta y))^2}{\sigma_i^2}, \tag{4.33}$$

where y_i and σ_i are the observed SIP values as a function of ϕ and their uncertainties and $SIP(\phi;\Delta x,\Delta y)$ is the function defined in Eq. 4.32. The fit is performed separately on events where all tracks are reconstructed purely in either left or right VELO halves, as shown in Fig. 4.40. Therefore, the misalignment biases are obtained separately for the left $(\Delta x_-, \Delta y_-)$ and right $(\Delta x_+, \Delta y_+)$ VELO halves. In addition, the points in the transitional region around $\phi = 0$ and $\phi = \pm\pi$, i.e. B candidates flying “up” and “down”, are not included in the fit since these points have low statistics and most of the B candidates in these regions have tracks which do not pass exclusively through one half only. These regions are therefore difficult to parametrize and are excluded from the fit. The fit results for the different data taking years of Run 1 and Run 2 $B^+ \to J/\psi K^+$ data samples across the two magnet polarities are given in Tab. 4.25. The results show that the direction of the bias is consistent across all years and smaller in Run 1 than in Run 2 samples. The values of the misalignment biases are on average about 5 μm along the x-axis and 1-2 μm along the y-axis. The results indicate that the misalignment is present mostly along x since this is the direction along which the two halves are opened and closed during each fill, while the misalignment along y is several times smaller.

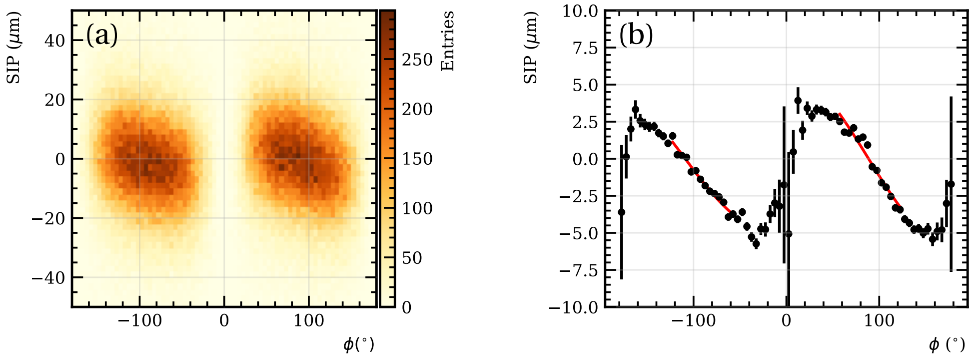

Figure 4.40: 2D event density in SIP *vs.* ϕ (a) and SIP as a function of ϕ (b) for the 2016 `MagDown` $B^+ \to J/\psi K^+$ data sample with tracks reconstructed entirely in either left or right VELO halves. The fit result, separate for each half, is shown in red.

Polarity	Shift	11	12	16	17	18
MagDown	Δx_+	-4.51 ± 0.25	-3.24 ± 0.18	-5.82 ± 0.14	-7.46 ± 0.13	-6.81 ± 0.12
	Δy_+	-0.44 ± 0.09	-0.45 ± 0.06	-0.15 ± 0.05	-0.54 ± 0.04	-0.72 ± 0.04
	Δx_-	2.71 ± 0.24	1.79 ± 0.18	4.53 ± 0.14	5.58 ± 0.13	5.73 ± 0.11
	Δy_-	-0.92 ± 0.09	1.58 ± 0.06	1.56 ± 0.05	1.87 ± 0.04	1.19 ± 0.04
MagUp	Δx_+	-4.02 ± 0.30	-2.42 ± 0.18	-5.67 ± 0.14	-6.93 ± 0.13	-6.92 ± 0.11
	Δy_+	-0.56 ± 0.10	-0.46 ± 0.06	0.40 ± 0.05	-0.32 ± 0.05	-0.33 ± 0.04
	Δx_-	2.47 ± 0.29	1.33 ± 0.18	4.11 ± 0.14	5.91 ± 0.13	5.77 ± 0.11
	Δy_-	-0.44 ± 0.10	1.63 ± 0.06	1.11 ± 0.05	1.30 ± 0.05	0.49 ± 0.04

Table 4.25: Fitted values of the misalignment biases in left and right VELO halves for the different years and magnet polarities of Run 1 and Run 2. All values are given in μm.

In order to correct for this effect, a procedure similar to the one described in Sec. 4.2 is implemented where each track state is shifted by either the (Δx_+, Δy_+) or (Δx_-, Δy_-) amounts determined by the fit (depending on which VELO half the track belongs to). The `DecayTreeFitter` algorithm is then used to refit the B vertex (the PV is not refitted since it is assumed that the shifts of the two VELO halves average out for a large number of tracks) and thus obtain a corrected set of coordinates for the B vertex. Using these corrected BV coordinates the SIP (Eq. 4.31) is recalculated and its dependence on ϕ is plotted. Fig. 4.41 shows the 2016 `MagDown` $B^+ \to J/\psi K^+$ data sample after the misalignment correction (the same plot before the correction was shown in Fig. 4.38). The figure shows that the bias is mostly removed and the remaining bias is $< 1\mu$m. The SIP *vs.* ϕ plots before and after applying the corrections with shifted track states for the rest of the Run 1 and Run 2 $B^+ \to J/\psi K^+$ control data samples are given in Appendix *D*.

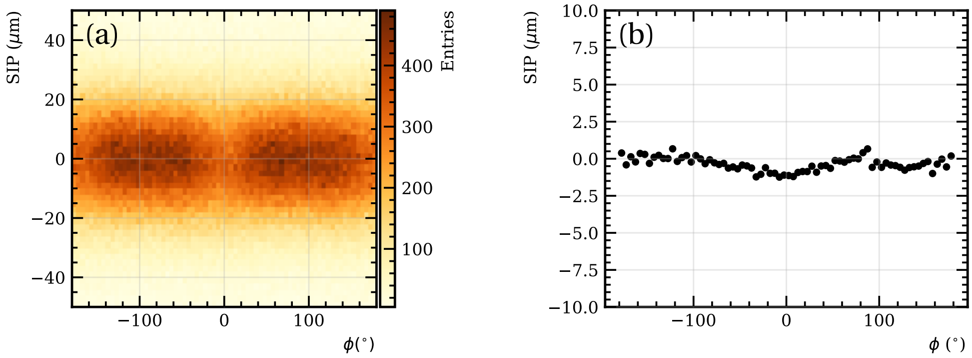

Figure 4.41: 2D event density in SIP *vs.* ϕ (a) and SIP as a function of ϕ (b) for the 2016 `MagDown` $B^+ \to J/\psi K^+$ data sample after correcting for the misalignment of the VELO

During Run 2, the alignment of the VELO was performed online, i.e. after the two halves of the VELO have been closed. The positions of the VELO halves are calibrated automatically at the beggining of each fill and as data is being recorded by LHCb, the positions are updated online if the variations with respect to either of the six alignment operations exceed a specific threshold. In particular, for the T_x and T_y translations, the threshold is 1.5 μm. An LHC fill lasts about 12h, however the LHCb data-taking scheme consists of *runs*, which typically last about one hour. Therefore, during one fill, the data collected by LHCb is split into several runs indexed by the so-called *run number*. Consequently, as the alignment is run online while data is being collected, the positions of the VELO halves can vary with different run numbers. Fig. 4.42 shows the SIP *vs.* ϕ dependence for the 2018 `MagUp` $B^+ \to J/\psi K^+$ samples corresponding to different run numbers. The motivation for choosing the specific run numbers shown in Fig. 4.42 is that the VELO calibration procedure was changed between them and whether this has any effect on the misalignment. The distributions show that the misalignment does not have a significant dependence on the run number. An additional check was performed to determine whether the VELO misalignment depends on the time passed since the start of the fill, i.e. if the VELO halves are moving during the fill. The SIP *vs.* ϕ dependence for different fill times is shown in Fig. 4.43 where it can be seen that the time during the fill does not have a significant impact on the misalignment of the two VELO halves.

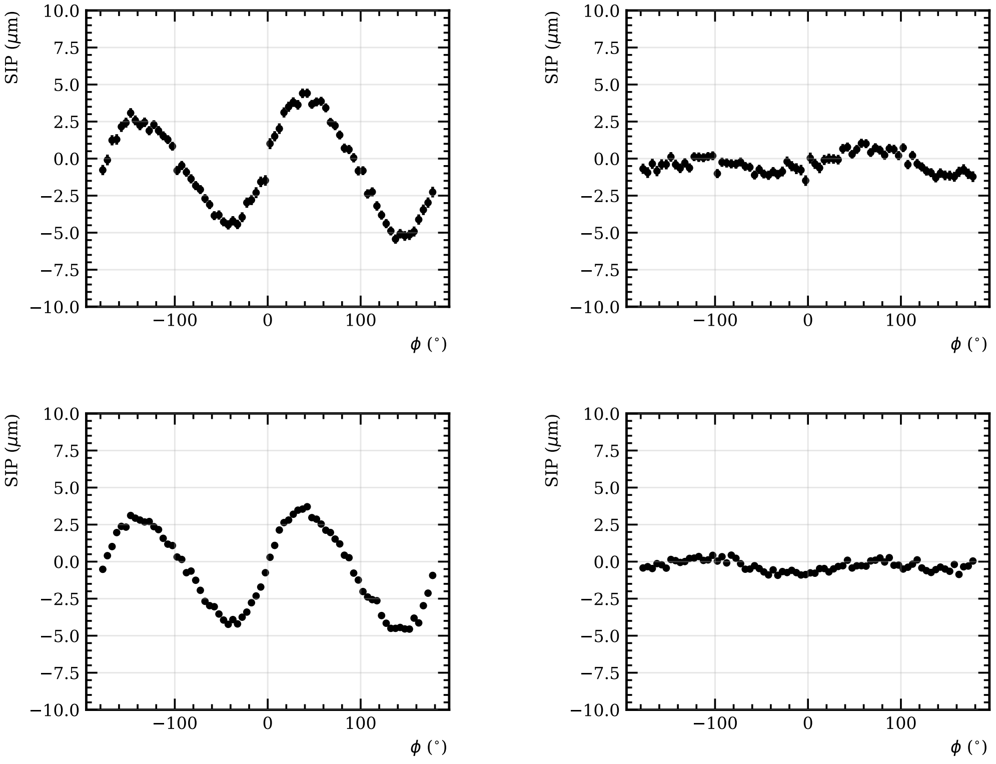

Figure 4.42: SIP *vs.* ϕ dependence for the 2018 `MagUp` $B^+ \to J/\psi K^+$ data sample for run number < 210500 (top) and run number > 211500 (bottom) before (left) and after (right) correcting for the misalignment of the VELO

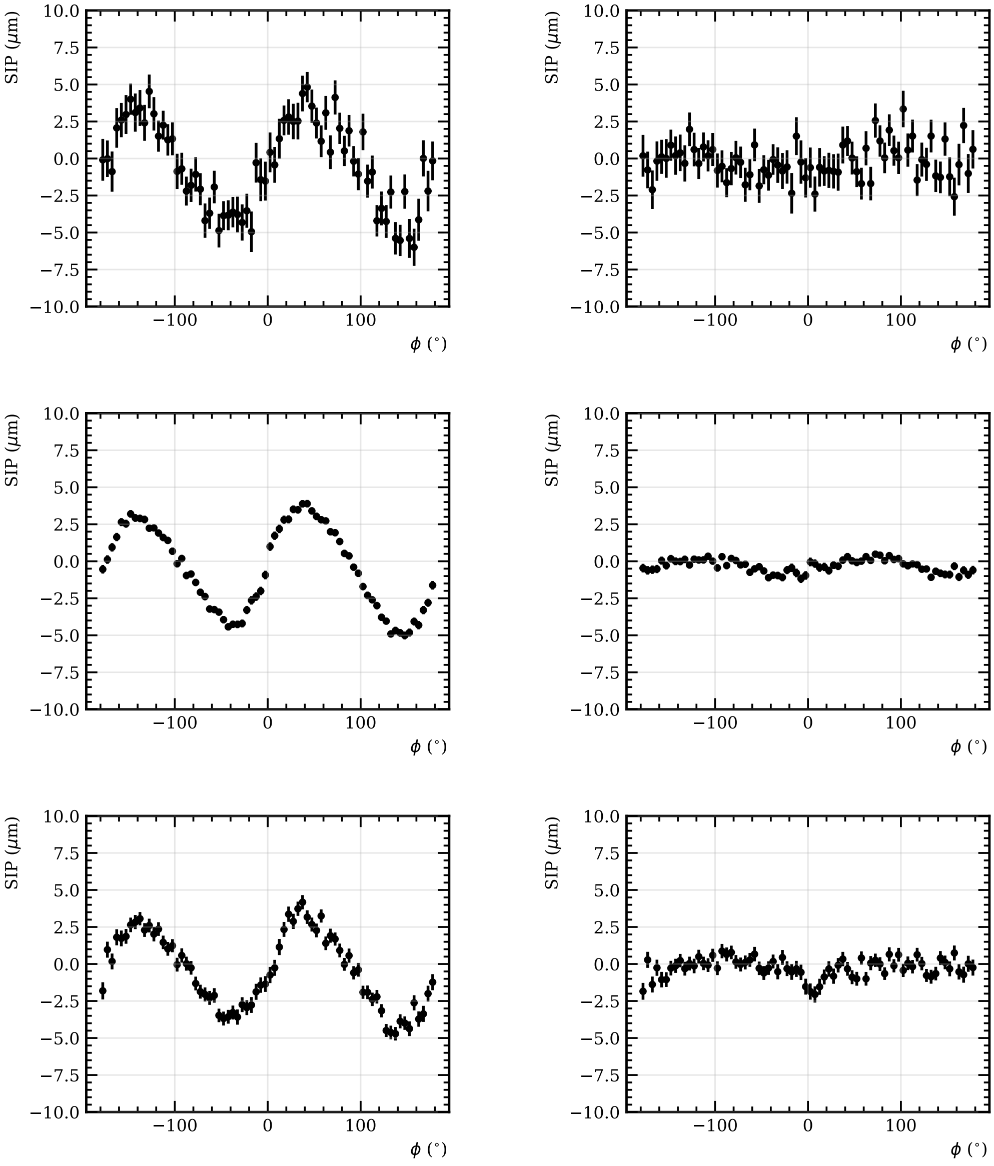

Figure 4.43: *SIP vs.* ϕ dependence for the 2018 `MagUp` $B^+ \to J/\psi K^+$ data sample for fill time < 10e3 seconds (top), fill time ∈ (30e3, 60e3) seconds (middle) and fill time > 80e3 seconds (bottom) before (left) and after (right) correcting for the misalignment of the VELO

4.6.2.2 P-odd effects in reconstruction efficiency

Besides the relative misalignment of the VELO halves, another instrumentation effect that can produce fake parity-odd terms in the reconstructed angular distribution is non-uniform reconstruction efficiency. That is, if the efficiency contains terms proportional to parity-odd quantities that can bias the parity-odd $\sin\chi$ variable and thus bias the NP couplings. These effects can appear in either single track or two-track efficiency terms as follows:

- **Single track efficiency terms**. These terms can appear if the track efficiency depends on both the impact parameter, i.e. the track coordinates at the origin, and the direction of the track. If the efficiency depends on the parity-odd cross product $[\vec{r} \times \vec{t}]$ then it would affect differently left-handed and right-handed tracks (see Fig. 4.33) and would introduce a parity-odd effect in the reconstructed angular distribution. This effect can appear in the VELO reconstruction efficiency since it is the only detector element that provides information on both track origin coordinates and direction. With respect to Eq. 4.28, this effect produces terms of the type $\sin(\phi_B - \phi_i)$ with i being a final state particle.
- **Two-track efficiency terms**. These terms can appear if the tracking efficiency depends on the track direction $\vec{t}$ (but not on $\vec{r}$) and this dependence is different for different particle species. This effect can come from the efficiency of the PID detector elements and would produce terms of the type $\sin(\phi_i - \phi_j)$ where i, j are different final state tracks. In addition, asymmetries in the opening angle $\Delta\phi$ between two tracks could also introduce terms proportional to $\sin(\phi_i - \phi_j)$.

In order to understand the effects of these potential parity-odd terms in the track reconstruction efficiency, a data control sample of $B^0 \to D^- \mu^+ \nu_\mu$ decays is used, where the D^- is reconstructed as $D^- \to K^+\pi^-\pi^-$. The control decay is reconstructed at LHCb as $D^-\mu^+$ combinations in a similar way as the signal decay. The same 2016, 2017 and 2018 data samples are used and the event selection closely follows the signal case in terms of trigger, stripping and offline selection. The trigger path required for the control data sample is exactly the same as for the signal sample. The stripping line used in the control sample case is `b2DpMuXB2DMuForTauMuLine` which is identical to the line used in the signal case (given in Tab. 4.5) with the only exception that the cuts applied to the D^0 and $D^0\mu$ combination are applied to D^- and $D^-\mu$ combination instead. The offline selection applied to the control sample is the same as the one given in Tab. 4.6 for the signal, except the cuts on the D^* and $D^*\mu$ candidates, which are not applicable and the cuts on the D^0 are applied to the D^- candidate instead. After all selection criteria have been passed, the combined control data sample over the three years consists of about 9 million events which is about three times the size of the signal data sample.

This control sample was chosen as it closely resembles the signal $B^0 \to D^{*-}\mu^+\nu_\mu$ decay, but since it consists of two three-body decays and the D^- is a scalar meson, i.e.

it has zero spin, it can not produce any parity or CP-violating effects. Consequently, in this control sample, any observed P-odd effect has to come from the P-odd effects in the track reconstruction efficiency discussed above. The largest background contribution in the $B^0 \to D^-\mu^+\nu_\mu$ data sample comes from $B^0 \to D^{*-}\mu^+\nu_\mu$ decays where $D^{*-} \to D^-\pi^0/\gamma$. Nevertheless, even if the NP that produces CP violation in $B^0 \to D^{*-}\mu^+\nu_\mu$ is present, the kinematic parameter distributions will remain parity-even since the degrees of freedom of the unreconstructed π^0 or γ will be integrated out. Therefore, this control sample can be used without the need to remove the background of D^- coming from excited charm decays.

The $B^0 \to D^-\mu^+\nu_\mu$ decay has the same final state particles as the signal decay, i.e. $K^+\pi^-\pi^-\mu^+$. The pion that gives the lower $K^+\pi^-$ invariant mass is used as a slow pion proxy, i.e. the pion coming from the $D^{*-} \to \overline{D}^0\pi^-$ decay, while the other pion is used to form the $K^+\pi^-$ combination that serves as the $\overline{D}^0$ proxy. Finally, with these proxies defined, the kinematic parameters $q^2, \theta_\ell, \theta_D$ and χ can be calculated. It is important to note that the distributions of these variables, and in particular of the angle χ, should be completely parity-even. The $\sin\chi$ and $\sin 2\chi$ asymmetry templates can thus be obtained and fitted to extract the bias in the NP couplings. To simulate the possible parity-odd effects in the efficiency, the following weights are applied in addition to the $\sin\chi$ and $\sin 2\chi$ weights when creating the asymmetry templates:

- **“Left-right” asymmetry in track efficiency (single track)**: Efficiency weight $\varepsilon = \text{sign}[\vec{r} \times \vec{t}]_z$, where $[\vec{r} \times \vec{t}]_z = (x_0 t_y - y_0 t_x)$
- **$[\vec{r} \times \vec{t}]$ term in track efficiency (single track)**: Efficiency weight $\varepsilon = [\vec{r} \times \vec{t}]_z / 1\,\text{mm}$.
- **ϕ dependence of track efficiency (two-track)**: Efficiency weight $\varepsilon = \sin\phi_i \cos\phi_j$.
- **$\Delta\phi$ dependence of track pair efficiency (two-track)**: Efficiency weight $\varepsilon = \sin(\phi_i - \phi_j)$.

These efficiency weights are $\mathcal{O}(1)$ such that they should be much larger than the actual P-odd effects that may appear in data. The effect of the P-odd efficiency weights is studied in both control data and signal MC samples. The samples are splitted by the two B^0 and $\overline{B}^0$ flavors and by the `MagUp` and `MagDown` magnet polarities such that four sub-samples are obtained for each of the two samples. The asymmetries are then fitted to obtain the NP couplings bias in these four categories. The reason behind the splitting is that the efficiency may depend on the curvature of the track, and consequently the dependence on ϕ might be different for B^0 and $\overline{B}^0$ and `MagUp` and `MagDown`. Therefore, these categories have to be studied separately in order to check whether they may lead to a cancellation of the bias in the control channel when looking at the full sample.

The 2D and flattened 1D CP asymmetries in the signal and control samples due to the $[\vec{r} \times \vec{t}]_z$ term in μ single track efficiency and the $\sin\phi_\mu \cos\phi_{\pi_s}$ two-track efficiency term are shown in Fig. 4.44 and 4.45 for the B^0 and `MagDown` category. The figures demonstrate that both the single track and two-track P-odd efficiency terms of $\mathcal{O}(1)$ introduce nonzero contributions to the asymmetry in both signal and control samples.

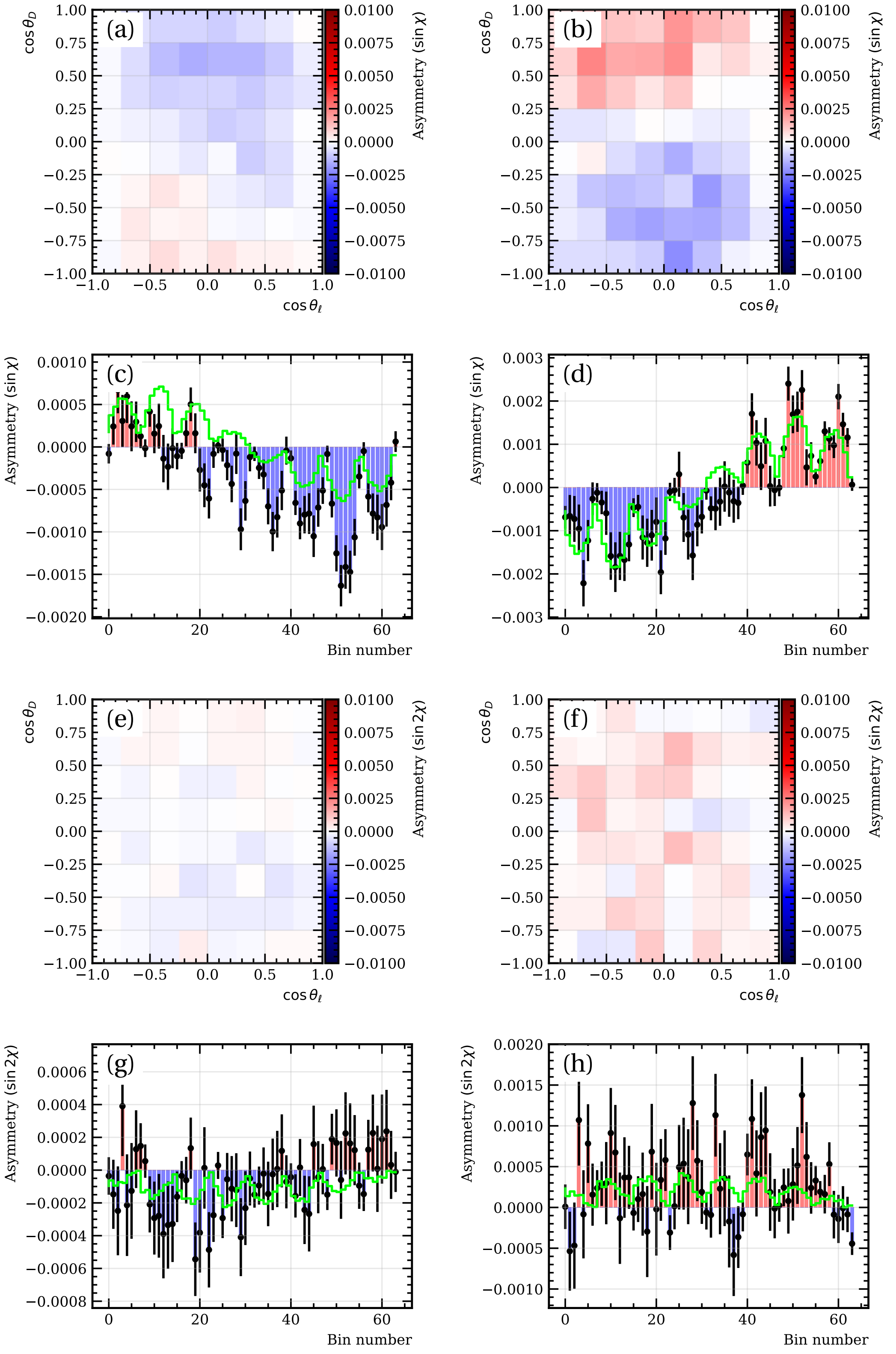

Figure 4.44: *CP* Asymmetry due to the μ single track $[\vec{r}\times\vec{t}]_z$ term. Comparison of the MC signal sample (left plots) and data control sample (right plots). (a,b,e,f) 2D binned asymmetries and (c,d,g,h) the corresponding flattened asymmetries for (a-d) $\sin\chi$ and (e-h) $\sin 2\chi$ asymmetry terms. The green solid line in plots (c,d,g,h) is the result of the template fit.

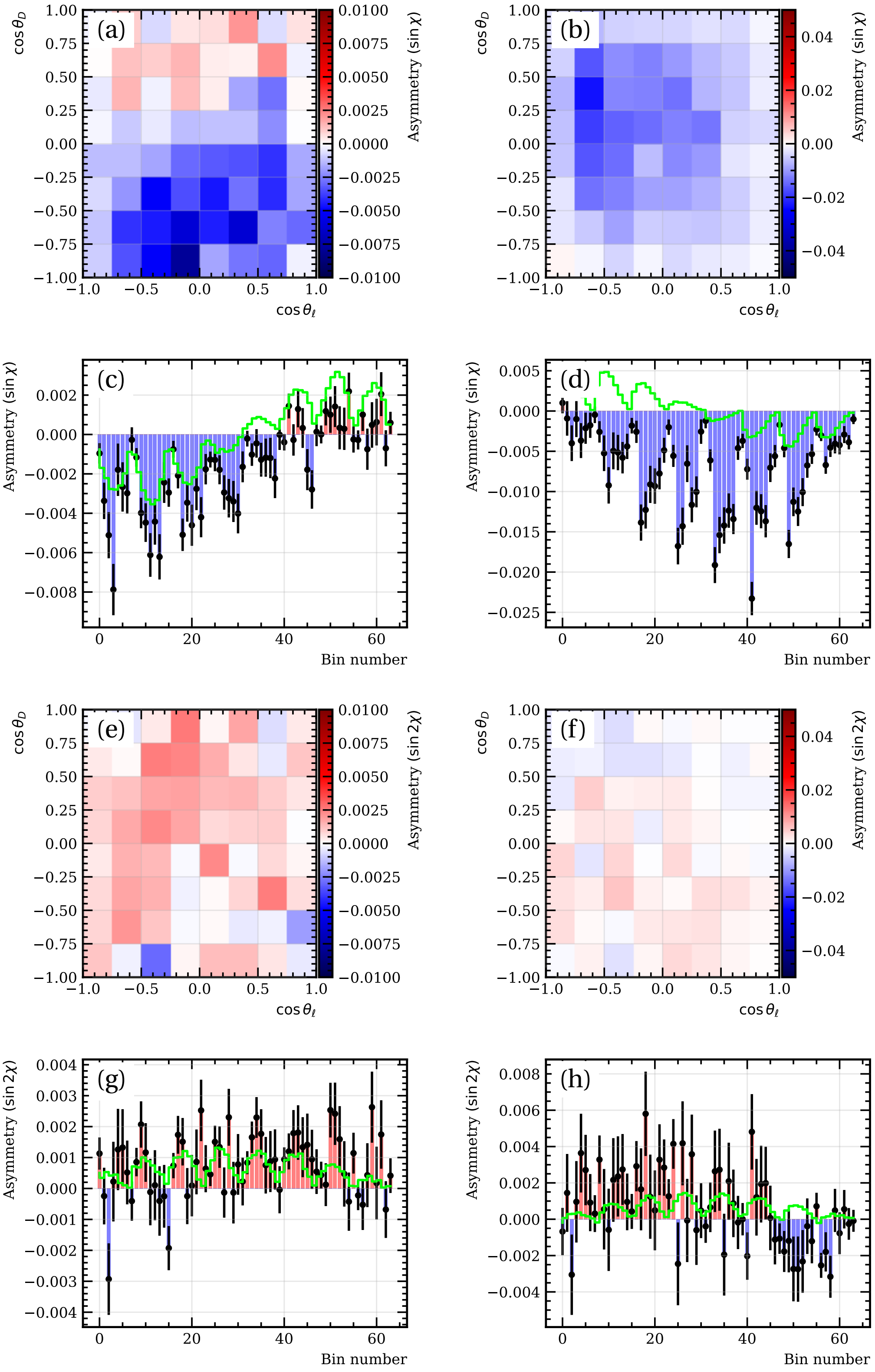

Figure 4.45: *CP* asymmetry due to the two-track term $\sin\phi_\mu \sin\phi_{\pi_s}$. Comparison of the MC signal sample (left plots) and data control sample (right plots). (a,b,e,f) 2D binned asymmetries and (c,d,g,h) the corresponding flattened asymmetries for (a-d) $\sin\chi$ and (e-h) $\sin 2\chi$ asymmetry terms. The green solid line in plots (c,d,g,h) is the result of the template fit.

Template fits are performed and biases in the two NP couplings are extracted using the four efficiency weights listed above for all possible single track and two-track combinations in the four categories. The biases on $\mathrm{Im}(g_R)$ are shown in Fig. 4.46 and 4.47, while the biases on $\mathrm{Im}(g_P g_T^*)$ are shown in Fig. 4.48 and 4.49. It can be seen that the biases in the control and signal samples are consistent with each other across all four categories indicating that the two samples behave in a similar way under all the P-odd efficiency weights and that the bias would not cancel out when looking at the full sample. In addition, the fact that the control sample shows a larger bias in both $\mathrm{Im}(g_R)$ and $\mathrm{Im}(g_P g_T^*)$ across almost all the P-odd effects suggests that the potential bias extracted from the control sample can be used as an upper limit systematic uncertainty in the signal sample.

In the ideal case, the systematic uncertainty in the signal sample due to any P-odd effecs in the efficiency could be estimated by fitting the control sample and using the extracted bias on the NP couplings to assign the systematic. However, since kinematic and topological distributions of the two samples are not fully compatible, the bias extracted from the control sample should not be used directly to assign a systematic uncertainty in the signal sample. Consequently, the control sample bias must be studied as a function of those kinematic and topological variables and a suitable way to extrapolate this information to the signal sample must be used.

As expected, the largest differences between the control and signal samples are in the kinematic and topological variables related to the D^0 and π_s, since these are the particles that are approximated in the control sample. The distributions of the $M(K^-\pi^+)$, $p_\mathrm{T}(K^-\pi^+)$, $p_\mathrm{T}(\pi_s)$ and $\chi^2_\mathrm{IP}(\pi_s)$ variables are shown in Fig. 4.50. A comparison of other kinematic and topological variables between the two samples can be found in Appendix C.

The invariant mass of the $K^+\pi^-$ combination, i.e. the $\overline{D}^0$ proxy, in the case of the control sample is a broad distribution going up to about 1800 MeV, just before the actual $\overline{D}^0$ mass, while in the case of the signal sample with a real $\overline{D}^0$ meson, the distribution is a delta function at the $\overline{D}^0$ mass. The p_T distribution of the real $\overline{D}^0$ in the signal sample is softer than the p_T distribution of the $K^+\pi^-$ combination in the control sample. The distribution of the p_T distribution of the proxy π_s is much softer than in the real π_s case. Since the proxy π_s comes from the D^- decay, i.e. from a tertiary vertex, whereas the real π_s in the signal decay comes from a secondary vertex, a large difference in the topological variable $\chi^2_\mathrm{IP}(\pi_s)$ is observed. The NP couplings biases in the control and signal samples are thus studied in bins of various kinematic and topological variables in the four categories split by B^0 flavor and magnet polarity. As an example, the control and signal bias in $\mathrm{Im}(g_R)$ in bins of $p_\mathrm{T}(K^+\pi^-)$ is shown in Fig. 4.51 in the four categories. The biases in the two NP couplings as a function of other variables for signal an control samples are shown in Appendix E. We note that these biases are due to the control and signal samples themselves, i.e. no P-odd efficiencies are applied. The biases show no trends in any of the investigated variables, are consistent across the four categories and are mostly consistent with zero. In this case, the results of the control sample bias may still be translated into the signal bias even if the kinematic distributions do not match between the two samples.

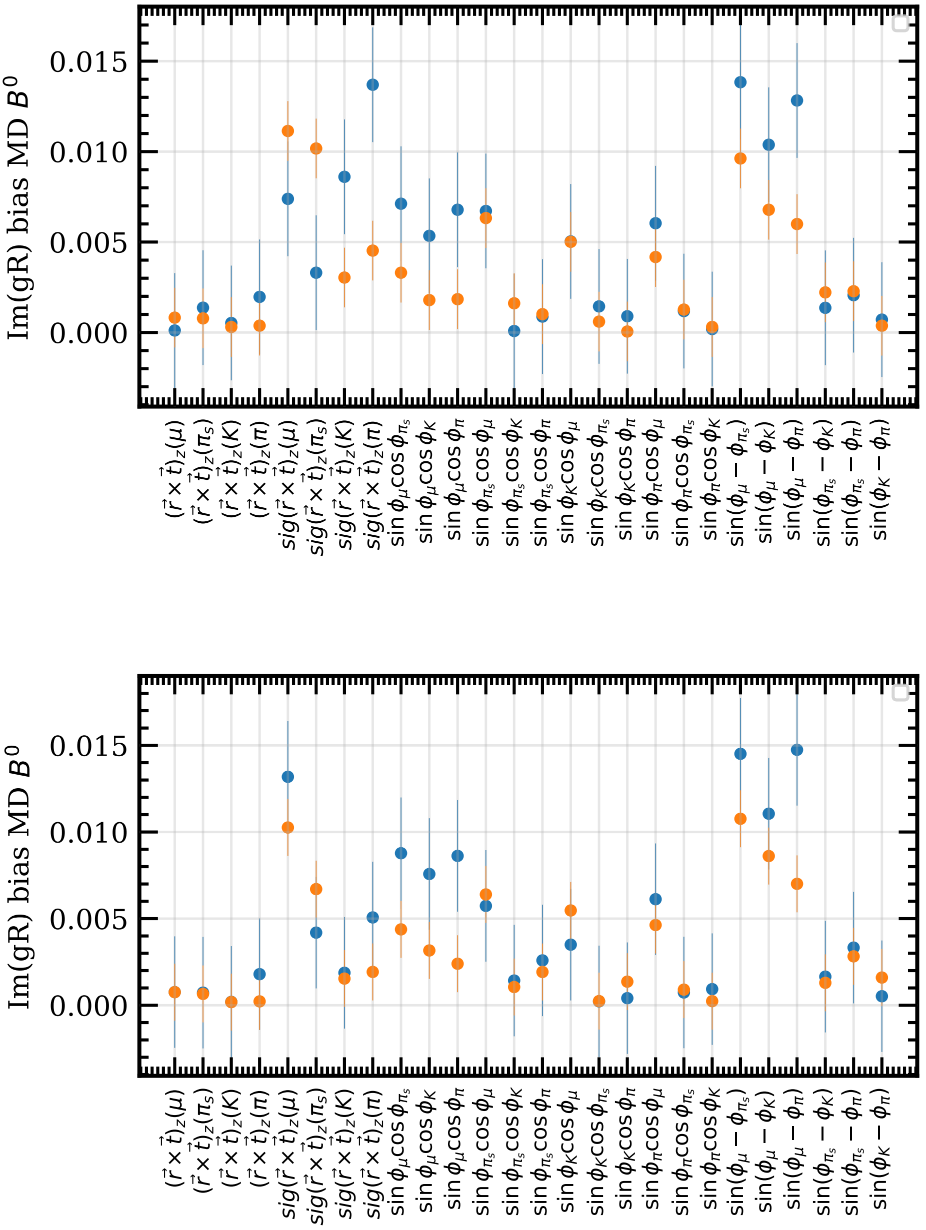

Figure 4.46: Im(g_R) biases due to all P-odd efficiency weights for signal (orange) and control (blue) samples in the `MagDown` B^0 (top) and $\overline{B}^0$ (bottom) categories.

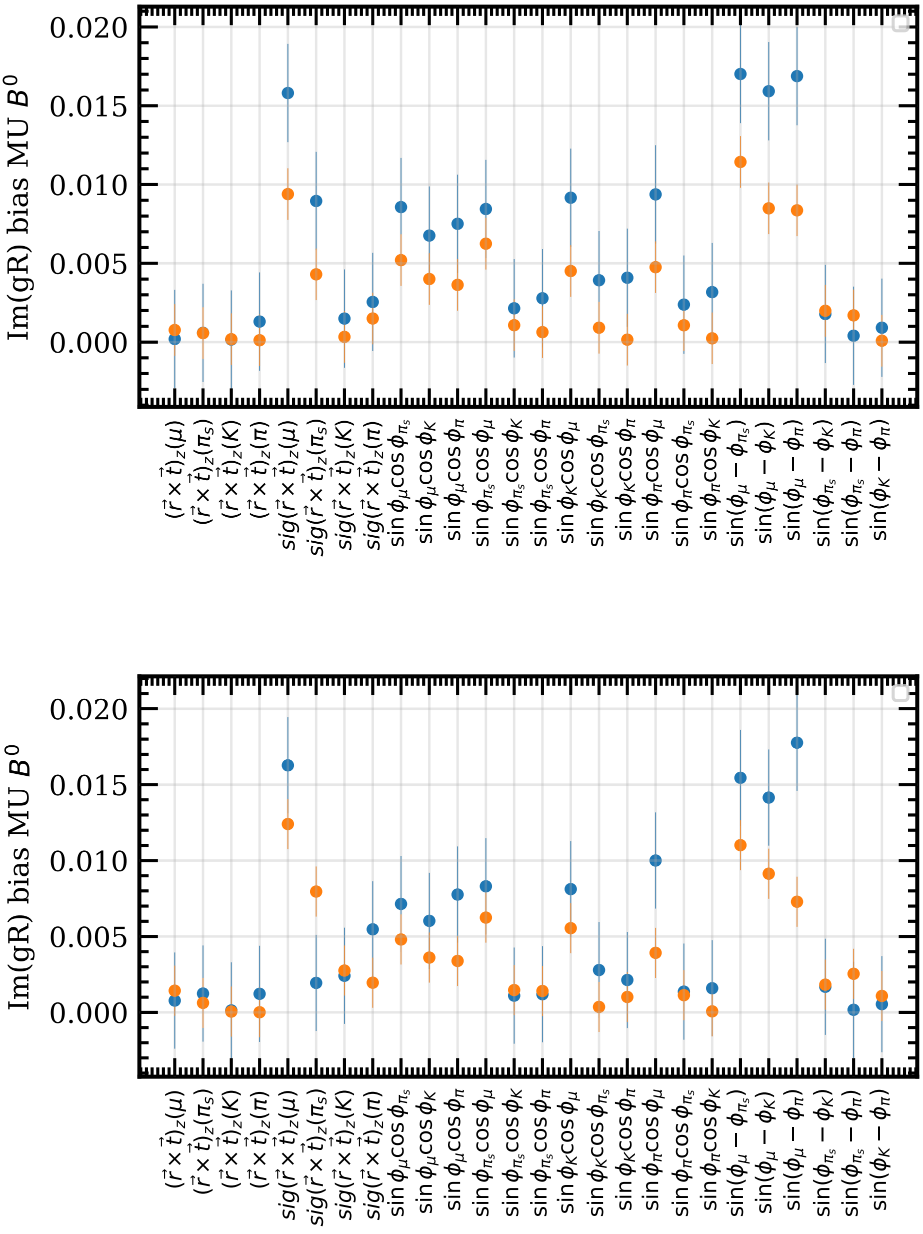

Figure 4.47: Im(g_R) biases due to all P-odd efficiency weights for signal (orange) and control (blue) samples in the `MagUp` B^0 (top) and $\overline{B}^0$ (bottom) categories.

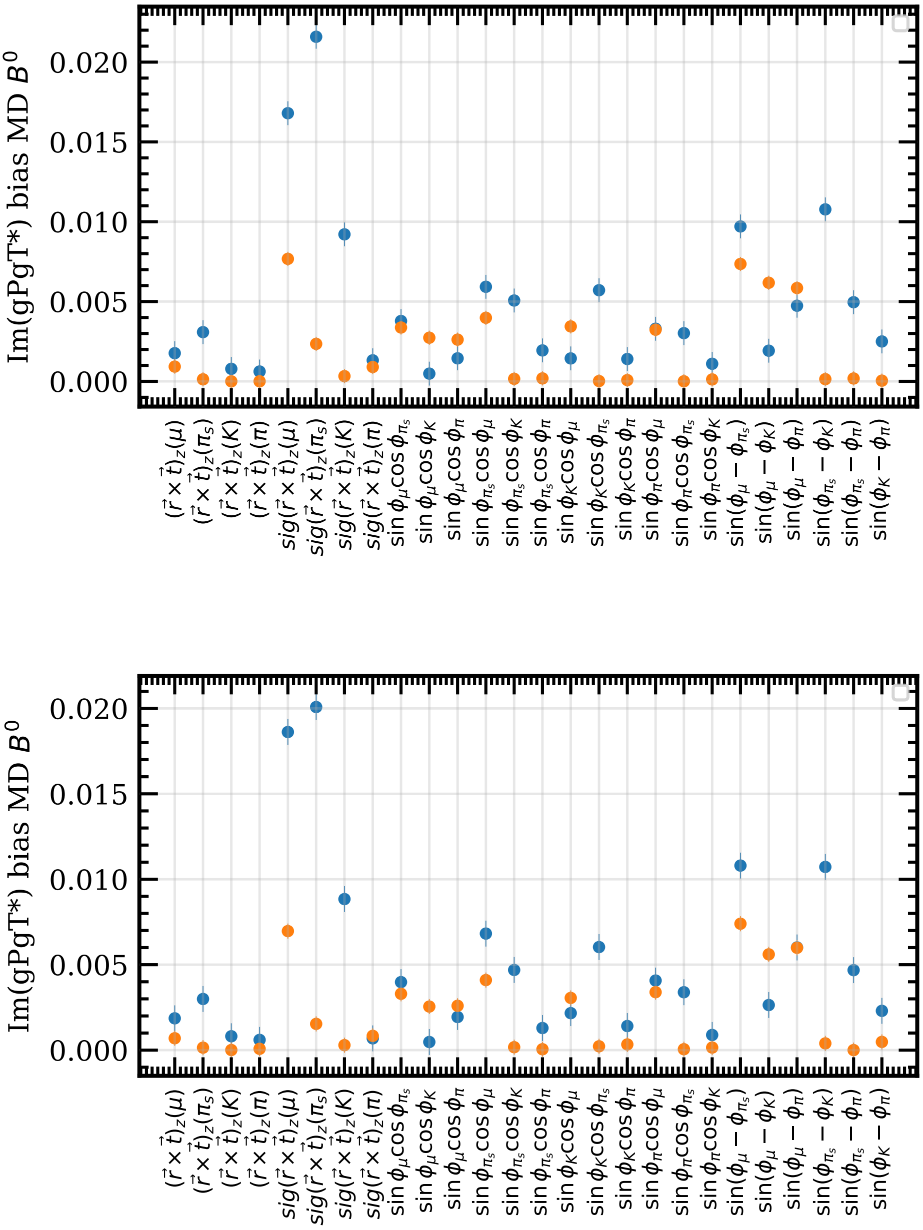

Figure 4.48: $\text{Im}(g_P g_T^*)$ biases due to all P-odd efficiency weights for signal (orange) and control (blue) samples in the `MagDown` B^0 (top) and $\overline{B}^0$ (bottom) categories.

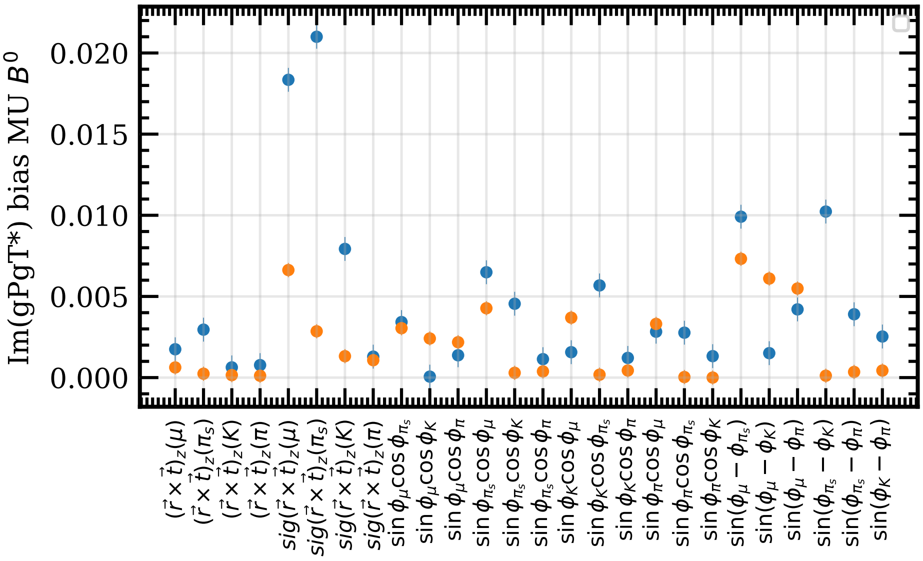

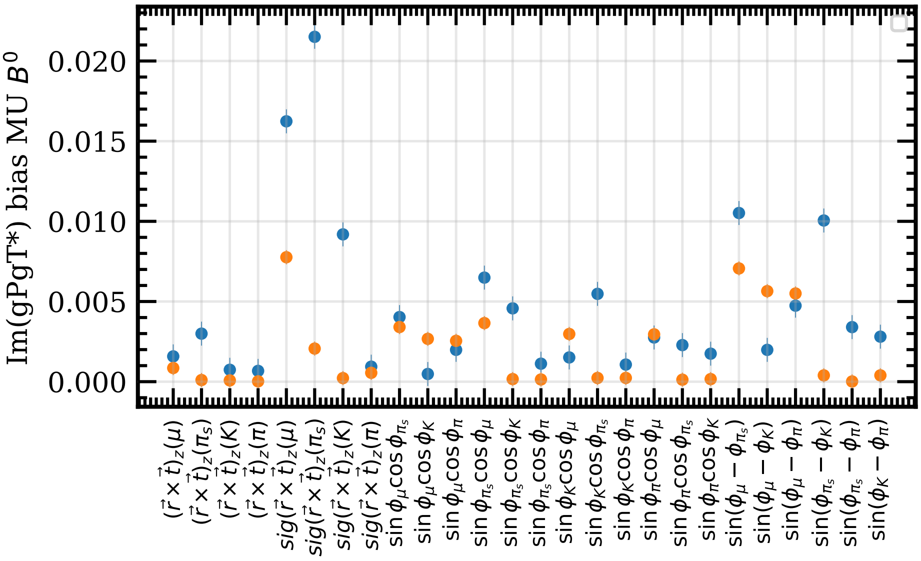

Figure 4.49: Im($g_P g_T^*$) biases due to all P-odd efficiency weights for signal (orange) and control (blue) samples in the `MagUp` B^0 (top) and $\overline{B}^0$ (bottom) categories.

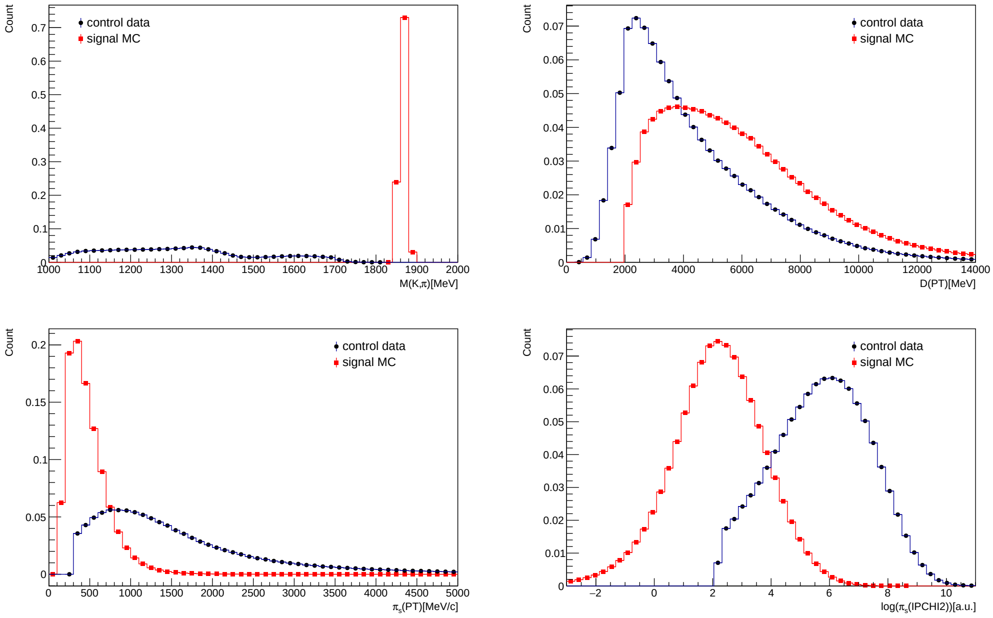

Figure 4.50: Comparison of the $M(K^+\pi^-), p_\mathrm{T}(K^+\pi^-), p_\mathrm{T}(\pi_s), \chi^2_\mathrm{IP}(\pi_s)$ variables between the signal and control samples.

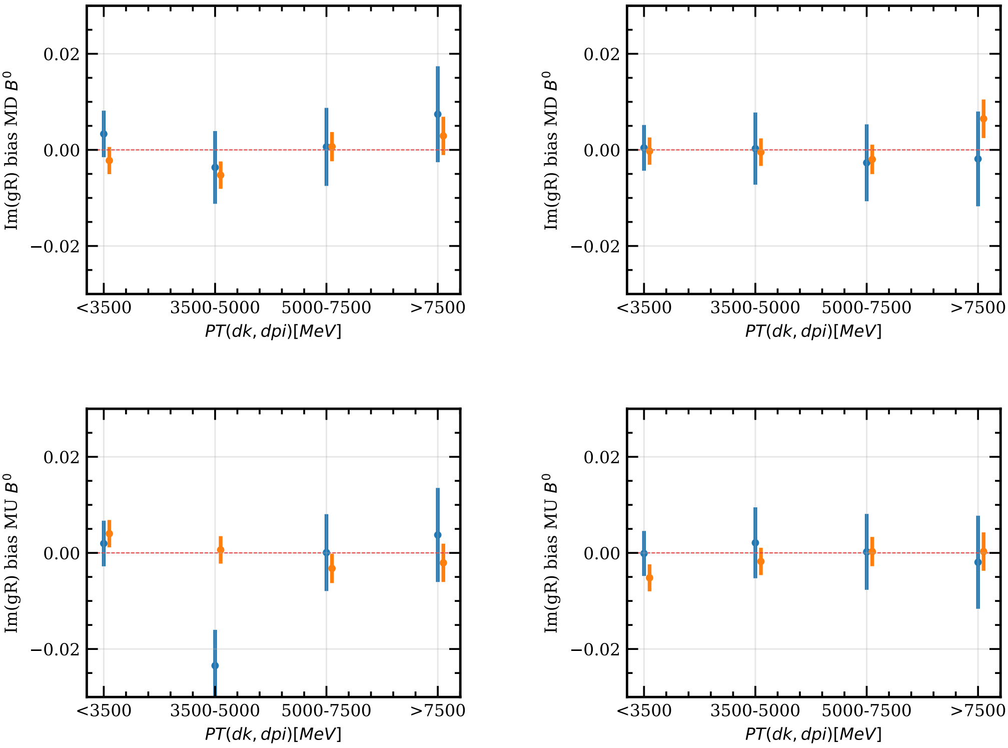

Figure 4.51: Im(g_R) bias for signal (orange) and control (blue) samples in bins of $p_\mathrm{T}(K^+\pi^-)$ across the four categories

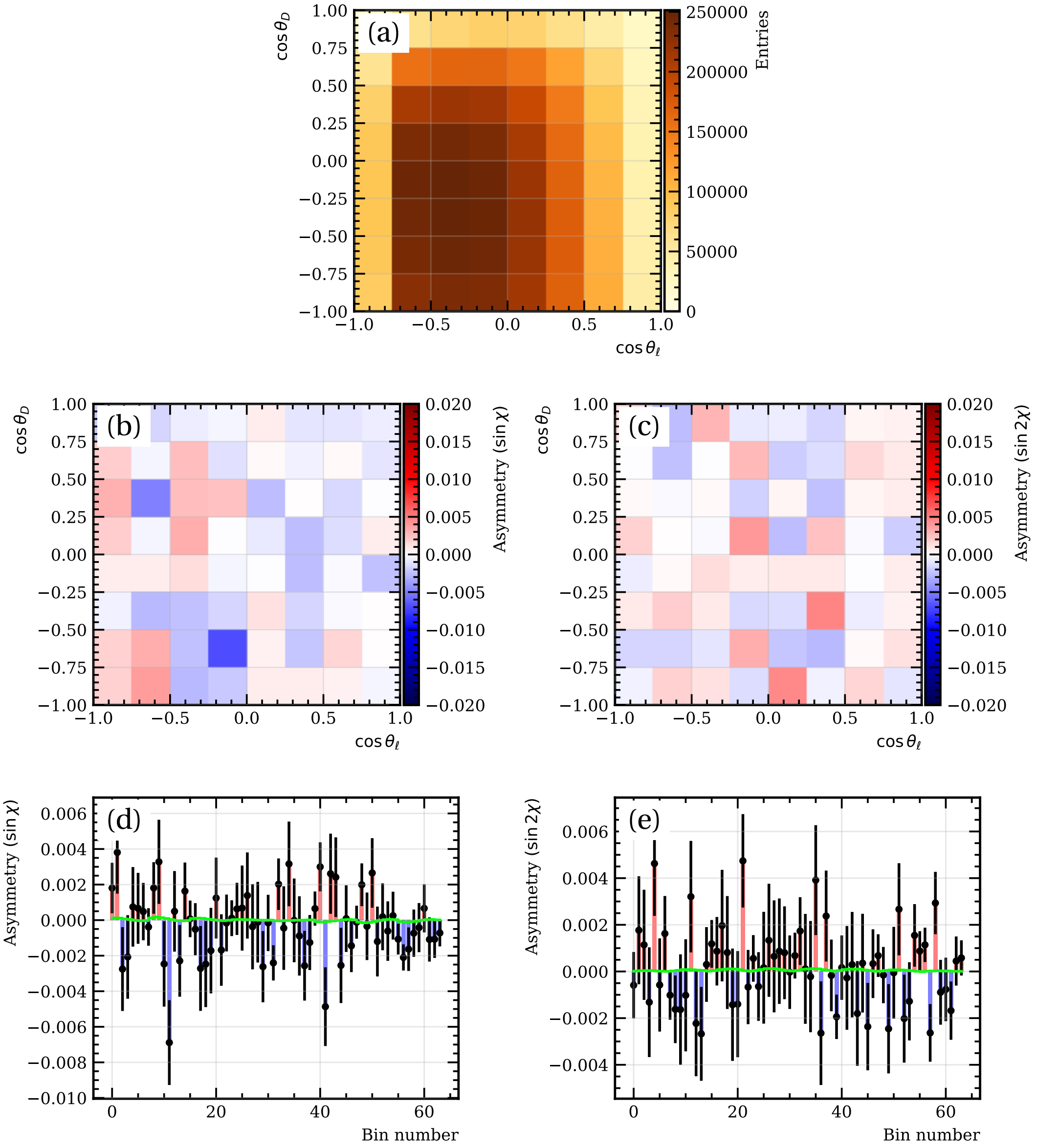

Figure 4.52: Binned density (a), binned 2D parity asymmetries (b,c) and flattened 1D parity asymmetries (d,e) of $\sin\chi$ and $\sin 2\chi$ terms in $(\cos\theta_D, \cos\theta_\ell)$ bins integrated over q^2 for the $B^0 \to D^-\mu^+\nu_\mu$ control data sample. Figures (d) and (e) also show the result of the best fit in green using the RH and PT templates.

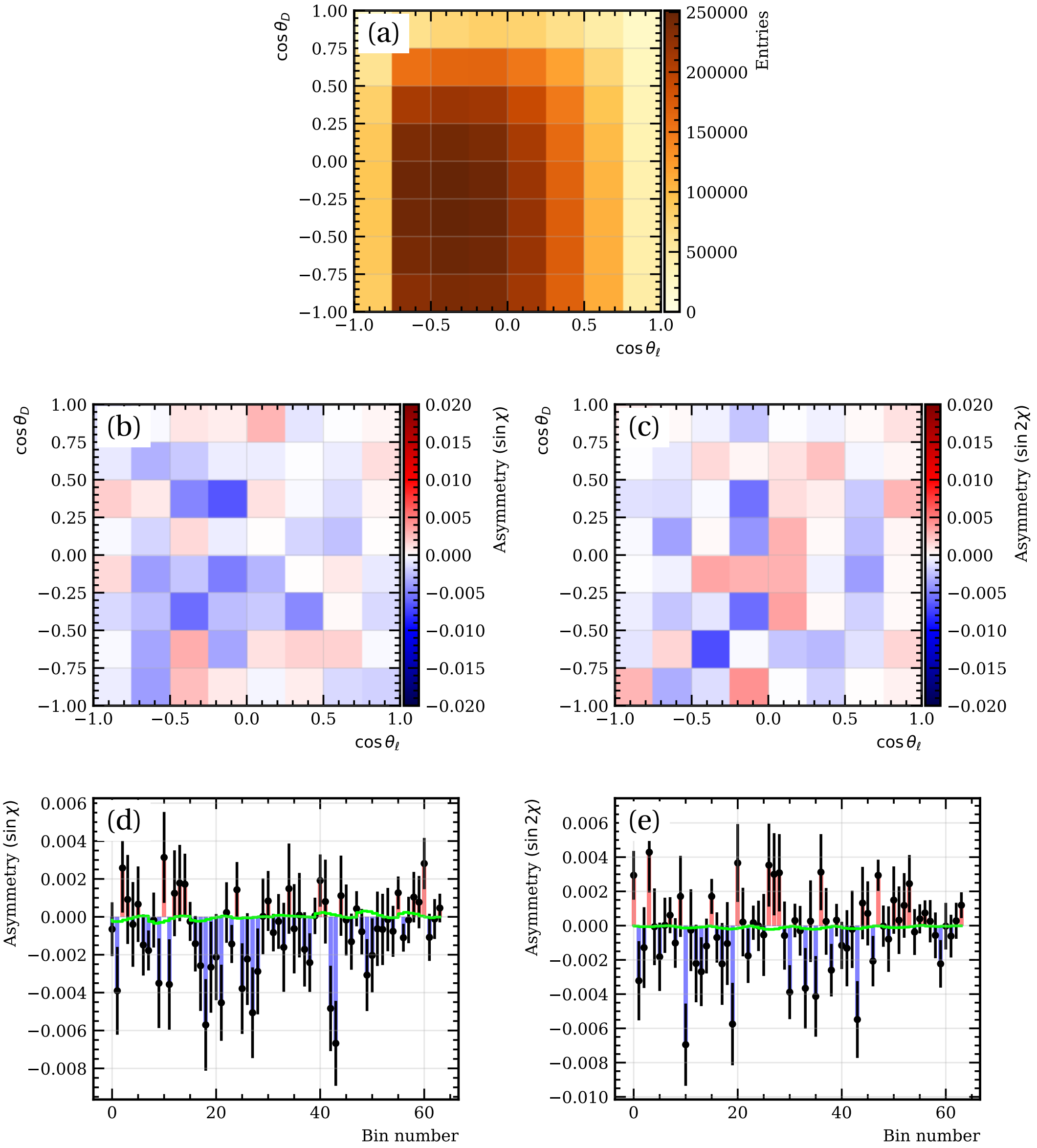

Figure 4.53: Binned density (a), binned 2D *CP* asymmetries (b,c) and flattened 1D *CP* asymmetries (d,e) of $\sin\chi$ and $\sin 2\chi$ terms in $(\cos\theta_D, \cos\theta_\ell)$ bins integrated over q^2 for the $B^0 \to D^-\mu^+\nu_\mu$ control data sample. Figures (d) and (e) also show the result of the best fit in green using the RH and PT templates.

The 2D $\cos\theta_\ell$ *vs.* $\cos\theta_D$ density, the 2D and the fitted 1D flattened parity and *CP* asymmetries in the $B^0 \to D^-\mu^+\nu_\mu$ control data sample are shown in Fig. 4.52 and 4.53. Due to the difference in kinematics, the control sample $\cos\theta_\ell$ *vs.* $\cos\theta_D$ distribution is different than the one in the signal sample (e.g. Fig. 4.19). The results of the template fit are given in Tab. 4.26. No bias is observed in any of the two NP couplings in the control sample in either parity- or *CP* asymmetry.

Asymmetry	$\Delta\,\mathrm{Im}(g_R)$	$\Delta\,\mathrm{Im}(g_P g_T^*)$
Parity	-0.0011 ± 0.0017	0.0002 ± 0.0004
CP	0.0006 ± 0.0017	0.0001 ± 0.0004

Table 4.26: Fitted values of the NP couplings from the binned parity and *CP* asymmetry fit to the $B^0 \to D^-\mu^+\nu_\mu$ control data sample

The study presented in this section of possible P-odd efficiencies in the reconstruction can be summarized in the following way:

1. We use signal MC and control data samples and apply (large) P-odd weights to them. We fit the NP couplings (in 4 categories to make sure the bias does not cancel out when looking at the full sample) and obtain the bias due to the P-odd efficiency weights.

2. We show that the control and signal samples behave similarly under these efficiency weights and have similar patterns across the 4 categories. In addition, the bias in the control sample is larger than the signal one in almost all cases. It is also important that there is no P-odd weight for which there is a bias in the signal but not in the control. If that would be the case, then for that particular efficiency term we would not be able to extrapolate from control to signal.

3. We fit the NP couplings in the control sample itself (without any efficiency weights). If there are any P-odd efficiency effects in real data, there will be a bias in the control sample fit. Since the bias seen in the control (with the efficiency weights) is (almost) always larger than the signal one, the bias extracted from the fit to the control sample (without the efficiency weights) can be used as an upper limit to assign systematic in the signal.

4. We present the results of the control sample fit to be consistent with zero. This result is used to assign the systematic uncertainty in the signal sample as is shown in the results section in Chapter 5.

5 Results

The magnitudes of the systematic biases coming from all P-odd background and instrumentation effects are summarized in Tab. 5.1 and 5.2 for the parity and CP asymmetries, respectively. The biases coming from P-odd effects in backgrounds are corrected by their fractions in data as determined by the template fit results presented in Sec. 4.3.3. As discussed in Sec. 4.6.1, the biases coming from the semileptonic and double charm backgrounds affect only the parity asymmetries.

Bias source	Δ Im(g_R)	Δ Im($g_P g_T^*$)
Misid	$(-0.68 \pm 0.30) \times 10^{-3}$	$(0.46 \pm 0.72) \times 10^{-4}$
Fake D^* comb	$(-0.01 \pm 0.17) \times 10^{-3}$	$(0.41 \pm 0.42) \times 10^{-4}$
True D^* comb	$(1.05 \pm 0.55) \times 10^{-3}$	$(-1.27 \pm 1.50) \times 10^{-4}$
$B^- \to D^{**+}\mu^-\bar{\nu}_\mu$	$(8.68 \pm 0.31) \times 10^{-3}$	$(2.55 \pm 0.87) \times 10^{-4}$
$\overline{B}^0 \to D^{*+}D_s^{*-}$	$(0.05 \pm 0.27) \times 10^{-3}$	$(0.79 \pm 0.79) \times 10^{-4}$
T_y $2\mu m$ misalignment	$(-0.37 \pm 0.85) \times 10^{-3}$	$(0.20 \pm 2.39) \times 10^{-4}$
Control sample	$(-1.10 \pm 1.70) \times 10^{-3}$	$(2.00 \pm 4.00) \times 10^{-4}$

Table 5.1: Overview of systematic biases in the case of parity asymmetries

Bias source	Δ Im(g_R)	Δ Im($g_P g_T^*$)
Misid	$(-0.46 \pm 0.30) \times 10^{-3}$	$(1.44 \pm 0.78) \times 10^{-4}$
Fake D^* comb	$(0.17 \pm 0.18) \times 10^{-3}$	$(0.16 \pm 0.41) \times 10^{-4}$
True D^* comb	$(0.74 \pm 0.55) \times 10^{-3}$	$(0.03 \pm 1.51) \times 10^{-4}$
T_y 2μm misalignment	$(-3.74 \pm 0.84) \times 10^{-3}$	$(3.10 \pm 2.39) \times 10^{-4}$
Control sample	$(0.60 \pm 1.70) \times 10^{-3}$	$(1.00 \pm 4.00) \times 10^{-4}$

Table 5.2: Overview of systematic bias in the case of CP asymmetries

The systematic uncertainty due to each effect is assigned using the 90% percentile of the bias according to the following formula:

$$\sigma_{\text{syst}} = |\mu_{\text{bias}}| + 1.28\sigma_{\text{bias}} \tag{5.1}$$

The final values of the systematic uncertainties for the parity and *CP* asymmetries are reported in Tab. 5.3 and 5.4. The dominant systematic uncertainty in the case of *CP* asymmetries is due to the T_y misalignment of the two VELO halves with respect to each other. The 2 μm misalignment used in the simulation to estimate the bias is obtained in a data-driven way using a $B^+ \to J/\psi K^+$ control sample.

Assigned systematic	Δ Im(g_R)	Δ Im($g_P g_T^*$)
Misid	1.07×10^{-3}	1.38×10^{-4}
Fake D^* comb	0.23×10^{-3}	0.96×10^{-4}
True D^* comb	1.76×10^{-3}	3.20×10^{-4}
$B^- \to D^{**+}\mu^-\bar{\nu}_\mu$	9.64×10^{-3}	3.67×10^{-4}
$\overline{B}^0 \to D^{*+}D_s^{*-}$	0.41×10^{-3}	1.81×10^{-4}
T_y 2μm misalignment	1.44×10^{-3}	3.27×10^{-4}
Control sample	3.27×10^{-3}	7.12×10^{-4}
Total	10.50×10^{-3}	9.55×10^{-4}

Table 5.3: Overview of assigned systematic uncertainties in the case of parity asymmetries

Assigned systematic	Δ Im(g_R)	Δ Im($g_P g_T^*$)
Misid	0.85×10^{-3}	2.45×10^{-4}
Fake D^* comb	0.40×10^{-3}	0.70×10^{-4}
True D^* comb	1.45×10^{-3}	1.98×10^{-4}
T_y $2\mu m$ misalignment	4.16×10^{-3}	4.33×10^{-4}
Control sample	2.78×10^{-3}	6.12×10^{-4}
Total	5.82×10^{-3}	9.27×10^{-4}

Table 5.4: Overview of assigned systematic uncertainties in the case of *CP* asymmetries

As argued in Sec. 2.2.3.1, the parity asymmetry in $B^0 \to D^{*-}\mu^+\nu_\mu$ has to be zero. Fitting the parity asymmetry in the signal data sample serves as an useful cross-check and any deviation from zero might indicate an unaccounted for source of systematic bias. Furthermore, since this fit is performed to the full signal data sample, the statistical uncertainty for the *CP* asymmetry measurement can be also extracted. For the purpose of this thesis, the fit to the *CP* asymmetry, and consequently the measurement of the Im(g_R) and Im($g_P g_T^*$) couplings, is still blinded.

The 2D $\cos\theta_\ell\, vs.\cos\theta_D$ density, the 2D parity asymmetry and the template fit to the flattened 1D parity asymmetry in the signal data sample is shown in Fig. 5.1. The results of the fit corrected by the fraction of signal events found in data are given in Eq. 5.2.

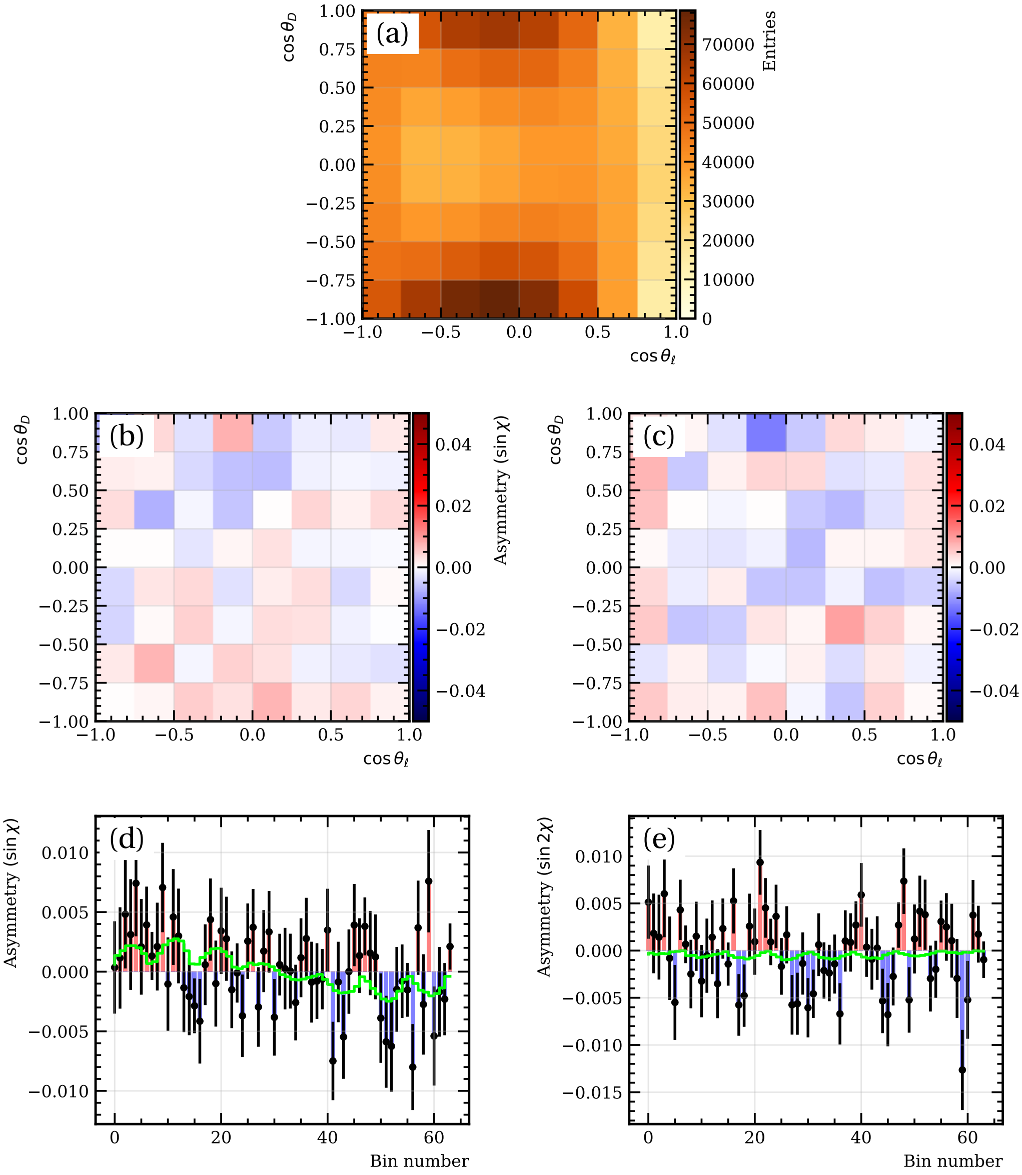

Figure 5.1: Binned density (a), binned 2D parity asymmetries (b,c) and flattened 1D parity asymmetries (d,e) of $\sin\chi$ and $\sin 2\chi$ terms in $(\cos\theta_D, \cos\theta_\ell)$ bins integrated over q^2 for the $B^0 \to D^{*-}\mu^+\nu_\mu$ signal data sample. Figures (d) and (e) also show the result of the best fit in green using the RH and PT templates.

$$\begin{aligned}\Delta\mathrm{Im}(g_R) &= -0.0057 \pm 0.0051,\\ \Delta\mathrm{Im}(g_P g_T^*) &= -0.0041 \pm 0.0013,\end{aligned} \tag{5.2}$$

where the uncertainty on the couplings represents the statistical uncertainty which is equally applicable for the *CP* asymmetry measurement. The statistical uncertainty achieved with the 2016-2018 Run 2 dataset is found to be 0.51% for the $\mathrm{Im}(g_R)$ and 0.13% for $\mathrm{Im}(g_P g_T^*)$.

The final results for the parity and the (blinded) *CP* asymmetry measurements including the statistical and estimated systematic uncertainties are given in Eqs. 5.3 and 5.4, respectively.

$$\begin{aligned}\Delta\mathrm{Im}(g_R) &= (-0.57 \pm 0.51\ (\text{stat.}) \pm 1.05\ (\text{syst.}))\%,\\ \Delta\mathrm{Im}(g_P g_T^*) &= (-0.41 \pm 0.13\ (\text{stat.}) \pm 0.10\ (\text{syst.}))\%.\end{aligned} \tag{5.3}$$

$$\begin{aligned}\mathrm{Im}(g_R) &= (\mathrm{X.XX} \pm 0.51\ (\text{stat.}) \pm 0.58\ (\text{syst.}))\%,\\ \mathrm{Im}(g_P g_T^*) &= (\mathrm{X.XX} \pm 0.13\ (\text{stat.}) \pm 0.09\ (\text{syst.}))\%.\end{aligned} \tag{5.4}$$

The fit results in the parity asymmetry control channel in the case of $\Delta\mathrm{Im}(g_P g_T^*)$ show a deviation of about 2.5σ from the expected null result even after including both statistical and systematic uncertainties. This result means that the current systematic uncertainties are not estimated accurately or that there is a possible unaccounted for parity-violating effect (e.g. coming from a background). At the time of the writing of this thesis, this effect is still under investigation. Nevertheless, a check that could give a clue on the source of this bias is to perform the asymmetry fit in bins of q^2. Thus, depending in which q^2 region this bias appears, it could be linked with a type of background (e.g. the semileptonic and double charm backgrounds that are studied in this thesis are mostly present in the low-q^2 region).

6 Conclusions and prospects

6.1 Conclusions

The search for *CP*-violating observables in the semileptonic $B^0 \to D^{*-}\mu^+\nu_\mu$ decay presented in this thesis is performed on 5.4 fb^{-1} of data collected by the LHCb experiment during the 2016-2018 years of Run 2 at the LHC. The novel model-independent method of extracting the parity- and *CP*-odd terms in the angular distribution of $B^0 \to D^{*-}\mu^+\nu_\mu$ while cancelling out the parity-even terms and their associated theoretical uncertainties is presented. This method gives access to the first direct measurement of two separate New Physics (NP) observables: the imaginary part of the right-handed vector coupling $\text{Im}(g_R)$ and the imaginary part of the interference between the pseudoscalar and tensor couplings $\text{Im}(g_P g_T^*)$.

Approximation techniques are employed to reconstruct the undetectable neutrino in the $B^0 \to D^{*-}\mu^+\nu_\mu$ final state and thus to reconstruct the kinematic parameters that describe the angular distribution. In order to improve the resolution on the kinematic parameters, a full refit of the decay tree that includes all possible kinematic information (including the approximation of the missing neutrino) and all possible correlations is implemented for the first time in a semileptonic analysis.

The binned parity- and *CP*-asymmetries are then obtained from the reconstructed kinematic parameters. A binned asymmetry template fit with NP templates derived from simulation is performed in order to extract the values of the NP couplings. In particular, the *CP* asymmetries are sensitive to NP while the parity asymmetries are expected to be zero in either SM or NP and thus serve as a control channel for the method.

The most significant sources of systematic uncertainties due to parity- and *CP*-odd effects in backgrounds and in the reconstruction procedure at LHCb are considered and upper limits are estimated. These systematic effects are specific to the method used in this analysis and have not been previously considered in other semileptonic angular analyses. Therefore, their contributions have been studied and evaluated for the first time.

The results of the fit to the parity asymmetry as a control channel are unblinded and are consistent with the expected values within the estimated uncertainties for one of the couplings while a 2.5σ deviation is found for the other coupling. This result indicates either a misestimation of the current systematic uncertainties or a possible unaccounted for parity-violating effect (e.g. coming from a background). At the time of the writing of this thesis, this effect is still under investigation. The fit to the *CP* asymmetries is still blinded and only the statistical and estimated systematic uncertainties are reported for the NP observables. The final results for the parity and the (blinded) *CP* asymmetry fits are given in Eq. 6.1 and 6.2, respectively.

$$\begin{aligned} \Delta\mathrm{Im}(g_R) &= (-0.57 \pm 0.51\ (\text{stat.}) \pm 1.05\ (\text{syst.}))\%, \\ \Delta\mathrm{Im}(g_P g_T^*) &= (-0.41 \pm 0.13\ (\text{stat.}) \pm 0.10\ (\text{syst.}))\%. \end{aligned} \tag{6.1}$$

$$\begin{aligned} \mathrm{Im}(g_R) &= (\text{X.XX} \pm 0.51\ (\text{stat.}) \pm 0.58\ (\text{syst.}))\%, \\ \mathrm{Im}(g_P g_T^*) &= (\text{X.XX} \pm 0.13\ (\text{stat.}) \pm 0.09\ (\text{syst.}))\%. \end{aligned} \tag{6.2}$$

The statistical precision obtained with the method and the used dataset is below 1% for the $\mathrm{Im}(g_R)$ coupling and about 0.1% for the $\mathrm{Im}(g_P g_T^*)$ coupling.

The largest systematic bias in the parity asymmetry case comes from the possible parity-violating effect in the semileptonic $B \to D^{**}\mu\nu_\mu$ background. The parity-odd effects arise from the potential presence of a strong phase in the interference of different excited charm resonances. The magnitude of this effect is found to be about two times larger than the statistical precision in the case of $\mathrm{Im}(g_R)$ and smaller than the statistical precision in the case of $\mathrm{Im}(g_P g_T^*)$ for the strong phase value that produces the maximal parity-violating effect.

The largest contribution to the systematic uncertainty in the *CP* asymmetries and consequently in the NP observables is found to come from parity-odd instrumentation effects. In particular, it was found that detector misalignments introduce a systematic bias at the level of the statistical precision in both $\mathrm{Im}(g_R)$ and $\mathrm{Im}(g_P g_T^*)$. The other main source of systematic bias is due to potential non-uniform reconstruction efficiencies at LHCb. A data-driven approach is proposed where a completely parity- and *CP*-even sample even in NP scenarios is used to control any parity-odd contributions in the efficiency. This systematic effect is found to contribute at the level of the statistical precision in both NP couplings.

6.2 Prospects

The measurement of the NP observables in this analysis is subject to systematic uncertainties that are at the same level with the statistical uncertainty. Several ways in which they can be improved are foreseen. The largest systematic uncertainty in the parity asymmetry case is assigned in a conservative way by considering the value of the strong phase in $B \to D^{**}\mu\nu_\mu$ that produces the maximal parity violation, since this phase is currently not known. A future measurement of the amplitude structure of these decays and consequently of the value of the strong phase (if any) will help estimate this systematic effect more accurately.

The largest systematic due to the VELO detector misalignments in the *CP* asymmetries case, and thus in the actual NP couplings measurement, can be mostly corrected for in a data-driven way using high-statistics fully reconstructed data samples such as $B^+ \to J/\psi K^+$. Furthermore, since the other source of systematic bias due to non-uniform reconstruction efficiencies is also controlled in a data-driven way, the statistical uncertainties estimated with these methods will improve as more data is collected by the LHCb with e.g. Run 3 and beyond. However, since the VELO detector has been completely replaced in Run 3 [152], and it consists of two L-shaped halves, its geometry is now mirror-asymmetric. This may result in additional parity-odd effects in the reconstruction that may be more difficult to control.

Although this analysis is performed in the case of $b \to c\mu\nu_\mu$ transitions, it could be performed in the $b \to ce\nu_e$ and $b \to c\tau\nu_\tau$ modes as well. The measurements of CP-violating observables in these modes would help constrain a wider range of NP scenarios that break lepton flavor universality. In particular, the τ mode could be more useful, since it is typically considered as the one that is potentially the most affected by NP.

Another possibility to obtain CP violation in charged current $b \to c\ell\nu_\ell$ transitions is by exploiting the interference of excited charm states in $B \to D^{**}\ell\nu_\ell$ decays [6]. The strong phase needed for a direct CP violation can appear due to the interference of different excited charm resonances while the weak phase may arise from any NP amplitude. This approach is in particular sensitive to the g_S, g_P and g_T couplings, rather than the g_R and the $g_P g_T^*$ interference that the approach presented in this thesis is sensitive to.

Appendices

Appendix A

Semileptonic background asymmetries and bias fits

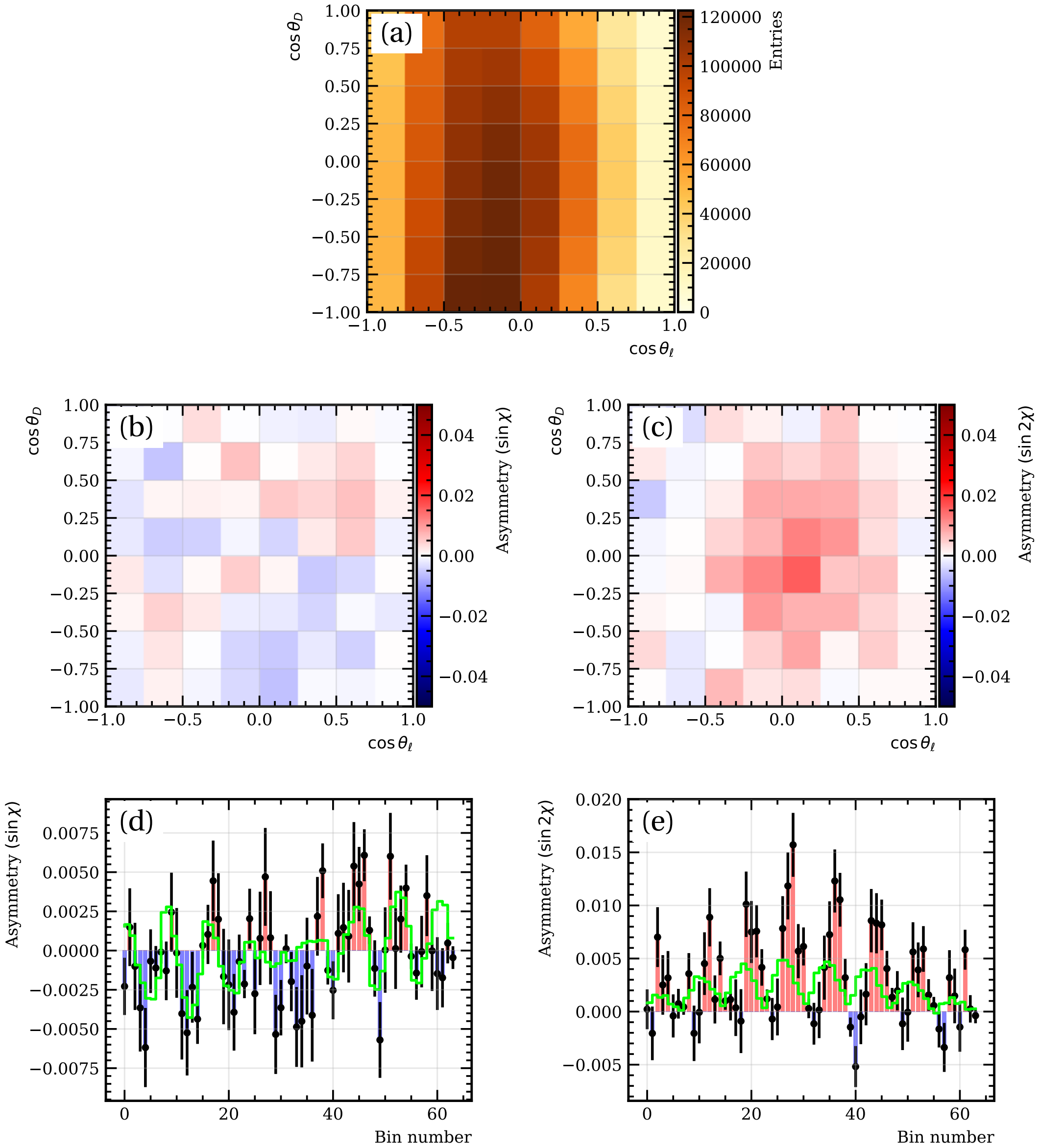

Figure 1: Binned density (a), binned 2D parity asymmetries (b,c) and flattened 1D parity asymmetries (d,e) of $\sin\chi$ and $\sin 2\chi$ terms in $(\cos\theta_D, \cos\theta_\ell)$ bins integrated over q^2 for the $B^+ \to D^{**0}\mu^+\nu_\mu$ with $\delta_D = 0°$. Figures (d) and (e) also show the result of the best fit in green using the RH and PT templates.

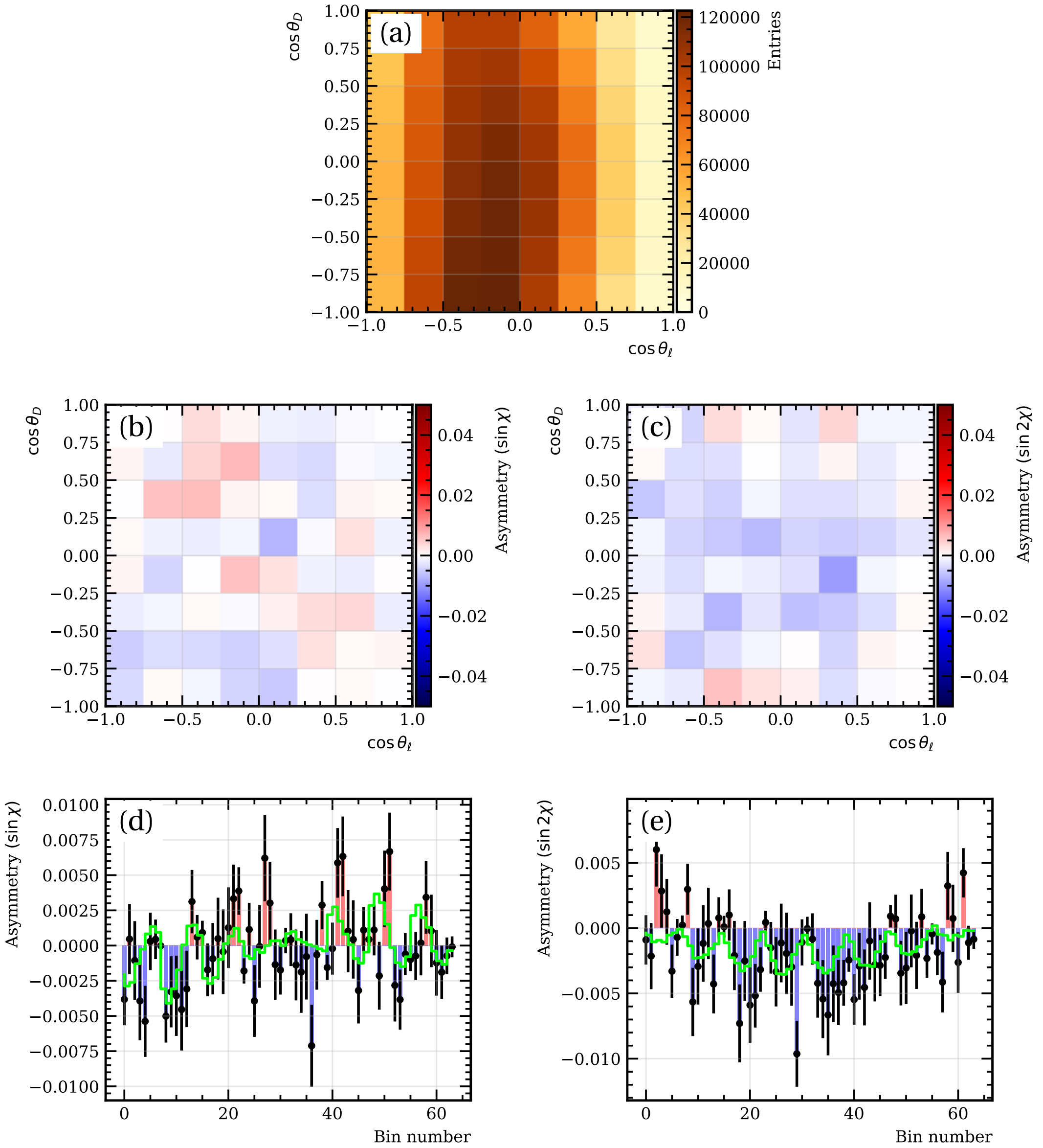

Figure 2: Binned density (a), binned 2D parity asymmetries (b,c) and flattened 1D parity asymmetries (d,e) of $\sin\chi$ and $\sin 2\chi$ terms in $(\cos\theta_D, \cos\theta_\ell)$ bins integrated over q^2 for the $B^+ \to D^{**0}\mu^+\nu_\mu$ with $\delta_D = 45°$. Figures (d) and (e) also show the result of the best fit in green using the RH and PT templates.

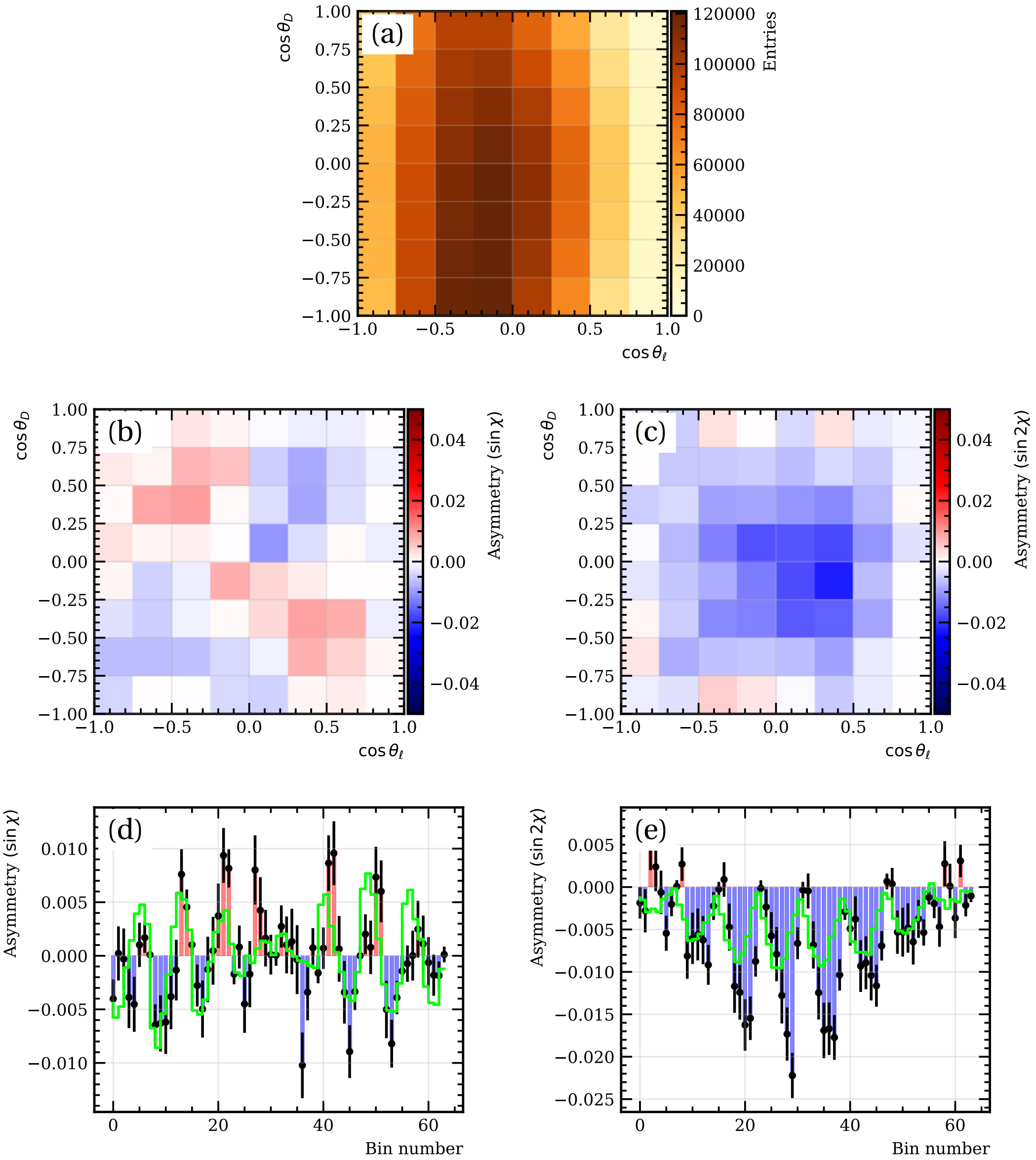

Figure 3: Binned density (a), binned 2D parity asymmetries (b,c) and flattened 1D parity asymmetries (d,e) of $\sin\chi$ and $\sin 2\chi$ terms in $(\cos\theta_D, \cos\theta_\ell)$ bins integrated over q^2 for the $B^+ \to D^{**0}\mu^+\nu_\mu$ with $\delta_D = 90°$. Figures (d) and (e) also show the result of the best fit in green using the RH and PT templates.

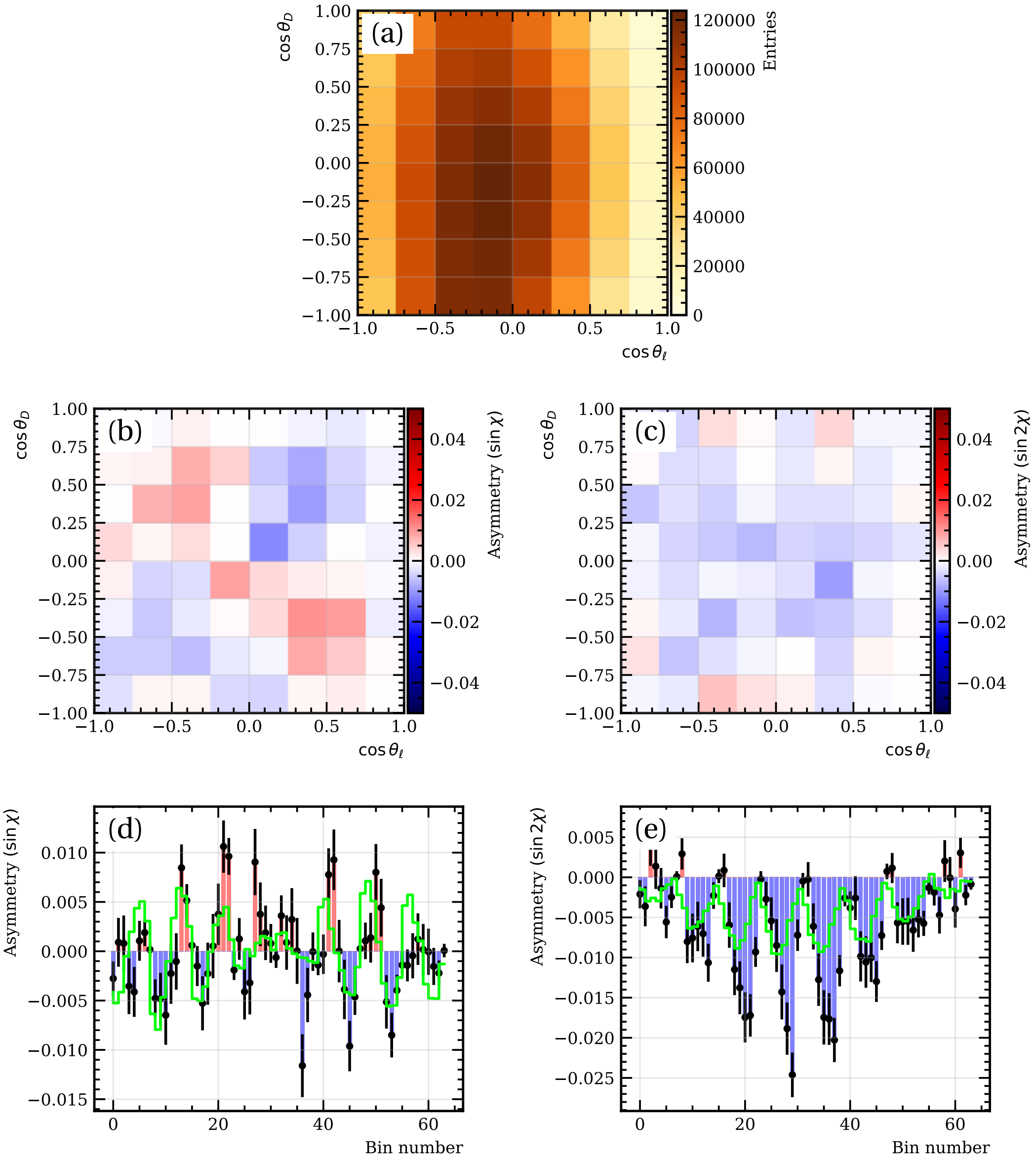

Figure 4: Binned density (a), binned 2D parity asymmetries (b,c) and flattened 1D parity asymmetries (d,e) of $\sin\chi$ and $\sin 2\chi$ terms in $(\cos\theta_D, \cos\theta_\ell)$ bins integrated over q^2 for the $B^+ \to D^{**0}\mu^+\nu_\mu$ with $\delta_D = 135°$. Figures (d) and (e) also show the result of the best fit in green using the RH and PT templates.

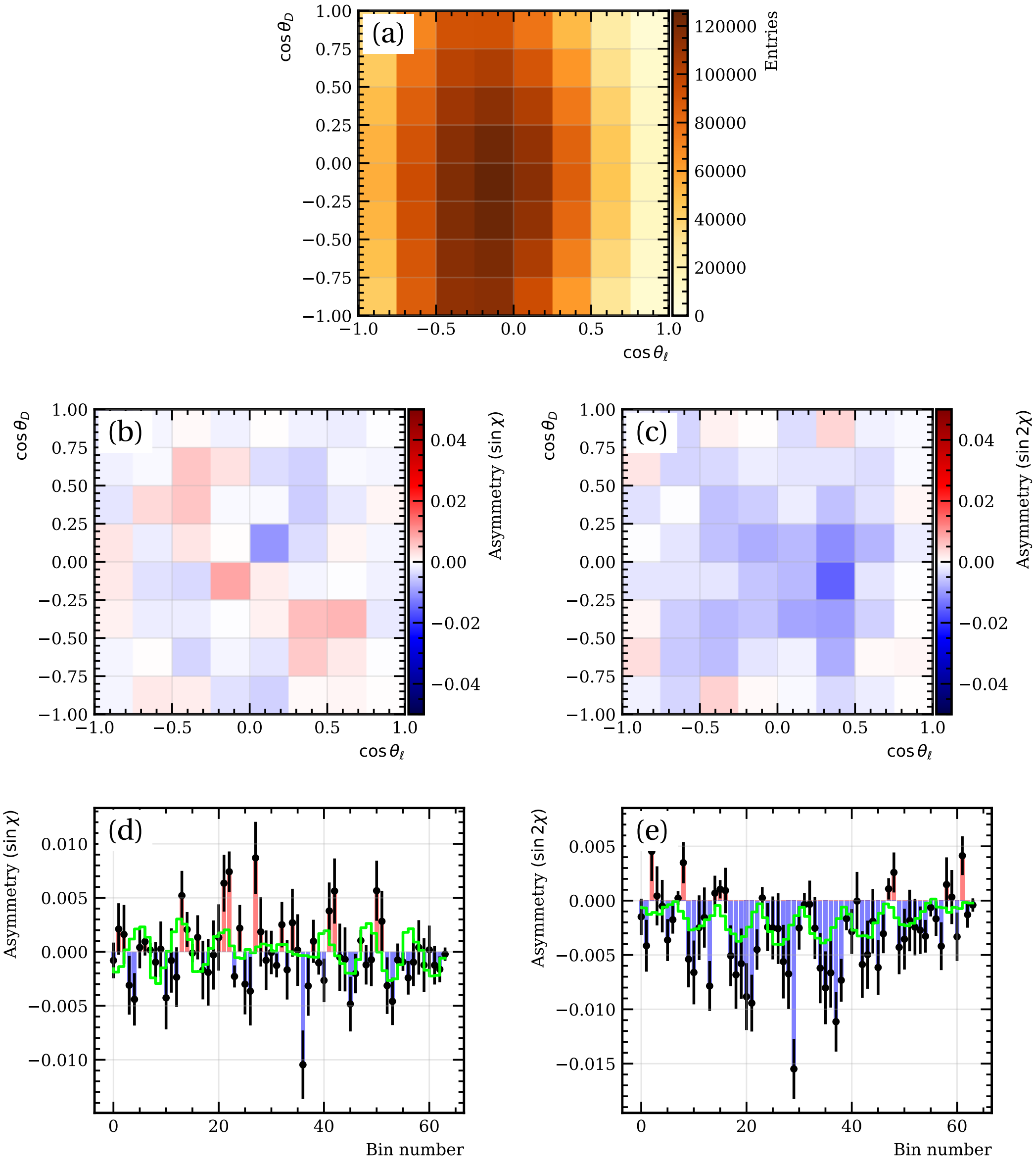

Figure 5: Binned density (a), binned 2D parity asymmetries (b,c) and flattened 1D parity asymmetries (d,e) of $\sin\chi$ and $\sin 2\chi$ terms in $(\cos\theta_D, \cos\theta_\ell)$ bins integrated over q^2 for the $B^+ \to D^{**0}\mu^+\nu_\mu$ with $\delta_D = 180°$. Figures (d) and (e) also show the result of the best fit in green using the RH and PT templates.

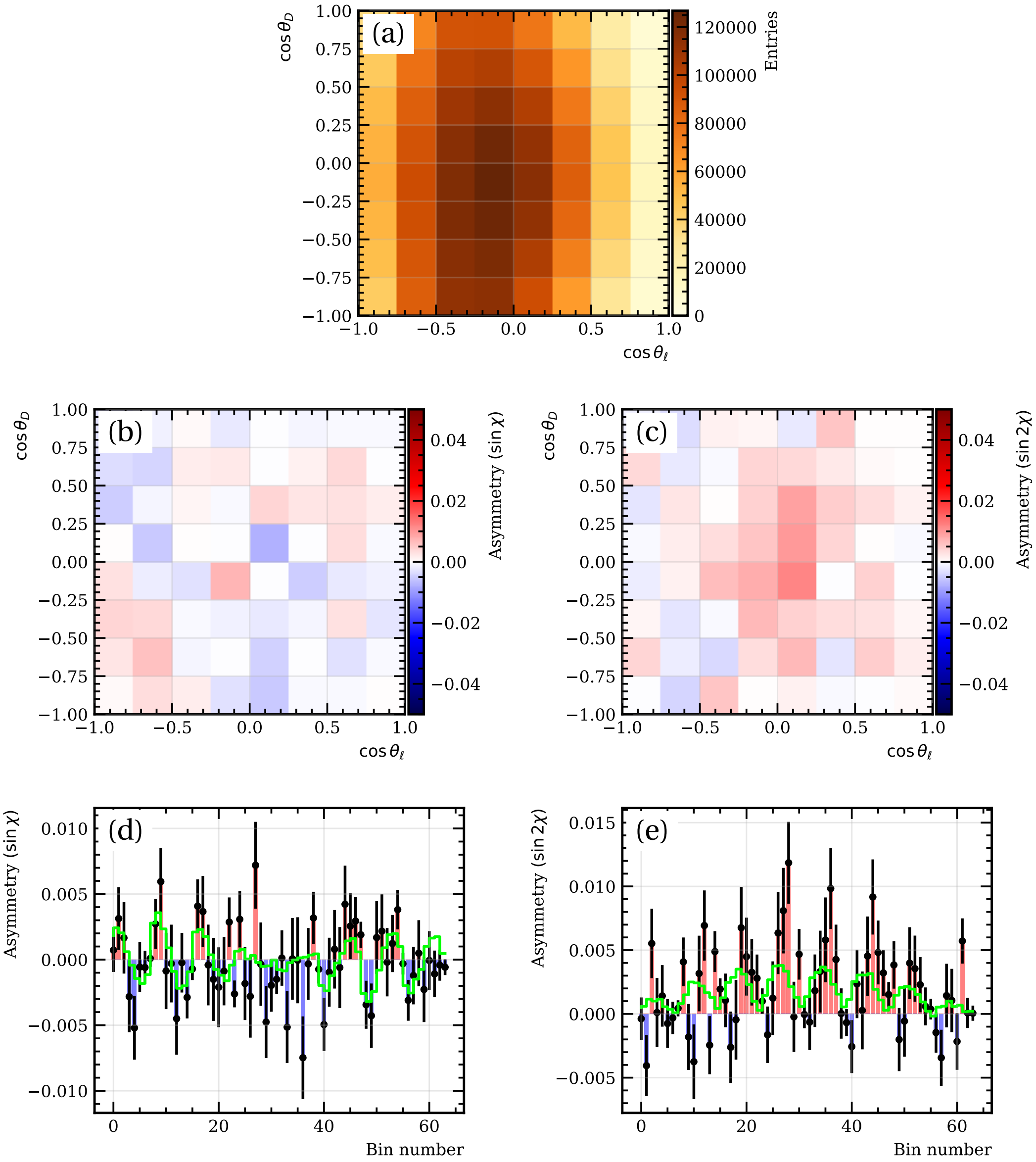

Figure 6: Binned density (a), binned 2D parity asymmetries (b,c) and flattened 1D parity asymmetries (d,e) of $\sin\chi$ and $\sin 2\chi$ terms in $(\cos\theta_D, \cos\theta_\ell)$ bins integrated over q^2 for the $B^+ \to D^{**0}\mu^+\nu_\mu$ with $\delta_D = 225°$. Figures (d) and (e) also show the result of the best fit in green using the RH and PT templates.

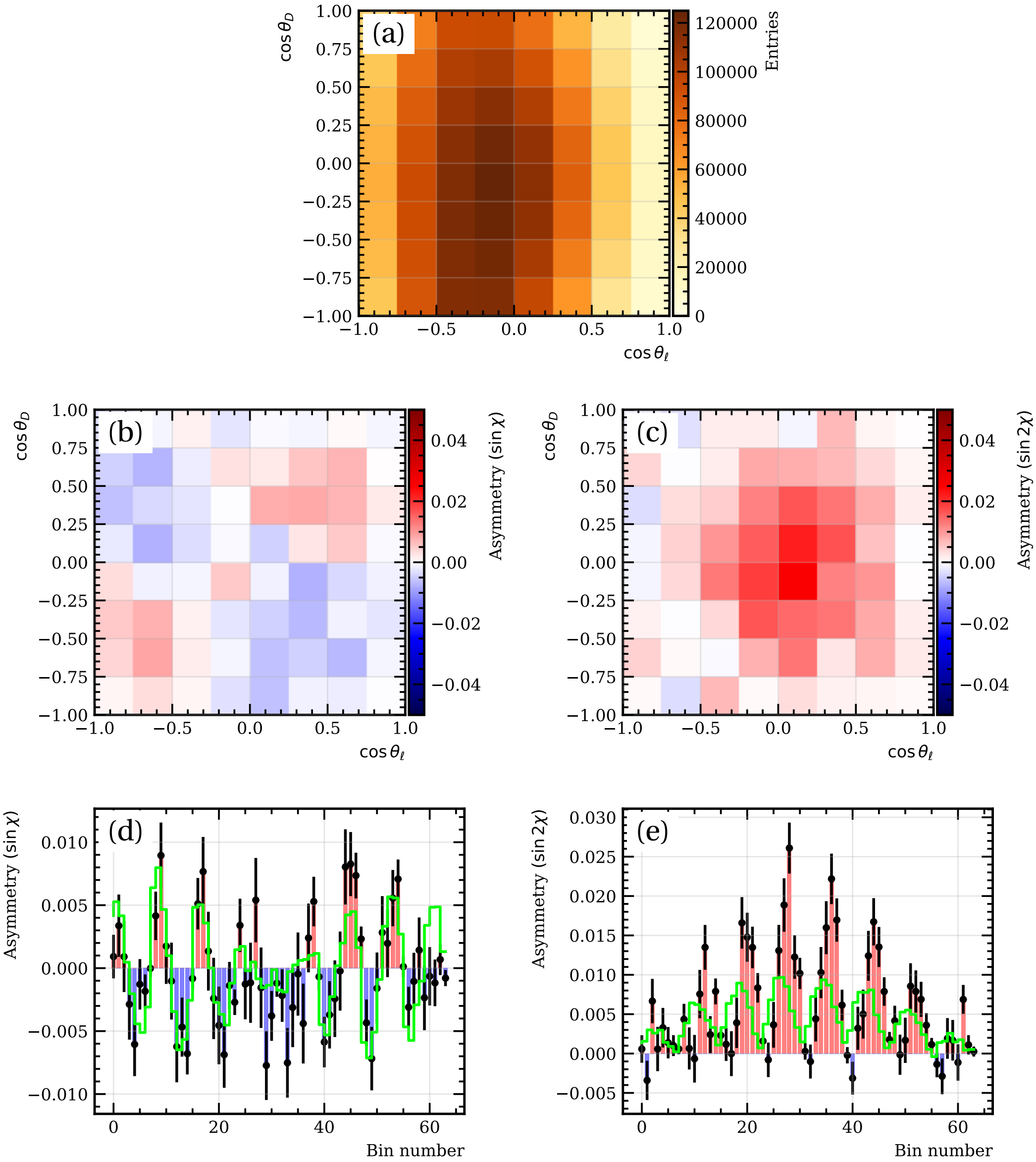

Figure 7: Binned density (a), binned 2D parity asymmetries (b,c) and flattened 1D parity asymmetries (d,e) of $\sin\chi$ and $\sin 2\chi$ terms in $(\cos\theta_D, \cos\theta_\ell)$ bins integrated over q^2 for the $B^+ \to D^{**0}\mu^+\nu_\mu$ with $\delta_D = 270°$. Figures (d) and (e) also show the result of the best fit in green using the RH and PT templates.

Appendix B

VELO misalignment asymmetries and bias fits

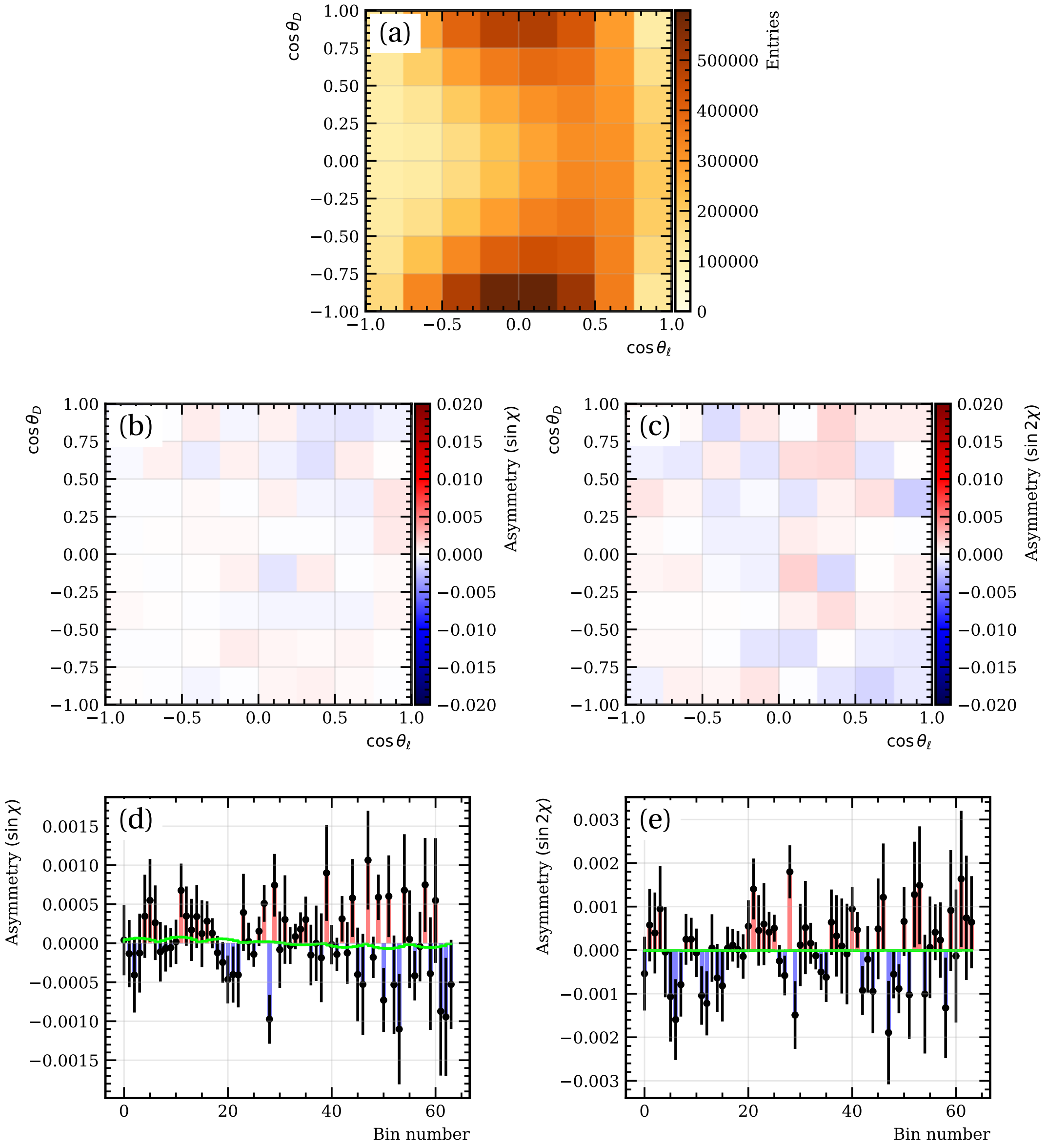

Figure 8: Binned density (a), binned 2D *CP* asymmetries (b,c) and flattened 1D *CP* asymmetries (d,e) of $\sin\chi$ and $\sin 2\chi$ terms in $(\cos\theta_D, \cos\theta_\ell)$ bins integrated over q^2 for the T_x misalignment sample. Figures (d) and (e) also show the result of the best fit in green using the RH and PT templates.

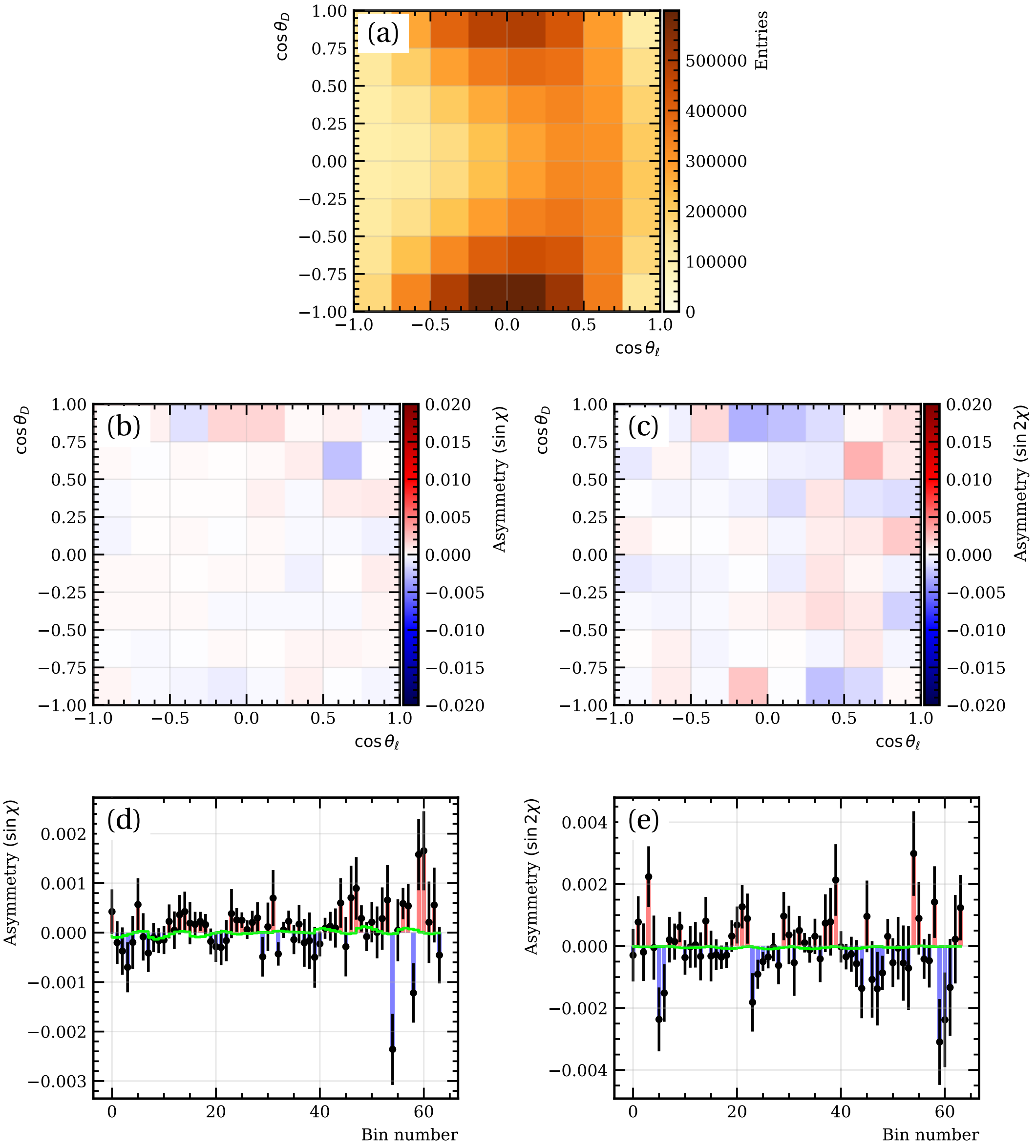

Figure 9: Binned density (a), binned 2D parity asymmetries (b,c) and flattened 1D parity asymmetries (d,e) of $\sin\chi$ and $\sin 2\chi$ terms in $(\cos\theta_D, \cos\theta_\ell)$ bins integrated over q^2 for the T_x misalignment sample. Figures (d) and (e) also show the result of the best fit in green using the RH and PT templates.

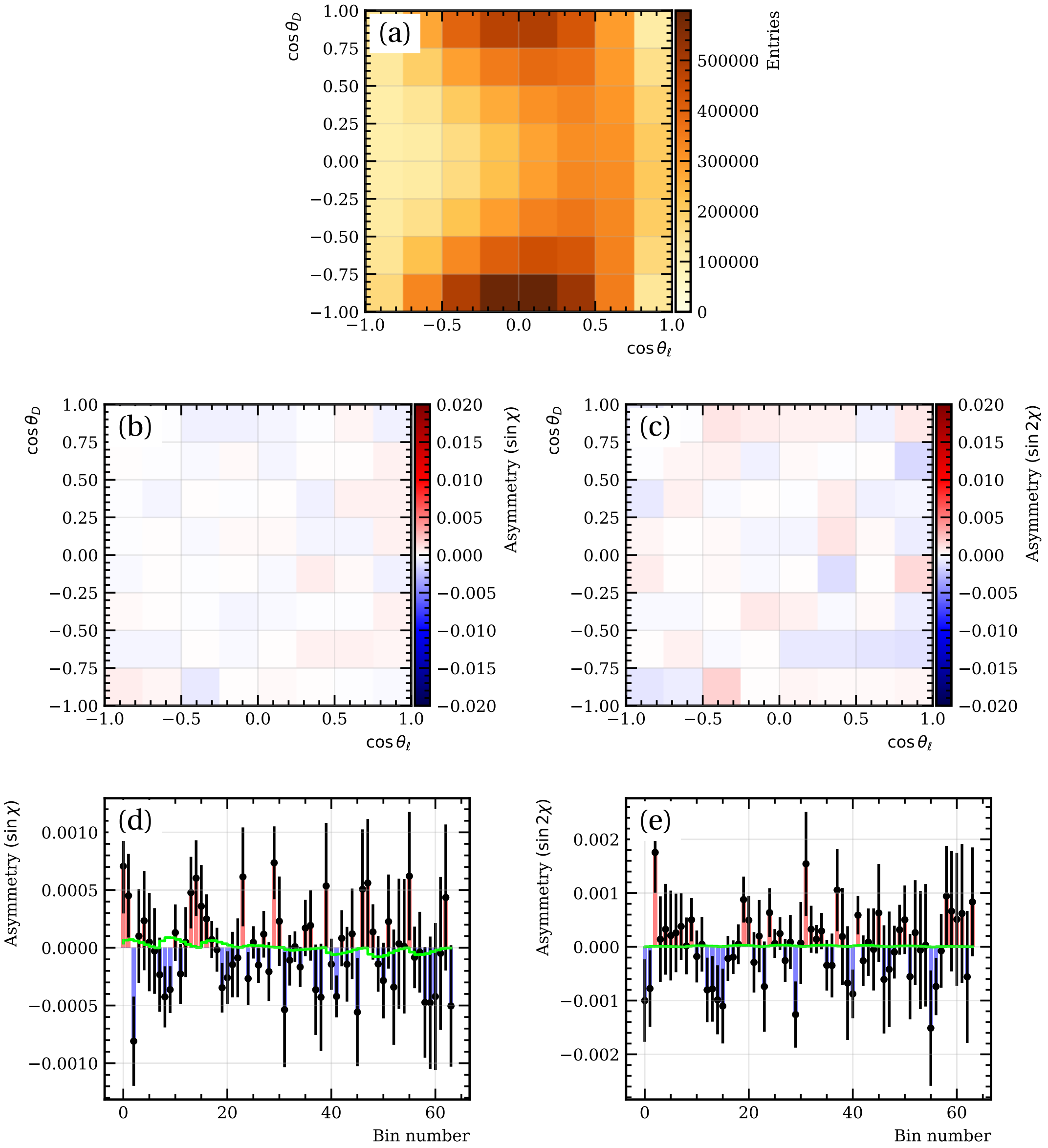

Figure 10: Binned density (a), binned 2D *CP* asymmetries (b,c) and flattened 1D *CP* asymmetries (d,e) of $\sin\chi$ and $\sin 2\chi$ terms in $(\cos\theta_D, \cos\theta_\ell)$ bins integrated over q^2 for the T_z misalignment sample. Figures (d) and (e) also show the result of the best fit in green using the RH and PT templates.

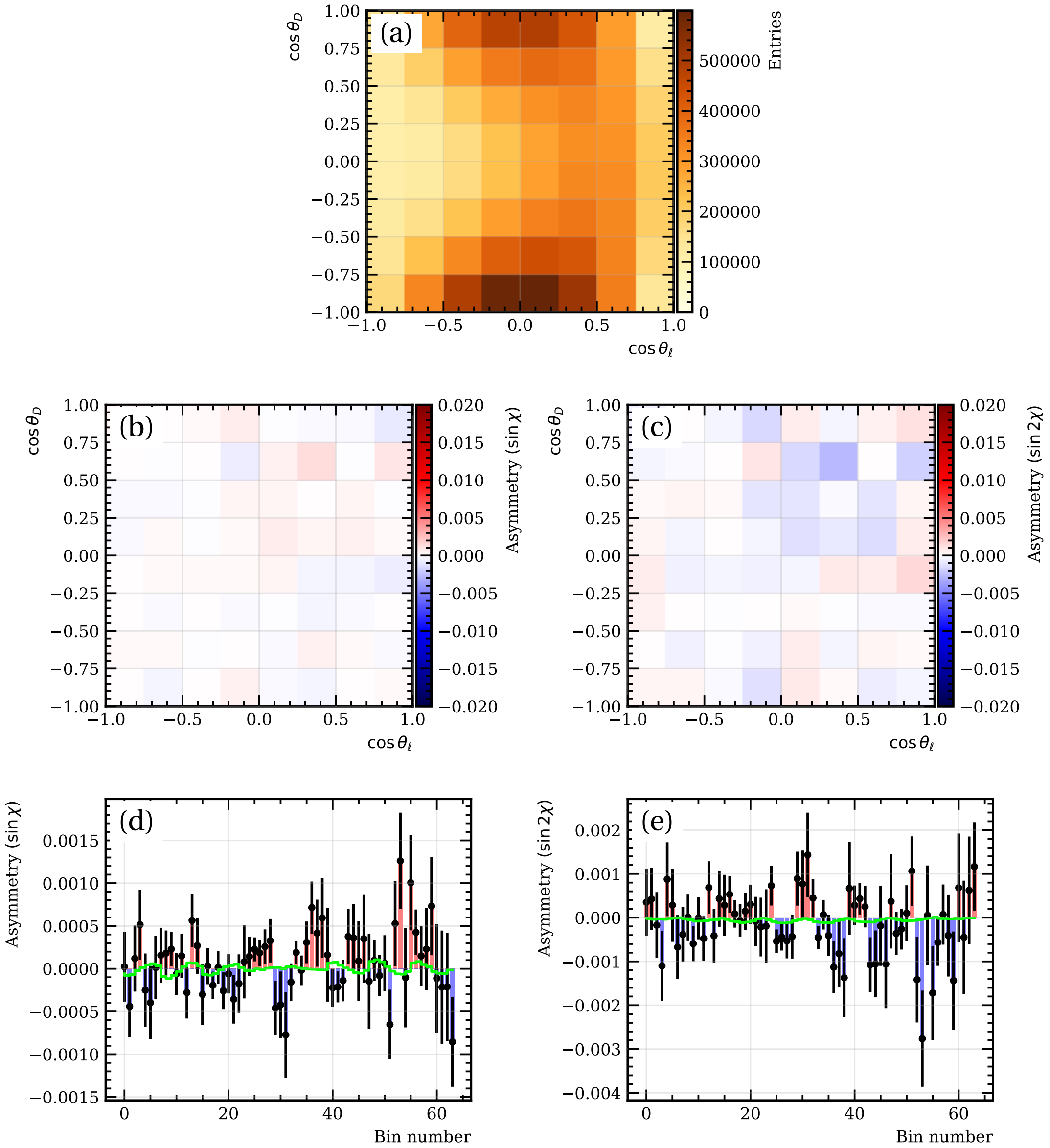

Figure 11: Binned density (a), binned 2D parity asymmetries (b,c) and flattened 1D parity asymmetries (d,e) of $\sin\chi$ and $\sin 2\chi$ terms in $(\cos\theta_D, \cos\theta_\ell)$ bins integrated over q^2 for the T_z misalignment sample. Figures (d) and (e) also show the result of the best fit in green using the RH and PT templates.

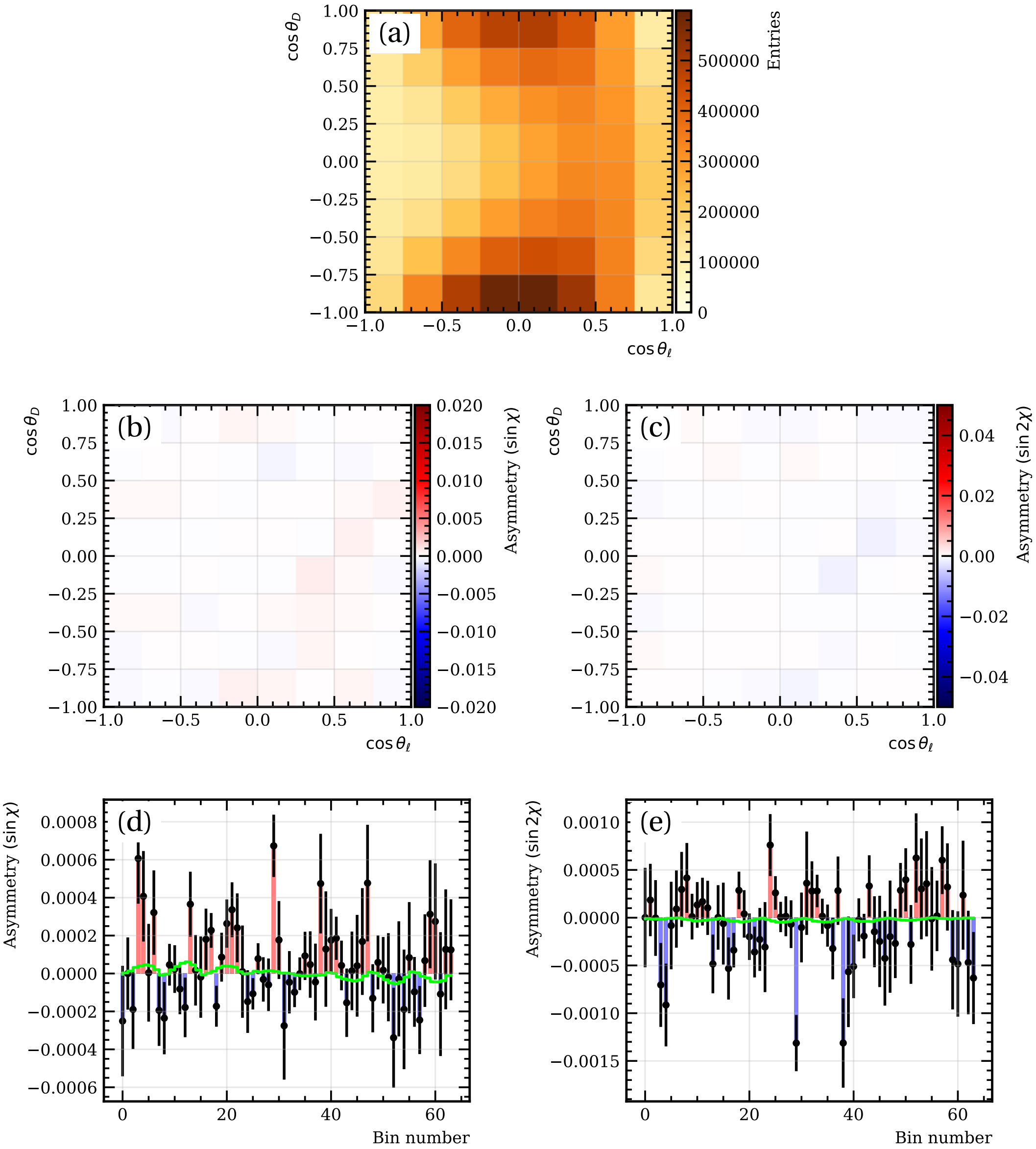

Figure 12: Binned density (a), binned 2D *CP* asymmetries (b,c) and flattened 1D *CP* asymmetries (d,e) of $\sin\chi$ and $\sin 2\chi$ terms in $(\cos\theta_D, \cos\theta_\ell)$ bins integrated over q^2 for the R_x misalignment sample. Figures (d) and (e) also show the result of the best fit in green using the RH and PT templates.

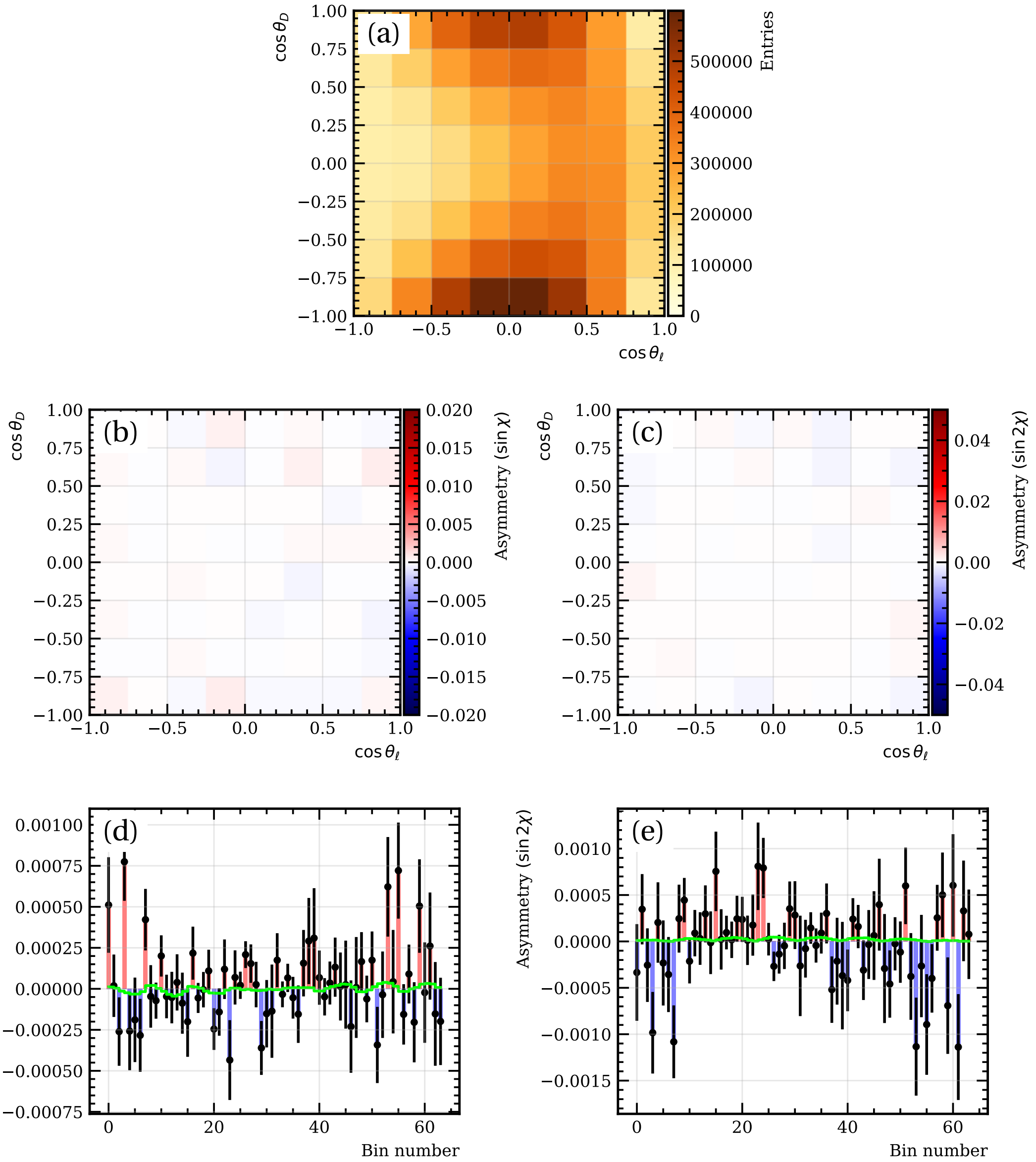

Figure 13: Binned density (a), binned 2D parity asymmetries (b,c) and flattened 1D parity asymmetries (d,e) of $\sin\chi$ and $\sin 2\chi$ terms in $(\cos\theta_D, \cos\theta_\ell)$ bins integrated over q^2 for the R_x misalignment sample. Figures (d) and (e) also show the result of the best fit in green using the RH and PT templates.

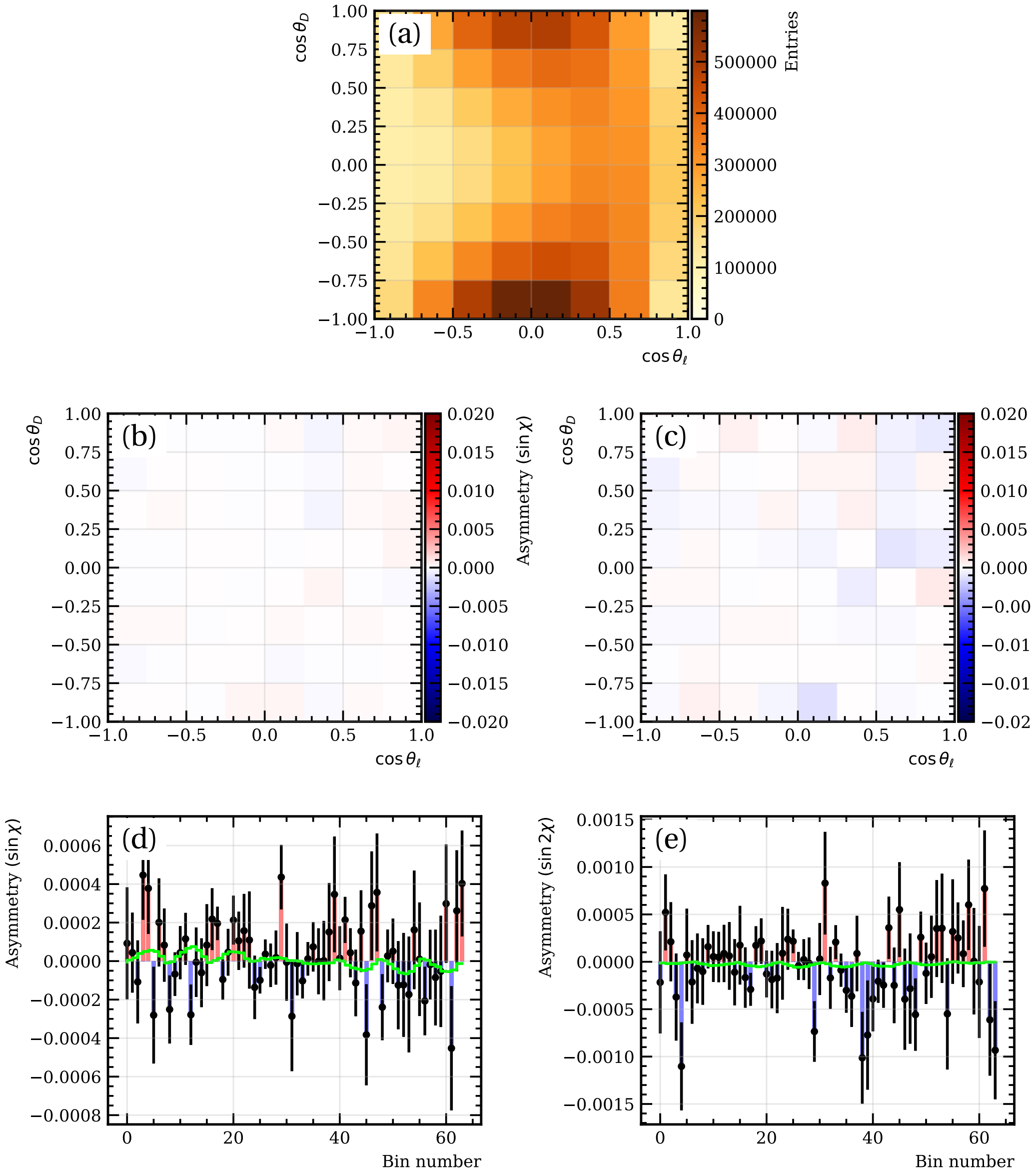

Figure 14: Binned density (a), binned 2D *CP* asymmetries (b,c) and flattened 1D *CP* asymmetries (d,e) of $\sin\chi$ and $\sin 2\chi$ terms in $(\cos\theta_D, \cos\theta_\ell)$ bins integrated over q^2 for the R_y misalignment sample. Figures (d) and (e) also show the result of the best fit in green using the RH and PT templates.

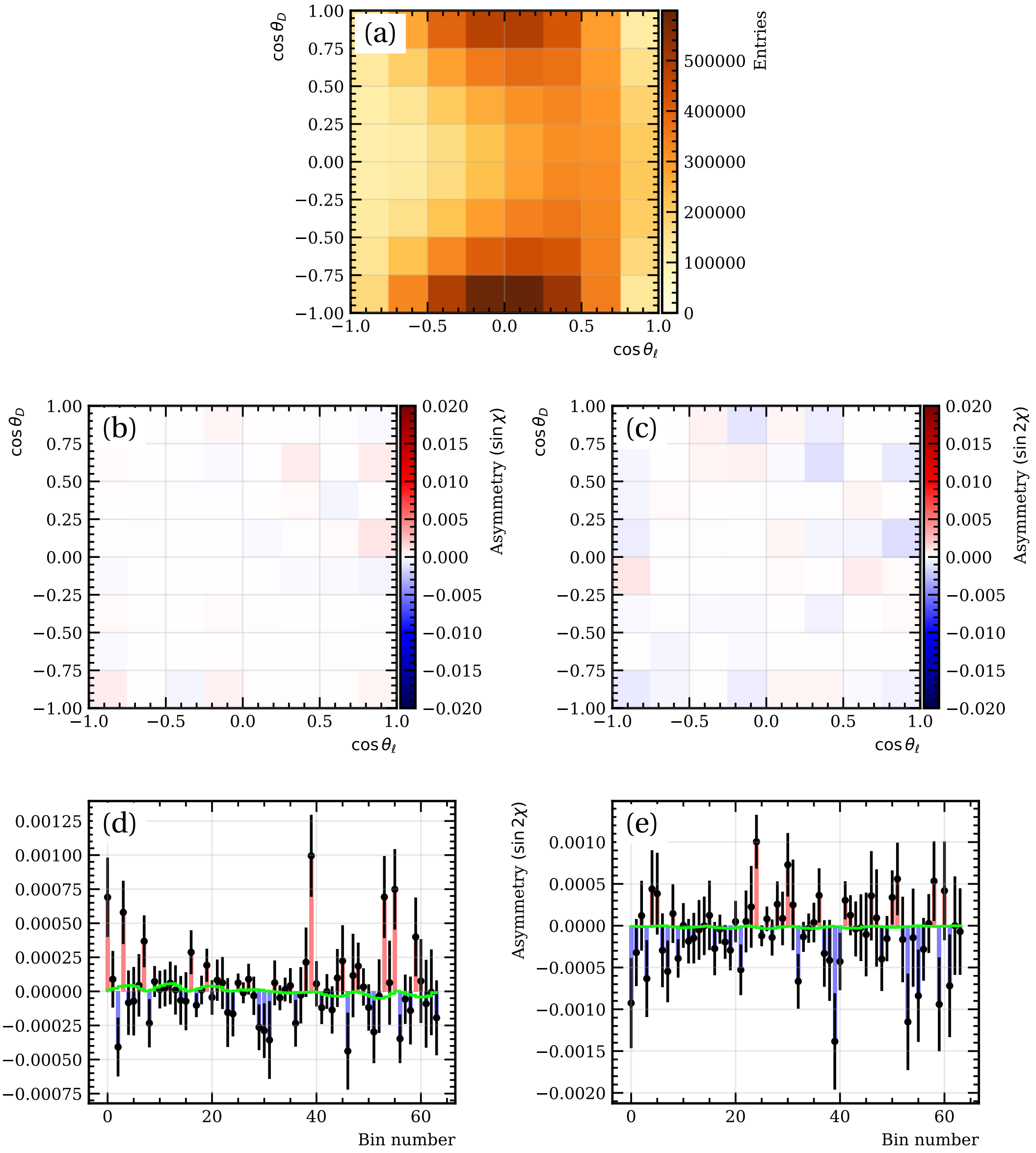

Figure 15: Binned density (a), binned 2D parity asymmetries (b,c) and flattened 1D parity asymmetries (d,e) of $\sin\chi$ and $\sin 2\chi$ terms in $(\cos\theta_D, \cos\theta_\ell)$ bins integrated over q^2 for the R_y misalignment sample. Figures (d) and (e) also show the result of the best fit in green using the RH and PT templates.

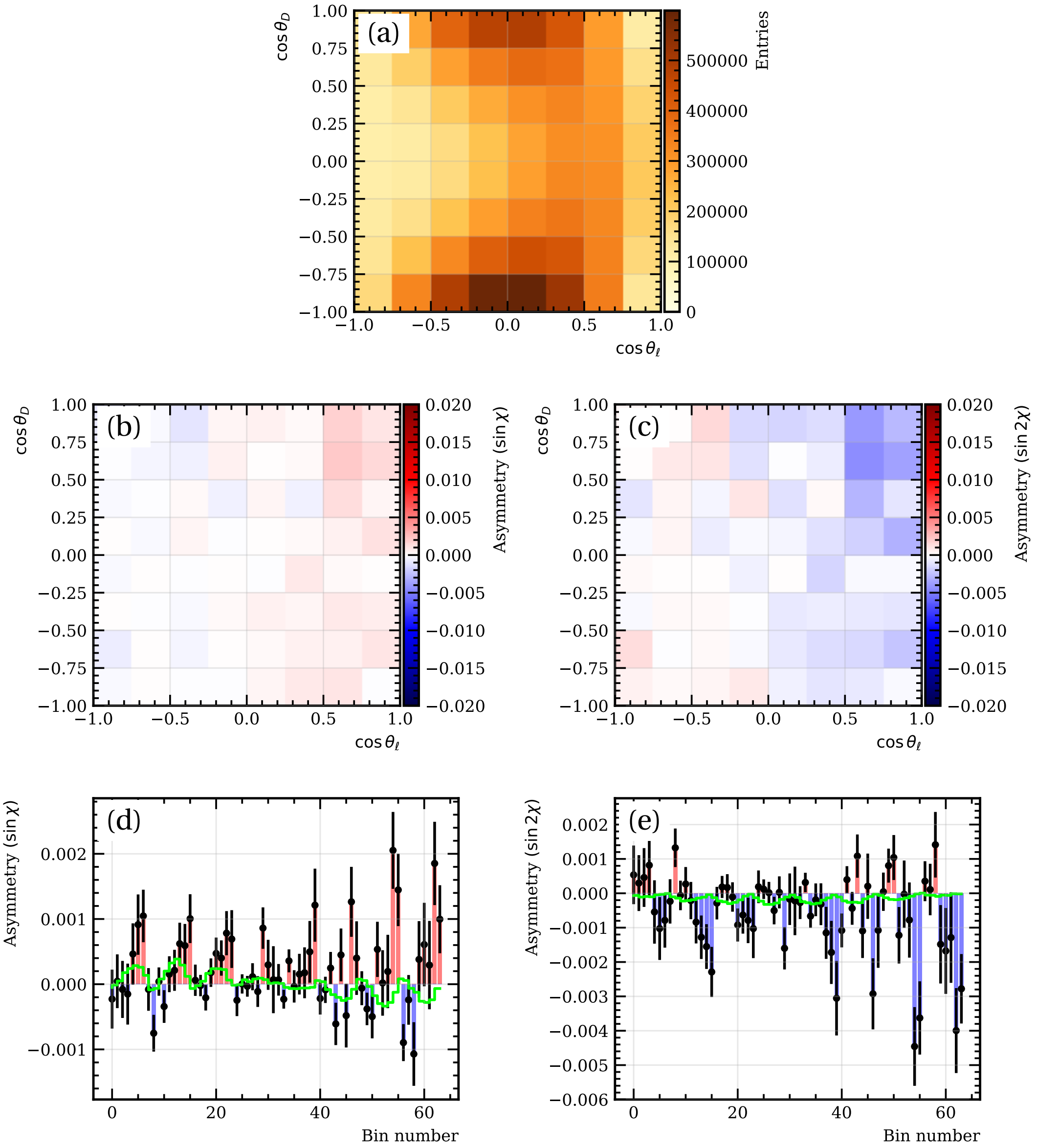

Figure 16: Binned density (a), binned 2D *CP* asymmetries (b,c) and flattened 1D *CP* asymmetries (d,e) of $\sin\chi$ and $\sin 2\chi$ terms in $(\cos\theta_D, \cos\theta_\ell)$ bins integrated over q^2 for the R_z misalignment sample. Figures (d) and (e) also show the result of the best fit in green using the RH and PT templates.

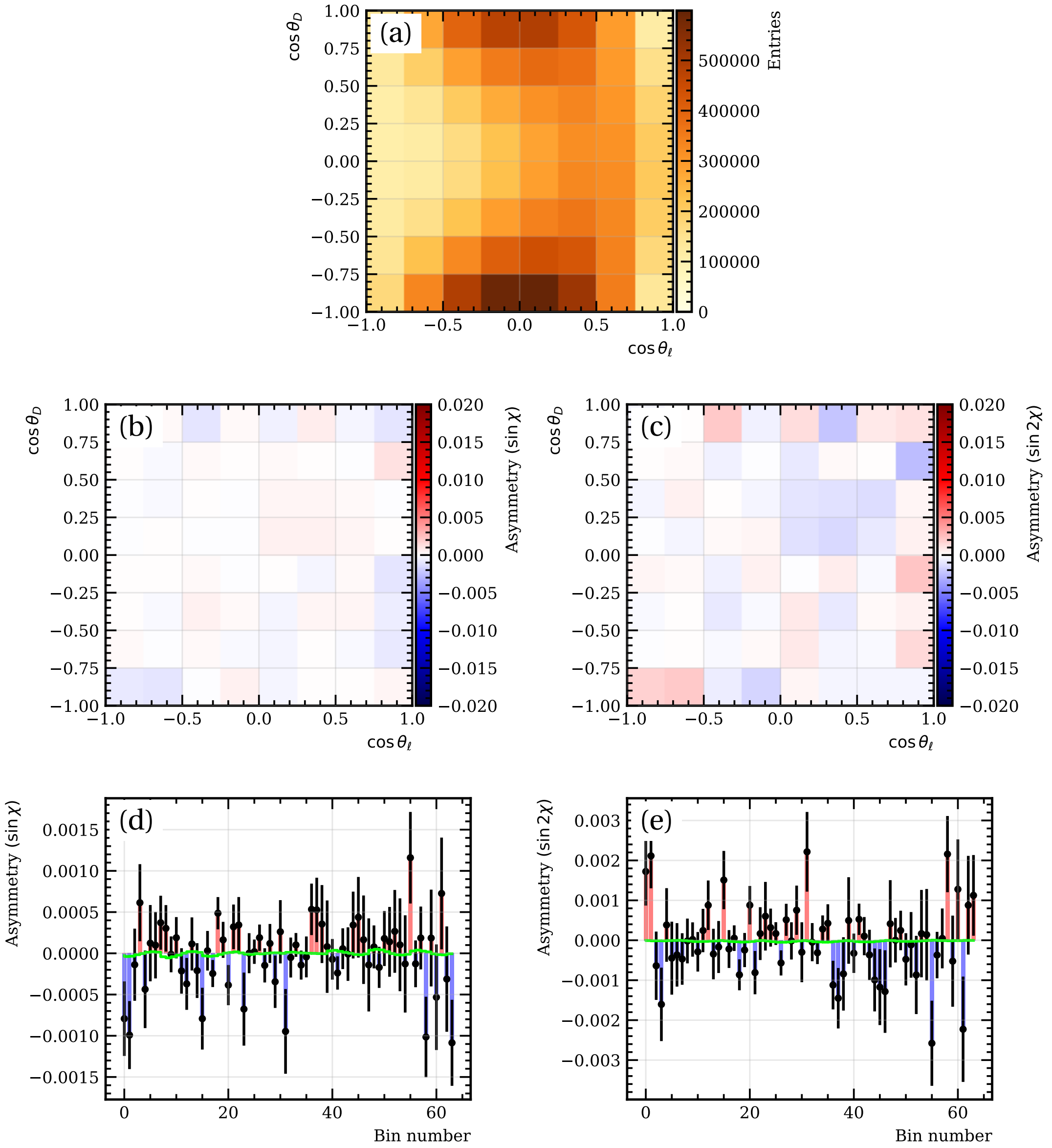

Figure 17: Binned density (a), binned 2D parity asymmetries (b,c) and flattened 1D parity asymmetries (d,e) of $\sin\chi$ and $\sin 2\chi$ terms in $(\cos\theta_D, \cos\theta_\ell)$ bins integrated over q^2 for the R_z misalignment sample. Figures (d) and (e) also show the result of the best fit in green using the RH and PT templates.

Appendix C

Comparison of kinematic and topological variables in signal $B^0 \to D^{*-}\mu^+\nu_\mu$ and control $B^0 \to D^-\mu^+\nu_\mu$ samples

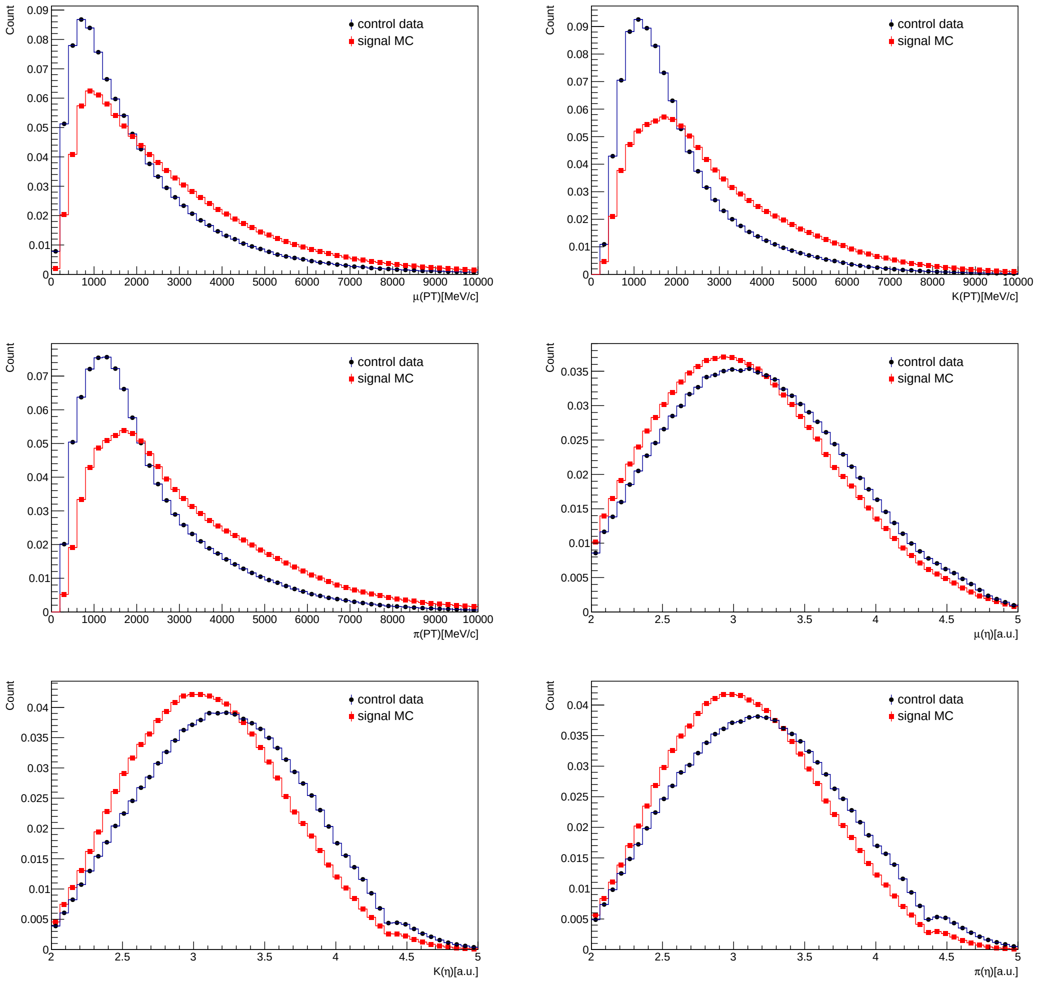

Figure 18: Comparison of kinematic variables between the signal and control samples.

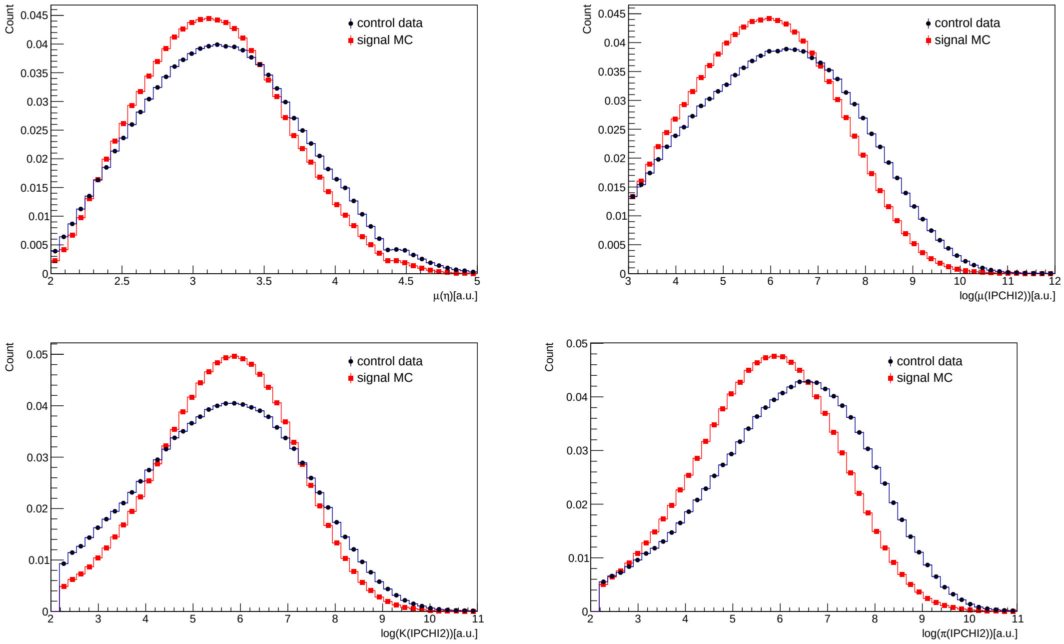

Figure 19: Comparison of topological variables between the signal and control samples.

Appendix D

VELO misalignment calibration

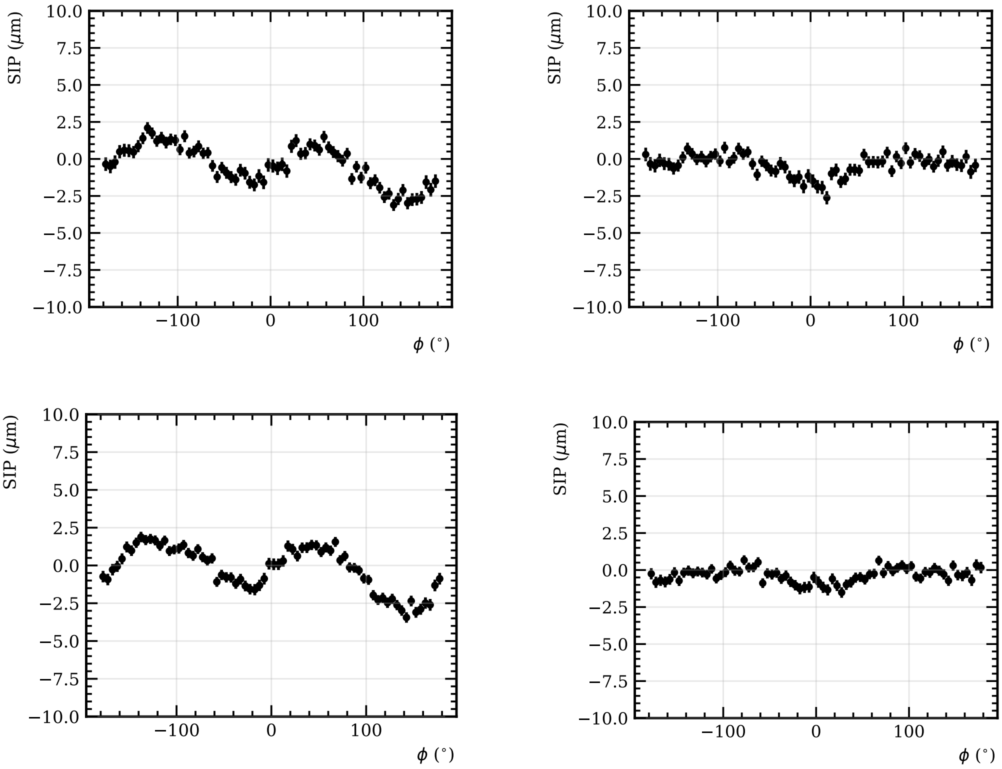

Figure 20: *SIP vs.* ϕ dependence for the 2011 `MagUp` (top) and `MagDown` (bottom) $B^+ \to J/\psi K^+$ data sample before (left) and after (right) correcting for the misalignment of the VELO

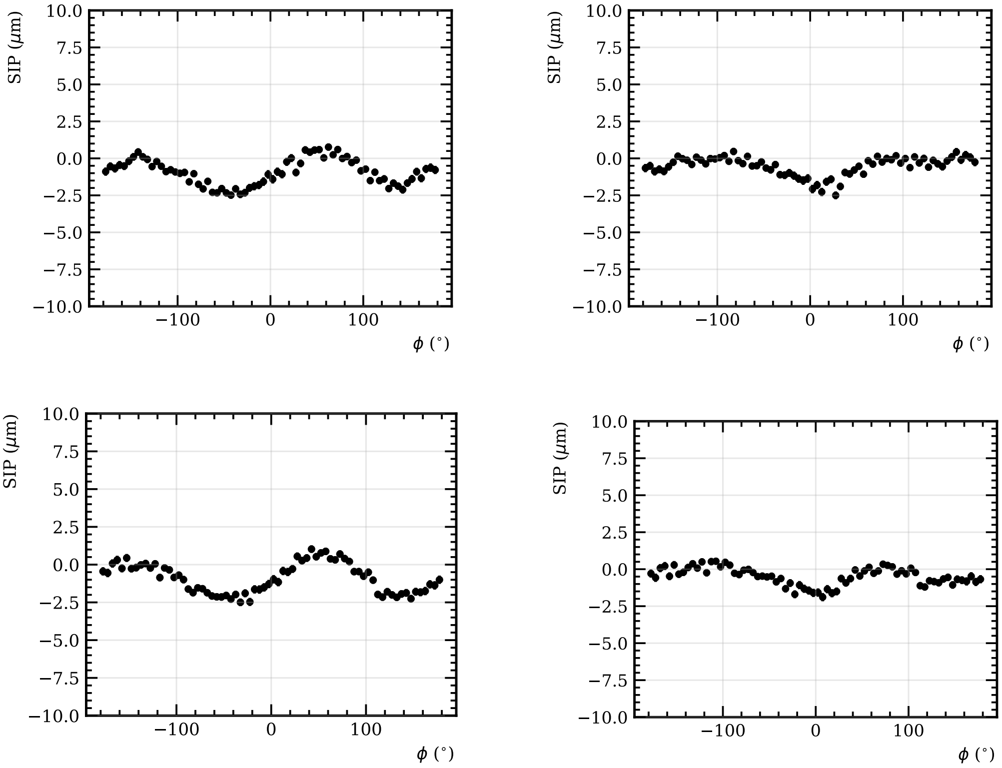

Figure 21: SIP *vs.* ϕ dependence for the 2012 `MagUp` (top) and `MagDown` (bottom) $B^+ \to J/\psi K^+$ data sample before (left) and after (right) correcting for the misalignment of the VELO

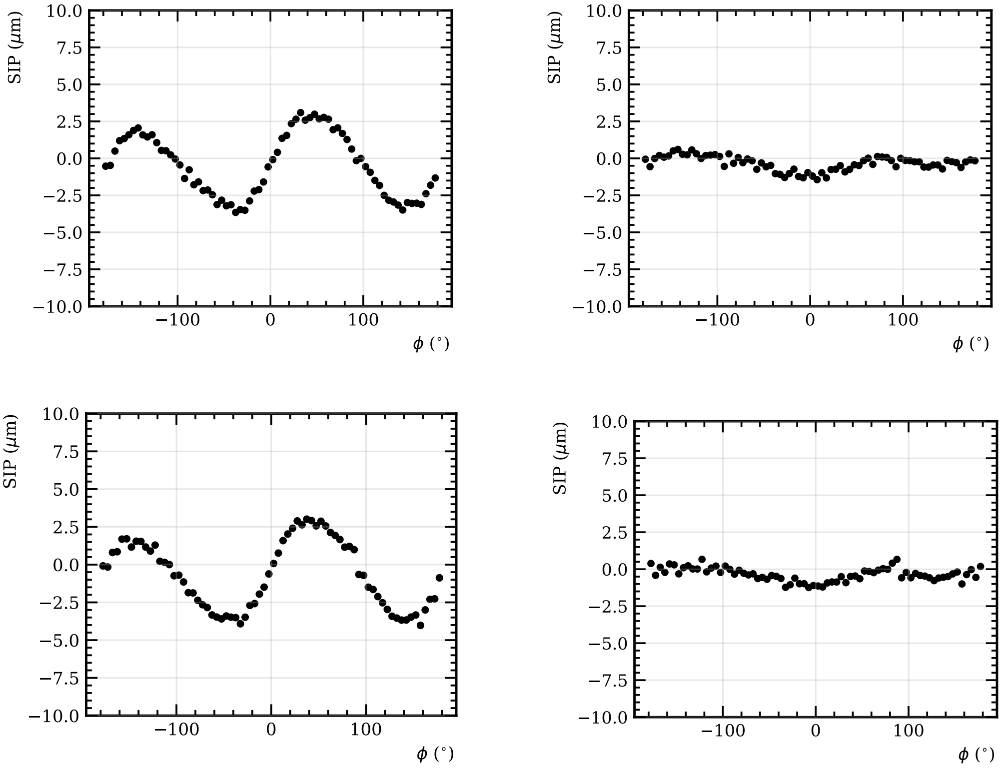

Figure 22: SIP *vs.* ϕ dependence for the 2016 `MagUp` (top) and `MagDown` (bottom) $B^+ \rightarrow J/\psi K^+$ data sample before (left) and after (right) correcting for the misalignment of the VELO

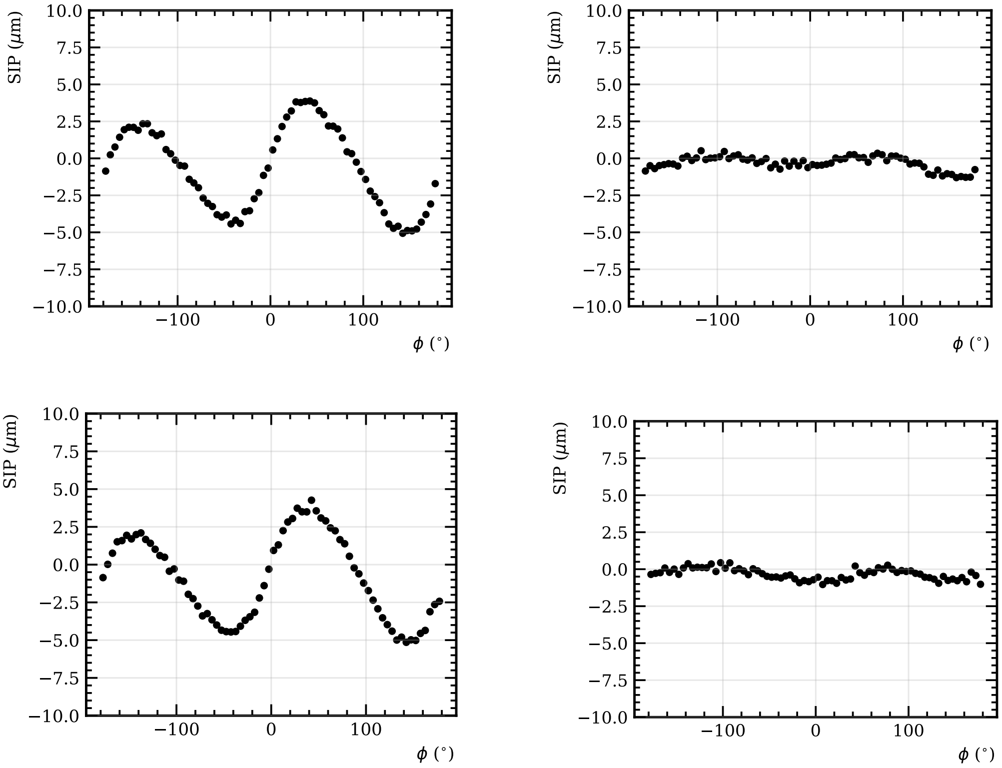

Figure 23: SIP *vs.* ϕ dependence for the 2017 `MagUp` (top) and `MagDown` (bottom) $B^+ \to J/\psi K^+$ data sample before (left) and after (right) correcting for the misalignment of the VELO

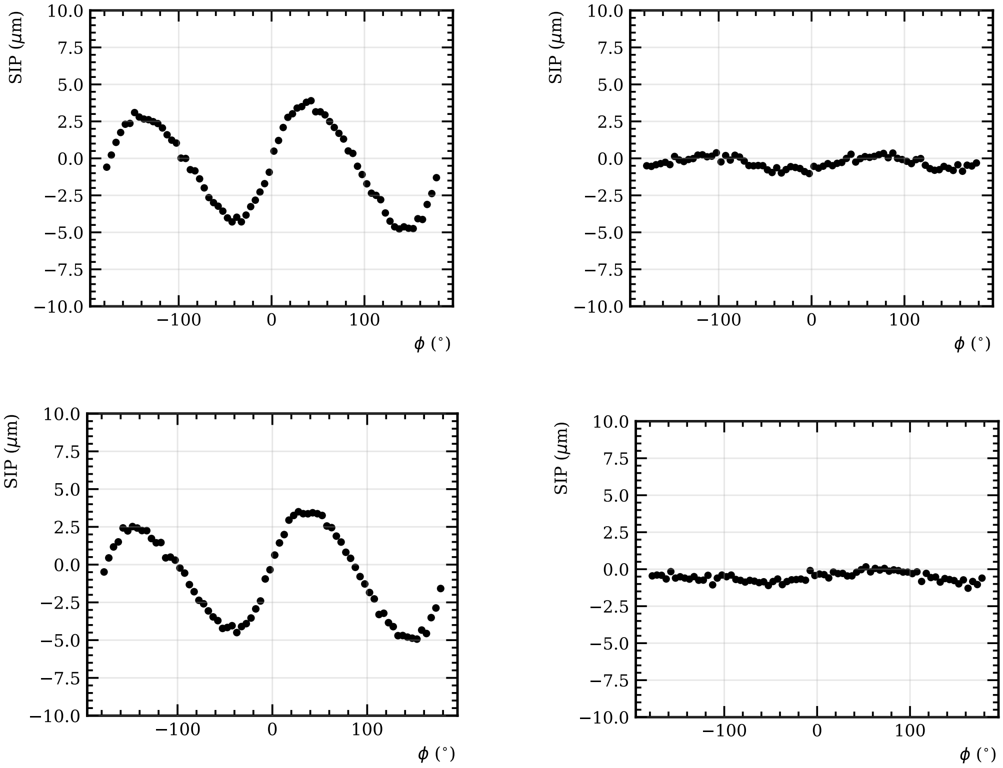

Figure 24: SIP *vs.* ϕ dependence for the 2018 `MagUp` (top) and `MagDown` (bottom) $B^{+} \rightarrow J/\psi K^{+}$ data sample before (left) and after (right) correcting for the misalignment of the VELO

Appendix E

Comparison of control and signal bias in bins of kinematic and topological variables

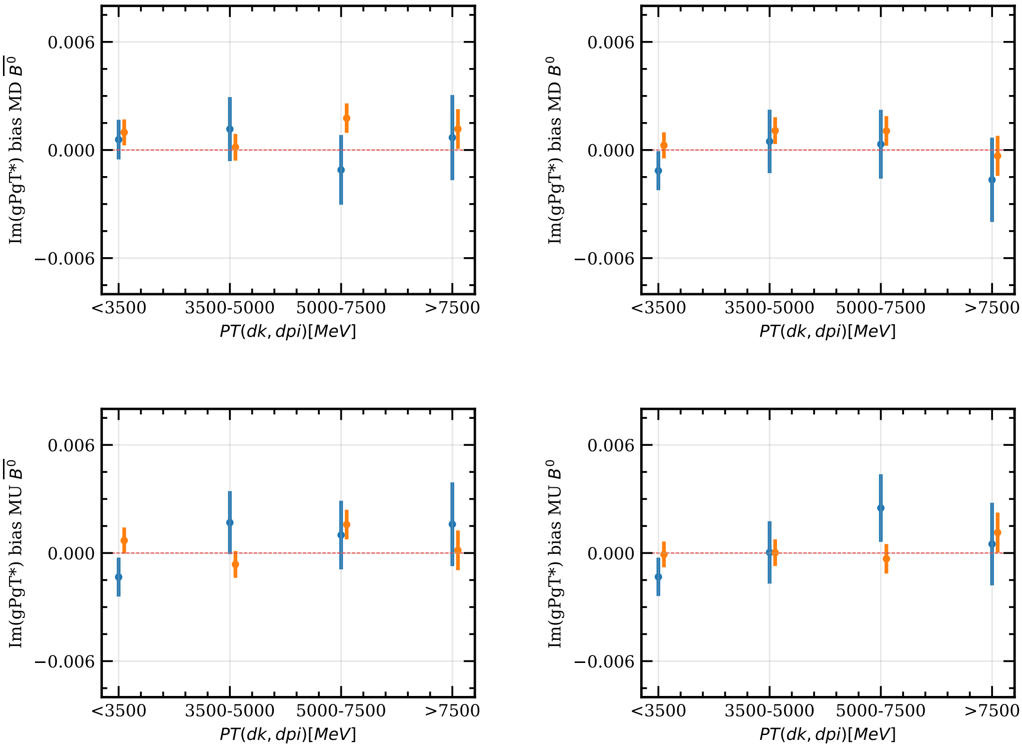

Figure 25: $\mathrm{Im}(g_P g_T^*)$ bias for signal (orange) and control samples in bins of $p_\mathrm{T}(K^+\pi^-)$ across the four categories

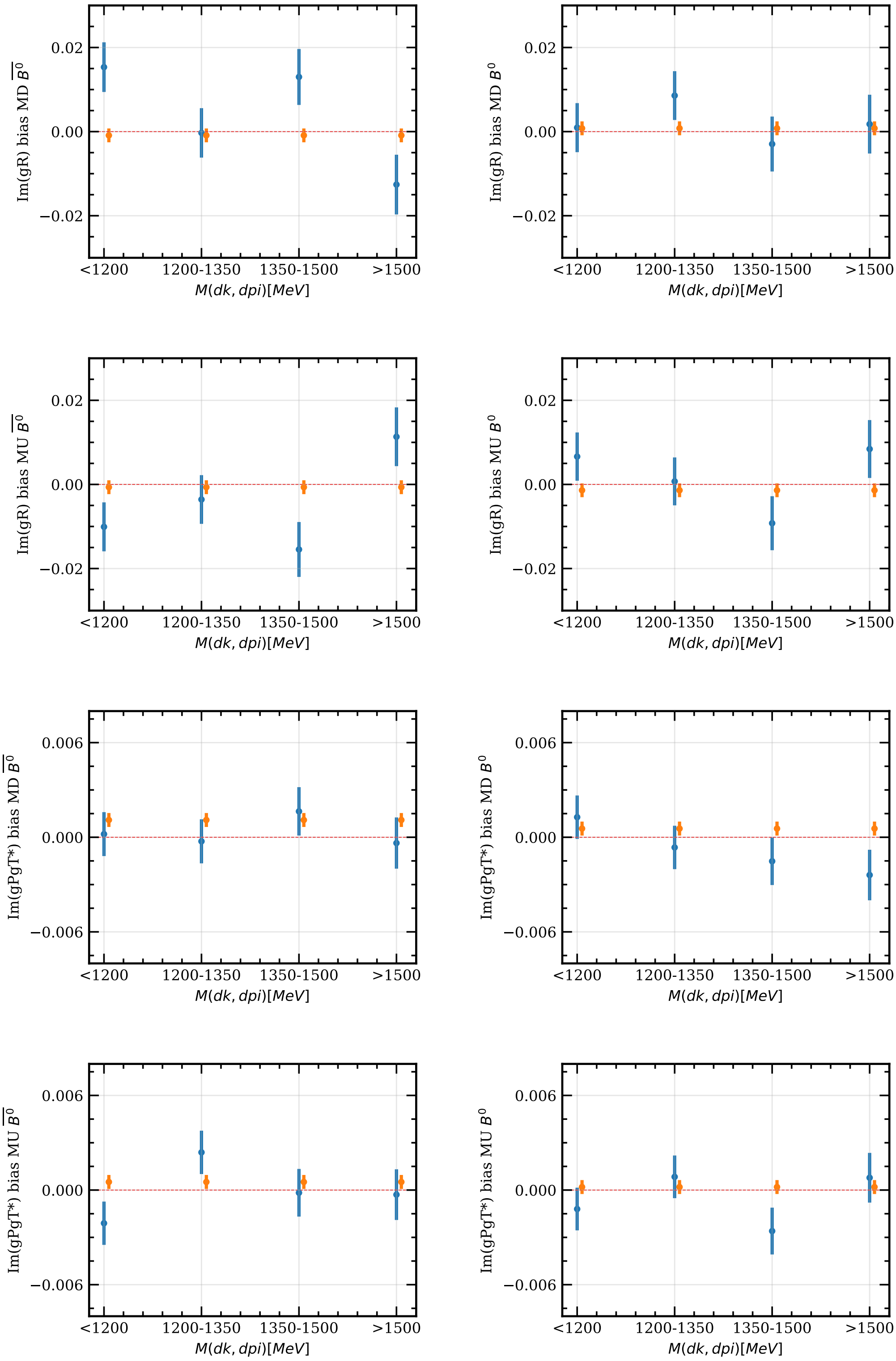

Figure 26: NP couplings bias for signal (orange) and control (blue) samples in bins of $M(K^+\pi^-)$ across the four categories

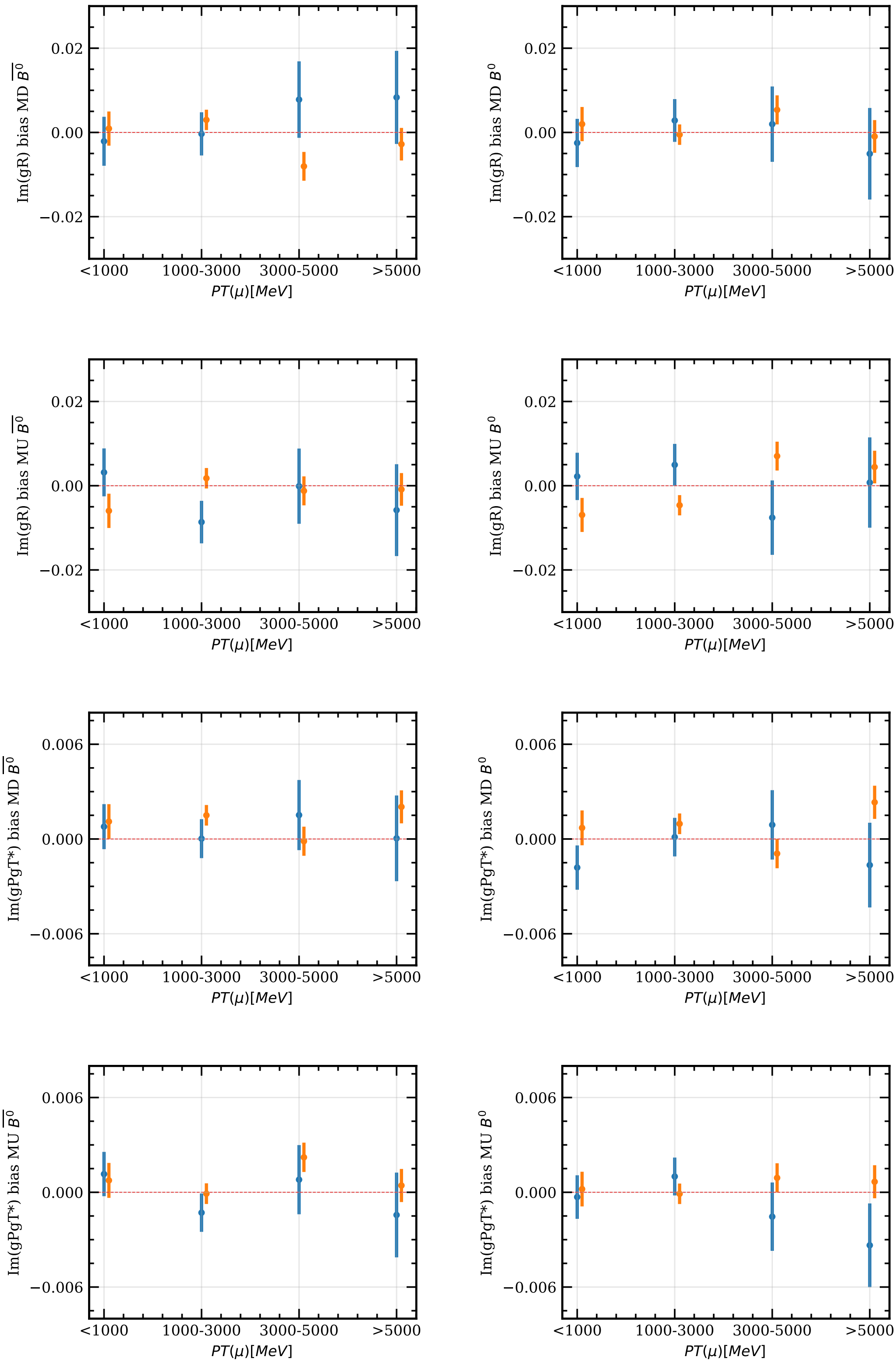

Figure 27: NP couplings bias for signal (orange) and control (blue) samples in bins of $p_\mathrm{T}(\mu)$ across the four categories

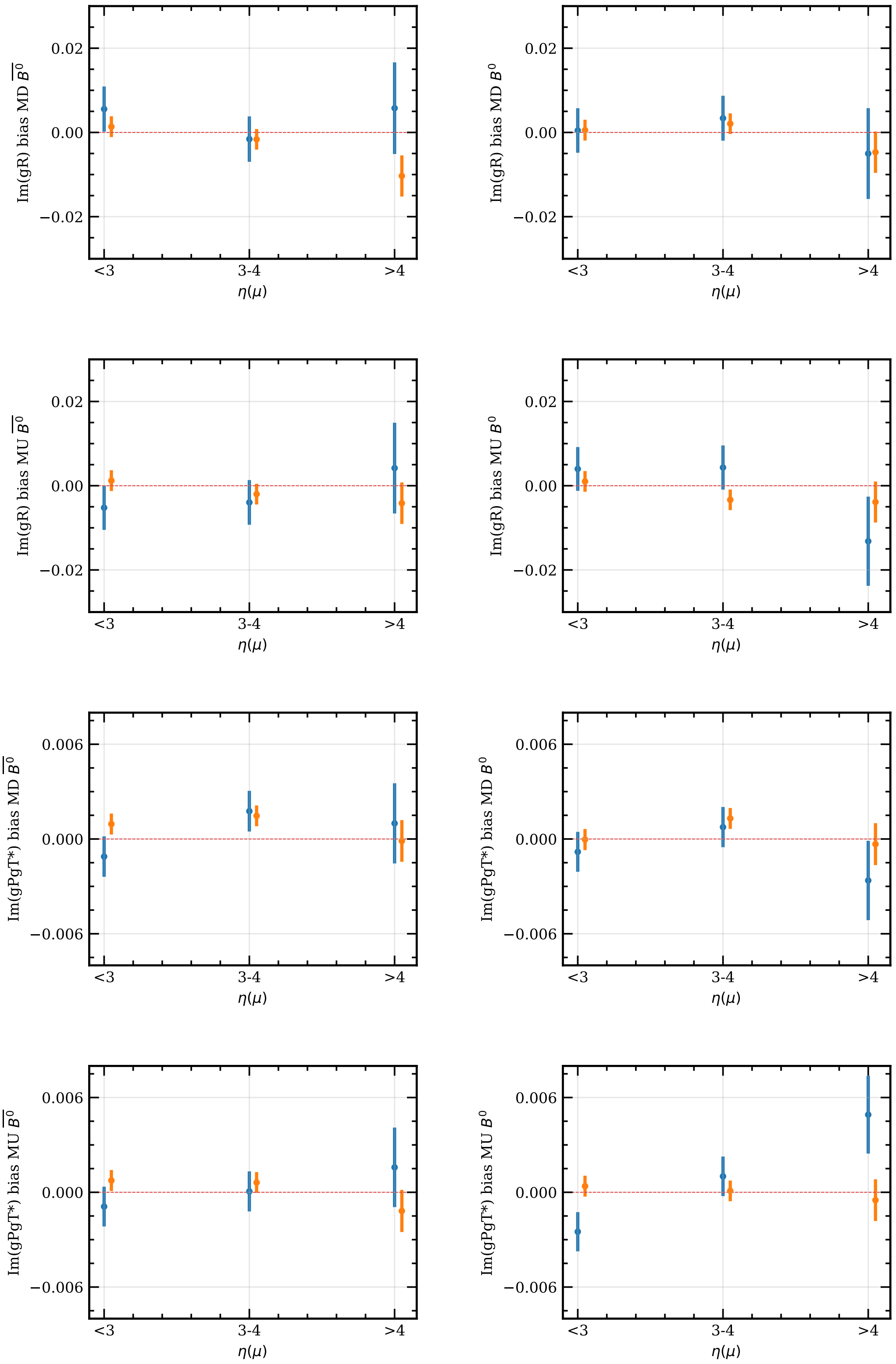

Figure 28: NP couplings bias for signal (orange) and control (blue) samples in bins of $\eta(\mu)$ across the four categories

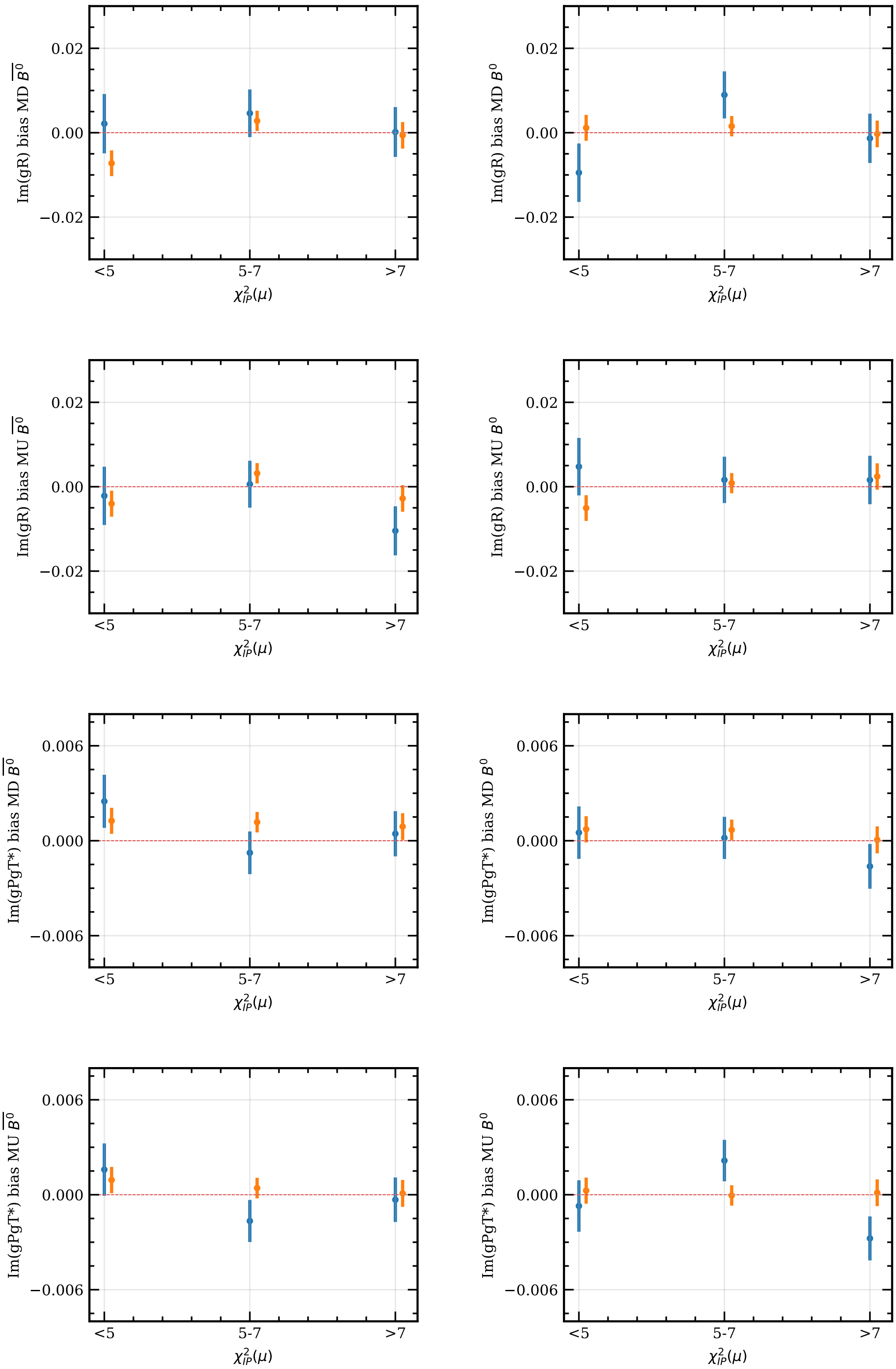

Figure 29: NP couplings bias for signal (orange) and control (blue) samples in bins of $\chi^2_{\mathrm{IP}}(\mu)$ across the four categories

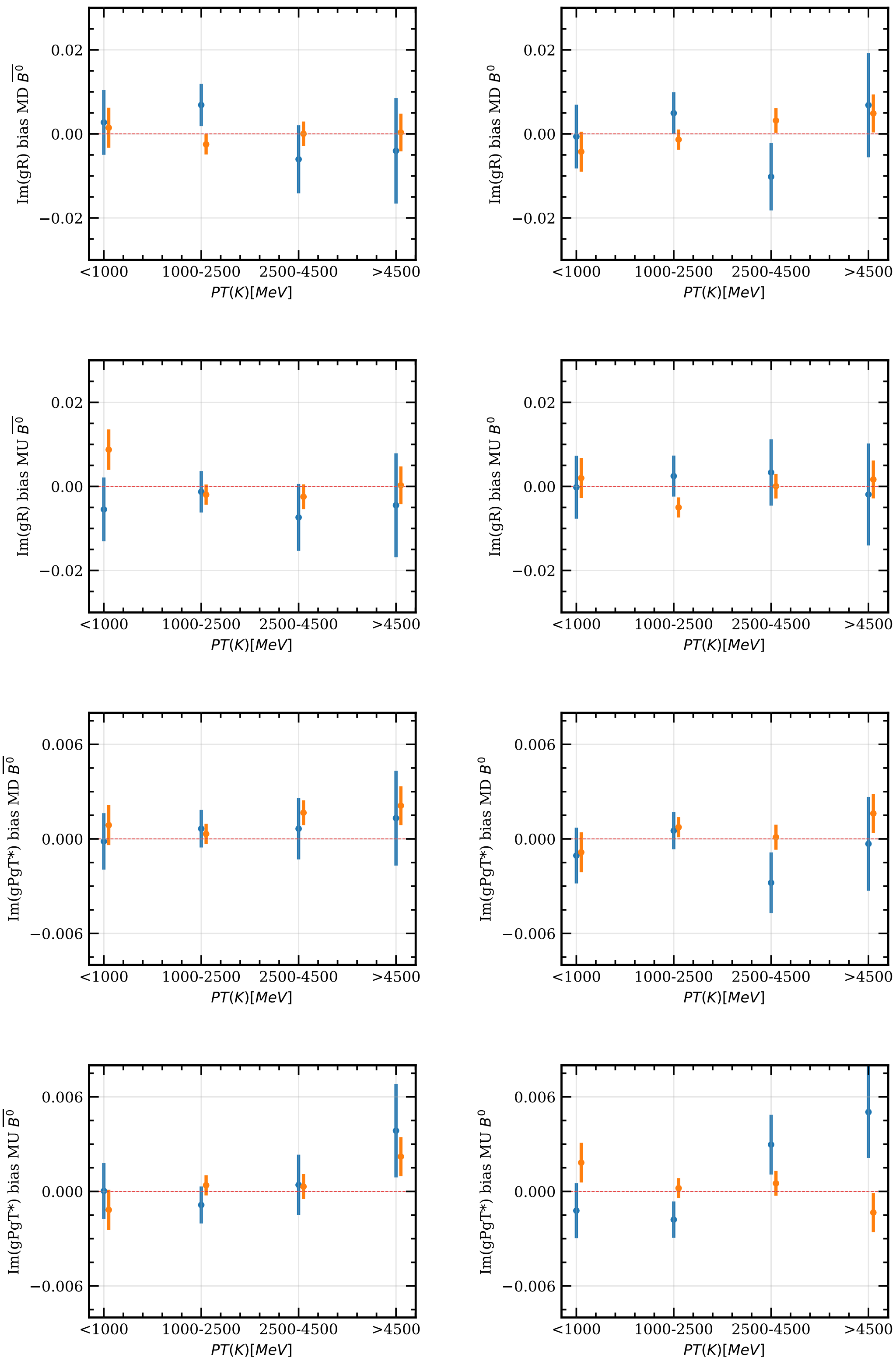

Figure 30: NP couplings bias for signal (orange) and control (blue) samples in bins of $p_{\mathrm{T}}(K)$ across the four categories

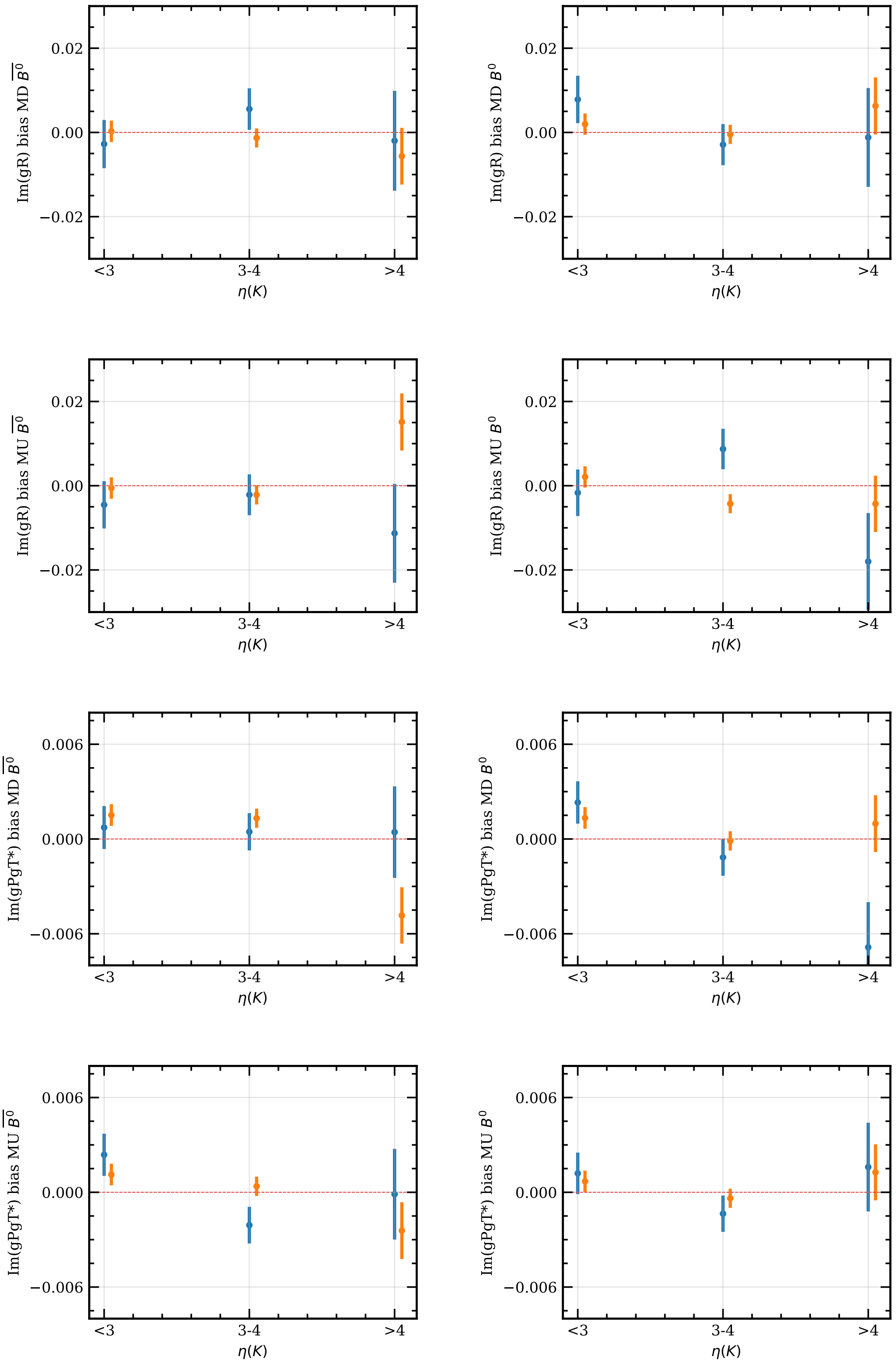

Figure 31: NP couplings bias for signal (orange) and control (blue) samples in bins of $\eta(K)$ across the four categories

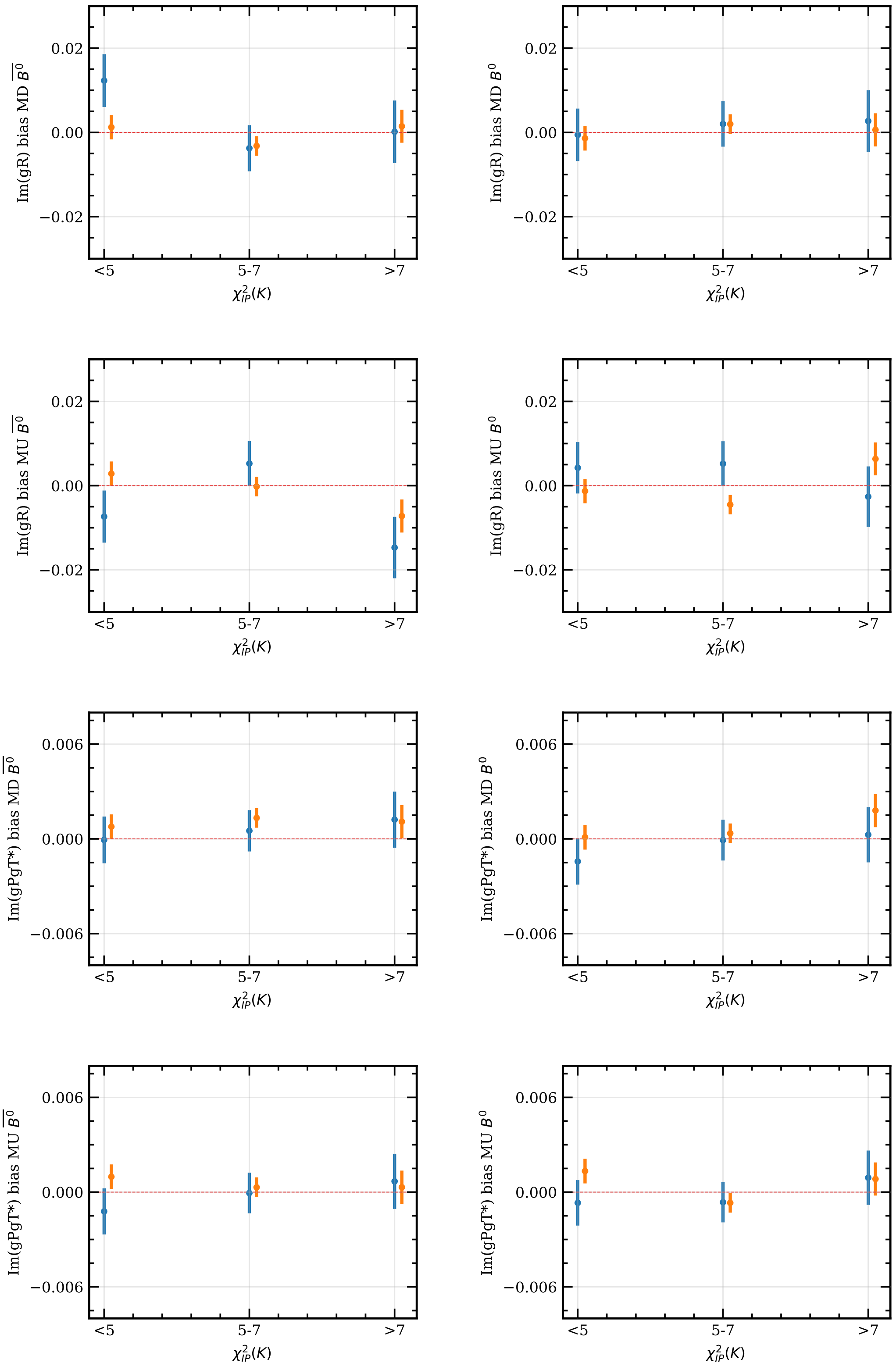

Figure 32: NP couplings bias for signal (orange) and control (blue) samples in bins of $\chi^2_{\mathrm{IP}}(K)$ across the four categories

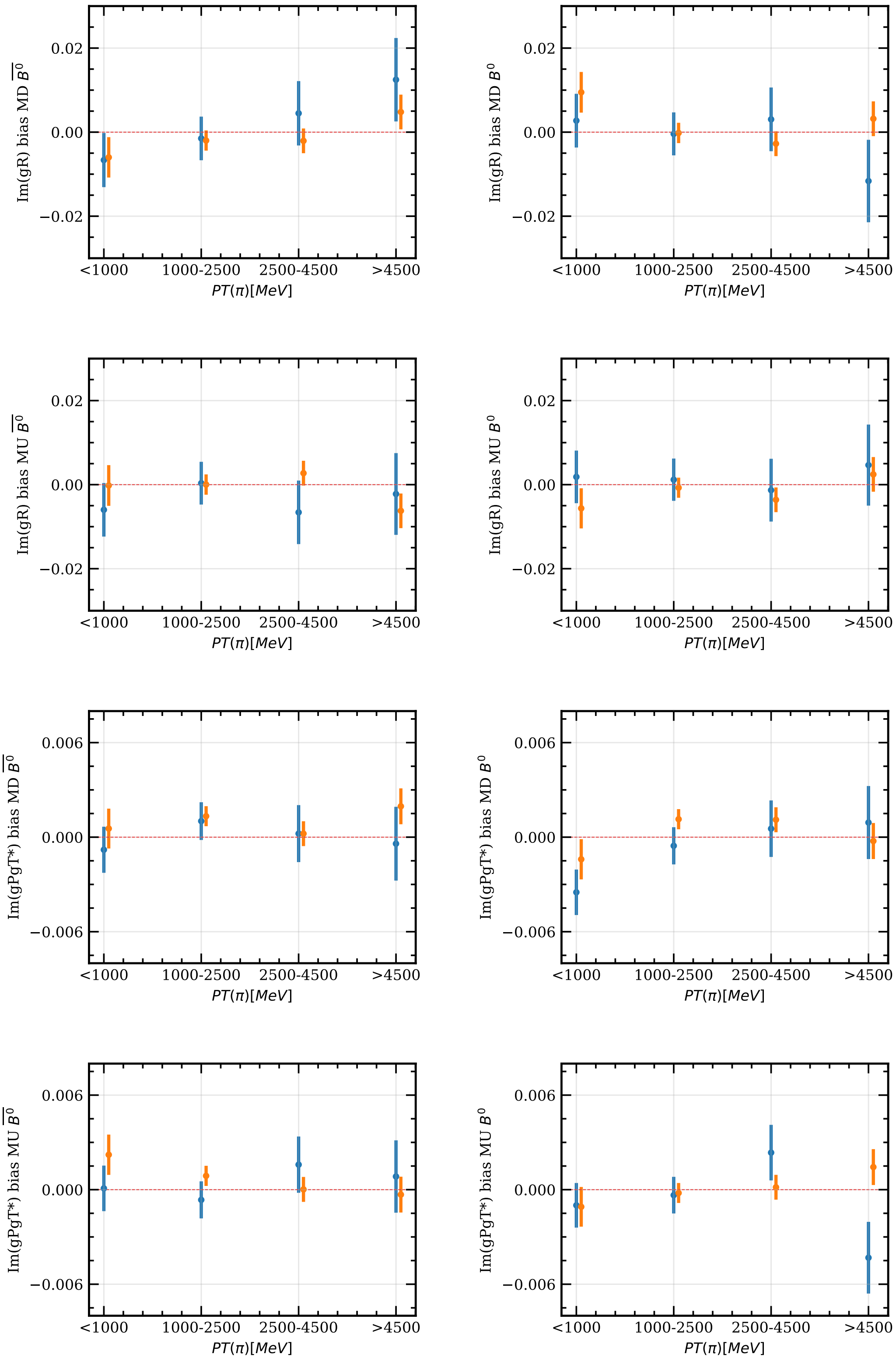

Figure 33: NP couplings bias for signal (orange) and control (blue) samples in bins of $p_{\mathrm{T}}(\pi)$ across the four categories

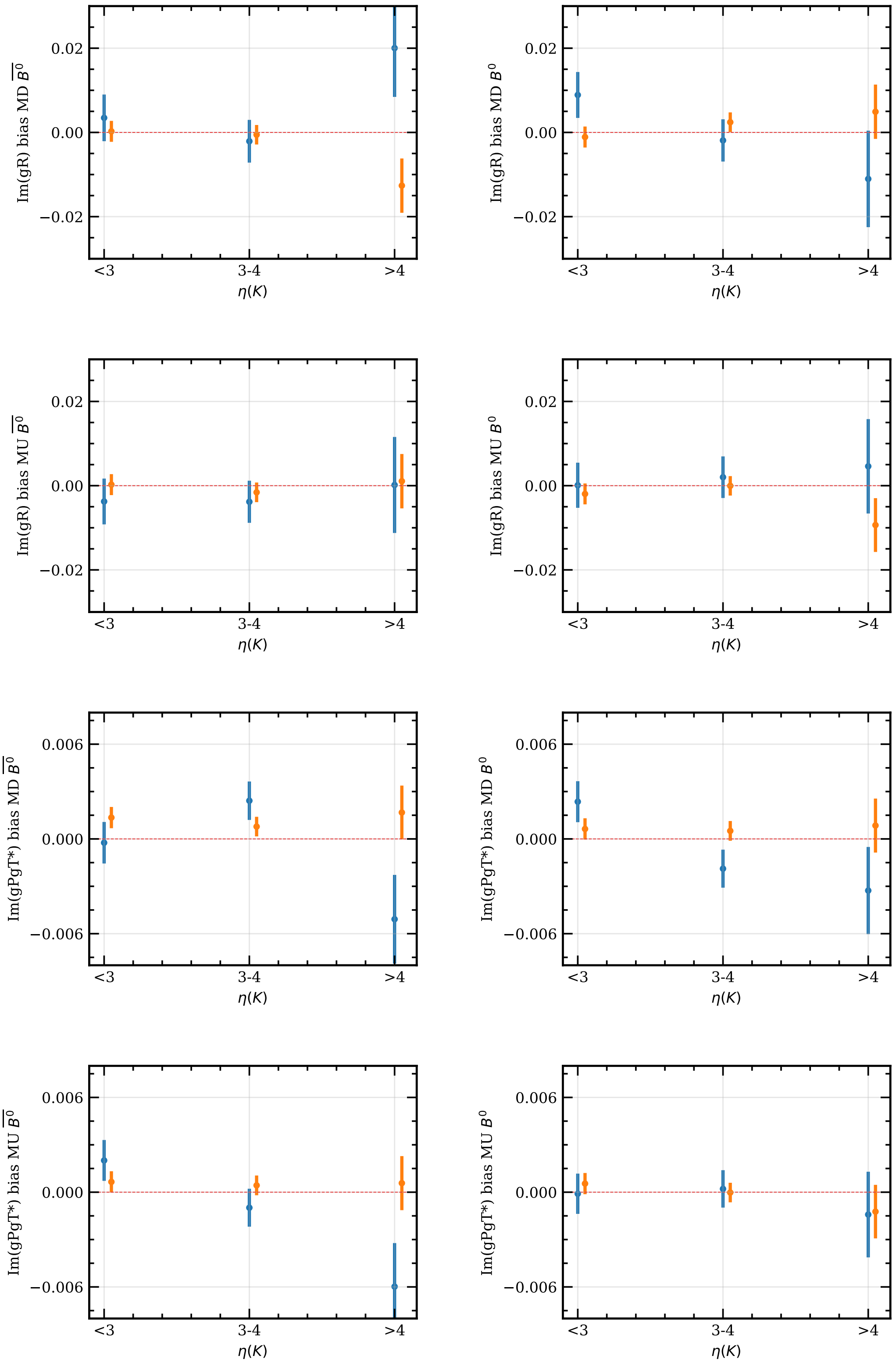

Figure 34: NP couplings bias for signal (orange) and control samples (blue) in bins of $\eta(\pi)$ across the four categories

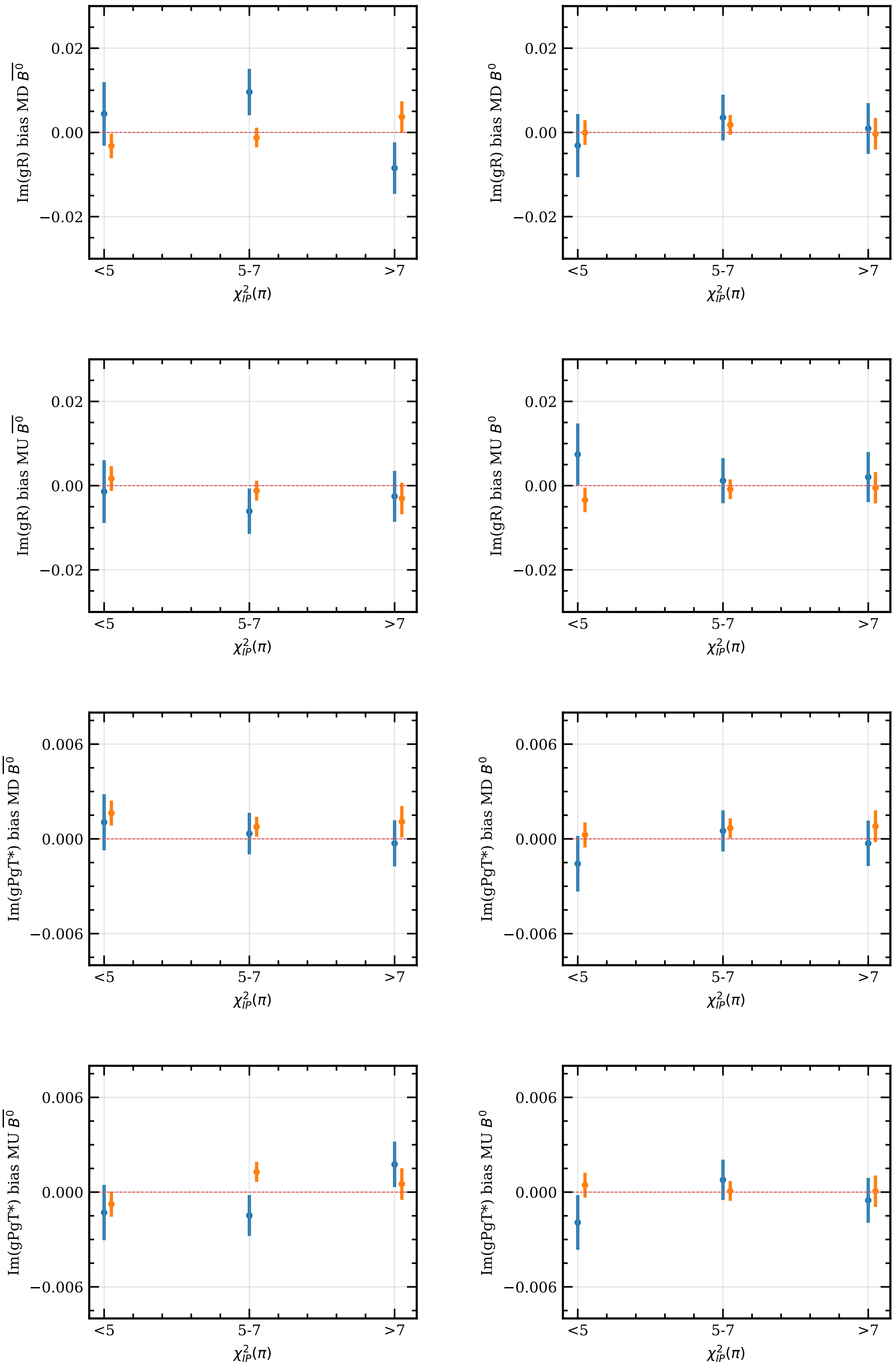

Figure 35: NP couplings bias for signal (orange) and control (blue) samples in bins of $\chi^2_{\text{IP}}(\pi)$ across the four categories

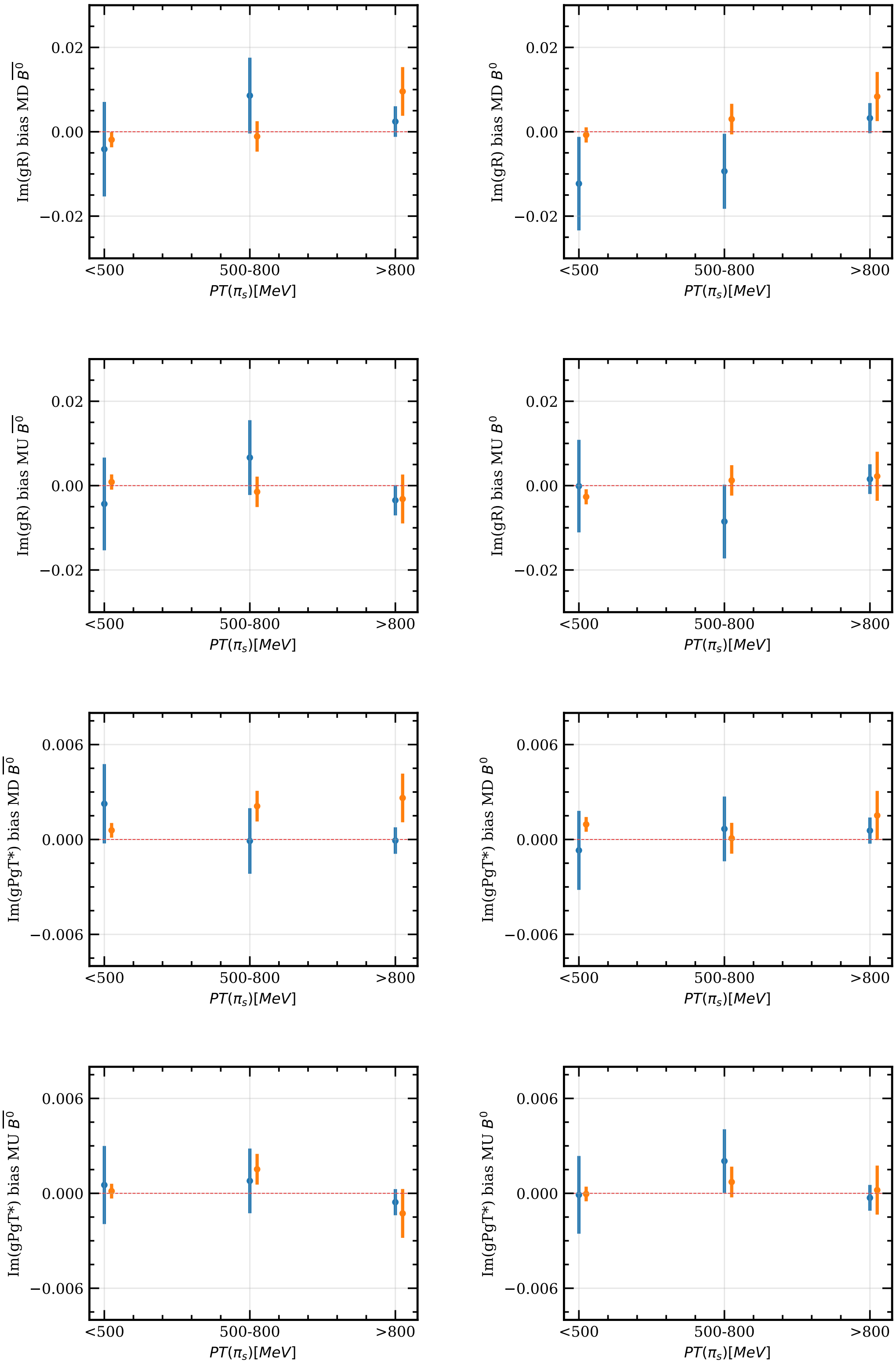

Figure 36: NP couplings bias for signal (orange) and control (blue) samples in bins of $p_{\mathrm{T}}(\pi_s)$ across the four categories

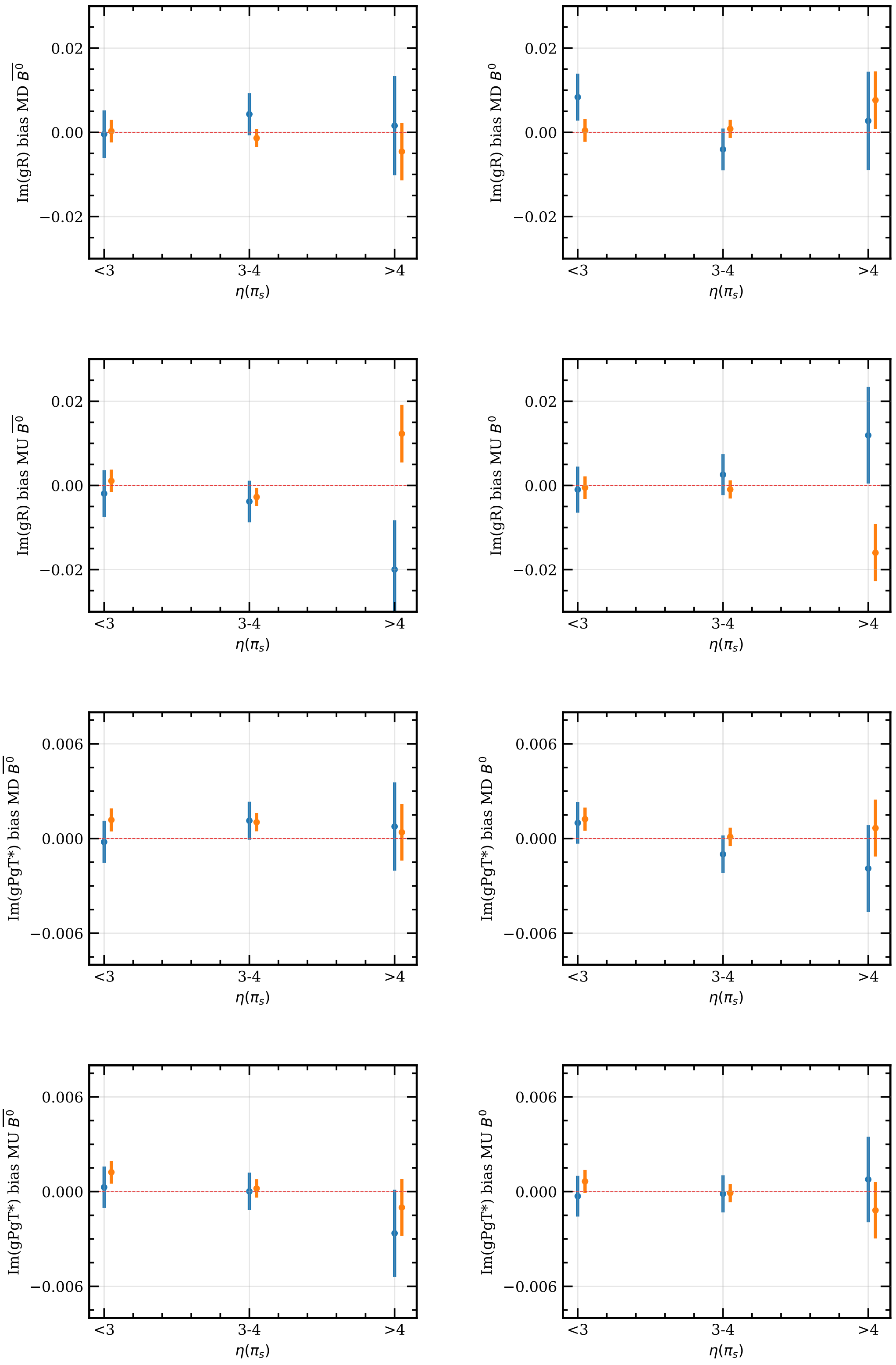

Figure 37: NP couplings bias for signal (orange) and control (blue) samples in bins of $\eta(\pi_s)$ across the four categories

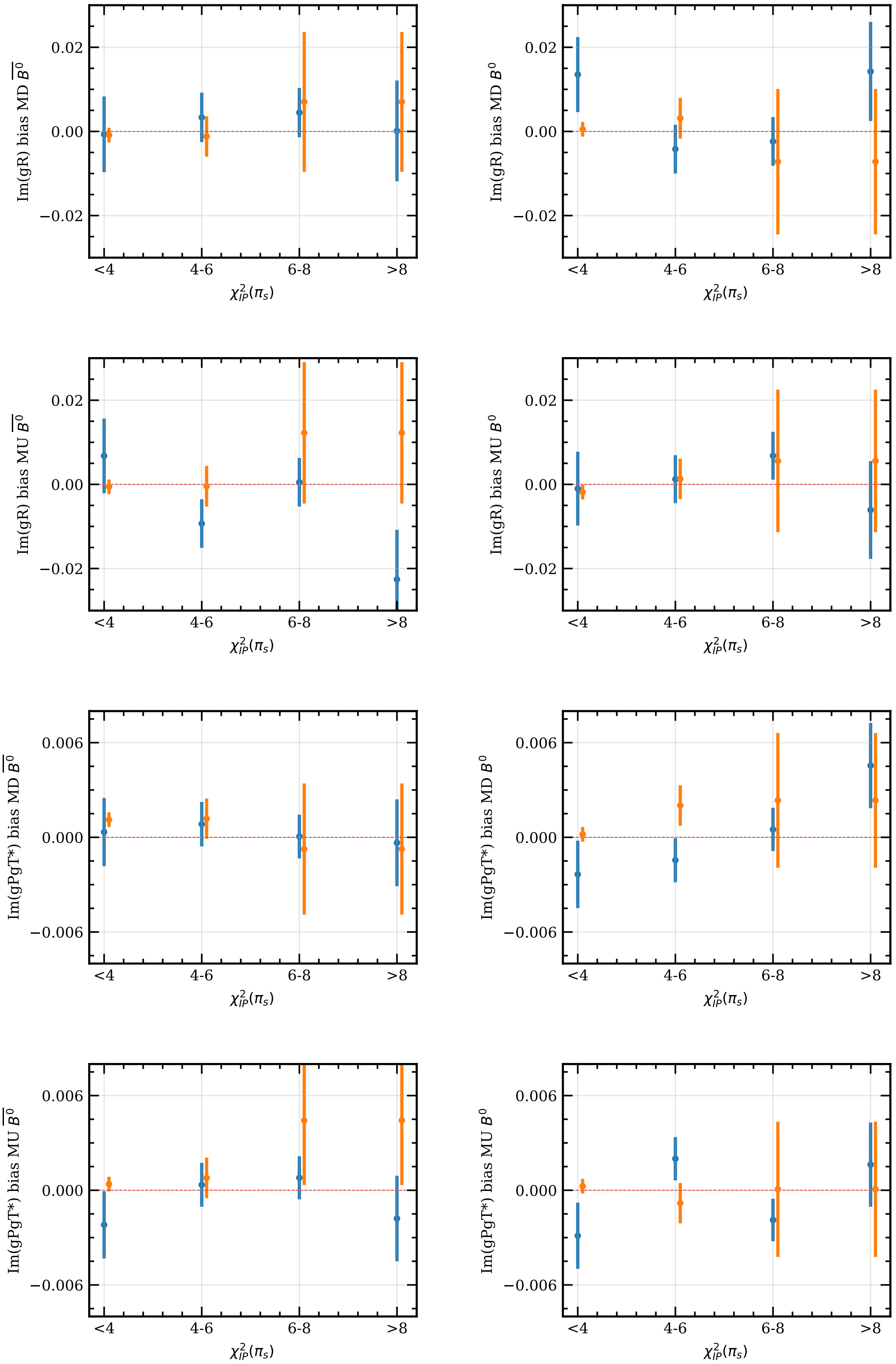

Figure 38: NP couplings bias for signal (orange) and control (blue) samples in bins of $\chi^2_{\mathrm{IP}}(\pi_s)$ across the four categories

Bibliography

[1] HFLAV, Y. Amhis *et al.*, *Averages of b-hadron, c-hadron, and τ-lepton properties as of 2021*, `arXiv:2206.07501`.

[2] B. Bhattacharya, A. Datta, S. Kamali, and D. London, *CP Violation in $\bar{B}^0 \to D^{*+}\mu^-\bar{\nu}_\mu$*, JHEP **05** (2019) 191, `arXiv:1903.02567`.

[3] D. Bečirević, M. Fedele, I. Nišandžić, and A. Tayduganov, *Lepton Flavor Universality tests through angular observables of $\overline{B} \to D^{(*)}\ell\overline{\nu}$ decay modes*, `arXiv:1907.02257`.

[4] LHCb collaboration, A. A. Alves Jr. *et al.*, *The LHCb detector at the LHC*, JINST **3** (2008) S08005.

[5] F. U. Bernlochner *et al.*, *Das ist der HAMMER: Consistent new physics interpretations of semileptonic decays*, Eur. Phys. J. C **80** (2020) 883, `arXiv:2002.00020`.

[6] D. Aloni, Y. Grossman, and A. Soffer, *Measuring CP violation in $b \to c\tau^-\bar{\nu}_\tau$ using excited charm mesons*, Phys. Rev. D **98** (2018) 035022, `arXiv:1806.04146`.

[7] LHCb, R. Aaij *et al.*, *Angular analysis of $B^0 \to D^{*-}D_s^{*+}$ with $D_s^{*+} \to D_s^+\gamma$ decays*, JHEP **06** (2021) 177, `arXiv:2105.02596`.

[8] B. Capdevila, A. Crivellin, and J. Matias, *Review of Semileptonic B Anomalies*, `arXiv:2309.01311`.

[9] M. Duraisamy and A. Datta, *The Full $B \to D^*\tau^-\bar{\nu}_\tau$ Angular Distribution and CP violating Triple Products*, JHEP **09** (2013) 059, `arXiv:1302.7031`.

[10] M. Thomson, *Modern particle physics*, Cambridge University Press, New York, 2013.

[11] B. de Wit, *Introduction to gauge theories and the Standard Model*, CERN (1995), `https://cds.cern.ch/record/292286`.

[12] R. Fleischer, *Flavour Physics and CP Violation: Expecting the LHC*, in *4th CERN-CLAF School of High-Energy Physics*, 105–157, 2008, `arXiv:0802.2882`.

[13] Y. Nir, *Flavour physics and CP violation*, CERN Yellow Rep. School Proc. **5** (2020) 79.

[14] Y. Grossman, *Introduction to flavor physics*, `arXiv:1006.3534`.

[15] N. Tuning, *Lectures Notes on CP violation*, Nikhef, Amsterdam, 2020, `https://www.nikhef.nl/~h71/Lectures/2020/ppII-cpviolation-14022020.pdf`.

[16] W. Hollik, *Quantum field theory and the Standard Model*, `arXiv:1012.3883`, Comments: 44 pages, Lectures given at the 2009 European School of High-Energy Physics, Bautzen, Germany, 14-27 Jun 2009.

[17] D. Hanneke, S. F. Hoogerheide, and G. Gabrielse, *Cavity Control of a Single-Electron Quantum Cyclotron: Measuring the Electron Magnetic Moment*, Phys. Rev. A **83** (2011) 052122, `arXiv:1009.4831`.

[18] G. Aad *et al.*, *Observation of a new particle in the search for the Standard Model Higgs boson with the ATLAS detector at the LHC*, Physics Letters B **716** (2012) 1.

[19] S. Chatrchyan *et al.*, *Observation of a new boson at a mass of 125 GeV with the CMS experiment at the LHC*, Physics Letters B **716** (2012) 30.

[20] C. Burgard, *Example: Standard model of physics*, , `https://texample.net/tikz/examples/model-physics/` (accessed 14/11/2022).

[21] Particle Data Group, R. L. Workman and Others, *Review of Particle Physics*, PTEP **2022** (2022) 083C01.

[22] C. Rovelli, *Quantum Gravity*, Cambridge Monographs on Mathematical Physics, Cambridge University Press, 2004.

[23] T. Rothman and S. Boughn, *Can gravitons be detected?*, Found. Phys. **36** (2006) 1801, `arXiv:gr-qc/0601043`.

[24] Belle Collaboration, S.-K. Choi *et al.*, *Observation of a Resonancelike Structure in the* $\pi^{+-}\psi^{'}$ *Mass Distribution in Exclusive* $B \to K\pi^{+-}\psi^{'}$ *Decays*, Phys. Rev. Lett. **100** (2008) 142001.

[25] LHCb Collaboration, R. Aaij *et al.*, *Observation of the Resonant Character of the* $Z(4430)^{-}$ *State*, Phys. Rev. Lett. **112** (2014) 222002.

[26] LHCb Collaboration, R. Aaij *et al.*, *Observation of* $J/\psi p$ *Resonances Consistent with Pentaquark States in* $\Lambda_b^0 \to J/\psi K^- p$ *Decays*, Phys. Rev. Lett. **115** (2015) 072001.

[27] V. E. Barnes *et al.*, *Observation of a Hyperon with Strangeness Minus Three*, Phys. Rev. Lett. **12** (1964) 204.

[28] M. Gell-Mann, *A Schematic Model of Baryons and Mesons*, Phys. Lett. **8** (1964) 214.

[29] G. Zweig, *An* SU_3 *model for strong interaction symmetry and its breaking; Version 1* CERN-TH-401, CERN, Geneva, 1964.

[30] F. Englert and R. Brout, *Broken Symmetry and the Mass of Gauge Vector Mesons*, Phys. Rev. Lett. **13** (1964) 321.

[31] P. W. Higgs, *Broken Symmetries and the Masses of Gauge Bosons*, Phys. Rev. Lett. **13** (1964) 508.

[32] G. Lüders, *Proof of the TCP theorem*, Annals of Physics **2** (1957) 1.

[33] C. S. Wu *et al.*, *Experimental Test of Parity Conservation in Beta Decay*, Phys. Rev. **105** (1957) 1413.

[34] R. L. Garwin, L. M. Lederman, and M. Weinrich, *Observations of the Failure of Conservation of Parity and Charge Conjugation in Meson Decays: the Magnetic Moment of the Free Muon*, Phys. Rev. **105** (1957) 1415.

[35] S. L. Glashow, *Partial Symmetries of Weak Interactions*, Nucl. Phys. **22** (1961) 579.

[36] S. Weinberg, *A Model of Leptons*, Phys. Rev. Lett. **19** (1967) 1264.

[37] A. Salam, *Weak and Electromagnetic Interactions*, Conf. Proc. C **680519** (1968) 367.

[38] J. Ellis, M. K. Gaillard, and D. V. Nanopoulos, in *A Historical Profile of the Higgs Boson*, L. Maiani and L. Rolandi, eds., pp. 255–274, 2016. `arXiv:1504.07217`.

[39] S. L. Glashow, J. Iliopoulos, and L. Maiani, *Weak Interactions with Lepton-Hadron Symmetry*, **2** (1970) 1285.

[40] N. Cabibbo, *Unitary symmetry and leptonic decays*, Phys. Rev. Lett. **10** (1963) 531.

[41] M. Kobayashi and T. Maskawa, *CP-violation in the renormalizable theory of weak interaction*, Prog. Theor. Phys. **49** (1973) 652.

[42] L.-L. Chau and W.-Y. Keung, *Comments on the Parametrization of the Kobayashi-Maskawa Matrix*, Phys. Rev. Lett. **53** (1984) 1802.

[43] CKMfitter group, J. Charles *et al.*, *CP violation and the CKM matrix: Assessing the impact of the asymmetric B factories*, Eur. Phys. J. **C41** (2005) 1, `arXiv:hep-ph/0406184`, updated results and plots available at `http://ckmfitter.in2p3.fr/`.

[44] L. Wolfenstein, *Parametrization of the Kobayashi-Maskawa Matrix*, Phys. Rev. Lett. **51** (1983) 1945.

[45] T. Gershon and V. V. Gligorov, *CP violation in the B system*, Reports on Progress in Physics **80** (2017) 046201.

[46] Z. Maki, M. Nakagawa, and S. Sakata, *Remarks on the Unified Model of Elementary Particles*, Progress of Theoretical Physics **28** (1962) 870.

[47] J. H. Christenson, J. W. Cronin, V. L. Fitch, and R. Turlay, *Evidence for the* 2π *Decay of the* K_2^0 *Meson*, Phys. Rev. Lett. **13** (1964) 138.

[48] LHCb collaboration, R. Aaij *et al.*, *Observation of CP violation in charm decays*, Phys. Rev. Lett. **122** (2019) 211803, `arXiv:1903.08726`.

[49] LHCb collaboration, R. Aaij *et al.*, *First observation of CP violation in the decays of* B_s^0 *mesons*, Phys. Rev. Lett. **110** (2013) 221601, `arXiv:1304.6173`.

[50] LHCb collaboration, R. Aaij *et al.*, *Measurement of CP violation in* $B^0 \to J/\psi K^0_S$ *and* $B^0 \to \psi(2S)K^0_S$ *decays*, JHEP **11** (2017) 170, `arXiv:1709.03944`.

[51] M. Bordone, G. Isidori, and A. Pattori, *On the Standard Model predictions for* R_K *and* R_{K^*}, Eur. Phys. J. C **76** (2016) 440, `arXiv:1605.07633`.

[52] S. Fajfer, *Theory Status - Puzzles in B Meson Decays and LFU?*, SciPost Phys. Proc. (2019) 010.

[53] LHCb collaboration, R. Aaij *et al.*, *Test of lepton universality with* $B^0 \to K^{*0}\ell^+\ell^-$ *decays*, JHEP **08** (2017) 055, `arXiv:1705.05802`.

[54] LHCb collaboration, R. Aaij *et al.*, *Test of lepton universality in beauty-quark decays*, Nature Phys. **18** (2022) 277, `arXiv:2103.11769`.

[55] LHCb collaboration, R. Aaij *et al.*, *Test of lepton universality in* $b \to s\ell^+\ell^-$ *decays*, `arXiv:2212.09152`.

[56] LHCb, *Measurement of lepton universality parameters in* $B^+ \to K^+\ell^+\ell^-$ *and* $B^0 \to K^{*0}\ell^+\ell^-$ *decays*, `arXiv:2212.09153`.

[57] LHCb, R. Aaij *et al.*, *Tests of lepton universality using* $B^0 \to K^0_S\ell^+\ell^-$ *and* $B^+ \to K^{*+}\ell^+\ell^-$ *decays*, Phys. Rev. Lett. **128** (2022) 191802, `arXiv:2110.09501`.

[58] LHCb collaboration, R. Aaij *et al.*, *Test of lepton universality using* $\Lambda_b^0 \to pK^-\ell^+\ell^-$ *decays*, `arXiv:1912.08139`, submitted to JHEP.

[59] LHCb collaboration, R. Aaij *et al.*, *Angular analysis of the* $B^0 \to K^{*0}\mu^+\mu^-$ *decay using* $3\,fb^{-1}$ *of integrated luminosity*, JHEP **02** (2016) 104, `arXiv:1512.04442`.

[60] LHCb collaboration, R. Aaij *et al.*, *Measurement of CP-averaged observables in the* $B^0 \to K^{*0}\mu^+\mu^-$ *decay*, `arXiv:2003.04831`, submitted to Phys. Rev. Lett.

[61] LHCb, R. Aaij *et al.*, *Angular Analysis of the* $B^+ \to K^{*+}\mu^+\mu^-$ *Decay*, Phys. Rev. Lett. **126** (2021) 161802, `arXiv:2012.13241`.

[62] BaBar, J. P. Lees *et al.*, *Evidence for an excess of* $\bar{B} \to D^{(*)}\tau^-\bar{\nu}_\tau$ *decays*, Phys. Rev. Lett. **109** (2012) 101802, `arXiv:1205.5442`.

[63] BaBar, J. P. Lees *et al.*, *Measurement of an Excess of* $\bar{B} \to D^{(*)}\tau^-\bar{\nu}_\tau$ *Decays and Implications for Charged Higgs Bosons*, Phys. Rev. D **88** (2013) 072012, `arXiv:1303.0571`.

[64] Belle, M. Huschle *et al.*, *Measurement of the branching ratio of* $\bar{B} \to D^{(*)}\tau^-\bar{\nu}_\tau$ *relative to* $\bar{B} \to D^{(*)}\ell^-\bar{\nu}_\ell$ *decays with hadronic tagging at Belle*, Phys. Rev. D **92** (2015) 072014, `arXiv:1507.03233`.

[65] Belle, S. Hirose *et al.*, *Measurement of the* τ *lepton polarization and* $R(D^*)$ *in the decay* $\bar{B} \to D^*\tau^-\bar{\nu}_\tau$, Phys. Rev. Lett. **118** (2017) 211801, `arXiv:1612.00529`.

[66] Belle, G. Caria *et al.*, *Measurement of* $\mathscr{R}(D)$ *and* $\mathscr{R}(D^*)$ *with a semileptonic tagging method*, Phys. Rev. Lett. **124** (2020) 161803, `arXiv:1910.05864`.

[67] LHCb, *Measurement of the ratios of branching fractions* $\mathscr{R}(D^*)$ *and* $\mathscr{R}(D^0)$, `arXiv:2302.02886`.

[68] LHCb collaboration, R. Aaij *et al.*, *Measurement of the ratio of branching fractions* $\mathscr{B}(B_c^+ \to J/\psi\tau^+\nu_\tau)/\mathscr{B}(B_c^+ \to J/\psi\mu^+\nu_\mu)$, Phys. Rev. Lett. **120** (2018) 121801, `arXiv:1711.05623`.

[69] LHCb, R. Aaij *et al.*, *Observation of the decay* $\Lambda_b^0 \to \Lambda_c^+\tau^-\overline{\nu}_\tau$, Phys. Rev. Lett. **128** (2022) 191803, `arXiv:2201.03497`.

[70] LATTICE-HPQCD, J. Harrison, C. T. H. Davies, and A. Lytle, $R(J/\psi)$ *and* $B_c^- \to J/\psi\ell^-\bar{\nu}_\ell$ *Lepton Flavor Universality Violating Observables from Lattice QCD*, Phys. Rev. Lett. **125** (2020) 222003, `arXiv:2007.06956`.

[71] F. U. Bernlochner, Z. Ligeti, D. J. Robinson, and W. L. Sutcliffe, *Precise predictions for* $\Lambda_b \to \Lambda_c$ *semileptonic decays*, Phys. Rev. D **99** (2019) 055008, `arXiv:1812.07593`.

[72] Belle, A. Abdesselam *et al.*, *Measurement of the* D^{*-} *polarization in the decay* $B^0 \to D^{*-}\tau^+\nu_\tau$, in *10th International Workshop on the CKM Unitarity Triangle*, 2019, `arXiv:1903.03102`.

[73] Belle, S. Hirose *et al.*, *Measurement of the* τ *lepton polarization and* $R(D^*)$ *in the decay* $\bar{B} \to D^*\tau^-\bar{\nu}_\tau$ *with one-prong hadronic* τ *decays at Belle*, Phys. Rev. D **97** (2018) 012004, `arXiv:1709.00129`.

[74] C. Bobeth *et al.*, *Lepton-flavour non-universality of* $\bar{B} \to D^*\ell\bar{\nu}$ *angular distributions in and beyond the Standard Model*, Eur. Phys. J. C **81** (2021) 984, `arXiv:2104.02094`.

[75] B. Bhattacharya *et al.*, *Implications for the* ΔA_{FB} *anomaly in* $\bar{B}^0 \to D^{*+}\ell^-\bar{\nu}$ *using a new Monte Carlo Event Generator*, `arXiv:2206.11283`.

[76] Z.-R. Huang, E. Kou, C.-D. Lü, and R.-Y. Tang, *Un-binned Angular Analysis of $B \to D^{*}\ell\nu_{\ell}$ and the Right-handed Current*, Phys. Rev. D **105** (2022) 013010, `arXiv:2106.13855`.

[77] D. Hill, M. John, W. Ke, and A. Poluektov, *Model-independent method for measuring the angular coefficients of $B^0 \to D^{*-}\tau^{+}\nu_{\tau}$ decays*, JHEP **11** (2019) 133, `arXiv:1908.04643`.

[78] V. Cirigliano, J. Jenkins, and M. Gonzalez-Alonso, *Semileptonic decays of light quarks beyond the Standard Model*, Nucl. Phys. B **830** (2010) 95, `arXiv:0908.1754`.

[79] W. Buchmüller and D. Wyler, *Effective lagrangian analysis of new interactions and flavour conservation*, Nuclear Physics B **268** (1986) 621.

[80] S. Bifani, S. Descotes-Genon, A. Romero Vidal, and M.-H. Schune, *Review of Lepton Universality tests in B decays*, J. Phys. G **46** (2019) 023001, `arXiv:1809.06229`.

[81] W. D. Goldberger, *Semileptonic B decays as a probe of new physics*, `arXiv:hep-ph/9902311`.

[82] M. Tanaka and R. Watanabe, *New physics in the weak interaction of $\bar{B} \to D^{(*)}\tau\bar{\nu}$*, Phys. Rev. D **87** (2013) 034028, `arXiv:1212.1878`.

[83] A. Datta and D. London, *Triple-product correlations in B –> V1 V2 decays and new physics*, Int. J. Mod. Phys. A **19** (2004) 2505, `arXiv:hep-ph/0303159`.

[84] M. Gronau and J. L. Rosner, *Triple product asymmetries in K, $D_{(s)}$ and $B_{(s)}$ decays*, Phys. Rev. D **84** (2011) 096013, `arXiv:1107.1232`.

[85] Belle, A. Abdesselam *et al.*, *Precise determination of the CKM matrix element $|V_{cb}|$ with $\bar{B}^0 \to D^{*\,+}\,\ell^{-}\,\bar{\nu}_{\ell}$ decays with hadronic tagging at Belle*, `arXiv:1702.01521`.

[86] N. Isgur, D. Scora, B. Grinstein, and M. B. Wise, *Semileptonic b and d decays in the quark model*, Phys. Rev. D **39** (1989) 799.

[87] I. Caprini, L. Lellouch, and M. Neubert, *Dispersive bounds on the shape of anti-B —> D(*) lepton anti-neutrino form-factors*, Nucl. Phys. B **530** (1998) 153, `arXiv:hep-ph/9712417`.

[88] C. G. Boyd, B. Grinstein, and R. F. Lebed, *Constraints on form-factors for exclusive semileptonic heavy to light meson decays*, Phys. Rev. Lett. **74** (1995) 4603, `arXiv:hep-ph/9412324`.

[89] F. U. Bernlochner, Z. Ligeti, M. Papucci, and D. J. Robinson, *Combined analysis of semileptonic B decays to D and D^{*}: $R(D^{(*)})$, $|V_{cb}|$, and new physics*, Phys. Rev. D **95** (2017) 115008, `arXiv:1703.05330`, [Erratum: Phys.Rev.D 97, 059902 (2018)].

[90] L. Evans and P. Bryant, *LHC Machine*, JINST **3** (2008) S08001.

[91] E. Mobs, The cern accelerator complex - 2019. July 2019. URL `https://cds.cern.ch/record/2684277`. General photo.

[92] ATLAS collaboration, G. Aad *et al.*, *The ATLAS Experiment at the CERN Large Hadron Collider*, JINST **3** (2008) S08003.

[93] CMS collaboration, S. Chatrchyan *et al.*, *The CMS experiment at the CERN LHC*, JINST **3** (2008) S08004.

[94] ALICE collaboration, K. Aamodt *et al.*, *The ALICE experiment at the CERN LHC*, JINST **3** (2008) S08002.

[95] LHCb Collaboration, Standard set of performance numbers, URL `https://lhcb.web.cern.ch/speakersbureau/html/PerformanceNumbers.html` (accessed 18/10/2022).

[96] ATLAS Collaboration, Luminosity public results, URL `https://twiki.cern.ch/twiki/bin/view/AtlasPublic/LuminosityPublicResults` (accessed 18/10/2022).

[97] CMS Collaboration, Public CMS Luminosity Information, URL `https://twiki.cern.ch/twiki/bin/view/CMSPublic/LumiPublicResults` (accessed 18/10/2022).

[98] BaBar, B. Aubert *et al.*, *The BaBar detector*, Nucl. Instrum. Meth. A **479** (2002) 1, `arXiv:hep-ex/0105044`.

[99] A. Abashian *et al.*, *The Belle detector*, Nuclear Instruments and Methods in Physics Research Section A: Accelerators, Spectrometers, Detectors and Associated Equipment **479** (2002) 117, Detectors for Asymmetric B-factories.

[100] Belle-II, T. Abe *et al.*, *Belle II Technical Design Report*, `arXiv:1011.0352`.

[101] LHCb collaboration, R. Aaij *et al.*, *Measurement of the b-quark production cross-section in 7 and 13 TeV pp collisions*, Phys. Rev. Lett. **118** (2017) 052002, Erratum ibid. **119** (2017) 169901, `arXiv:1612.05140`.

[102] LHCb collaboration, C. Elsässer, *$\overline{b}b$ production angle plots*, CERN, `https://lhcb.web.cern.ch/speakersbureau/html/bb_ProductionAngles.html` (accessed 19/10/2022).

[103] LHCb collaboration, *LHCb VELO (VErtex LOcator): Technical Design Report*, CERN-LHCC-2001-011, 2001.

[104] R. Aaij *et al.*, *Performance of the LHCb Vertex Locator*, JINST **9** (2014) P09007, `arXiv:1405.7808`.

[105] R. Aaij *et al.*, *Performance of the LHCb trigger and full real-time reconstruction in Run 2 of the LHC*, JINST **14** (2019) P04013.

[106] LHCb collaboration, *LHCb magnet: Technical Design Report*, CERN-LHCC-2000-007, 2000.

[107] M. Losasso *et al.*, *Tests and field map of lhcb dipole magnet*, Applied Superconductivity, IEEE Transactions on **16** (2006) 1700 .

[108] M. Vesterinen, *Considerations on the LHCb dipole magnet polarity reversal*, , CERN, Geneva, 2014, `https://cds.cern.ch/record/1642153`.

[109] LHCb collaboration, *LHCb inner tracker: Technical Design Report*, CERN-LHCC-2002-029, 2002.

[110] LHCb collaboration, *LHCb outer tracker: Technical Design Report*, CERN-LHCC-2001-024, 2001.

[111] J. R. Harrison, *Radiation damage studies in the LHCb VELO detector and searches for lepton flavour and baryon number violating tau decays*, 2014. `https://cds.cern.ch/record/1712972` Presented 16 05 2014.

[112] C. Abellan Beteta *et al.*, *Monitoring radiation damage in the LHCb Tracker Turicensis*, `arXiv:1809.05063`.

[113] R. Arink *et al.*, *Performance of the LHCb Outer Tracker*, JINST **9** (2014) P01002, `arXiv:1311.3893`.

[114] S. Meloni, *Test of lepton flavour universality with the simultaneous measurement of $\mathcal{R}(D^{+})$ and $\mathcal{R}(D^{*+})$ with $\tau^{-} \to \mu^{-}\nu_{\tau}\overline{\nu}_{\mu}$ decays at the LHCb experiment*, 2021. `https://cds.cern.ch/record/2800599` Presented 19 Jan 2022.

[115] LHCb collaboration, R. Aaij *et al.*, *Measurement of the track reconstruction efficiency at LHCb*, JINST **10** (2015) P02007, `arXiv:1408.1251`.

[116] W. D. Hulsbergen, *The global covariance matrix of tracks fitted with a kalman filter and an application in detector alignment*, Nuclear Instruments and Methods in Physics Research Section A: Accelerators, Spectrometers, Detectors and Associated Equipment **600** (2009) 471.

[117] R. Frühwirth, *Application of kalman filtering to track and vertex fitting*, Nuclear Instruments and Methods in Physics Research Section A: Accelerators, Spectrometers, Detectors and Associated Equipment **262** (1987) 444.

[118] M. De Cian, S. Farry, P. Seyfert, and S. Stahl, *Fast neural-net based fake track rejection in the LHCb reconstruction*, LHCb-PUB-2017-011, 2017.

[119] LHCb, R. Aaij *et al.*, *LHCb Detector Performance*, Int. J. Mod. Phys. A **30** (2015) 1530022, `arXiv:1412.6352`.

[120] R. A. et al, *Design and performance of the lhcb trigger and full real-time reconstruction in run 2 of the lhc*, Journal of Instrumentation **14** (2019) P04013.

[121] LHCb collaboration, *LHCb RICH: Technical Design Report*, CERN-LHCC-2000-037, 2000.

[122] LHCb RICH, A. Papanestis and C. D'Ambrosio, *Performance of the LHCb RICH detectors during the LHC Run II*, Nucl. Instrum. Meth. A **876** (2017) 221, `arXiv:1703.08152`.

[123] LHCb collaboration, *LHCb calorimeters: Technical Design Report*, CERN-LHCC-2000-036, 2000.

[124] M. Borsato, *Study of the $B^0 \to K^{*0}e^+e^-$ decay with the LHCb detector and development of a novel concept of PID detector: the Focusing DIRC*, 2015. `https://cds.cern.ch/record/2104825` Presented 08 Sep 2015.

[125] LHCb collaboration, *LHCb reoptimized detector design and performance: Technical Design Report*, CERN-LHCC-2003-030, 2003.

[126] D. A. Berninghoff, J. Albrecht, and V. Gligorov, *Bremsstrahlung Recovery of Electrons using Multivariate Methods* , CERN, Geneva, 2016. `https://cds.cern.ch/record/2146447`.

[127] C. Abellán Beteta *et al.*, *Calibration and performance of the LHCb calorimeters in Run 1 and 2 at the LHC*, `arXiv:2008.11556`.

[128] A. A. Alves, Jr. *et al.*, *Performance of the LHCb muon system*, JINST **8** (2013) P02022, `arXiv:1211.1346`.

[129] LHCb collaboration, *LHCb muon system: Technical Design Report*, CERN-LHCC-2001-010, 2001.

[130] R. Aaij *et al.*, *Selection and processing of calibration samples to measure the particle identification performance of the LHCb experiment in Run 2*, Eur. Phys. J. Tech. Instr. **6** (2018) 1, `arXiv:1803.00824`.

[131] F. Archilli *et al.*, *Performance of the Muon Identification at LHCb*, JINST **8** (2013) P10020, `arXiv:1306.0249`.

[132] LHCb collaboration, *LHCb trigger system: Technical Design Report*, CERN-LHCC-2003-031, 2003.

[133] LHCb collaboration, *LHCb Trigger and Online Technical Design Report*, CERN-LHCC-2014-016, 2014.

[134] R. Aaij *et al.*, *The LHCb Trigger and its Performance in 2011*, JINST **8** (2013) P04022, `arXiv:1211.3055`.

[135] B. Sciascia, *LHCb Run 2 Trigger Performance*, PoS **BEAUTY2016** (2016) 029.

[136] LHCb collaboration, Trigger schemes `http://lhcb.web.cern.ch/lhcb/speakersbureau/html/TriggerScheme.html` (accessed 06/11/2022).

[137] H. Voss, A. Hoecker, J. Stelzer, and F. Tegenfeldt, *TMVA - Toolkit for Multivariate Data Analysis with ROOT*, PoS **ACAT** (2007) 040.

[138] LHCb collaboration, *LHCb computing: Technical Design Report*, CERN-LHCC-2005-019, 2005.

[139] G. Barrand *et al.*, *GAUDI — A software architecture and framework for building HEP data processing applications*, Computer Physics Communications **140** (2001) 45, CHEP2000.

[140] P. Mato, *GAUDI-Architecture design document* , CERN, Geneva, 1998.

[141] LHCb Collaboration, `https://lhcb.github.io/starterkit-lessons/first-analysis-steps/dataflow.html` (accessed 08/11/2022).

[142] R. Brun and F. Rademakers, *ROOT — An object oriented data analysis framework*, Nuclear Instruments and Methods in Physics Research Section A: Accelerators, Spectrometers, Detectors and Associated Equipment **389** (1997) 81, New Computing Techniques in Physics Research V.

[143] M. Clemencic *et al.*, *The LHCb Simulation Application, Gauss: Design, Evolution and Experience*, Journal of Physics: Conference Series **331** (2011) 032023.

[144] T. Sjöstrand, S. Mrenna, and P. Skands, *A brief introduction to PYTHIA 8.1*, Computer Physics Communications **178** (2008) 852.

[145] D. J. Lange, *The EvtGen particle decay simulation package*, Nuclear Instruments and Methods in Physics Research Section A: Accelerators, Spectrometers, Detectors and Associated Equipment **462** (2001) 152, BEAUTY2000, Proceedings of the 7th Int. Conf. on B-Physics at Hadron Machines.

[146] P. Golonka and Z. Was, *PHOTOS Monte Carlo: A precision tool for QED corrections in Z and W decays*, Eur. Phys. J. **C45** (2006) 97, `arXiv:hep-ph/0506026`.

[147] S. A. et al. *Geant4—a simulation toolkit*, Nuclear Instruments and Methods in Physics Research Section A: Accelerators, Spectrometers, Detectors and Associated Equipment **506** (2003) 250.

[148] LHCb collaboration, *LHCb Tracker Upgrade Technical Design Report*, CERN-LHCC-2014-001, 2014.

[149] LHCb collaboration, *Framework TDR for the LHCb Upgrade: Technical Design Report*, CERN-LHCC-2012-007, 2012.

[150] LHCb collaboration, *LHCb Upgrade Software and Computing*, CERN-LHCC-2018-007, 2018.

[151] LHCb collaboration, *LHCb PID Upgrade Technical Design Report*, CERN-LHCC-2013-022, 2013.

[152] LHCb collaboration, *LHCb VELO Upgrade Technical Design Report*, CERN-LHCC-2013-021, 2013.

[153] S. Tolk, J. Albrecht, F. Dettori, and A. Pellegrino, *Data driven trigger efficiency determination at LHCb*, LHCb-PUB-2014-039, 2014.

[154] P. Hamilton, H. Jawahery, and G. M. Ciezarek, *Simultaneous extraction of the branching fraction ratios $\mathcal{R}(D)$ and $\mathcal{R}(D^*)$ with the Run 1 Dataset using the $\tau^+ \to \mu^+ \nu_\mu \overline{\nu}_\tau$ decay*, , https://cds.cern.ch/record/2728837.

[155] Y. Sun, *Measurement of $\mathcal{R}(D^{(*)})$ in semileptonic B decays and upgrade of the LHCb Upstream Tracker*, 2023. https://cds.cern.ch/record/2855625. Presented 01 Mar 2023.

[156] M. Calvi *et al.*, *Emulation of the hadronic trigger for tracker-only simulation* , CERN, Geneva, 2019. https://cds.cern.ch/record/2703802.

[157] R. Aaij *et al.*, *Selection and processing of calibration samples to measure the particle identification performance of the LHCb experiment in Run 2*, EPJ Tech. Instrum. **6** (2019) 1, arXiv:1803.00824.

[158] M. Pivk and F. R. Le Diberder, *sPlot: A statistical tool to unfold data distributions*, Nucl. Instrum. Meth. **A555** (2005) 356, arXiv:physics/0402083.

[159] S. Dambach, U. Langenegger, and A. Starodumov, *Neutrino reconstruction with topological information*, Nucl. Instrum. Meth. A **569** (2006) 824, arXiv:hep-ph/0607294.

[160] G. Ciezarek, A. Lupato, M. Rotondo, and M. Vesterinen, *Reconstruction of semileptonically decaying beauty hadrons produced in high energy pp collisions*, JHEP **02** (2017) 021, arXiv:1611.08522.

[161] W. D. Hulsbergen, *Decay chain fitting with a Kalman filter*, Nucl. Instrum. Meth. **A552** (2005) 566, arXiv:physics/0503191.

[162] W. Verkerke and D. P. Kirkby, *The RooFit toolkit for data modeling*, eConf **C0303241** (2003) MOLT007, arXiv:physics/0306116.

[163] LHCb collaboration, R. Aaij *et al.*, *Measurement of the ratio of branching fractions $\mathcal{B}(\overline{B}^0 \to D^{*+}\tau^-\overline{\nu}_\tau)/\mathcal{B}(\overline{B}^0 \to D^{*+}\mu^-\overline{\nu}_\mu)$*, Phys. Rev. Lett. **115** (2015) 111803, Publisher's Note ibid. **115** (2015) 159901, arXiv:1506.08614.

[164] Particle Data Group, P. A. Zyla *et al.*, *Review of Particle Physics*, Progress of Theoretical and Experimental Physics **2020** (2020) , 083C01.

[165] F. U. Bernlochner, Z. Ligeti, and D. J. Robinson, *Model independent analysis of semileptonic B decays to D^{**} for arbitrary new physics*, Phys. Rev. D **97** (2018) 075011, `arXiv:1711.03110`.

[166] LHCb Collaboration, R. Aaij *et al.*, *Precise measurement of the f_s/f_d ratio of fragmentation fractions and of B_s^0 decay branching fractions*, Phys. Rev. D **104** (2021) 032005.

[167] Z. Ligeti, M. Papucci, and D. J. Robinson, *New Physics in the Visible Final States of $B \to D^{(*)}\tau\nu$*, JHEP **01** (2017) 083, `arXiv:1610.02045`.

[168] V. Dedu and A. Poluektov, *Towards the precision measurement of CP violation in $B \to D^{*}\mu\nu$ decays at LHCb*, JHEP **07** (2023) 063, `arXiv:2304.00966`.